

UNIVERSIDAD DE CANTABRIA

Departamento de Ingeniería Estructural y Mecánica E.T.S. de Ingenieros Industriales y de Telecomunicación

RESEARCH ON DYNAMIC CHARACTERISTICS OF A DOUBLE-HELICAL TWO-STAGE PARALLEL COMPOUND MARINE GEAR TRANSMISSION SYSTEM

PH.D. THESIS

Guanghe Huo

Santander, 2024

Dissertation for the Doctoral Degree in Engineering

RESEARCH ON DYNAMIC CHARACTERISTICS OF A DOUBLE-HELICAL TWO-STAGE PARALLEL COMPOUND MARINE GEAR TRANSMISSION SYSTEM

Candidate: Guanghe Huo

Supervisor: Prof. Dr. Fernando Viadero-Rueda

Prof. Dr. Miguel Iglesias-Santamaria

Prof. Dr. Yinghou Jiao

Academic Degree Applied

Doctor of Engineering

for:

Speciality: Mechanical Engineering

Affiliation: Ph.D. School

Date of Defence: 12, 2024

Degree-Conferring-

University of Cantabria

Institution:

Abstract

The reducer system is one of the critical core components of the marine propulsion system, tasked with adjusting the output speed of steam turbines or gas turbines to the optimal speed for propeller propulsion. Its dynamic performance is crucial to the overall performance level and the stable, efficient operation of the entire marine power system. Compared to traditional two-stage series structures, the two-stage parallel compound gear system offers advantages such as a higher transmission ratio and a more compact design, which are better suited to the spatial constraints of marine installations. However, the transmission coupling relationships in compound gear systems are complex, making the modeling of flexible large components challenging, with high degrees of freedom in the model equations. Moreover, as the compound gear system experiences additional motion during the ship voyage, the accuracy of modeling significantly influences the analysis of complex movements. Therefore, this paper focuses on a two-stage parallel compound gear transimission system used in ships and proposes a modeling method suitable for this parallel structure. A mechanical model of the ship two-stage parallel compound gear transimission system in the non-inertial reference frame of the planet carrier is establishes, and an improved numerical solution method is proposed. The study investigates the dynamic and static mechanical behaviors and further reveals the nonlinear vibration characteristics associated with its motion states. Finally, dynamic models of the two-satge parallel compound gear transimission system under navigation conditions in two non-inertial reference frames is constructed and the dynamic behavior of the gear system under fundamental ship motion is studied. The main research contents are as follows:

(1) Based on the motion of the carriers and structural characteristics in the two-stage gear system, a hybrid modeling strategy, wherein the first planetary gear set is modeled using a moving reference frame, while the second stage employs a fixed reference frame, is proposed. This approach accounts for additional terms that arise during the modeling process, and through the combination of moving and fixed coordinate systems, the mechanical model of the two-stage parallel compound gear system is established, including quasi-static and dynamic model. By introducing the non-inertial reference frame of the carrier, factors such as Coriolis and centrifugal accelerations are comprehensively considered in this method, effectively addressing the complexities associated with modeling the two-stage parallel compound gear system. Compared to traditional

unified coordinate system modeling methods, this approach successfully overcomes challenges such as extensive transformation matrix calculations, the potential loss of additional terms, and difficulties in solving time-varying stiffness matrices.

- (2) Based on the quasi-static and dynamic model, the static characteristics, including load-sharing properties and global transmission errors, are first analyzed. The effects of planet pin position errors and eccentricity errors on loadsharing properties and global transmission errors are investigated. Furthermore, the accuracy of the proposed modeling strategy is preliminarily explored by analyzing the axial trajectories of components under eccentric error using the static model. Due to the Newmark-beta method isn't suitable for solving directly equations with time-varying stiffness matrix, and the accumulation and accuracy are ignored during the solving process. Therefore, a Newmark-beta method is improved by proposing a strategy to verify the relative error during the calculation process of each loop iteration. By using this method, the dynamic response of the system is obtained and the dynamic and static vibration results are compared to verify the accuracy of the dynamic model. Finally, the effects of gravity, centrifugal force, and various errors on the dynamical characteristics are investigated. It is found that the vibration frequency of the output shaft of the studied compound gear system is related to the meshing phase and the meshing frequency and its harmonic frequency is obtained through the analysis of the global transmission error. Compared with the traditional Runge-Kutta method, the improved Newmark-beta method is computationally fast and suitable for solving the equations of multiple degrees of freedom and time-varying stiffness. The dynamic model of the marine gearbox system is able to take into account a variety of error factors, which comprehensively verifies the accuracy of the proposed dynamic model, as well as demonstrates the ability of the dynamic model to accurately capture errors and more accurately reflect the vibration characteristics of the actual system.
- (3) Regarding the nonlinear dynamic characteristics of the two-stage parallel compound gear train, a pure torsional nonlinear dynamics model of a two-stage parallel compound gear system for ships is firstly developed. The bifurcation way of this compound gear system, which transforms its state of motion from chaotic motion to stable periodic motion with the increase of the meshing damping ratio for certain parameters, is revealed as a Hopf bifurcation by the combination of bifurcation diagrams, Poincaré maps, phase trajectories, and time history diagrams. The influence of the speed and the magnitude of the meshing error on its nonlinear characteristics is investigated. Considering the transverse vibration, a translational-torsional nonlinear dynamics model is developed to explore the

nonlinear characteristics. It is shown that, based on the pure torsional model, it is concluded that the period-doubling number of the ultimately stable motion of the compound gear train is related to the least common multiple of the internal meshing stiffness periods of the two stages. Compared with the pure torsion model, the translational-torsion nonlinear dynamics model exhibits more complex motion states, but the period-doubling number of the final stable motion is still related to the least common multiple of multiple exciations' cycles.

(4) Considering the external non-inertial system of the ship hull, combined with the ship working environment and motion characteristics, the mathematical models of absolute acceleration and absolute velocity of the sun and planet gears in two non-inertial systems are derived. The dynamics model of the studied compound gear system in the internal and external non-inertial systems is established. The effects of the ship rocking motion and pitching motion conditions on the dynamics of the components of the compound gear system during normal navigation have been investigated. The study shows that the motion trend of each component of the ship matches well with that of the rocking motion, the maximum rocking angle of the vibration response of the components also agrees with that of the external rocking motion, and the response results prove the correctness of the constructed dynamics model. The analysis of the results of the load sharing ratio of the first stage shows that under the influence of the ship pitching motion, the planet gears exist in disengaged contact, which results in the non-uniformity of the load transferred by the planets and affects the reliability of the whole gear system.

In this paper, based on the combination of moving and fixed coordinate system modelling method, the dynamics model of two-stage parallel compound gear system of ship is proposed, and the research results provide a theoretical basis for the design and maintenance of the compound gear system of the ship, and it has an important role and significance for promoting the development of the two-stage parallel compound marine gear system.

Keywords: Double-helical gear, Planetary gear train, Dynamic modeling, Vibration characteristics, Ship motion

Contents

| ABSTRACT | I |
|---|------|
| CONTENTS | V |
| CHAPTER 1 GENERAL INTRODUCTION | 1 |
| 1.1 RESEARCH BACKGROUND AND SIGNIFICANCE | 1 |
| 1.2 Literature review | 3 |
| 1.2.1 Solving methods of gear meshing stiffness | 3 |
| 1.2.2 Research status on single-pair gear dynamics systems | 4 |
| 1.2.3 Research status on planetary gear system dynamics | 7 |
| 1.2.4 Research status on the double-helical planetary gear train dynamics | 13 |
| 1.2.5 Research status of the marine gear transmission systems | . 14 |
| 1.2.6 A brief analysis of literature review | . 15 |
| 1.3 Research object | . 17 |
| 1.4 Research outline | . 18 |
| CHAPTER 2 MECHANICAL MODEL OF THE DOUBLE-HELICAL TWO- | |
| STAGE PARALLEL COMPOUND MARINE GEAR TRAIN | . 21 |
| 2.1 Preface | . 21 |
| 2.2 CALCULATION OF MESHING ERRORS AND MESH PHASING | . 21 |
| 2.2.1 Calculation of meshing error considering errors | . 21 |
| 2.2.2 Mesh phasing | . 24 |
| 2.3 Translational-torsional quasi-static model of the two-stage | |
| PARALLEL COMPOUND MARINE GEAR TRANSMISSION SYSTEM | . 25 |
| 2.3.1 Static balance equation of sun and planet #i meshing | . 28 |
| 2.3.2 Static balance equation of ring and planet #i meshing | . 30 |
| 2.3.3 Static balance equation between carrier and planet #i | . 32 |
| 2.3.4 Quasi-static equation of the overall system | . 34 |
| 2.4 Translational-torsional dynamic model of the two-stage parali | LEL |
| COMPOUND MARINE GEAR TRANSMISSION SYSTEM | . 35 |
| 2.4.1 Kinematic analysis of different components in the moving coordina | te |
| system | . 37 |
| 2.4.2 Dynamic model of sun and planet #i meshing | |
| 2.4.3 Dynamic model of ring and planet #i meshing | . 41 |
| 2.4.4 Dynamic model of carrier and planet #i | |
| 2.4.5 Dynamic model of bearing | . 43 |

| 2.4.6 Dynamic model of the beam element | . 44 |
|--|------|
| 2.4.7 Dynamic model of the overall system | . 45 |
| 2.5 Brief summary | . 47 |
| CHAPTER 3 STUDY ON THE STATIC CHARACTERISTICS OF THE | |
| DOUBLE-HELICAL TWO-STAGE PARALLEL COMPOUND MARINE GEA | ٩R |
| TRANSMISSION SYSTEM | . 49 |
| 3.1 Preface | . 49 |
| 3.2 Study on load sharing ratio and transmission error | . 49 |
| 3.2.1 Load sharing ratio and transmission error analysis without error in | |
| fixed sun configuration | . 50 |
| 3.2.2 Load sharing ratio and transmission error analysis considering error | r in |
| fixed sun configuration | . 51 |
| 3.2.3 Influence of different supporting configuration of sun on load sharing | ng |
| ratio | . 57 |
| 3.3 Study on eccentricity error | . 58 |
| 3.3.1 Analysis of system states considering eccentricity error | . 58 |
| 3.3.2 Analysis of meshing parameters in compound Gear train considering | _ |
| eccentricity error | |
| 3.3.3 Influence of eccentricity error on orbit | |
| 3.4 Brief summary | . 80 |
| CHAPTER 4 STUDY ON THE DYNAMIC CHARACTERISTICS OF THE | |
| DOUBLE-HELICAL TWO-STAGE PARALLEL COMPOUND MARINE GEA | |
| TRANSMISSION SYSTEM | . 83 |
| 4.1 Preface | . 83 |
| 4.2 Improved Newmark- <i>B</i> numerical solution method | . 83 |
| 4.3 Analysis of dynamic vibration response results | . 85 |
| 4.3.1 Comparison of sun orbit between dynamic model and quasi-static | |
| model | . 85 |
| 4.3.2 Comparison of planets orbit between dynamic model and quasi-stat | ic |
| model | . 87 |
| 4.3.3 Comparison of the load sharing ratio between dynamic model and | |
| quasi-static model | . 90 |
| 4.3.4 Vibration angular displacement in dynamic model | . 90 |
| 4.4 Influence of the gravity force and centrifugal force on dynamic | С |
| VIBRATION CHARACTERISTICS | . 92 |
| 4.4.1 Influence of the gravity force on dynamic vibration characteristics | . 92 |
| 4.4.2 Influence of the centrifugal force on dynamic vibration characterist | ics |

| | 98 |
|---|-----------|
| 4.5 Analysis of coupling relationship between two stages | |
| 4.5.1 Influence of indexing error on the coupling relationship | 101 |
| 4.5.2 Influence of run-out error on the coupling relationship | 102 |
| 4.6 Brief summary | 104 |
| CHAPTER 5 NONLINEAR DYNAMIC MODEL AND ANALYSIS OF | THE |
| DOUBLE-HELICAL TWO-STAGE PARALLEL COMPOUND MARIN | E GEAR |
| TRANSMISSION SYSTEM | 107 |
| 5.1 Preface | 107 |
| 5.2 Pure torsional nonlinear dynamic model | 107 |
| 5.2.1 Pure torsional modeling | 107 |
| 5.2.2 Relative displacements | 108 |
| 5.2.3 Equations of motion | 109 |
| 5.2.4 Torsional results and discuss | 109 |
| 5.2.5 Dimensionless equations of motion | 115 |
| 5.3 Nonlinear dynamic characteristics analysis of the pure to | RSIONAL |
| MODEL | 118 |
| 5.3.1 Contact separation specification | 118 |
| 5.3.2 Influence of the damping ratio coefficient on the dynamic res | ponse 121 |
| 5.3.3 Influence of damping ratio coefficient and input speed on the | = |
| response | |
| 5.3.4 Influence of the meshing error amplitude on the dynamic resp | onse 132 |
| 5.4 Translational-torsional nonlinear dynamic model | |
| 5.4.1 Relative displacement | |
| 5.4.2 Equation of motion | |
| 5.4.3 Dimensionless equations of motion | 138 |
| 5.5 Nonlinear dynamics characteristics analysis of the | |
| TRANSLATIONAL-TORSIONAL MODEL | 141 |
| 5.5.1 Influence of the damping ratio coefficient on the dynamic res | ponse 141 |
| 5.5.2 Influence of the speed on the dynamic response | 143 |
| 5.5.3 Analysis of the motion states in the translational-torsional co | _ |
| nonlinear model | 144 |
| 5.6 Brief summary | |
| CHAPTER 6 ANALYSIS OF THE DYNAMIC CHARACTERISTICS O | F THE |
| DOUBLE-HELICAL TWO-STAGE PARALLEL COMPOUND MARIN | E GEAR |
| TRANSMISSION SYSTEM UNDER NAVIGATIONAL CONDITIONS | 151 |
| 6.1 Preface | 151 |

| 6.2 Special ship motions in navigational states | |
|---|-------|
| 6.2.1 Rocking motion | |
| 6.2.2 Picthing motion | 152 |
| 6.3 Dynamics model of the two-stage parallel compound marine g | EAR |
| TRANSMISSION SYSTEM IN NON-INERTIAL REFERENCE FRAME | 153 |
| 6.3.1 Kinematic analysis of components in two non-inertial frames | 154 |
| 6.3.2 Dynamic model of the two-stage parallel compound marine gear | |
| transmission system in two non-inertial frames | 156 |
| 6.4 Dynamic characteristics analysis of compound marine gear | |
| TRANSMISSION SYSTEM CONSIDERING SHIP ROCKING MOTION | 157 |
| 6.4.1 Calculation of generalized acceleration considering ship rocking | |
| motion | 157 |
| 6.4.2 Influence of ship rocking motion on the vibrational response of | |
| central components | 159 |
| 6.4.3 Influence of ship rocking motion on the vibration response of pla | inets |
| | 163 |
| 6.4.4 Influence of ship rocking motion on the motion state of the comp | ound |
| gear train | 164 |
| 6.5 Dynamic characteristics analysis of compound marine gear | |
| TRANSMISSION SYSTEM CONSIDERING SHIP PITCHING MOTION | 166 |
| 6.5.1 Calculation of generalized acceleration considering ship pitching | ; |
| motion | 166 |
| 6.5.2 Vibration response analysis of components considering ship pitch | ning |
| motion | 169 |
| 6.5.3 Influence of picthing motion on the meshing characteristics | 171 |
| 6.6 Brief summary | 172 |
| CONCLUSIONS | 175 |
| REFERENCES | 179 |
| APPENDIX | 197 |
| PAPERS PUBLISHED IN THE PERIOD OF PH.D. EDUCATION | |
| ACKOWLEDGEMENT | |
| | |

Chapter 1 General Introduction

1.1 Research background and significance

Gear structures have been essential and indispensable components in many machines, significantly enhancing productivity since their invention. The planetary gear train, also known as the epicyclic gear train, is one such gear structure and finds widespread use in various mechanical industries, including helicopters, wind turbines[1–3], robot arms[4], and other rotary machinery. As shown in Fig.1-1, a basic planetary gear train comprises a sun gear, a ring gear, a carrier, and N planet gears. The sun gear, ring gear, and carrier are regarded as the central components and can be configured in various combinations of input and output members. This configuration allows for the attainment of different transmission ratio values and rotation directions for the output members based on the kinematic relationships[5].

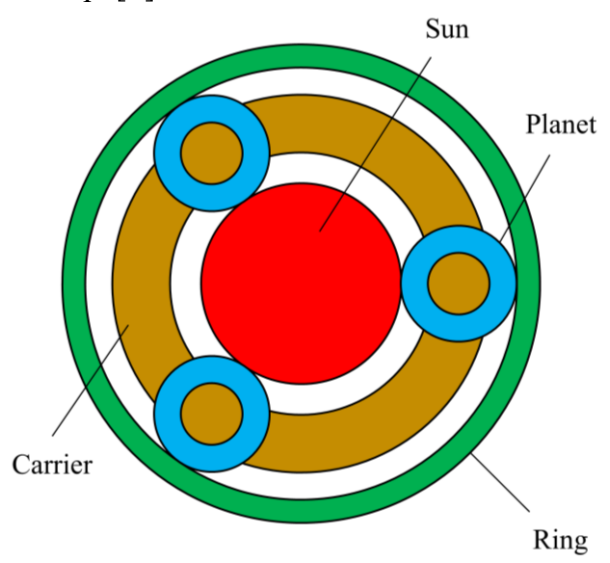


Fig.1-1 Basic components of planetary gear train

Specifically speaking, compared to a pair of gears, the planetary gear train transmission offers several advantages. One of the main benefits is power split. The input power is theoretically equally distributed among each path of the planet gears, reducing the load carried by each planet gear and thereby extending its working life. Another significant advantage is its compact layout, i.e., enabling the accommodation of more gears within the same space, thus enhancing flexibility in the application. Addationally, other advantages include a high transmission ratio, smooth operation, efficient power transmission, durability, the

capability for compound stages designs, and so on [6].

In many industries, planetary gear transmissions utilize either spur or helical gears, the former are commonly employed in heavy-load machinery operating at low speeds, whereas the latter are easily found in automatic transmission requiring low vibration and noise levels. This reference is due to the smoother and quieter nature of helical transmissions compared to spur gear transmissions. However, helical gear transmissions generate significant axial forces, necessitating the use of thrust bearings for offsetting. Consequently, in industries with heavy-load and high-speed such as Geared Turbofan Engines (GTF), a double-helical planetary gear system is often the preferred choice, as depicted in Fig.1-2.

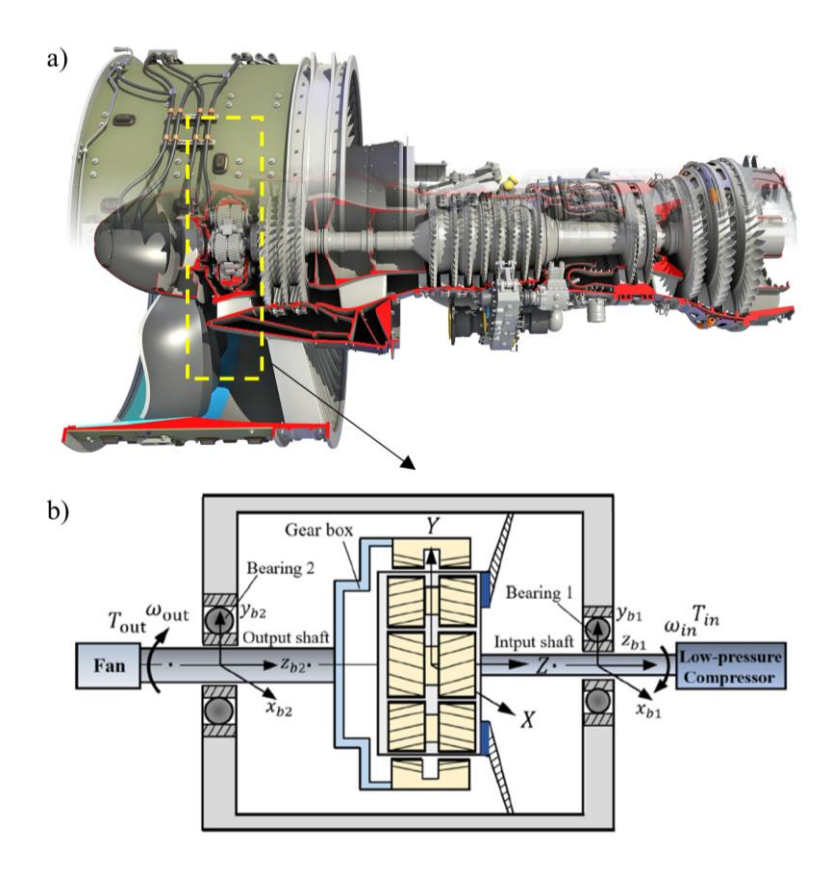


Fig.1-2 Diagram of GTF. a) Engine (from Internet) and b) Fan drive gear system [7]

In practical applications, despite the perfection of gear designs and the implementation of vibration reduction measures, vibration and noise inevitably exist. Currently, the benchmark for high-quality machines is to control vibration and noise within specific tolerances.

Moreover, due to the complexity of planetary gear transmissions and the multitude of meshing contacts, accurately obtaining the dynamic behavior of planetary gear systems remains a formidable challenge. Factors such as timevarying meshing stiffness, dynamic positioning, and various errors further

complicate this task, especially for configurations with multiple stages and complex structures. Many aspects of planetary gear dynamics, especially in terms of coupling dynamics, remain inadequately understood.

Therefore, in this research, the focus is on the compound planetary gear system, with the objective of establishing a coupling dynamics model. This model incorporates rotor dynamics, gear system dynamics, nonlinear dynamics, and other methodologies, while comprehensively considering the working environment and nonlinear factors. Investigating the dynamic characteristics of the system is deemed essential and meaningful in light of complexities.

1.2 Literature review

According to existing research articles, the modeling for gears has developed from a linear time-invariant model and a linear time-varying model to a nonlinear time-varying model. One of the primary time-varying parameters is the meshing stiffness. Thus, research on the meshing stiffness remains hotpot in the literature.

1.2.1 Solving methods of gear meshing stiffness

In general, gear meshing stiffness (GMS) represents one kind of stiffness excitation, and displacement excitation is another main factor. The variation in meshing stiffness depends on the number of teeth pairs engaged in a meshing cycle, which is related to the contact ratio.

1.2.1.1 Spur Gear

Typically, the contact ratio of spur gears ranges between 1 and 2, i.e., contact alternating instantaneously between one and two pairs of teeth. Currently, analytical methods, finite element methods(FEM), and hybrid methods are the primary approaches for calculating the meshing stiffness of spur gears.

Kuang and Yang [8] proposed an analytical method, namely Kuang and Yang method. Cai and Hayashi [9] proposed another analytical method known as Cai and Hayashi method, which calculates the meshing stiffness of a pair of spur gears, based on mean stiffness and contact ratio. In recent years, the development of analytical methods has been developed rapidly, some authors [10 - 17] enhanced these methods to account for factors such as tip relief, profile modification, actual manufacturing, tooth faults (e.g., pitting and wear), friction and so on.

Since the 21st century, due to the advancements in computer computing processing power, the finite element method has been gradually developed. Therefore, many researchers have begun using FEM and hybrid method. Cooley [18] and others [19 - 21] have employed FEM to calculate meshing stiffness.

For hybrid models, Vedmar and Henriksson [22] proposed a hybrid approach in 1998, which combines global linear deformation and local nonlinear deformation. Fernandez et al [23] proposed an advanced hybrid method for calculating the meshing stiffness of external gears based on the FEM and Hertzian contact theory, and verified the model by comparing it to Cai method and Kuang method. Subsequently, Iglesias et al [24] expanded this method to calculate the meshing stiffness for internal gears, accounting for mesh coupling of gear body deformation, and applied it to planetary gear systems. Zheng et al [25] developed an analytical-FEM method to incorporate the effect of centrifugal force into the calculation of mesh stiffness.

1.2.1.2 Helical gear

Unlike spur gears, the engagement and disengagement of teeth in helical gears occur gradually, resulting in a smoother transmission compared to spur gears.

Based on three methods used of spur gear, the slice method [26 - 30] is the most commonly used method for calculating the meshing stiffness of helical gear. Moreover, several factors [31 - 33], such as time-varying backlash, root profile, and spatial crack, have been taken into account.

1.2.2 Research status on single-pair gear dynamics systems

The investigation of gears can be tracted back to the works of Ross [34], Bckingham [35] from the 1920s to the 1930s. In the 1950s, Tuplin [36] employed mass-spring models to calculate the dynamic load of high-speed gear pairs, and tooth dynamic loads was their primary research focus. Subsequently, Gregory et al [37] conducted experimental studies to extend the theoretical analysis results of spur gear pairs. Since the 1980s, models, incorporating addational components such as shafts, rotors, bearings, and squeeze film dampers, appeared [38 – 40].

For a pair of gears, numerous models have been proposed and developed in the past decades. Research on gear pair models is mainly divided into transmission error or quasi-static models, single and multi-degree of freedom models, and linear and nonlinear models.

1.2.2.1 Transmission error

Transmission error and related aspects are another area of study for spur, helical or double-helical gears. Due to losses in the transmission process, the actual position of the output shaft may deviate from the ideal position, resulting in transmission error.

In 1978, Mark [41] derived a general expression for the static transmission error (STE). In 1986, Tavakoli and Houser [42] employed an optimization algorithm to study the minimization of STE. Ozguven and Houser [43] studied dynamic mesh and tooth load by using loaded STE and dynamic transmission error (DTE), analyzed subsequently the influence of mesh stiffness, damping, and error. In 1996, Houser et al [44] compared the predicted DTE and STE with measured results to validate the prediction model. Zhang and Fang [45] presented the load transmission error of helical gear with modified tooth surfaces in 1997. Song and Singh [46] developed an analytical expression to predict DTE by considering friction, results showed that the influence of sliding friction on the DTE of helical gears could be ignored compared to spur gears. By considering tip contact that can happen when a teeth pair engages, a semi-analytical model and a non-Hertzian contact mechanics model were combined by Bruzzone et al [47] to study static transmission error. Lee et al [48] proposed an analytical method to calculate the TE and analyzed the range of the transmission error caused by various uncertainties such as mechanical and thermal deformation.

In addition, several authors have conducted significant work based on transmission errors. Lin et al [49] utilized STE to predict dynamic loading responses. In 2006, Velex and Ajmi [50] presented some original formulas simulating gear excitations by using simulated or measured transmission errors, and validated their effectiveness by comparing results with references. The following year, the same authors [51] derived analytical expressions for dynamic tooth loads or tooth dynamic factors based on the harmonics of the load quasistatic transmission error. In 2011, Velex et al [52] also presented approximate analytical results for quasi-static transmission errors in spur and helical gears with low and high contact ratios. Lin and He [53] proposed an analytical method to determine transmission errors in helical gears considering assembly errors, machining errors, and tooth modifications. Velex et al [54] presented analytical formulas for the optimum combinations of profile relief and lead crown for narrow-faced helical gears based on transmission error.

In recent years, both theoretical and experimental research on double-helical gear pairs has been done. In 2015, Kang and Karhaman [55] conducted theoretical and experimental studies on the dynamic behavior of double-helical gear pairs. They built a double-helical gears test plotform, allowing for the adjustment of left and right staggered angles, and implemented a measurement system capable of capturing three-dimensional vibration motion and dynamic transmission errors under high-speed conditions. The accuracy of the proposed model in predicting 3D gear vibration was demonstrated through direct comparison with measured data. It was shown that the left and right stagger angle is the most critical

parameter affecting the dynamic response. In 2021, the same authors [56] researched the quasi-static characteristics of double-helical gear pairs under low-speed conditions. Their focus was on the key design and manufacturing parameters related to double-helical gears. They directly compared measured and predicted values, including loaded static transmission errors, axial stress, root stress, and right-to-left load-sharing factors, to validate quasi-static models. Consequently, these two research studies contribute to a deeper understanding of the quasi-static behavior of double-helical gear pairs.

1.2.2.2 Research methods of single-degree-of-freedom and multi-degree-of-fre edom dynamical systems

At the beginning, single-mesh gear models with a single degree of freedom (pure torsional models) predominated. The simplest model was the pure torsional model, which considered only one DOF for each component. However, as the need for more accurate actual models, additional factors such as damping and friction were incorporated.

Amabili and Rivola [57] proposed a single-degree-of-freedom (SDOF) model with meshing damping, in which the damping was assumed to be proportional to mesh stiffness. Li and Kahraman [58] proposed a transient, non-Newtonian, mixed electrohydrodynamic lubrication model of spur gear pairs for capturing the transient behavior of the contact process from the root to the top of gear teeth. The following year, the same authors [59] presented a two-degree-of-freedom (2DOF) interface damping model for gear pairs.

Friction is a common factor considered in the gear dynamic model. Vaishya and Singh [60] presented a dynamic model incorporating sliding friction to accurately obtain dynamic meshing force among gear teeth.

Subsequently, models with more DOF were studied. Various studies [61 - 66] explored coupling motion among transverse, torsional, and axial, some of them also took eccentricity and gyroscopic effect into account.

1.2.2.3 Research methods of nonlinear dynamical systems

Nonlinear factors have a significant influence on gear dynamics, particularly at high speeds.

Wang et al [67] conducted a review of basic concepts, mathematical models, and solving methods for nonlinear gear-driven systems. They summarized the effects of nonlinear factors (such as backlash, time-varying meshing stiffness, and vibro-impact) on both linear and nonlinear systems and discussed critical issues in further research on the nonlinear vibration.

Gill-Jeong et al [68] analyzed the effects of viscosity, film width, and backlash on the nonlinear dynamic behavior considering lubrication and sliding friction.

Zhou et al [69] established a nonlinear model considering backlash, transmission error, and meshing stiffness. They studied nonlinear dynamic response using the Incremental Harmonic Balance Method (IHBM) and observed jump discontinuity phenomena caused by backlash.

Various excitations, including vibro-impacts and periodic excitation [70,71], were considered to study nonlinear behavior.

Bifurcation and chaos are typical nonlinear phenomena. Chang-Jian et al [72] established a single-degree-of-freedom spur gear system with and without nonlinear suspension, analyzed dynamic orbits of the system using bifurcation diagrams and phase diagrams. They demonstrated a diverse range of periodic, subharmonic, and chaotic behaviors.

Xia et al [73] developed a nonlinear model considering time-varying meshing stiffness, gear backlash, static transmission error, and tooth-face friction. They researched bifurcations and chaos characteristics of the system under lightly and heavily loaded conditions and investigated in detail the parametric effects of rotational speed, damping ratio, and gear backlash on the dynamic behaviors.

Other studies [74 - 83] have explored errors (eccentricity, pitch deviation), multi-meshing, faults (cracks and wear), tooth features, modifications, Hertz contacts, and rattle, contributing to the understanding of nonlinearity in nonlinear gear dynamics.

So far, research on gear pairs models has become increasingly sophisticated, with consideration for a wide range of factors including lubrication, friction, internal excitation, noise, and rattle prediction. Additionally, there is a growing interest in gear vibration control and fault diagnosis. Concurrently, numerical mathematical solving methods have been developed to address the complexities of differential equations.

1.2.3 Research status on planetary gear system dynamics

Currently, the research on planetary gear is still a focal point, with a plethora of analytical modeling, numerical analysis, and experimental studies focusing on both static and dynamic aspects of planetary gear systems, primarily centered around spur or helical configurations. However, compared to spur and helical gears, research work on double-helical gears, especially for planetary gear trains, has been relatively slow. Nonetheless, over the past two decades, planetary gear sets have found extensive applications across various industries such as

automotive, aerospace, wind power generation, and marine. Simultaneously, double-helical gears, also known as herringbone gears, offer distinct advantages over their spur and helical counterparts. Consequently, in recent years, several universities and scholars have initiated studies on the dynamic characteristics of double-helical planetary gear systems.

1.2.3.1 Dynamic modeling methods

Planetary gear models can be categorized based on degrees of freedom (DOF) into 1-Dimensional models (pure torsional models), 2-Dimensional models (transversal-torsional models), and 3-Dimensional models (transversal-torsional-axial models). According to modeling methods, planetary gear models can also be divided into analytical models (lumped mass method), Finite element models, and hybrid models. Additionally, planetary gear models can be classified based on equations as linear time-invariant models, linear time-varying models, and nonlinear time-varying models. Time-varying parameters consist of meshing stiffness, damping, contact ratio, and others, while nonlinear parameters include backlash, lubrication, and more.

According to the research content, the research on planetary gear systems can be mainly categorized into three categories in terms of vibration characteristics: free vibration, forced vibration, and vibration control. More specifically.

Cooley and Parker [84] summarize the dynamic research of planetary gear system in paper that published in past 20 years, as shown in Fig.1-3, which can be seen from Fig.1-3 that there is an overall upward trend for vibration research of planetary gear system. In this review paper, mathematical models, most of which was lumped-parameter models, vibration mode, dynamic force response including linear and nonlinear equations, mesh phasing, high-speed effect such as gyroscopic, errors effects and experiment were studied and analyzed.

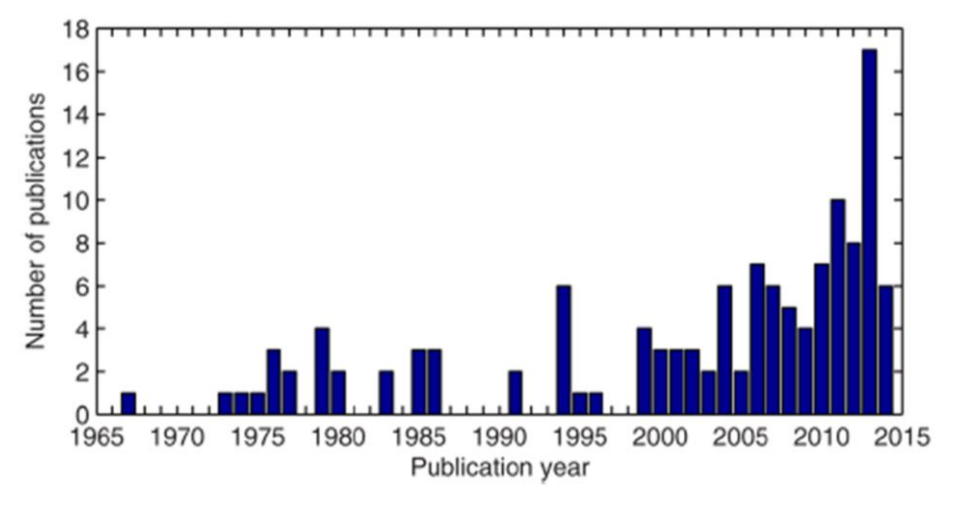


Fig.1-3 Histogram of research papers on vibration of planetary gear system

In the lumped mass model, the gear body is assumed to be rigid, while the contacting teeth are considered to be flexible, and the entire gear mass is seen as one single center point. Kahraman [85] could develop the first 3D dynamic model of a single-stage helical planetary gear train with full DOFs based on the lumped parameter method, as illustrated in Fig.1-4. In this paper, meshing stiffness was assumed to be constant, and a linear time-invariant model was presented. A bending-torsional-axial coupling model of a double-helical gear system with journal bearings considered was developed by Yin et al [86], and they analyzed the influence of external excitation and internal parameters on the dynamic response.

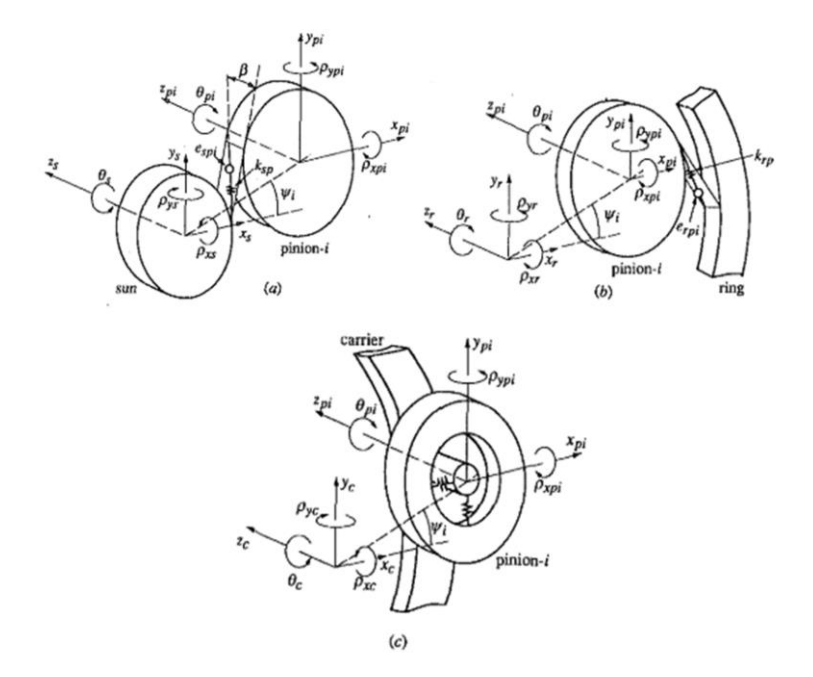


Fig.1-4 Dynamic models of (a) a sun/planet pair, (b) a ring/planet pair, and (c) a carrier/planet pair.

With the development of computers, FEM offers the advantage of calculation speed. In FEM, all parts, including gear bodies, contacts, and bearings are defined to be flexible. Combining the lumped mass method, many finite element models [87] and hybrid models [88] have been developed. In 2006, Abousleiman and Velex [89] introduced a hybrid 3D model to analyze the quasi-static and dynamic behavior of epicyclic gear systems, where deformable rings and carriers were modeled via using beam elements. This approach served as a reference for modeling flexible components. The following year, the same authors [90] studied the quasi-static and dynamic behavior of spur and helical gears with flexible parts, demonstrating the feasibility of the proposed model and the necessity of considering flexible components. In 2019, Velex et al [91] explored the influence

of tooth modifications on dynamic behavior.

Liu et al [92] proposed a dynamic model of a pair of double-helical gears by using the hybrid-defined user elements, with experimental results matching well with simulation results in terms of meshing frequencies and vibration responses.

Planetary dynamic models with elasticity components have been considered by some researchers since 2000. Abousleiman et al [89] presented a hybrid 3D model to study static and dynamic behavior of planetary/epicyclic gears with deformable parts such as ring-gears and carriers, demonstrated the potential of the proposed hybrid model. Kahraman et al [93] studied the effect of flexibility on the dynamic of planetary gear systems and indicated that it was necessity of considering deformable body analysis to predict overall planetary gear set modes with flexible gear rims.

Furthermore, in recent years, an increasing number of scholars have utilized the elastic-body method to establish dynamic models. Wang et al [94] considered the flexible pins to research the load-sharing characteristics of herringbone planetary gear systems in GTF, with results indicating that Montestruc pins exhibited the best load-sharing performance among the four types of pin models. Ericson and Parker [95] combined experimental measurements with finite element simulations to study the importance of mode of the elastic-body, especially for elastic ring gears, which may lead to excessive noise and other issues. Guan et al [96] introduced a new multibody dynamic model of planetary gear systems considering elastic shaft-ring gears and studied the influence of elasticity on the accuracy of the transmission and vibration intensity of light-weight gears. Ge et al [97] considered the ring as a flexible part to accurately obtain internal meshing stiffness.

1.2.3.2 Natural frequencies and mode

Natural frequencies and modes are fundamental characteristics of planetary gear systems, and research in this area has been extensive.

Some scholars began studying modes with single-stage planetary gear trains. In 1994, Kahraman [98] proposed torsional models for planetary gear sets and derived closed-form expressions for natural frequencies and modal shapes [85] applicable to planetary systems with any number of planets. In 1995, Saada and Velex [99] proposed a planetary group dynamics model to study the influence of gear meshing stiffness and support stiffness on the natural frequency of the system. Subsequently, in 1999, J. Lin and R.G. Parker [100] established a 3DOF translation-torsion model for spur planetary gear trains and investigated its natural frequencies and vibration modes. In 2007, Parker et al [101] explored the structured vibration mode and natural frequency properties of compound

planetary gears, and results showed that the vibration modes were classified into rotational, translational, and planet modes and the unique properties of each type.

Multi-stage systems have also been studied. In 2014, Sun et al [102] analyzed the natural frequency and coupled mode characteristics of multi-stage planetary gear systems, which developed research of multi-stage planetary gear system in this area. Rotational, translational, and planet modes were identified as the main three modes, with coupling observed between planetary stages in each rotational and translational mode. The following year, the same authors [103] investigated the sensitivity of natural frequencies and coupled modes to system parameters of multi-stage planetary gears.

1.2.3.3 Research on load sharing characteristics and mesh phasing

Another research focus is load sharing characteristics, as good load sharing can evenly distribute stress among planet gears, reduce unwanted vibration and noise, and prolong the working life of planetary gear systems.

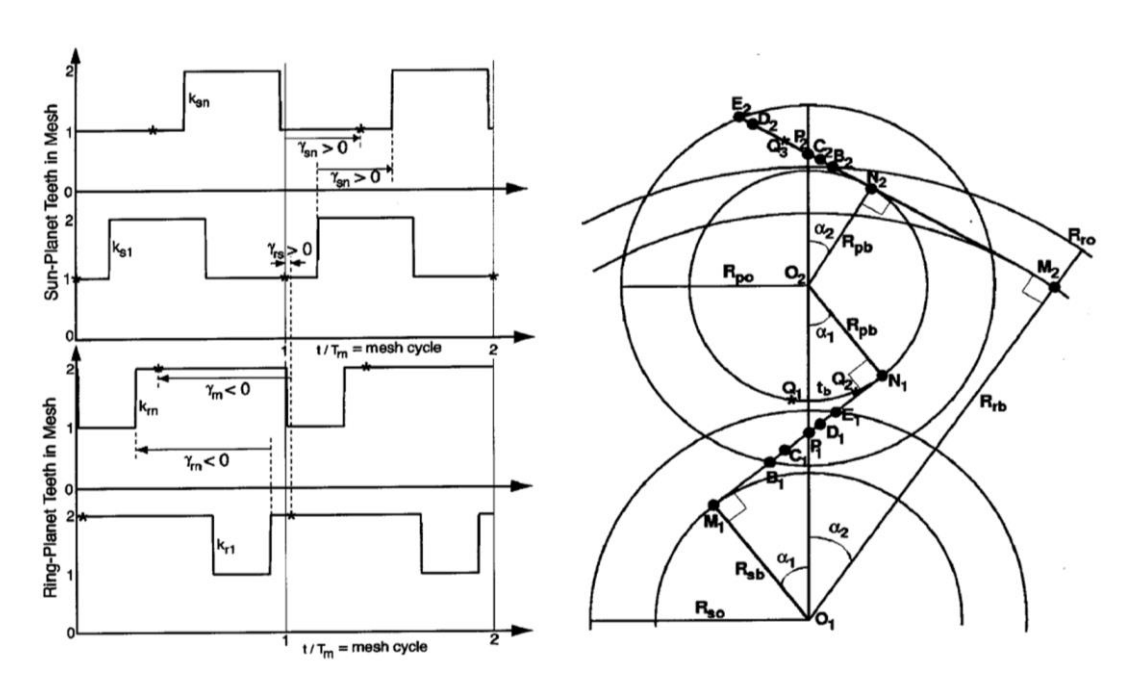
Kahraman et al [104] pioneered the study of load sharing characteristics of planetary gear systems in 1990s, and numerous model [105 - 112] have since been developed under a variety of conditions. Singh [113] proposed a generalized formulation for load sharing behavior in planetary gear trains with any number of planets.

Iglesias et al [114] studied the influence of error and configuration on load sharing characteristics, while Sanchez-Espiga et al [115] summarized the influence rules of common errors (such as tooth thickness and pinhole position errors) on load sharing ratio based on different mesh phasing. The following year, the same authors [116] proposed a simple and effective model using virtual tooth root strain-gauges method to evaluate the effect of mesh phasing on load sharing ratio. In subsequent work, they [117] expanded this approach by considering the strain of more components to study load sharing ratio.

In 2021, Ge et al [97] theoretically and experimentally conducted the study on the load sharing properties of planetary gear systems, with results showing that the error of load sharing coefficient calculated by theory and experiment was less than 5%.

Mesh phasing is a crucial factor that significantly influences the dynamic response of planetary gear trains. It is determined based on the basic parameters such as the number of teeth on the gears and the number of planet gears. There are five main mesh phasing relationships: equally spaced in-phase (ESIP), equally spaced sequentially phased (ESSP), non-equally spaced in-phase (NESIP), non-equally spaced sequentially phased (NESSP) and non-equally spaced arbitrarily phase (NESAP) [115].

The study of mesh phasing was initiated by Kahraman and Parker. Kahraman [85] investigated the effects of planet mesh phasing on dynamics, while Kahraman et al [118] provide the first generalized phasing formulation for planetary gear systems with N planet. Parker and Lin [119] given an analytical calculate formular for calculating adjacent sun-planet meshing or ring-planet meshing. They also provide mesh phasing relationships between sun meshes with planet and ring meshes with same planet, such as S-P1 and R-P1, based on detail mesh processes, as depicted in Fig.1-5. Subsequently, many researchers referenced these formulas in their work [119]. In 2011, Guo and Parker [120] developed general analytical formular for mesh phase relations in compound planetary gear sets based on the work of Parker and Lin [119]. Canchi and Parker [121] investigated the effect of mesh phasing and contact ratio on the parametric instabilities of planetary gear rings. Wang and Parker [122][123] analyzed mesh phasing-based spectra of quasistatic deformations and studied the impact of planet mesh phasing on the vibration of planetary gear systems.



- (a) Mesh phase quantities γ_{sn} , γ_{rn} and γ_{rs}
- (b) detail of mesh process

Fig.1-5 Diagram of mesh phasing in a planetary gear system

Despite advancements in manufacturing and processing technology, common errors remain inevitable in gear systems. Numerous studies [106,124 - 129] have explored the influence of errors, which include eccentricity error, radius error, tangential error, and assembly error, on the modeling and dynamics of planetary gear systems.

1.2.4 Research status on the double-helical planetary gear train dynamics

With the development of automatic machining centers and the improvements in precision, the application of double-helical gears and herringbone gears in modern industry has become increasingly popular, particularly in large machinery such as gas turbines and aero engines. Over the past 10 years, significant research has been conducted on double-helical planetary trains, covering dynamic modeling, tooth contact analysis, load-sharing characteristics analysis, nonlinear analysis, and more.

In 2013, Sondkar et al [130][131] employed the Euler beam method and lumped mass method to develop a linear, time-invariant dynamic model of a single stage double-helical planetary gear system. They studied the influence of gear teeth stagger on the dynamic behavior. Tan et al [132] provided a modeling method for a double-planetary gearbox based on bond graphs.

Sheng et al [133] investigated the vibration modal properties of double-helical planetary gear trains and obtained three different types of modes: planet mode (PM), rotational-axial mode (RAM), and planet-translational mode (PTM). In 2016, Mo et al [134] established an axial-transverse-torsional dynamic model of double-helical star gear systems with considering machining errors and assembly errors for GTF aero-engines. They analyzed vibration modes, natural characteristics, and dynamic responses, noting differences in vibration modes between the left and right sides in certain orders. K. Khoozani et al [135] considered gyroscopic effects and studied natural frequencies of double-helical planetary gear systems.

In 2014, Velex et al [136] studied the effects of planet position errors and pitch deviations on dynamic tooth loads. Wang et al [137] studied the effect of transmission error excitation, external load, and clearance on dynamic load coefficients. Schlecht et al [138] conducted analyses of loaded tooth contact. Chapron et al [139] examined symmetric linear optimum profile modifications (PMs) for helical and double-helical gears to minimum dynamic tooth loads, and analyzed the sensitivity of optimum PMs to speed and load.

In 2015, Leque [140] pioneered the development of a load sharing model for double-helical epicyclic gear sets, which accounted for various types of manufacturing errors, both constant and time-varying with respect to gear. Subsequently, the study of the orbit under all types of error and the effect rule was conducted. The quasi-static load sharing behavior of double-helical epicyclic gear sets was theoretically investigated based on the proposed 3D model. In 2021, Götz et al [141] from the Technical University of Munich experimentally analyzed

the load-sharing characteristics of double-helical planetary gearboxes under variable working speeds (from 0 to 6800rpm) by using the strain-gauge method. They analyzed the influence of speed on static and dynamic load sharing. Liu et al [142] studied the dynamic characteristics of a split-torque transmission system with double-helical gears, they revealed that modification significantly improved dynamic load characteristics while slightly improving load sharing characteristics.

Lu et al [143] proposed a nonlinear dynamics model of the double-helical planetary gear train by considering sliding friction, time-varying meshing stiffness, backlash, axial stagger, and mesh errors. The study investigated the influence of tooth friction on the periodic vibration and nonlinear vibration.

In 2020, Wang [144] researched the effect of planetary gear/star gear (two common planetary stage) on the transmission efficiency in the closed differential double-helical gear train. Hu et al [145] studied load-sharing analysis of the closed differential planetary transmission gear systems by using theoretical and experimental methods.

1.2.5 Research status of the marine gear transmission systems

Regarding the marine gear transmission system, multi-stage transmission systems is still main structure. The power on ships is derived from multiple steam turbines or gas turbines, which is transmitted through one or more pairs of double helical gears to a large gear, achieving the purpose of speed reduction. This gear is connected to the propeller, driving the ship navigation. Fig.1-6 illustrates a 3D schematic of a typical propulsion system for large ships, which includes high-pressure and low-pressure turbines, with the double-input single-output double-helical gear transmission system as a critical component of the propulsion system. Xu et al [146] from Shanghai Jiao Tong University established a lateral-torsional-axial model of this propulsion system, considering multiple nonlinear and time-varying factors, based on the principles of gear transmission and finite-width journal bearing theory. They studied and quantified the impact of unsymmetrical load parameters on the stability of the entire coupled system. The results indicate that instability phenomena gradually occur with increasing excitation frequency, decreasing load ratio between the two inputs, or decreasing input load values, with more severe vibrations observed in the gear pairs on the low-load side. Furthermore, the vibration amplitude is related not only to load parameters but also to the distance between the gear pairs and the load input. They also concluded that the influence of oil film on system stability is crucial, especially in unstable states. Their research presents the stability boundaries of the propulsion system, providing theoretical references for the optimization and adjustment of load parameters.

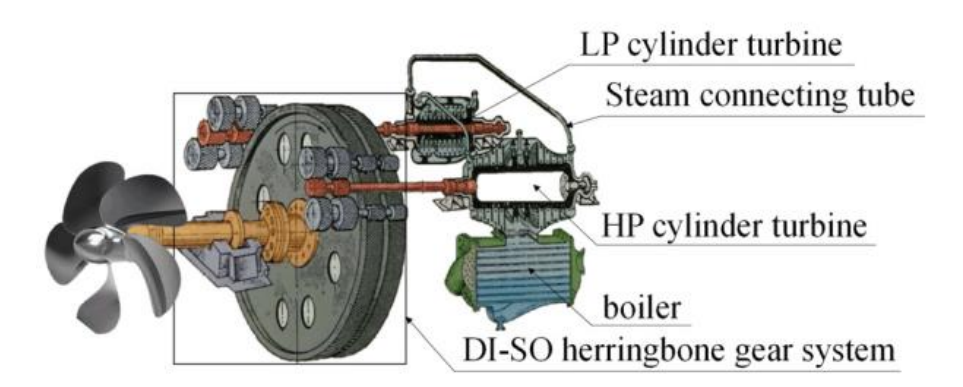


Fig.1-6 Schematic diagram of the power system for a large ship [146]

However, to the author's knowledge, there is currently limited research on two-stage parallel compound gear systems for marine applications, particularly regarding a unified and effective dynamic modeling method, the study of nonlinear motion states, and the development of dynamic models considering the ship navigation conditions.

1.2.6 A brief analysis of literature review

From the current research status, it is evident that scholars worldwide have made numerous attempts to study the dynamics of planetary gear reducer systems. They have established dynamics models of gear systems based on methods such as finite element method, T-beam element method, and potential energy method.

Gears and rolling bearings commonly form a typical gear system dynamics model. Scholars from various countries have developed four main dynamic models of planetary gear reducers, categorized by degrees of freedom as follows:

- (1) Pure torsional model (1st model), (2) Transverse-torsional model (2nd model),
- (3) Transverse-axial-torsional model (3rd model) or transverse-axial-torsion-swing model, and (4) Nonlinear model (4th model). Among these, the first three models are common in practical application.

In terms of time and linearity classification, the gear dynamics model evolves from (1) the linear time-invariant model to (2) the linear time-invariant model with rotation effect, and further to (3) the linear time-varying model, and (4) the nonlinear time-varying model. The time-varying factors mainly consider changes in time-varying meshing stiffness, as the number of teeth involved in meshing changes throughout a meshing cycle. However, the main difference between spur gear and helical gear lies in the range of stiffness change. Nonlinear factors mainly include backlash and friction, affecting the stiffness and damping of the entire system.

Various influences, such as gear eccentricity, tooth profile error, meshing

stiffness in the inertial coordinate system, and the centrifugal force and additional rotational inertia of planetary gear in the non-inertial coordinate system, are considered concerning the vibration characteristics of the gear system. Addationally, measures like gear modification algorithm are proposed to reduce vibration and noise.

However, to the authors' knowledge and the aboved reviewed literature, there are few researches on the complex planetary gear trains, such as the two-stage closed differential double-helical planetary gear system, particularly regarding dynamics research. In order to more accurately analyse the dynamic characteristics of the two-stage parallel compound gear train for marine, reveal the dynamic behaviour of the whole system, and help to improve the design and maintenance level of the ship power system, there is an urgent need to increase the research efforts on the nonlinear dynamic characteristics of two-stage parallel compound gear train used in the ship, as well as the overall power system with regard to the coupling dynamics. According to the references, and combining with the research object of this topic and the influence of the working environment, the existing problems and deficiencies in the study of planetary gear systems, especially in the application of two-stage closed differential double-helical composund gear systems in power systems of ship, are mainly focused on the following aspects.

- (1) Based on the characteristics of the two classical planetary system structures (epicycal planetary gear system and star planetary gear system) in the two-stage parallel compound gear system, there is not uniform modeling method for this compound gear system. If the modelling method of fixed coordinate system is directly adopted in this compound gear system structure, the coordinate transformation matrix needs to be calculated from time to time in the computation process, resulting in problems such as the slow speed of the computation. The research on the general modelling method of two-stage parallel compound gear system is less, and there is an urgent need to propose a mechanical modelling method applicable to this compound gear system structure, so as to calculate the vibration response of the whole compound gear system more quickly and accurately.
- (2) Due to the load sharing characteristic and transmission error are the most basic indexes in evaluating a planetary gear system, and the meshing phase is the basic condition in a planetary gear system that is determined based on the number of teeth and planets. However, based on the existing studies, there are few reports on different meshing phases for two-stage parallel compound gear systems in terms of the load sharing characteristics, global transmission error, and dynamic coupling characteristics.

- (3) Due to the operating conditions of this compound gear system in the ship power system belonging to the characteristics of large transmission torque, compact layout space and complex transmission paths. The transmission between the compound gear system is quite complex and it is challenging to reveal its nonlinear dynamics behaviour. Therefore, it is very meaningful to study the nonlinear dynamics of this two-stage parallel compound gear system.
- (4) When a ship carries out a mission on the sea surface, the working environment of the sea surface cannot be calm all the time, and by the influence of the waves, the common motion of the ship includes rocking, pitching, and other non-inertial system motions belonging to the hull of the ship. Most of the existing studies assume that the planetary gear system is fixed on the ground or the base coordinate system is stationary, and the motion of the ship hull on the sea surface is not taken into account. Although the motion of the ship hull is not like the aircraft engine that does dive in the air, flip, and other large-scale space motion, but by the influence of the non-inertial system of the ship hull, the absolute acceleration of the various parts of the modeling process and the inertial coordinate system are very different, which will result in the inertial motion of the ship. There is a big difference between the inertial coordinate system and the modelling of the hull of ship, which generates additional terms such as Kurtosis acceleration and implicated acceleration, and the impact on the overall dynamic response is also fundamentally different.

1.3 Research object

In this thesis, the research object focuses on a double-helical two-stage compound marine gear reansmission system, also called the closed differential planetary gear trainsmission system. It is composed of two stages: the differential planetary gear train and the closed planetary gear train. The transmission diagram is depicued in Fig.1-7, where the sun, planet and ring gear in each stage are all double-helical gears. To clearly distinguish between the parameters of the two stages, the suffix 1 represents the parameters of the first-stage differential planetary gear train, and the suffix 2 represents the parameters of the second-stage closed planetary gear train, unless otherwise specified.

As illustrated in Fig.1-7, S1, P1, C1 and R1 consist of the differential planetary transmission gear train, while S2, P2 and R2 form the closed planetary transmission gear train. Consequently, the input power and torque are divided into two paths. One path is transmitted from the sun in the 1st stage (S1) to the planet in the 1st stage (P1) and finally output through the carrier in the 1st stage (C1). The other path is transmitted to the sun in the 2nd stage (S2) through the ring in

the 1st stage (R1), then output through the ring in the 2nd stage (R2), and ultimately combined with the output the torque of C1 to the output shaft.

Furthermore, the choice of a double-helical planetary gear train as the research object is motivated by two main reasons. Firstly, planetary gear trains can effectively distribute the input power. Secondly, double-helical gears are capable of counteracting the axial forces generated by the respective helical gear.

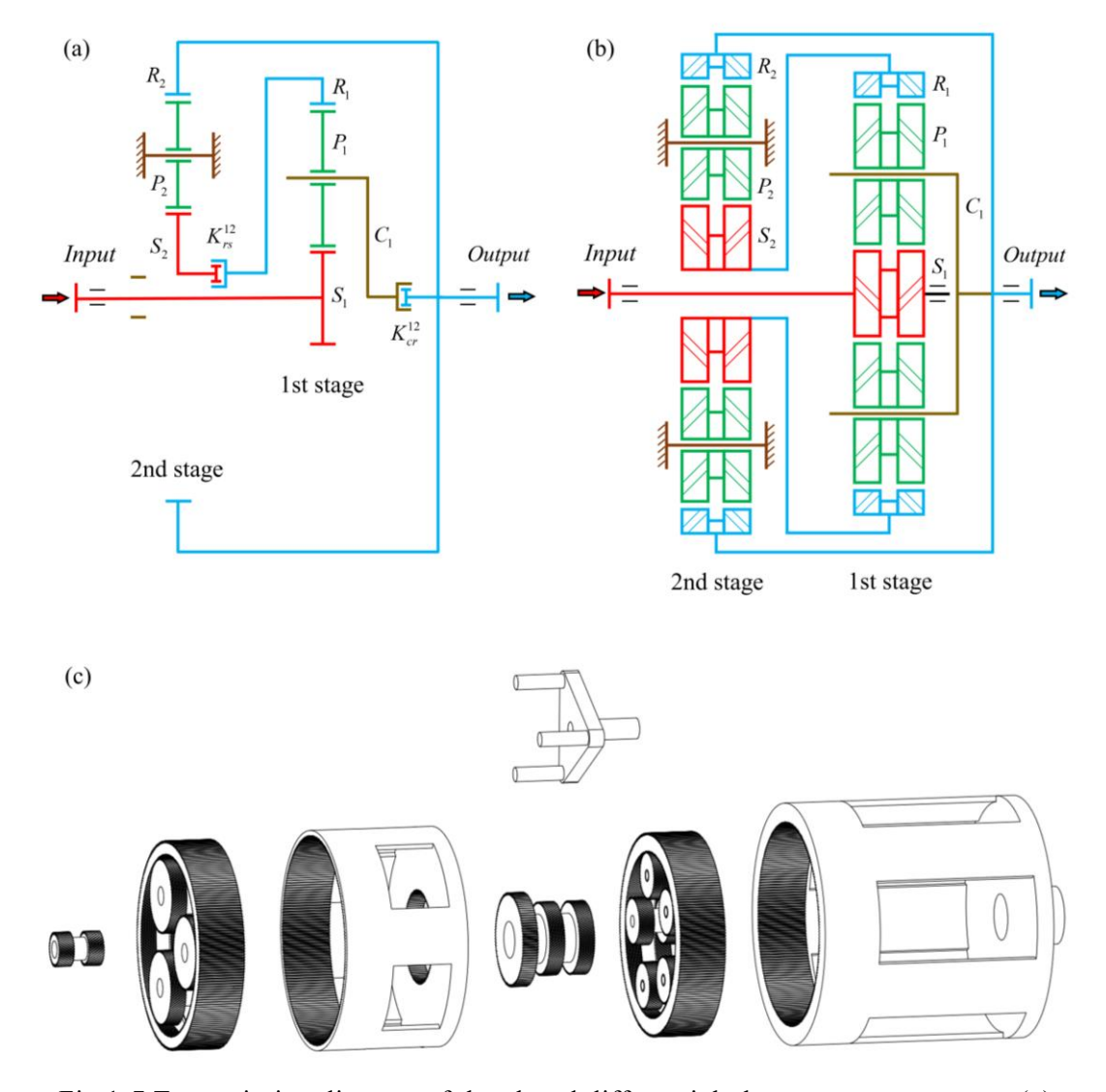


Fig.1-7 Transmission diagram of the closed differential planetary gear system: (a)
Transmission diagram, (b) double-helical, and (c) 3D diagram

1.4 Research outline

In addition to the introduction of Chapter 1, the main contents of this thesis

are as follows:

Chapter 2 is focused on the development of the mechanical model, including quasi-static and dynamic model, of a double-helical compound marine gear transmission set. The results of the quasi-static model are used to verify the accuracy of the established model, expand the modelling method of this parallel compound gear system. The dynamics model of this parallel compound gear system is established by using the finite element method, providing a research basis for the subsequent analyses.

In Chapter 3 and Chapter 4, based on the quasi-static model, the global transmission error and the load sharing ratio of the two-stage parallel compound gear system are calculated. The influence of the pin position error and eccentricity error on quasi-static characteristics such as the load sharing ratio and global transmission error are analysed. The important law that the excitation frequency of the error for the global transfer error is related to the meshing phase is obtained. In addition, the influence law of eccentricity error on the axial trajectory of each component in the compound gear system is also explored in detail, and it is obtained that the shape of the axial trajectory of a gear with eccentricity error is related to the number of teeth of that gear. Based on the dynamic model, aiming at the time-varying nonlinear dynamic equations, an improved Newmark-beta numerical method is proposed to study the dynamic vibration characteristics and coupling characteristics of the investigated compound gear system.

In Chapter 5, the pure torsional and tramslational-torsional nonlinear dynamics model containing backlash, time-varying meshing stiffness and meshing damping are established. Based on the pure torsional nonlinear dynamics model, the nonlinear characteristics of the compound gear system are analysed in detail. The influences of factors such as the meshing damping ratio, the input rotational speed and the magnitude of meshing error on the nonlinear characteristics are revealed, providing some guidance for the design of this compound gear system to avoid undesired motion states in operation. Based on the translational-torsional nonlinear dynamics model, and a detailed analysis is carried out for the emergence of complex nonlinear dynamics behaviours, and its connection with the pure torsional model is obtained.

In Chapter 6, Based on the ship motion state during sea voyage, the non-inertial system on the sea surface is taken into account, and the expressions of absolute velocity and absolute acceleration of each component in the compound gear system under the two non-inertial systems, including internal and external coordinate systems, are derived. Thus, the dynamics of a two-stage parallel compound marine gear transmission system under two non-inertial coordinate systems is modelled. The dynamic characteristics of the whole gear system under

typical motions of the ship (rocking and pitching motions) are analysed and some conclusions are given.

Chapter 2 Mechanical Model of the Double-helical Two-stage Parallel Compound Marine Gear Train

2.1 Preface

Before the dynamic analysis, the most important thing is to establish an accurate mechanical model. Each double-helical gear (sun, planet and ring) composed of planetary gear train can be regarded as two helical gears with opposite helix angle. At the same time, the two planetary gear trains are composed in parallel, and there are a lot of meshing relations, and some of them are connected. Here, the connection between the two stages is represented by torsional stiffness. Center components such as sun, ring and carrier can be connected to the gearbox structure by torsional spring. If one of the central components is not fixed, its torsional stiffness value can be regarded as zero.

Therefore, in this chapter, each stage of two-stage compound gear trains was firstly modeled separately. Then, combining with the lumped mass method and beam element method. Finally, the static and dynamic models are obtained according to the connection relation between the two stages.

2.2 Calculation of meshing errors and mesh phasing

In the practical application, due to the existence of manufacturing tolerance and installation accuracy, the actual center position and ideal center position of the gear can't perfectly coincide. Therefore, all kinds of errors must exist in gear system, which affect the transmission behavior of the gear system.

2.2.1 Calculation of meshing error considering errors

2.2.1.1 Effect of planet pinhole position error on meshing error

Pinhole position error is the difference between actual position of mounting position of planet gear and ideal mounting position. This kind of error is common in the assembly of planetary gear system. And pinhole position error can be divided into two kinds of position error, radial error and tangential error, as shown in Fig.2-1. The positive value of the radial error is outward along the centerline of two gears, while the positive value of the tangential error is perpendicular to the radial direction and consistent with the tangential direction of the rotation of the sun gear.

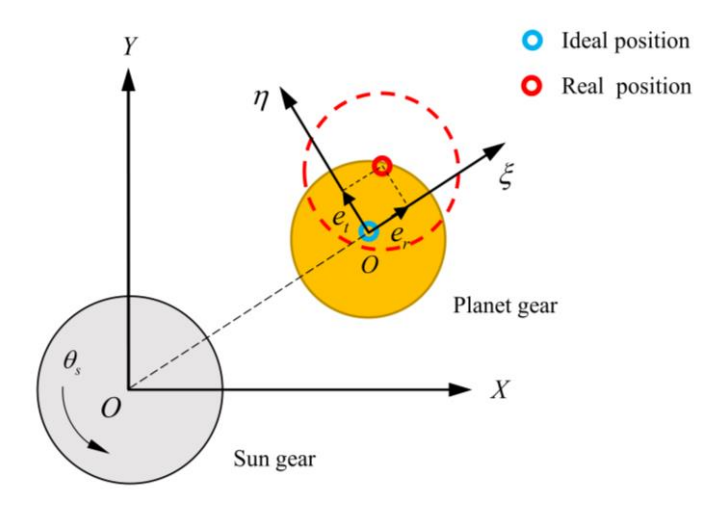


Fig.2-1 Diagram of planet pinhole position error

The equation for the meshing error affected by the planet pinhole position error that can be obtained by translating that, shown in Fig.2-1, into the direction normal to the two engagement lines of S-Pi and R-Pi.

$$e_{spi-ppi} = -e_{ppi} \sin(\lambda_{ppi} + \alpha_{sp})$$

$$e_{rpi-ppi} = -e_{ppi} \sin(\lambda_{ppi} - \alpha_{rp})$$
(2-1)

where, e_{ppi} and λ_{ppi} are the error and initial phase, respectively.

2.2.1.2 Eccentricity error

Eccentricity error is also called run-out error, it is a time-varying error, which can be decomposed into two components in the coordinate system and represented as transverse plane translations of the central point of rotation of the gear. Therefore, the run-out error on the sun gear and planet can be projected into the normal direction of meshing. Taking the sun-planet (S-Pi) meshing in a planetary gear train shown in Fig.2-2 as an example, the eccentricity errors of the respective gears are converted into the mesh error by the formula expressed below.

$$e_{spi-s}(t) = e_{es} \sin[(\omega_s - \omega_c)t + \lambda_s + \alpha_{sp} - \phi_{pi}]$$

$$e_{spi-pi}(t) = -e_{epi} \sin[(\omega_{pi})t + \lambda_{pi} + \alpha_{sp}]$$
(2-2)

Similarly, for the ring-planet (R-Pi) meshing, the meshing error affected by the eccentricity error are shown as follows.

$$e_{rpi-r}(t) = e_{er} \sin[(\omega_r - \omega_c)t + \lambda_r - \alpha_{rp} - \phi_{pi}]$$

$$e_{rpi-pi}(t) = -e_{epi} \sin[(\omega_{pi})t + \lambda_{pi} - \alpha_{rp}]$$
(2-3)

where, e_{es} , e_{epi} and e_{er} are magnitude of the run-out error for sun, planet and ring,

respectively. λ_s , λ_{pi} and λ_r are initial phase angle of the run-out error for sun, planet and ring, respectively.

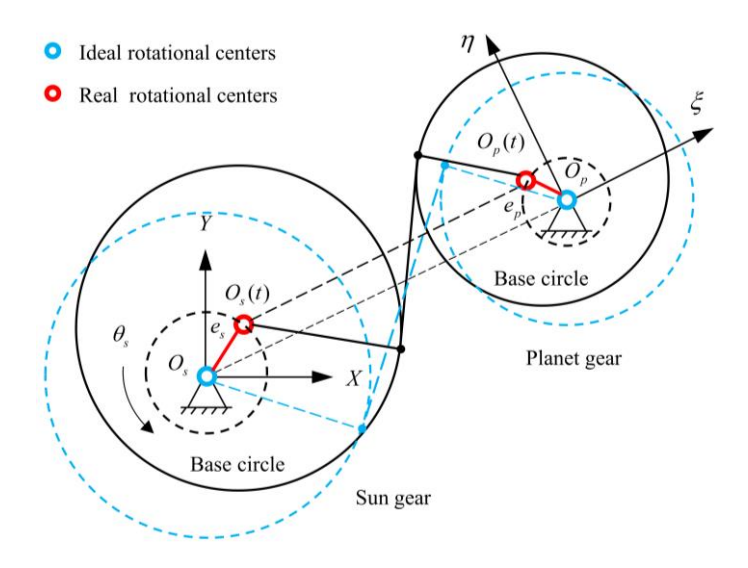


Fig.2-2 Diagram of eccentricity error

Here, it is noted that there is a connection between the eccentricity error and the pinhole position error for same magnitude of same planet. When the rotational angle is zero, the eccentricity error is pure radial error. In the same way, when the rotational angle become 90 degrees, it becomes pure tangential error.

2.2.1.3 Indexing error

Gear tooth indexing error is also called as pitch error, as shown in Fig.2-3, which is the deviation of the actual position (red tooth) from the reference theoretical position (black tooth) of teeth. This kind of error is one of common errors because of the precision of the gear manufacturing process. In addition, it is noted that the sum of error value ε_i (shown in Fig.2-3) should be zero.

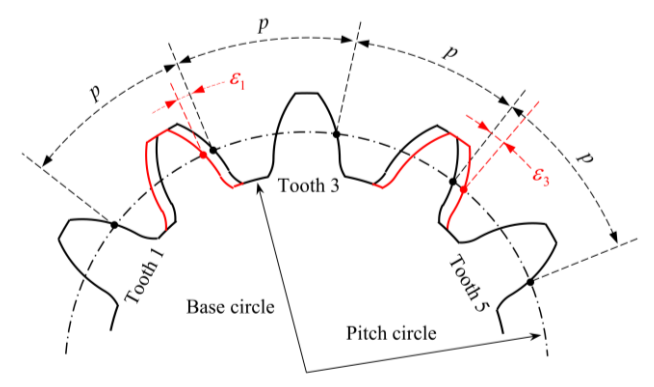


Fig.2-3 Diagram of indexing error

Assuming that the tooth shown in Fig.2-3 above is the sun gear, the equation

for the meshing error obtained by translating its tooth indexing error to the meshing line is shown as below.

$$e_{spi-s}(t) = e_{fps} \cos(\alpha_{sp}) \sin(\omega_{s}t)$$
 (2-4)

where, e_{fps} is the indexing error, and ω_s is the rotational speed.

2.2.1.4 Thickness error

Tooth thickness error is the difference between the actual tooth thickness and the nominal tooth thickness.

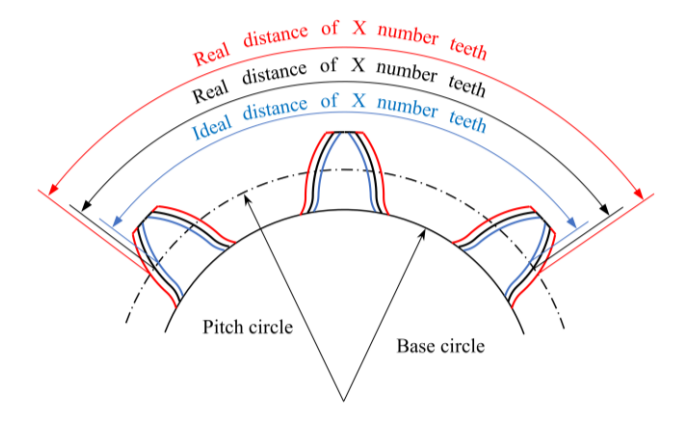


Fig.2-4 Diagram of thickness error

As shown in Fig.2-4, it is noted that a positive value (red line) means that the teeth are thicker than nominal (black line), while a negative value (blue line) means that teeth are thinner than nominal. In this thesis, the tooth thickness error is symmetric on both flanks. The sickness error is a special condition of indexing error.

2.2.2 Mesh phasing

Mesh phasing is a basic characteristic of a planetary gear train, which affects the lead or delay of the contact between two adjacent planet gears which mesh with sun or ring. In total, there are three types of conditions, they are in phasing, sequential phasing and arvitrarily phasing, which depend on its geometry (the teeth numbers and planet position angle). Moreover, in terms of the assemble position of the planet gear, there are two types of condition, equally space assembly (i.e., planets are equally spaced around the center gear) and non-equally space assembly.

As above mentioned, for a planetary gear train, the combined configuration conditions are shown in Tab.2-1.

Mathematical conditions Configuration $\psi_i = \frac{2\pi(i-1)}{N}, \ \frac{Z_r \psi_i}{2\pi} = \text{integer}$ **Equally Spaced In Phasing** (ESIP) $\psi_i \neq \frac{2\pi(i-1)}{N}, \ \frac{Z_r \psi_i}{2\pi} = \text{integer}$ Non-Equally Spaced In Phasing (NESIP) $\psi_i = \frac{2\pi(i-1)}{N}, \ \frac{Z_r \psi_i}{2\pi} \neq \text{integer}, \ \sum_{i=1}^N Z_r \psi_i = \text{integer} \cdot \pi$ Equally Spaced Sequential Phasing (ESSP) $\psi_i \neq \frac{2\pi(i-1)}{N}, \ \frac{Z_r \psi_i}{2\pi} \neq \text{integer}, \ \sum_{i=1}^N Z_r \psi_i = \text{integer} \cdot \pi$ Non-Equally Spaced Sequential Phasing (NESSP) $\psi_i \neq \frac{2\pi(i-1)}{N}, \ \frac{Z_r \psi_i}{2\pi} \neq \text{integer}, \ \sum_{i=1}^N Z_r \psi_i \neq \text{integer} \cdot \pi$ Non-Equally Spaced Arbitrarily Phasing (NESAP)

Tab.2-1 Assembly and Mesh phasing configurations (adapted from [147,148])

where, ψ_i is planet i spacing angle, N is planet numbers and Z_r is teeth of ring gear.

2.3 Translational-torsional quasi-static model of the two-stage parallel compound marine gear transmission system

The two-dimensional quasi-static model of differential stage (the first stage) planetary gear system is shown in Fig.2-5. Correspondingly, the two-dimensional quasi-static model of closed stage (the second stage) planetary gear system is shown in Fig.2-6. The only difference between two stages is whether the carrier rotates.

As shown in Fig.2-5 and Fig.2-6, the meshing relationship between gears is equivalent to a spring, and the red straight line in the rectangular diagram on the right represents the meshing force direction on the normal plane when the single side helical gear of double-helical gear meshes. At the same time, firstly, the supporting spring can be used to represent the supporting connection relationship between the sun gear, ring gear, carrier and their respective main shafts, secondly, the planet gear and planet carrier. k_{xi} , k_{yi} (i = s, r, c) can be used to represent the stiffness of each supporting spring in the transverse and vertical directions, k_{ξ} , k_{η} is the supporting stiffness in the radial and tangential direction of planet, their units are N/m. k_{ti} (i = s, r, c) is used to represent the stiffness of each torsion spring of every component in their rotational direction, and corresponding units are Nm/rad.

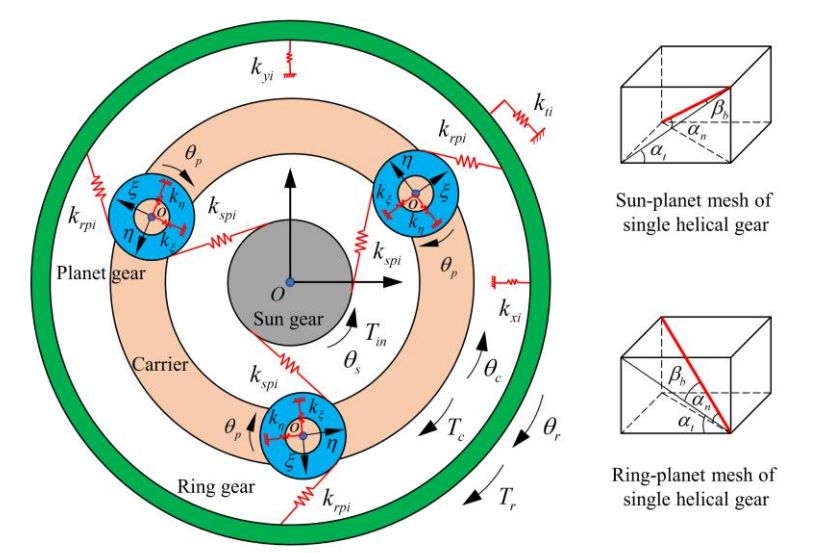


Fig.2-5 The statics model of the differential planetary gear train

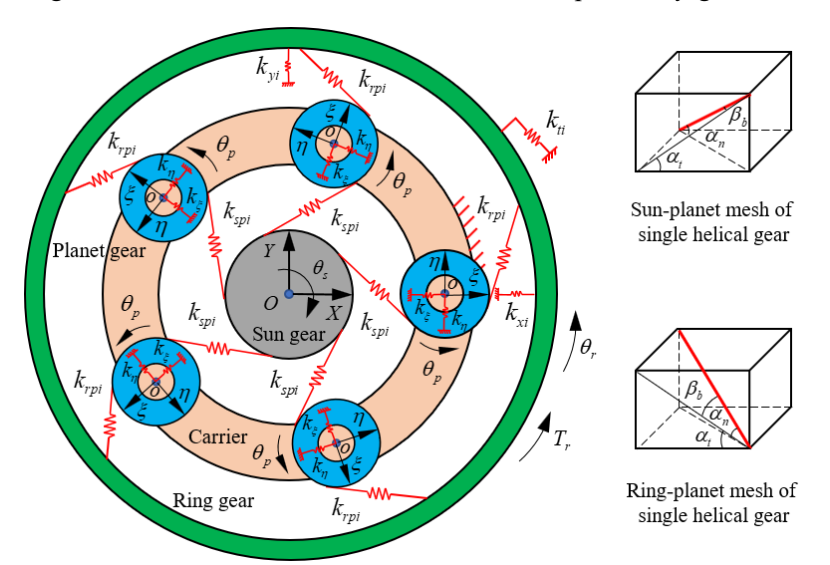


Fig.2-6 The statics model of the closed planetary gear train

In the compound gear system, the planets of the first stage not only rotates around its axis, but also rotates with the carrier around the centre of the planetary gear train, so three types of coordinate systems are established in this thesis.

- (1) Fixed coordinate system XOY. The origin point is at the centre of the whole compound gear system, which is in fact the whole ground coordinate system. All components of the second stage are modelled in the fixed coordinate system.
- (2) Moving coordinate system of carrier xoy. The origin is located at the centre of the carrier in first stage, rotating with the carrier piece under an angular velocity ω_c . Sun, ring and carrier in the first-stage are modelled in this coordinate system.
 - (3) Moving coordinate system of planets $\xi o \eta$. The origin is located at the

centre of the planets in the first stage, the ξ axis direction is radial direction, and the η axis direction is tangential direction. The planets in first stage is modelled in this coordinate system.

The angle formed by the meshing plane of a pair of meshing gears (sun-planet and ring-planet) in a planetary gear system and the Y-axis of the static coordinate system is shown as Fig.2-7. As diagram shown, ψ_{spi} represents the angle formed between the meshing plane of sun-planet and Y-axis, and ψ_{rpi} represents the angle formed between the meshing plane of ring-planet and Y-axis, and the calculation formula is as follows.

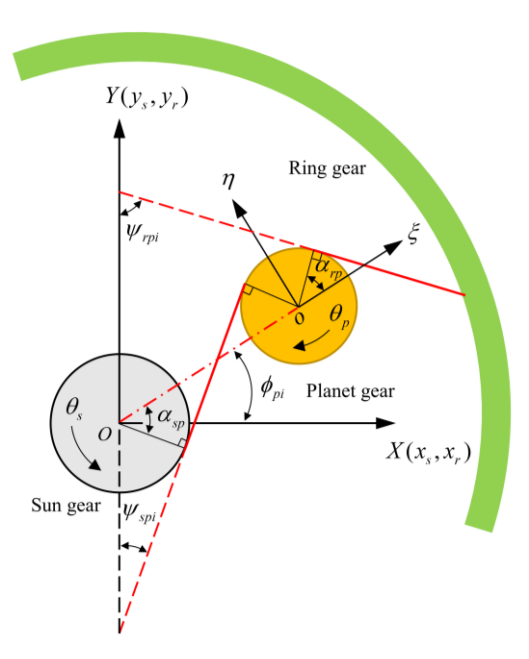


Fig.2-7 A diagram of the angle formed by the meshing plane and the Y axis of the static coordinate system XOY

$$\psi_{spi} = \alpha_{sp} - \lambda \phi_{pi}$$

$$\psi_{rpi} = \alpha_{rp} + \lambda \phi_{pi}$$
(2-5)

in which, $\lambda=1$ represents the counterclockwise rotation directions of sun gear, $\lambda=1$ represents the clockwise rotation directions of the sun gear. α_{sp} is the transverse pressure angle of sun-planet meshes, α_{rp} is the transverse pressure angle of ring-planet meshes and ϕ_{pi} is the positional angle of the planet *i*. Here, defines the initial position of the first planet gear as being on the X-axis, with $\phi_{pl}=0$. The formula for the position of the planet gear is shown in the following Eq.(2-6):

$$\phi_{pi} = \frac{2\pi(i-1)}{N}$$
 (2-6)

where, N is the number of the planet gear.

2.3.1 Static balance equation of sun and planet #i meshing

Firstly, considering the left side helical gear in the double-helical sun gear, which engages with one side of the double-helical planet gear, as shown Fig.2-8. A planet i which is located in a positional angle ϕ_{pi} , the meshing teeth between sun and the planet i are seen as the spring shown in Fig.2-8.

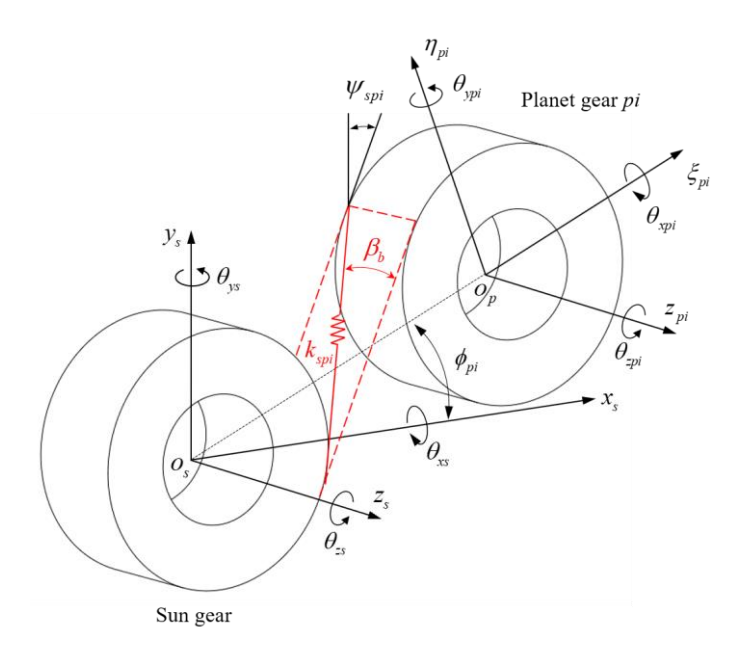


Fig.2-8 The sun gear meshes with the planet gear

When the sun gear s meshes with the planet gear pi (i=1,2,...,N), the 6DOF static balance equation (force and moment balance) of the sun can be listed, for the static equilibrium equation of helical gear meshing on the other side, only the helical angle of the base circle needs to be negative, and other parameters are the same. Therefore, the static equilibrium equation of the double-helical sun gear meshing with N double-helical planet gear is shown in Equation (2-7).

$$\begin{cases}
\sum_{j=1}^{2} \sum_{i=1}^{N} F_{mspi}^{j} \cos(\beta_{b}^{j}) \sin(\psi_{spi}) = 0 \\
\sum_{j=1}^{2} \sum_{i=1}^{N} F_{mspi}^{j} \cos(\beta_{b}^{j}) \cos(\psi_{spi}) = 0 \\
\sum_{j=1}^{2} \sum_{i=1}^{N} F_{mspi}^{j} \sin(\beta_{b}^{j}) = 0 \\
\sum_{j=1}^{2} \sum_{i=1}^{N} F_{mspi}^{j} \sin(\beta_{b}^{j}) \sin(\psi_{spi}) R_{bs} = 0 \\
\sum_{j=1}^{2} \sum_{i=1}^{N} F_{mspi}^{j} \sin(\beta_{b}^{j}) \cos(\psi_{spi}) R_{bs} = 0 \\
\sum_{j=1}^{2} \sum_{i=1}^{N} F_{mspi}^{j} \cos(\beta_{b}^{j}) R_{bs} = T_{in}
\end{cases}$$
(2-7)

where, β_b is helix angle of base circle. j=1 is left helical gear, j=2 is right helical

gear, and it is defined that $\beta_b^2 = -\beta_b^1$. T_{in} is input torque, R_{bs} is radius of base circle. F_{mspi} is meshing force of single side of double-helical gear meshing, as shown in Equation (2-8).

$$F_{mspi} = k_{spi} \times \delta_{spi} \tag{2-8}$$

in which, k_{spi} is meshing stiffness. δ_{spi} is relative meshing displacement between the helical sun-planet gear pair, which is combined by the displacement of the gear in six directions projected onto the meshing line. Here, it is defined that the spring compression should be positive, as shown in Fig.2-7 and Fig.2-8. Then the calculation formula of the relative meshing displacement of the sun-planet pair is shown in Formula (2-9).

$$\delta_{spi} = [(x_s \sin \psi_{spi} + \kappa_1 y_s \cos \psi_{spi} + \kappa_1 (\theta_{zs} - \theta_{zc}) R_{bs} - \xi_{pi} \sin \alpha_{sp} - \kappa_1 \eta_{pi} \cos \alpha_{sp} + \kappa_1 \cdot (\theta_{zpi} - \theta_{zc}) R_{bp})] \cos \beta_b + [(\kappa_2 \cdot \theta_{xs} \sin \psi_{spi} + \kappa_1 \cdot \kappa_2 \cdot \theta_{ys} \cos \psi_{spi}) R_{bs} - \kappa_1 \cdot \kappa_2 \cdot z_s + (\kappa_2 \cdot \theta_{\xi pi} \sin \alpha_{sp} + \kappa_1 \cdot \kappa_2 \cdot \theta_{\eta pi} \cos \alpha_{sp}) R_{bp} + \kappa_1 \cdot \kappa_2 \cdot z_{pi}] \sin \beta_b$$
 (2-9)

Here, R_{bp} is the radius of the base circle of the planet engaged with the sun.

According to Equation (2-9), the projection vector and sub-vector of s-pi meshing pair can be obtained as follows:

$$\mathbf{V}_{spi} = \begin{bmatrix} s\psi c\beta_{b}, & \kappa_{1}c\psi c\beta_{b}, & -\kappa_{1}\kappa_{2}s\beta_{b}, & \kappa_{2}R_{bs}s\psi s\beta_{b}, & \kappa_{1}\kappa_{2}R_{bs}c\psi s\beta_{b}, & \kappa_{1}R_{bs}c\beta_{b}, \cdots \\ -s\alpha c\beta_{b}, & -\kappa_{1}c\alpha c\beta_{b}, & \kappa_{1}\kappa_{2}s\beta_{b}, & \kappa_{2}R_{bp}s\alpha s\beta_{b}, & \kappa_{1}\kappa_{2}R_{bp}c\alpha s\beta_{b}, & \kappa_{1}R_{bp}c\beta_{b} \end{bmatrix}$$

$$\mathbf{V}_{s}^{spi} = \begin{bmatrix} s\psi c\beta_{b} & \kappa_{1}\cdot c\psi c\beta_{b} & -\kappa_{1}\cdot \kappa_{2}\cdot s\beta_{b} \dots \\ \kappa_{2}\cdot R_{bs}s\psi s\beta_{b} & \kappa_{1}\cdot \kappa_{2}\cdot R_{bs}c\psi s\beta_{b} & \kappa_{1}R_{bs}c\beta_{b} \end{bmatrix}$$

$$\mathbf{V}_{c}^{spi} = \begin{bmatrix} 0 & 0 & 0 & 0 & -\kappa_{1}R_{bc}c\beta_{b} \end{bmatrix}$$

$$\mathbf{V}_{pi}^{spi} = \begin{bmatrix} -s\alpha c\beta_{b} & -\kappa_{1}\cdot c\alpha c\beta_{b} & \kappa_{1}\cdot \kappa_{2}\cdot s\beta_{b} & \dots \\ \kappa_{2}\cdot R_{bp}s\alpha s\beta_{b} & \kappa_{1}\cdot \kappa_{2}\cdot R_{bp}c\alpha s\beta_{b} & \kappa_{1}R_{bp}c\beta_{b} \end{bmatrix}$$

$$(2-10)$$

where, $\kappa_1 = \pm 1$ represents the counterclockwise and clockwise directions of the input torque of sun gear, and $\kappa_2 = \pm 1$ represents right-handed or left-handed of sun gear, and β_b represents the magnitude of the helical angle of the base circle. Here, simplified notation is used to represent the following expression:

$$s\psi = \sin \psi_{spi}$$
, $c\psi = \cos \psi_{spi}$, $s\alpha = \sin \alpha_{sp}$, $c\alpha = \cos \alpha_{sp}$, $s\beta_b = \sin \beta_b^j$, $c\beta_b = \cos \beta_b^j$

Equations (2-8) and (2-9) are imported into Equation (2-7) and sorted out, then the force and moment balance equation of equation (2-7) can be expressed in matrix form as follows:

$$\begin{bmatrix} \sum_{i=1}^{N} \mathbf{K}_{mspi}^{11} & \sum_{i=1}^{N} \mathbf{K}_{msp1}^{12} & \mathbf{K}_{msp1}^{13} & \cdots & \mathbf{K}_{mspN}^{13} \\ \mathbf{0} & \mathbf{0} & \mathbf{0} & \cdots & \mathbf{0} \\ \mathbf{K}_{msp1}^{21} & \mathbf{K}_{msp1}^{22} & \mathbf{K}_{msp1}^{23} & \cdots & \mathbf{0} \\ \vdots & \vdots & \mathbf{0} & \ddots & \vdots \\ \mathbf{K}_{mspN}^{21} & \mathbf{K}_{mspN}^{22} & \mathbf{0} & \cdots & \mathbf{K}_{mspN}^{23} \end{bmatrix} \begin{bmatrix} \mathbf{q}_{s} \\ \mathbf{q}_{c} \\ \mathbf{q}_{p1} \\ \vdots \\ \mathbf{q}_{pN} \end{bmatrix} = \begin{bmatrix} \mathbf{f}_{s} \\ \mathbf{0} \\ \mathbf{0} \\ \vdots \\ \mathbf{0} \end{bmatrix}$$
(2-11)

where, the stiffness submatrix, displacement and external force sub-vector in the equation (2-11) are defined as follows:

$$\mathbf{K}_{mspi}^{11} = k_{spi} (\mathbf{V}_{s}^{spi})^{T} \mathbf{V}_{s}^{spi}, \quad \mathbf{K}_{mspi}^{12} = k_{spi} (\mathbf{V}_{s}^{spi})^{T} \mathbf{V}_{c}^{spi},$$

$$\mathbf{K}_{mspi}^{13} = k_{spi} (\mathbf{V}_{s}^{spi})^{T} \mathbf{V}_{pi}^{spi}, \quad \mathbf{K}_{mspi}^{21} = k_{spi} (\mathbf{V}_{pi}^{spi})^{T} \mathbf{V}_{s}^{spi},$$

$$\mathbf{K}_{mspi}^{22} = k_{spi} (\mathbf{V}_{pi}^{spi})^{T} \mathbf{V}_{c}^{spi}, \quad \mathbf{K}_{mspi}^{23} = k_{spi} (\mathbf{V}_{pi}^{spi})^{T} \mathbf{V}_{pi}^{spi}.$$

$$\mathbf{q}_{s} = \begin{pmatrix} x_{s} \\ y_{s} \\ \theta_{xs} \\ \theta_{ys} \\ \theta_{zs} \end{pmatrix}, \quad \mathbf{q}_{pi} = \begin{pmatrix} \xi_{pi} \\ \eta_{pi} \\ \theta_{\xi pi} \\ \theta_{\eta pi} \\ \theta_{zpi} \end{pmatrix}, \quad \mathbf{f}_{s} = \begin{pmatrix} 0 \\ 0 \\ 0 \\ 0 \\ T_{in} / 2 \end{pmatrix}.$$

$$(2-12)$$

2.3.2 Static balance equation of ring and planet #i meshing

The meshing diagram of a ring gear and a planet gear i with positional angle ϕ_{pi} is shown in Fig.2-9. Therefore, the static equilibrium equation of the double-helical ring gear meshing with N double-helical planet gear is given by.

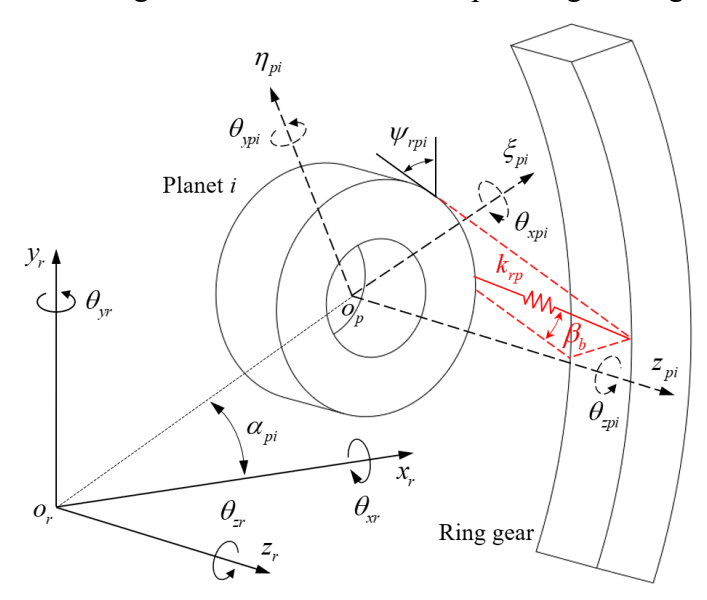


Fig.2-9 The ring gear meshes with the planet gear

$$\begin{cases}
\sum_{j=1}^{2} \sum_{i=1}^{N} F_{mrpi}^{j} \cos(\beta_{b}^{j}) \sin(\psi_{rpi}) = 0 \\
\sum_{j=1}^{2} \sum_{i=1}^{N} F_{mrpi}^{j} \cos(\beta_{b}^{j}) \cos(\psi_{rpi}) = 0 \\
\sum_{j=1}^{2} \sum_{i=1}^{N} F_{mrpi}^{j} \sin(\beta_{b}^{j}) = 0 \\
\sum_{j=1}^{2} \sum_{i=1}^{N} F_{mrpi}^{j} \sin(\beta_{b}^{j}) \sin(\psi_{rpi}) R_{br} = 0 \\
\sum_{j=1}^{2} \sum_{i=1}^{N} F_{mrpi}^{j} \sin(\beta_{b}^{j}) \cos(\psi_{rpi}) R_{br} = 0 \\
\sum_{j=1}^{2} \sum_{i=1}^{N} F_{mrpi}^{j} \cos(\beta_{b}^{j}) R_{br} = T_{r}
\end{cases}$$
(2-13)

where, R_{br} is radius of base circle of ring gear, T_r is torque, ψ_{rpi} is shown as equation (2-5). Similarly, F_{mrpi} shown (2-13) is meshing force between ring and planet for single side of double-helical gear.

$$F_{mrpi} = k_{rpi} \times \delta_{rpi} \tag{2-14}$$

in which, k_{rpi} is meshing stiffness of ring-planet, δ_{rpi} is relative meshing displacement of ring-planet.

The meshing displacement δ_{rpi} is combined by the displacement projection of six directions of the meshing gear pair onto the meshing line. Here, it is stipulated that the spring should be positive when compressed. Then the calculation formula of the relative meshing displacement of the ring-planet meshing pair is shown in Equation (2-15).

$$\delta_{rpi} = [(\kappa_{1} \cdot y_{r} \cos \psi_{rpi} - x_{r} \sin \psi_{rpi} + \kappa_{1} \cdot (\theta_{zr} - \theta_{zc}) R_{br} + \xi_{pi} \sin \alpha_{rp} - \kappa_{1} \cdot \eta_{pi} \cos \alpha_{rp} - \kappa_{1} \cdot (\theta_{zpi} - \theta_{zc}) R_{bp})] \cos \beta_{b} + [(\kappa_{2} \cdot \theta_{xr} \sin \psi_{rpi} - \kappa_{1} \cdot \kappa_{2} \cdot \theta_{yr} \cos \psi_{rpi}) R_{br} + \kappa_{1} \cdot \kappa_{2} \cdot z_{r} + (\kappa_{1} \cdot \kappa_{2} \cdot \theta_{\eta pi} \cos \alpha_{rp} - \kappa_{2} \cdot \theta_{\xi pi} \sin \alpha_{rp}) R_{bp} - \kappa_{1} \cdot \kappa_{2} \cdot z_{pi}] \sin \beta_{b}$$

$$(2-15)$$

where, according to the above equation (2-15) and summary, the projection subvector of ring-planet meshing pair can be obtained as follows:

$$\mathbf{V}_{r}^{rpi} = \begin{bmatrix} s\overline{\psi}c\beta_{b} & \kappa_{1} \cdot c\overline{\psi}c\beta_{b} & -\kappa_{1} \cdot \kappa_{2} \cdot s\beta_{b} \dots \\ \kappa_{2} \cdot R_{br}s\overline{\psi}s\beta_{b} & \kappa_{1} \cdot \kappa_{2} \cdot R_{br}c\overline{\psi}s\beta_{b} & \kappa_{1}R_{br}c\beta_{b} \end{bmatrix}$$

$$\mathbf{V}_{c}^{rpi} = \begin{bmatrix} 0 & 0 & 0 & 0 & -\kappa_{1}R_{bc}c\beta_{b} \end{bmatrix}$$

$$\mathbf{V}_{pi}^{rpi} = \begin{bmatrix} -s\overline{\alpha}c\beta_{b} & -\kappa_{1} \cdot c\overline{\alpha}c\beta_{b} & \kappa_{1} \cdot \kappa_{2} \cdot s\beta_{b} & \dots \\ \kappa_{2} \cdot R_{bp}s\overline{\alpha}s\beta_{b} & \kappa_{1} \cdot \kappa_{2} \cdot R_{bp}c\overline{\alpha}s\beta_{b} & \kappa_{1}R_{bp}c\beta_{b} \end{bmatrix}$$

$$(2-16)$$

here, simplified notation is used to represent the following expression:

$$s\overline{\psi} = \sin\psi_{rpi}, \ c\overline{\psi} = \cos\psi_{rpi}, \ s\overline{\alpha} = \sin\alpha_{rp}, \ c\overline{\alpha} = \cos\alpha_{rp}$$

Putting equations (2-14) and (2-15) into equation (2-13) and arrange them, then the force and moment balance equation of equation (2-13) can be expressed in matrix form as follows:

$$\begin{bmatrix} \sum_{i=1}^{N} \mathbf{K}_{mrpi}^{11} & \sum_{i=1}^{N} \mathbf{K}_{mrp1}^{12} & \mathbf{K}_{mrp1}^{13} & \cdots & \mathbf{K}_{mrpN}^{13} \\ \mathbf{0} & \mathbf{0} & \mathbf{0} & \cdots & \mathbf{0} \\ \mathbf{K}_{mrp1}^{21} & \mathbf{K}_{mrp1}^{22} & \mathbf{K}_{mrp1}^{23} & \cdots & \mathbf{0} \\ \vdots & \vdots & \mathbf{0} & \ddots & \vdots \\ \mathbf{K}_{mrpN}^{21} & \mathbf{K}_{mrpN}^{22} & \mathbf{0} & \cdots & \mathbf{K}_{mrpN}^{23} \end{bmatrix} \begin{bmatrix} \mathbf{q}_{r} \\ \mathbf{q}_{c} \\ \mathbf{q}_{p1} \\ \vdots \\ \mathbf{q}_{pN} \end{bmatrix} = \begin{bmatrix} \mathbf{f}_{r} \\ \mathbf{0} \\ \mathbf{0} \\ \vdots \\ \mathbf{0} \end{bmatrix}$$
(2-17)

where, the stiffness submatrix, displacement sub-vector and external force sub-vector are defined as follows:

$$\mathbf{K}_{rpi}^{11} = k_{rpi} (\mathbf{V}_{r}^{rpi})^{T} \mathbf{V}_{r}^{rpi}, \quad \mathbf{K}_{rpi}^{12} = k_{rpi} (\mathbf{V}_{r}^{rpi})^{T} \mathbf{V}_{c}^{rpi},$$

$$\mathbf{K}_{rpi}^{13} = k_{rpi} (\mathbf{V}_{r}^{rpi})^{T} \mathbf{V}_{pi}^{rpi}, \quad \mathbf{K}_{rpi}^{21} = k_{rpi} (\mathbf{V}_{pi}^{rpi})^{T} \mathbf{V}_{r}^{rpi},$$

$$\mathbf{K}_{rpi}^{22} = k_{rpi} (\mathbf{V}_{pi}^{rpi})^{T} \mathbf{V}_{c}^{rpi}, \quad \mathbf{K}_{rpi}^{23} = k_{rpi} (\mathbf{V}_{pi}^{rpi})^{T} \mathbf{V}_{pi}^{rpi},$$

$$\mathbf{q}_{r} = \begin{pmatrix} \boldsymbol{\xi}_{pi} \\ \boldsymbol{\eta}_{pi} \\ \boldsymbol{\xi}_{pi} \\ \boldsymbol{\theta}_{qpi} \\ \boldsymbol{\theta}_{rpi} \end{pmatrix}, \quad \mathbf{f}_{r} = \begin{pmatrix} \boldsymbol{0} \\ \boldsymbol{0} \\ \boldsymbol{0} \\ \boldsymbol{0} \\ \boldsymbol{0} \\ \boldsymbol{T}_{r} / 2 \end{pmatrix}.$$

$$(2-18)$$

2.3.3 Static balance equation between carrier and planet #i

In a planetary gear train, the carrier and planets are connected via bearings, so the motion displacement of the planetary frame must be considered. Here, its distance from the z axis of the carrier is the installation distance of the planet gear. Meanwhile, the compliance of the planetary wheel bearing can be regarded as a diagonal stiffness matrix, as shown below.

$$K_{bpi} = diag \left\{ k_{\xi} \quad k_{\eta} \quad k_{z} \quad k_{\theta\xi} \quad k_{\theta\eta} \quad k_{\theta z} \right\}$$
 (2-19)

Here the supporting stiffness of bearing in in two perpendicular directions are seen as k_{ξ} and k_{η} . Therefore, the bearing force is given as the following equation (2-20). Hence, the static equation of the planet is obtained, which is equation (2-21).

$$\begin{cases} F_{b\xi pi}^{j} = k_{\xi} (y_{c} \sin \phi_{pi} + x_{c} \cos \phi_{pi} - \xi_{pi}^{(j)}) \\ F_{b\eta pi}^{j} = k_{\eta} (y_{c} \cos \phi_{pi} - x_{c} \sin \phi_{pi} + R_{c} \theta_{zc} - \eta_{pi}^{(j)}) \\ F_{bzpi}^{j} = k_{z} (z_{c} - z_{pi}^{(j)} + R_{c} \sin \phi_{pi} \theta_{zc} - R_{c} \cos \phi_{pi} \theta_{yc}) \\ M_{b\xi pi}^{j} = k_{\theta\xi} (\theta_{zc} \cos \phi_{pi} - \theta_{\xi pi}^{(j)}) \\ M_{b\eta pi}^{j} = k_{\theta\xi} (\theta_{yc} \sin \phi_{pi} - \theta_{\eta pi}^{(j)}) \\ M_{bzpi}^{j} = 0 \end{cases}$$

$$(2-20)$$

$$\begin{cases}
\sum_{j=1}^{2} (F_{mrpi}^{j} \sin \alpha_{rp} - F_{mspi}^{j} \sin \alpha_{sp}) \cos(\beta_{b}^{j}) = F_{b\xi pi}^{j} \\
\sum_{j=1}^{2} (-F_{mrpi}^{j} \cos \alpha_{rp} - F_{mspi}^{j} \cos \alpha_{sp}) \cos(\beta_{b}^{j}) = F_{b\eta pi}^{j} \\
\sum_{j=1}^{2} (F_{mrpi}^{j} - F_{mspi}^{j}) \sin(\beta_{b}^{j}) = F_{bzpi}^{j} \\
\sum_{j=1}^{2} (F_{mspi}^{j} \sin \alpha_{sp} - F_{mrpi}^{j} \sin \alpha_{rp}) \sin(\beta_{b}^{j}) R_{bp} = M_{b\xi pi}^{j} \\
\sum_{j=1}^{2} (F_{mspi}^{j} \cos \alpha_{sp} + F_{mrpi}^{j} \cos \alpha_{rp}) \sin(\beta_{b}^{j}) R_{bp} = M_{b\eta pi}^{j} \\
\sum_{j=1}^{2} (F_{mrpi}^{j} - F_{mspi}^{j}) \cos(\beta_{b}^{j}) R_{bp} = 0
\end{cases} \tag{2-21}$$

Correspondingly, the static equilibrium equation of the carrier is shown as follows:

$$\begin{cases} \sum_{j=1}^{2} \sum_{i=1}^{N} (F_{b\xi pi}^{j} \cos \phi_{pi} - F_{b\eta pi}^{j} \sin \phi_{pi}) = 0, \\ \sum_{j=1}^{2} \sum_{i=1}^{N} (F_{b\xi pi}^{j} \sin \phi_{pi} + F_{b\eta pi}^{j} \cos \phi_{pi}) = 0, \\ \sum_{j=1}^{2} \sum_{i=1}^{N} F_{bzpi}^{j} = 0 \\ \sum_{j=1}^{2} \sum_{i=1}^{N} (M_{b\xi pi}^{j} \cos \phi_{pi} + F_{bzpi}^{j} R_{c} \sin \phi_{pi}) = 0, \\ \sum_{j=1}^{2} \sum_{i=1}^{N} (M_{b\eta pi}^{j} \sin \phi_{pi} - F_{bzpi}^{j} R_{c} \cos \phi_{pi}) = 0, \\ \sum_{j=1}^{2} \sum_{i=1}^{N} F_{b\eta pi}^{j} R_{c} = T_{c} \end{cases}$$

$$(2-22)$$

where, T_c is the external torque of carrier.

The equations (2-21) and (2-22) are rewritten into a matrix form as follows:

$$\begin{bmatrix} \sum_{i=1}^{N} \mathbf{K}_{cpi}^{11} & \mathbf{K}_{cpi}^{12} & \mathbf{K}_{cp2}^{12} & \cdots & \mathbf{K}_{cpN}^{12} & \mathbf{f}_{cpN}^{12} \\ & \mathbf{K}_{cp1}^{22} & \mathbf{0} & \cdots & \mathbf{0} \\ & & \mathbf{K}_{cp2}^{22} & \mathbf{0} & \mathbf{0} \\ & & & \ddots & \vdots \\ & & & & \mathbf{K}_{cpN}^{22} & \mathbf{f}_{cpN}^{22} \end{bmatrix} \begin{bmatrix} \mathbf{q}_{c}^{(j)} \\ \mathbf{q}_{p1}^{(j)} \\ \mathbf{q}_{p2}^{(j)} \\ \vdots \\ \mathbf{q}_{pN}^{(j)} \end{bmatrix} = \begin{bmatrix} \mathbf{f}_{c}^{(j)} \\ \mathbf{0} \\ \mathbf{0} \\ \vdots \\ \mathbf{0} \end{bmatrix}$$
(2-23)

where, the, displacement and force vector are shown as follows in equation (2-24).

$$\mathbf{q}_{c} = \begin{pmatrix} x_{c} \\ y_{c} \\ z_{c} \\ \theta_{xc} \\ \theta_{yc} \\ \theta_{zc} \end{pmatrix}, \qquad \mathbf{q}_{pi} = \begin{pmatrix} \xi_{pi} \\ \eta_{pi} \\ z_{pi} \\ \theta_{\xi pi} \\ \theta_{\eta pi} \\ \theta_{z pi} \end{pmatrix}, \qquad \mathbf{f}_{c} = \begin{pmatrix} 0 \\ 0 \\ 0 \\ 0 \\ 0 \\ T_{c} / 2 \end{pmatrix}$$

$$(2-24)$$

It is noted that the stiffness submatrices are given in the following equation, and they are all symmetric matrix.

$$\begin{split} \mathbf{K}_{cpi}^{11}(1,1) &= k_{\xi i}c^{2}\phi + k_{\eta i}s^{2}\phi, \mathbf{K}_{cpi}^{11}(1,2) = k_{\xi i}c\phi s\phi - k_{\eta i}c\phi s\phi, \mathbf{K}_{cpi}^{11}(1,6) = -k_{\eta i}R_{c}s\phi, \\ \mathbf{K}_{cpi}^{11}(2,1) &= \mathbf{K}_{cpi}^{11}(1,2), \mathbf{K}_{cpi}^{11}(2,2) = k_{\xi i}s^{2}\phi + k_{\eta i}c^{2}\phi, \mathbf{K}_{cpi}^{11}(2,6) = k_{\eta i}R_{c}c\phi, \\ \mathbf{K}_{cpi}^{11}(3,3) &= \mathbf{K}_{ci}^{11}(3,4) = k_{ci}R_{c}s\phi, \mathbf{K}_{cpi}^{11}(3,5) = -k_{zi}R_{c}c\phi, \\ \mathbf{K}_{cpi}^{11}(4,3) &= \mathbf{K}_{cpi}^{11}(3,4), \mathbf{K}_{cpi}^{11}(4,4) = k_{\theta_{\xi i}}c^{2}\phi + k_{zi}R_{c}^{2}s^{2}\phi, \mathbf{K}_{cpi}^{11}(4,5) = -k_{zi}R_{c}^{2}s\phi_{pi}c\phi, \\ \mathbf{K}_{cpi}^{11}(5,3) &= \mathbf{K}_{cpi}^{11}(3,5), \mathbf{K}_{cpi}^{11}(5,4) = \mathbf{K}_{cpi}^{11}(4,5), \mathbf{K}_{cpi}^{11}(5,5) = k_{\theta_{\eta i}}s^{2}\phi + k_{zi}R_{c}^{2}c^{2}\phi, \\ \mathbf{K}_{cpi}^{11}(6,1) &= \mathbf{K}_{cpi}^{11}(1,6), \mathbf{K}_{cpi}^{11}(6,2) = \mathbf{K}_{cpi}^{11}(2,6), \mathbf{K}_{cpi}^{11}(6,6) = k_{\eta i}R_{c}^{2}. \\ \mathbf{K}_{cpi}^{12} &= \begin{bmatrix} -k_{\xi i}c\phi & k_{\eta i}s\phi & 0 & 0 & 0 & 0 \\ 0 & 0 & -k_{zi} & 0 & 0 & 0 \\ 0 & 0 & -k_{zi} & 0 & 0 & 0 \\ 0 & 0 & -k_{zi} & 0 & 0 & 0 \\ 0 & 0 & -k_{zi}R_{c}s\phi & -k_{\theta_{\xi i}}c\phi & 0 & 0 \\ 0 & 0 & -k_{\eta i}R_{c} & 0 & 0 & 0 & 0 \end{bmatrix}, \quad \mathbf{K}_{cpi}^{21} &= (\mathbf{K}_{cpi}^{12})^{T}, \\ \mathbf{K}_{cpi}^{22} &= diag\left\{k_{\xi i} & k_{\eta i} & k_{zi} & k_{\theta} & k_{\theta} & k_{\theta} \right\}. \end{split}$$

where, the shorthand form in the matrix is $s\phi_{pi}=\sin\phi_{pi}$, $c\phi_{pi}=\cos\phi_{pi}$. The position angle of the planet can be constant or time-varying, which depends on whether the planetary gear train is fixed-axis or cyclic.

2.3.4 Quasi-static equation of the overall system

By consolidating the force balance relationships and generalized coordinates of the individual components, the overall quasi-static equation of the compound gear system can be obtained.

$$\mathbf{K}_{overall}\mathbf{q}_{overall} = \mathbf{F}_{overall} \tag{2-25}$$

where, $\mathbf{K}_{overall}$, $\mathbf{q}_{overall}$ and $\mathbf{F}_{overall}$ are the overall stiffness matrix, displacement vector and force vector, respectively.

2.4 Translational-torsional dynamic model of the two-stage parallel compound marine gear transmission system

The dynamic meshing diagram of double-helical planetary gear train is shown in Fig.2-10, the meshing relationship between gears is equivalent to a spring-damper model, where k_{spi} , c_{spi} and e_{spi} represent the meshing stiffness, damping and transmission error of the sun-planet meshing pair, respectively. Corresponding, k_{rpi} , c_{rpi} and e_{rpi} represent the meshing stiffness, damping and transmission error of the ring-planet meshing pair, respectively. β_b represents the helix angle of the base circle.

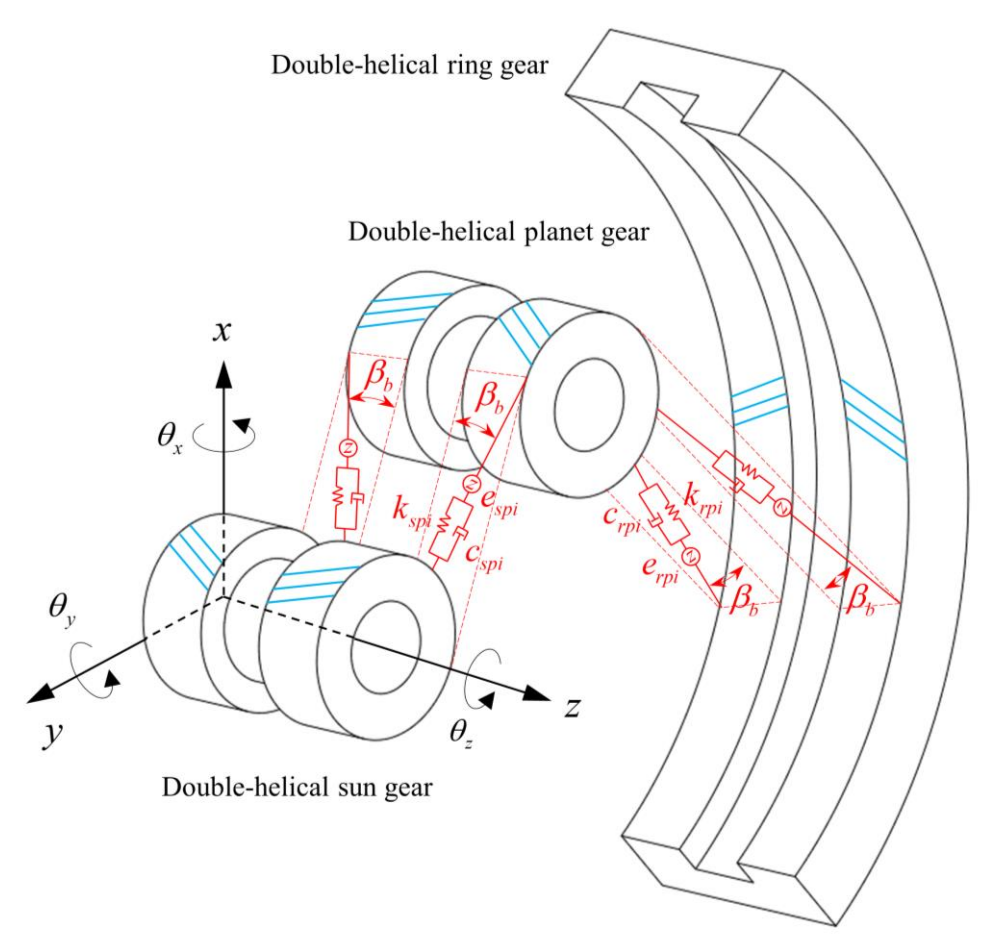


Fig.2-10 Schematic diagram of meshing of double-helical planetary gear train

The transverse face meshing diagrams of differential and closed stage gear trains are shown as Fig.2-11 and Fig.2-12, respectively.

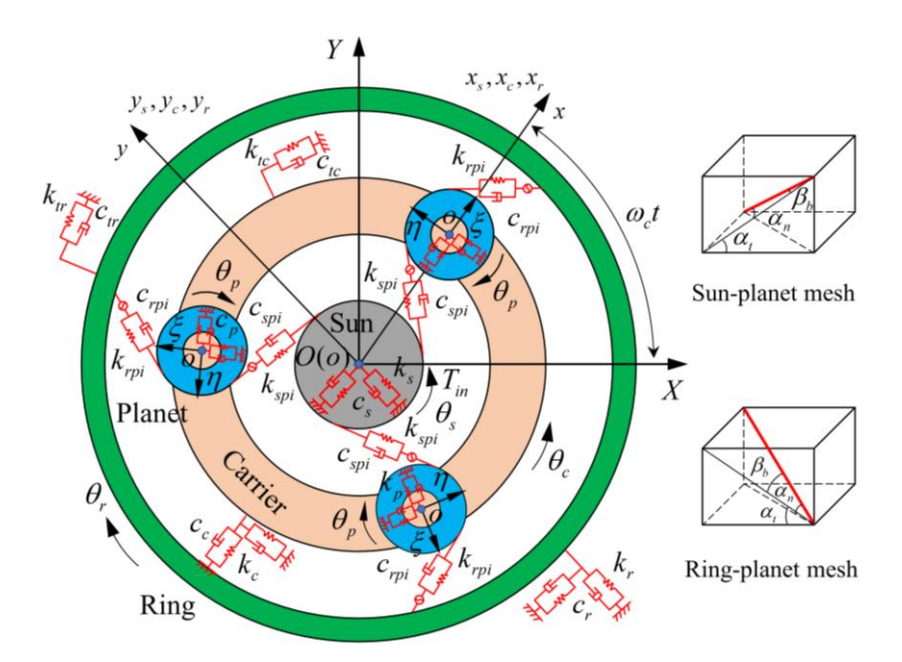


Fig.2-11 The dynamics model of the differential planetary gear train

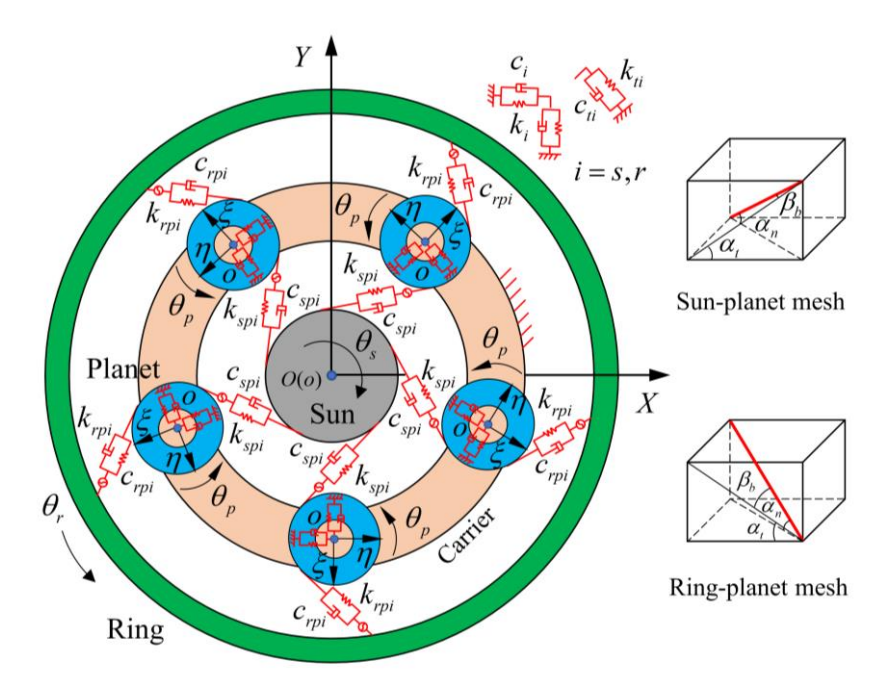


Fig.2-12 The dynamics model of the closed planetary gear train

The meaning of the symbols is consistent with static model. Since double-helical gear are composed of two helical gears with opposite helical angles and other parameters are completely consistent, only one helical gear of one side (left side) can be given in the meshing equation here and in the subsequent ones. For the meshing equation on the other side (right side), only a negative sign can be added in front of the helical angle.

2.4.1 Kinematic analysis of different components in the moving coordinate system

In this subsection, the kinematic relationship of the components of first stage in the corresponding moving coordinate is analyzed. Fig.2-13 shows the vector relations between the displacements of the central components (sun gear, planet carrier and ring gear) and the planet gear in two coordinate systems, where the moving coordinate system is $o_r - \zeta_p \eta_p z_p$, and the unit vectors of the coordinate systems are i, j, k. The coordinate $o_c - x_c y_c z_c$ is parallel to $o_s - x_s y_s z_s$. Each coordinate system rotates around the o point, and the rotational angular velocity of the carrier is ω_c .

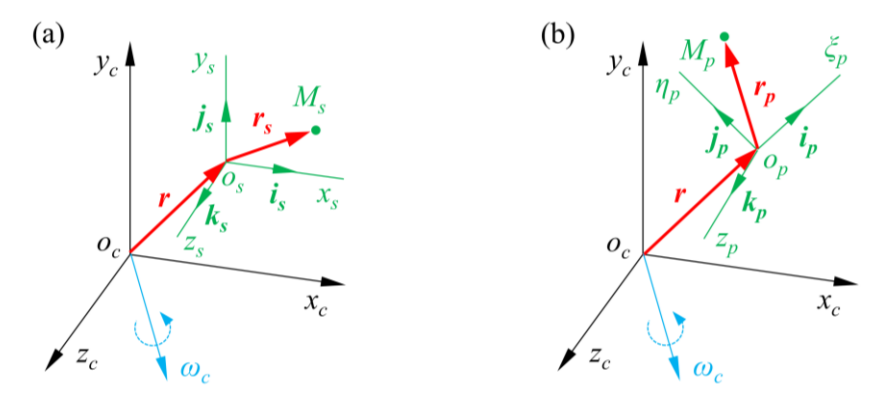


Fig.2-13 Displacement vectors for components: (a) sun and (b) planet

As depicted in Fig.2-13, assuming that the node of the sun in its own coordinate system is M_s , the displacement vector is \mathbf{r}_s , and the vector of the o_s point with respect to the o point is \mathbf{r} , then the displacement vector of the point M_s in the moving coordinate is $\mathbf{r}_{ms}=\mathbf{r}_s+\mathbf{r}$. Thus, the displacement, velocity and acceleration of the node M_s with respect to the moving coordinate system (o- $x_c y_c z_c$) can be relative displacement, relative velocity and relative acceleration, denoted as.

$$\mathbf{r}_{s} = x_{s} \mathbf{i}_{s} + y_{s} \mathbf{j}_{s} + z_{s} \mathbf{k}_{s}$$

$$\mathbf{v}_{s} = \dot{x}_{s} \mathbf{i}_{s} + \dot{y}_{s} \mathbf{j}_{s} + \dot{z}_{s} \mathbf{k}_{s}$$

$$\mathbf{a}_{s} = \ddot{x}_{s} \mathbf{i}_{s} + \ddot{y}_{s} \mathbf{j}_{s} + \ddot{z}_{s} \mathbf{k}_{s}$$
(2-26)

where, i_s , j_s and k_s are the unit vector of the coordinate, respectively. The scalars, such as x_s , y_s , z_s , \dot{x}_s , \dot{y}_s , \dot{z}_s , \ddot{x}_s , \ddot{y}_s and \ddot{z}_s , in front of the unit vector are the vibration response value.

Thus, the vector \mathbf{r}_s takes two derivatives, respectively, for time t to obtain the vector expressions for the absolute acceleration of the node M_s are given as

follows:

$$a_{is} = a_{s} + 2\omega \times v_{s} + \dot{\omega} \times r_{s} + \omega \times (\omega \times r_{s})$$
 (2-27)

Then, based on the vector product algorithm, the absolute acceleration of the sun is decomposed into two translation directions, which is given as:

$$a_{sx} = \ddot{x}_s - 2\omega_c \dot{y}_s - \dot{\omega}_c y_s - \omega_c^2 x_s$$

$$a_{sy} = \ddot{y}_s + 2\omega_c \dot{x}_s + \dot{\omega}_c x_s - \omega_c^2 y_s$$
(2-28)

In the same way, the absolute acceleration of the planet is decomposed into two translation directions, which is given as:

$$a_{px} = \ddot{\xi}_p - 2\omega_c \dot{\eta}_p - \dot{\omega}_c \eta_p - \omega_c^2 \xi_p - \omega_c^2 r_{bc}$$

$$a_{py} = \ddot{\eta}_p + 2\omega_c \dot{\xi}_p + \dot{\omega}_c \xi_p - \omega_c^2 \eta_p + \dot{\omega}_c r_{bc}$$
(2-29)

where, ω_c is the rotational angular velocity magnitude of the carrier in the first stage, and r_c is the distance from central point to planet pin. x_s , y_s , ξ_p and η_p are the vibration response displacement in their own coordinate, respectively. The item of $\omega_c^2 r_c$ and $\dot{\omega}_c r_c$ is the item related to the inertial force, which mainly depends on the angular velocity and acceleration of the carrier.

2.4.2 Dynamic model of sun and planet #i meshing

The meshing diagram of unilateral helical sun and planet is illustrated in Fig.2-14, the teeth in contact are equivalent to a spring damping unit.

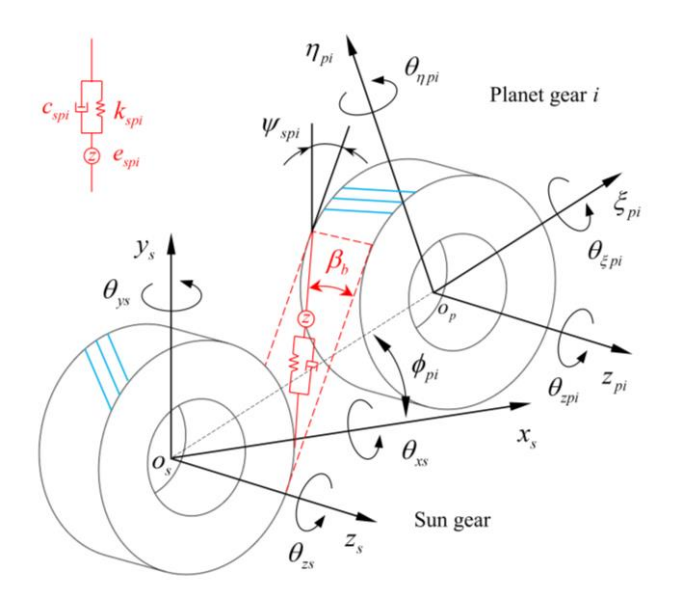


Fig.2-14 Diagram of sun-planet i meshing

As shown in Fig.2-14, the contact transmission of the teeth is represented by

the meshing stiffness k_{spi} , meshing damping c_{spi} and transmission error e_{spi} . As mentioned above, the components of the first-stage gear system are modeled in the moving coordinate system, with the formulas for acceleration and velocity as described in the previous section. Unlike most literature, the axial angular displacements $(\theta_{zs}, \theta_{zr}, \theta_{zc}, \theta_{zpi})$ of the components in the first stage are not defined in the moving coordinate system but rather in the fixed coordinate system, highlighting a key distinction in this modeling approach. Taking the example of the sun-planet gear mesh (S-Pi) shown in Fig.2-14, the meshing displacement and meshing velocity are expressed as follows:

$$\begin{split} & \delta_{spi} = [(x_s \sin \psi_{spi} + y_s \cos \psi_{spi} + (\theta_{zs} - \theta_{zc}) R_{bs} \\ & - \xi_{pi} \sin \alpha_{sp} - \eta_{pi} \cos \alpha_{sp} + (\theta_{zpi} - \theta_{zc}) R_{bp})] \cos \beta_b \\ & + [(\theta_{xs} \sin \psi_{spi} + \theta_{ys} \cos \psi_{spi}) R_{bs} - z_s \\ & + (\theta_{\xi pi} \sin \alpha_{sp} + \theta_{\eta pi} \cos \alpha_{sp}) R_{bp} + z_{pi}] \sin \beta_b - e_{spi}(t) \\ & \dot{\delta}_{spi} = [((\dot{x}_s - \omega_c y_s) \sin \psi_{spi} + (\dot{y}_s + \omega_c x_s) \cos \psi_{spi} + (\dot{\theta}_{zs} - \dot{\theta}_{zc}) R_{bs} \\ & - (\dot{\xi}_{pi} - \omega_c \eta_{pi}) \sin \alpha_{sp} - (\dot{\eta}_{pi} + \omega_c \xi_{pi}) \cos \alpha_{sp} + (\dot{\theta}_{zpi} - \dot{\theta}_{zc}) R_{bp})] \cos \beta_b \\ & + [(\dot{\theta}_{xs} \sin \psi_{spi} + \dot{\theta}_{ys} \cos \psi_{spi}) R_{bs} - \dot{z}_s \\ & + (\dot{\theta}_{\xi pi} \sin \alpha_{sp} + \dot{\theta}_{\eta pi} \cos \alpha_{sp}) R_{bp} + \dot{z}_{pi}] \sin \beta_b - \dot{e}_{spi}(t) \end{split}$$

In dynamics, the meshing displacement consists of the projection of the displacements in various directions of the meshing gear pair onto the meshing direction, along with the transmission error. Therefore, based on equation (2-30), the projection vector for the S-Pi meshing pair in the dynamic modeling is given by:

$$\mathbf{V}_{s}^{spi} = \begin{bmatrix} s\psi c\beta_{b} & c\psi c\beta_{b} & -s\beta_{b} & R_{bs}s\psi s\beta_{b} & R_{bs}c\psi s\beta_{b} & R_{bs}c\beta_{b} \end{bmatrix}
\mathbf{V}_{c}^{spi} = \begin{bmatrix} 0 & 0 & 0 & 0 & -R_{bc}c\beta_{b} \end{bmatrix}
\mathbf{V}_{pi}^{spi} = \begin{bmatrix} -s\alpha c\beta_{b} & -c\alpha c\beta_{b} & s\beta_{b} & R_{bp}s\alpha s\beta_{b} & R_{bp}c\alpha s\beta_{b} & R_{bp}c\beta_{b} \end{bmatrix}
\Delta \mathbf{V}_{s}^{spi} = \begin{bmatrix} \omega_{c}c\psi c\beta_{b} & -\omega_{c}s\psi c\beta_{b} & 0 & 0 & 0 & 0 \end{bmatrix}
\Delta \mathbf{V}_{pi}^{spi} = \begin{bmatrix} -\omega_{c}c\alpha c\beta_{b} & \omega_{c}s\alpha c\beta_{b} & 0 & 0 & 0 & 0 \end{bmatrix}$$

Based on equation (2-31), it is noted that, unlike in reference [149], there is an additional projection vector related to the carrier \mathbf{V}_c^{spi} , as well as extra projection vectors $\Delta \mathbf{V}_s^{spi}$, $\Delta \mathbf{V}_{pi}^{spi}$ arising from the velocity terms. Furthermore, during the calculation, the extra projection vectors such as $\Delta \mathbf{V}_s^{spi}$, $\Delta \mathbf{V}_{pi}^{spi}$ is similar to that of the projection vectors \mathbf{V}_s^{spi} , \mathbf{V}_{pi}^{spi} . Therefore, for brevity, the detailed

computation process is not provided here.

Therefore, the matrix form of the dynamic equation for the S-Pi is presented as follows:

$$\begin{bmatrix} \mathbf{M}_{s} & \mathbf{0} \\ \mathbf{0} & \mathbf{M}_{pi} \end{bmatrix} \begin{Bmatrix} \ddot{\mathbf{q}}_{s}(t) \\ \ddot{\mathbf{q}}_{pi}(t) \end{Bmatrix} + \mathbf{C}_{mesh}^{spi}(t) \begin{Bmatrix} \dot{\mathbf{q}}_{s}(t) \\ \dot{\mathbf{q}}_{c}(t) \\ \dot{\mathbf{q}}_{pi}(t) \end{Bmatrix} + \mathbf{K}_{mesh}^{spi}(t) \begin{Bmatrix} \mathbf{q}_{s}(t) \\ \mathbf{q}_{c}(t) \\ \mathbf{q}_{pi}(t) \end{Bmatrix} = \begin{Bmatrix} \mathbf{f}_{s} + \mathbf{f}_{s}^{spi} \\ \mathbf{f}_{pi}^{spi} \end{Bmatrix}$$

$$\mathbf{K}_{mesh}^{spi}(t) = k_{spi}(t) \begin{bmatrix} \mathbf{K}_{spi}^{11} & \mathbf{K}_{spi}^{12} & \mathbf{K}_{spi}^{13} \\ \mathbf{K}_{spi}^{21} & \mathbf{K}_{spi}^{22} & \mathbf{K}_{spi}^{23} \end{bmatrix}$$

$$\mathbf{C}_{mesh}^{spi}(t) = c_{spi}(t) \begin{bmatrix} \mathbf{C}_{spi}^{11} & \mathbf{C}_{spi}^{12} & \mathbf{C}_{spi}^{13} \\ \mathbf{C}_{spi}^{21} & \mathbf{C}_{spi}^{22} & \mathbf{C}_{spi}^{23} \end{bmatrix}$$

$$(2-32)$$

where, \mathbf{M}_s , \mathbf{M}_{pi} —the mass matrix of sun and planet;

 $\ddot{\mathbf{q}}_{s}, \ddot{\mathbf{q}}_{pi}$ —The acceleration vector of sun and planet;

 $\dot{\mathbf{q}}_{s}, \dot{\mathbf{q}}_{c}, \dot{\mathbf{q}}_{ni}$ -- The velocity vector of sun, carrrier and planet;

 \mathbf{q}_s , \mathbf{q}_c , \mathbf{q}_{pi} —The displacement vector of sun, carrier and planet;

 $\mathbf{K}_{spi}(t)$, $\mathbf{C}_{spi}(t)$ —Time-varying stiffness and damping matrix of S-Pi;

 \mathbf{f}_{s}^{spi} , \mathbf{f}_{pi}^{spi} -- The column vector of the meshing error force on sun and planet;

 $k_{spi}(t), c_{spi}(t)$ —Time-varying stiffness and damping of S-Pi.

In this case, the overall format of the meshing stiffness matrix and the meshing damping matrix is a 2×3 format, and the sub-matrices at each position are 6×6 matrices. The form of the sub-matrix in them is the same, the difference is that the front of the matrix is multiplied by the meshing stiffness and the meshing damping, respectively. In order to avoid redundancy, the following formulas will only give the form of the sub-matrix calculation in the matrix of meshing stiffness, and will not describe too much for the matrix of meshing damping.

$$\mathbf{K}_{spi}^{11} = (\mathbf{V}_{s}^{spi})^{T} \mathbf{V}_{s}^{spi}, \quad \mathbf{K}_{spi}^{12} = (\mathbf{V}_{s}^{spi})^{T} \mathbf{V}_{c}^{spi}, \quad \mathbf{K}_{spi}^{13} = (\mathbf{V}_{s}^{spi})^{T} \mathbf{V}_{pi}^{spi},$$

$$\mathbf{K}_{spi}^{21} = (\mathbf{V}_{pi}^{spi})^{T} \mathbf{V}_{s}^{spi}, \quad \mathbf{K}_{spi}^{22} = (\mathbf{V}_{pi}^{spi})^{T} \mathbf{V}_{c}^{spi}, \quad \mathbf{K}_{spi}^{23} = (\mathbf{V}_{pi}^{spi})^{T} \mathbf{V}_{pi}^{spi}.$$

$$(2-33)$$

according to Equation, the extra sub-matrices of the meshing stiffness of the S-Pi meshing pair are the sub-matrices at positions 12 and 22 of the Meshing stiffness matrix \mathbf{K}_{spi} , which are the key to removing the effect of the rotation of the carrier for first stage. Furthermore, the remaining sub-matrices and sub-vectors are shown below. It is worthwhile to note here that the additional acceleration terms

and velocities caused by the presence of the carrier moving coordinate system in the first stage need to be additionally assigned to the respective meshing stiffness and engagement damping matrices.

Additionally, the submatrix and subvector are given.

$$\begin{aligned} \mathbf{M}_{s} &= Diag[m_{s} \quad m_{s} \quad m_{s} \quad I_{s} \quad I_{s} \quad J_{s}], \\ \mathbf{M}_{pi} &= Diag[m_{pi} \quad m_{pi} \quad m_{pi} \quad I_{pi} \quad I_{pi} \quad J_{pi}], \\ \mathbf{f}_{s} &= \left\{0 \quad 0 \quad 0 \quad 0 \quad T_{in} / 2\right\}^{T}, \\ \mathbf{f}_{si}^{spi}(t) &= (k_{spi}(t)e_{spi}(t) + c_{spi}(t)\dot{e}_{spi}(t))(\mathbf{V}_{s}^{spi})^{T}, \\ \mathbf{f}_{pi}^{spi}(t) &= (k_{spi}(t)e_{spi}(t) + c_{spi}(t)\dot{e}_{spi}(t))(\mathbf{V}_{pi}^{spi})^{T}. \end{aligned}$$

2.4.3 Dynamic model of ring and planet #i meshing

The meshing diagram of unilateral helical sun and planet is shown in Fig.2-15, the teeth in contact are equivalent to a spring damping unit. As shown in Fig.2-15, the blue lines in planet and ring present the helix direction of the helical gear. The contact transmission of the teeth is represented by the meshing stiffness k_{rpi} , meshing damping c_{rpi} and transmission error e_{rpi} .

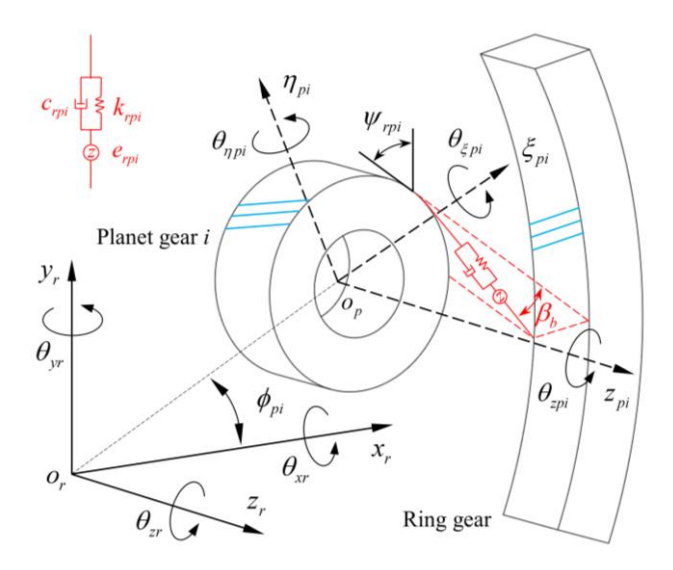


Fig.2-15 Diagram of ring-planet i meshing

In the same way, the dynamic balanced equations in matrix form of R-Pi meshing of single helical gear are derived as follows:

$$\begin{bmatrix} \mathbf{M}_{r} & \mathbf{0} \\ \mathbf{0} & \mathbf{M}_{pi} \end{bmatrix} \begin{pmatrix} \ddot{\mathbf{q}}_{r}(t) \\ \ddot{\mathbf{q}}_{pi}(t) \end{pmatrix} + \mathbf{C}_{rpi}(t) \begin{pmatrix} \dot{\mathbf{q}}_{r}(t) \\ \dot{\mathbf{q}}_{c}(t) \\ \dot{\mathbf{q}}_{pi}(t) \end{pmatrix} + \mathbf{K}_{rpi}(t) \begin{pmatrix} \mathbf{q}_{r}(t) \\ \mathbf{q}_{c}(t) \\ \mathbf{q}_{pi}(t) \end{pmatrix} = \begin{pmatrix} \mathbf{f}_{ri}^{rpi}(t) \\ \mathbf{f}_{pi}^{rpi}(t) \end{pmatrix}$$
(2-34)

where, M_r , M_{pi} —the mass matrix of ring and planet;

 $\ddot{\mathbf{q}}_r, \ddot{\mathbf{q}}_{ni}$ —The acceleration vector of ring and planet;

 $\dot{\mathbf{q}}_r, \dot{\mathbf{q}}_c, \dot{\mathbf{q}}_{pi}$ -- The velocity vector of ring, carrrier and planet;

 \mathbf{q}_r , \mathbf{q}_c , \mathbf{q}_{pi} —The displacement vector of ring, carrier and planet;

 $\mathbf{K}_{rpi}(t)$, $\mathbf{C}_{rpi}(t)$ —Time-varying stiffness and damping matrix of R-Pi;

 \mathbf{f}_r^{rpi} , \mathbf{f}_{pi}^{rpi} -- The column vector of the meshing error force on ring and planet;

 $k_{rpi}(t)$, $c_{rpi}(t)$ —Time-varying stiffness and damping of R-Pi.

The mass matrix and the external force are shown in the following equations.

$$\begin{aligned} \mathbf{M}_r &= Diag[m_r \quad m_r \quad m_r \quad I_r \quad I_r \quad J_r], \\ \mathbf{f}_r^{rpi}(t) &= (k_{rpi}(t)e_{rpi}(t) + c_{rpi}(t)\dot{e}_{rpi}(t))(\mathbf{V}_r^{rpi})^T, \\ \mathbf{f}_{pi}^{rpi}(t) &= (k_{rpi}(t)e_{rpi}(t) + c_{rpi}(t)\dot{e}_{rpi}(t))(\mathbf{V}_{pi}^{rpi})^T. \end{aligned}$$

2.4.4 Dynamic model of carrier and planet #i

The meshing diagram of unilateral helical sun and planet is depicted in Fig.2-16, the teeth in contact are equivalent to a spring damping unit. As shown in Fig.2-16, the supporting relationship is represented by the supporting stiffness k_{cpi} and supporting damping c_{cpi} .

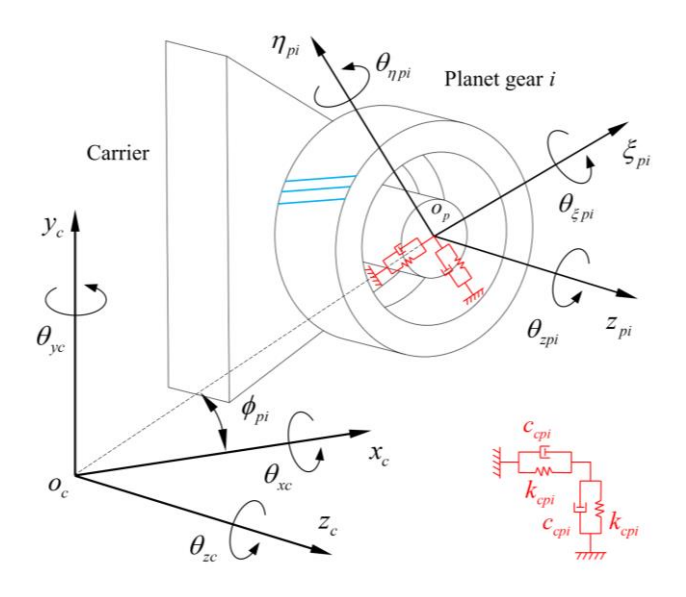


Fig.2-16 Supporting diagram of carrier and planet i

According to static model of carrier and planet, the dynamic balanced equations in matrix form of c-pi of single helical gear are derived as follows:

$$\begin{bmatrix} \mathbf{M}_{c} & \mathbf{0} \\ \mathbf{0} & \mathbf{M}_{pi} \end{bmatrix} \begin{Bmatrix} \ddot{\mathbf{q}}_{c}(t) \\ \ddot{\mathbf{q}}_{pi}(t) \end{Bmatrix} + \mathbf{C}_{cpi} \begin{Bmatrix} \dot{\mathbf{q}}_{c}(t) \\ \dot{\mathbf{q}}_{pi}(t) \end{Bmatrix} + \mathbf{K}_{cpi} \begin{Bmatrix} \mathbf{q}_{c}(t) \\ \mathbf{q}_{pi}(t) \end{Bmatrix} = \begin{Bmatrix} \mathbf{f}_{c} \\ \mathbf{0} \end{Bmatrix}$$
(2-35)

where, \mathbf{K}_{cpi} --Supporting stiffness matrix;

C_{cpi}--Supporting damping matrix;

M_c--Mass matrix of carrier;

 \mathbf{f}_{c} —The torque vector of carrier.

The calculation of the support stiffness matrix is derived from the static model. The support damping matrix has a similar form to the support stiffness matrix, with the stiffness values of the bearings replaced by damping values. The mass matrix and the torque vector are as follows:

$$\mathbf{M}_{c} = Diag[m_{c} \quad m_{c} \quad m_{c} \quad I_{c} \quad I_{c} \quad J_{c}],$$

$$\mathbf{f}_{c} = \left\{0 \quad 0 \quad 0 \quad 0 \quad T_{out}\right\}^{T}$$

2.4.5 Dynamic model of bearing

In this study, the bearing is rolling bearing and the schematic diagram is shown in Fig.2-17. As shown in Fig.2-17, the rolling bearing is composed of three parts, one inner ring, one outer ring and N rolling elements. The bearing is used to support the shafts, sun, carrier, ring and so on to insure normal work of the mechanical system.

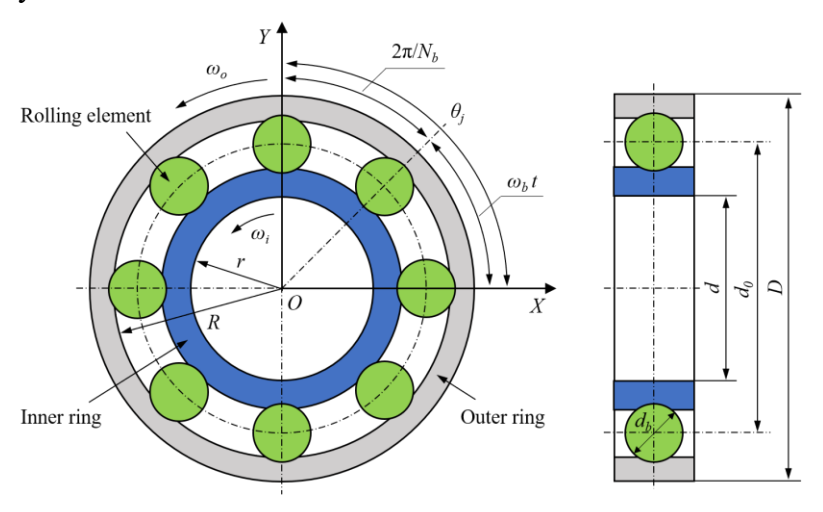


Fig.2-17 Schematic diagram of the rolling bearing

For instance, the supporting matrix of the sun, planet and ring is shown as:

$$\mathbf{K}_{bi} = diag\{k_{bx} \quad k_{by} \quad k_{bz} \quad k_{\theta x} \quad k_{\theta y} \quad 0\}$$
 (2-36)

where, i presents the sun, carrier and ring, respectively.

Therefore, the motion equation in matrix form for bearing node j can be

expressed as below equation.

$$\mathbf{M}_{bj}\ddot{\mathbf{X}}_{bj} + \mathbf{C}_{bj}\dot{\mathbf{X}}_{bj} + \mathbf{K}_{bj}\mathbf{X}_{bj} = \mathbf{0}$$
 (2-37)

in which, \mathbf{M}_{bj} and \mathbf{X}_{bj} represent the mass matrix and displacement column vector for the bearing node j, respectively.

2.4.6 Dynamic model of the beam element

The above three subsections only given the dynamic model of one side of double-helical gears. But for an actual double-helical gear, it is one piece (sun and planet) or rigidly connected by two helical gears (ring). Here, Timoshenko beam element is used to connect both sides by referring to Ajmi and Velex's work[150]. As illustrated in Fig.2-18 to explain the nodes and beam elements, for two sides of double-helical gears, nodes 2 and 6 (for middle positions of two sides) are defined as mesh nodes (red nodes), which mesh with mesh nodes of other gears, and every element consist of two nodes. Node 4 (the middle node of a double-helical gear) is used to connect another support structure (bearing or spline support).

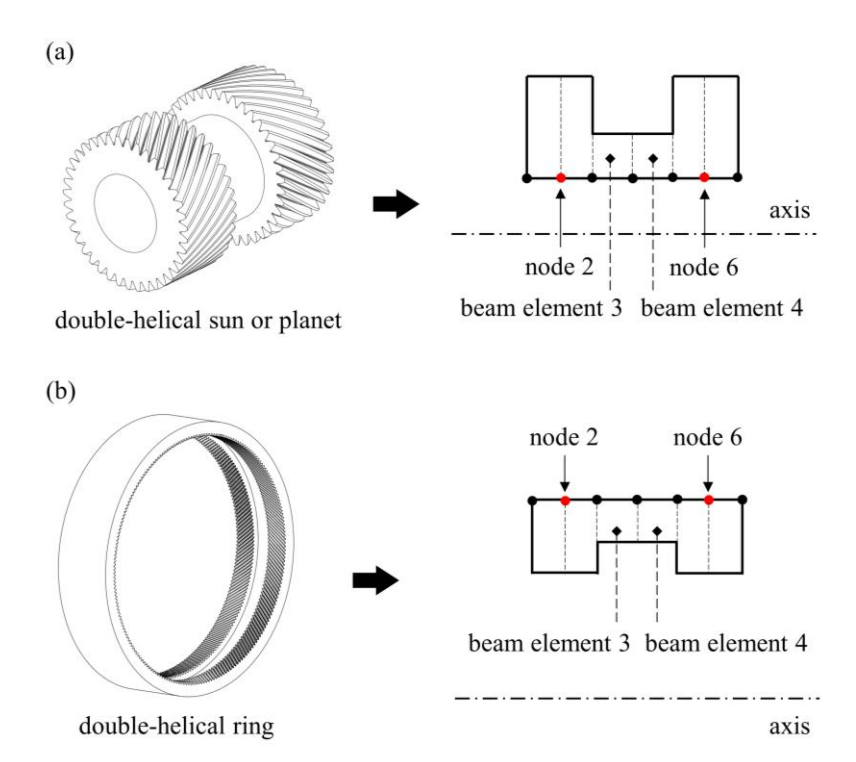


Fig.2-18 Diagram of nodes of double-helical gears

Therefore, the dynamic equation in matrix form is given as follow:

$$\mathbf{M}_{beam}\ddot{\mathbf{q}}_{beam}(t) + \Omega \mathbf{G}_{beam}\dot{\mathbf{q}}_{beam}(t) + \mathbf{K}_{beam}\mathbf{q}_{beam}(t) = \mathbf{0}$$
 (2-38)

where, in the equation (2-38), \mathbf{M}_{beam} , \mathbf{G}_{beam} , \mathbf{K}_{beam} and \mathbf{q}_{beam} represent the mass matrix, gyroscope matrix, stiffness matrix and displacement vector of the beam element, respectively.

In addition, according to the finite element assembly principle, for instance, the assembly stiffness matrix (or mass matrix) of adjacent elements i and i+1 is shown as below.

$$\mathbf{K}_{i(i+1)} = \begin{bmatrix} \mathbf{K}_{i}^{11} & \mathbf{K}_{i}^{12} & \mathbf{0} \\ & \mathbf{K}_{i}^{22} + \mathbf{K}_{i+1}^{11} & \mathbf{K}_{i+1}^{12} \\ sym. & \mathbf{K}_{i+1}^{22} \end{bmatrix}$$
(2-39)

where, the sub-matrices of *i*th Timoshenko beam element in Equation (2-39) are given in Appendix.

2.4.7 Dynamic model of the overall system

The above sub-system matrices shown in Eq. (2-32), (2-34) and (2-35) are assembled based on assemble method defined by Eq. (2-39) to obtain the overall dynamic equations of a double-helical planetary gear train consisting of N planets. As shown in Fig.2-19, for the sake of simplicity, only one side of the double-helical gear meshing (red node) is shown here.

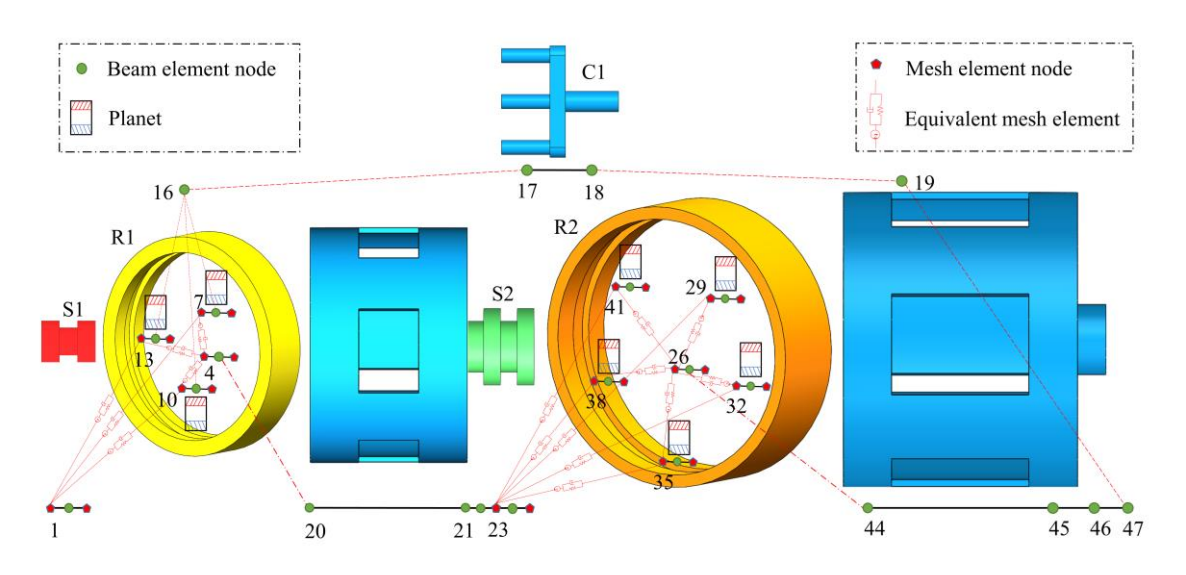


Fig.2-19 The node diagram of the overall system

According to the above equations, the overall dynamic equation in matrix form of the studied planetary gear system is shown as follows.

$$\mathbf{M}_{overall}\ddot{\mathbf{q}}_{overall} + \mathbf{C}_{overall}\dot{\mathbf{q}}_{overall} + \mathbf{K}_{overall}\mathbf{q}_{overall} = \mathbf{F}_{overall}$$
(2-40)

in which, $\mathbf{M}_{overall}$, $\mathbf{K}_{overall}$ and $\mathbf{C}_{overall}$ are the overall mass, stiffness and damping matrix, respectively. $\mathbf{K}_{overall}$ and $\mathbf{C}_{overall}$ have similar form, they are obtained based on the finite assemble method, for instance, the assemble diagram of the overall stiffness matrix is shown as the Fig.2-20.

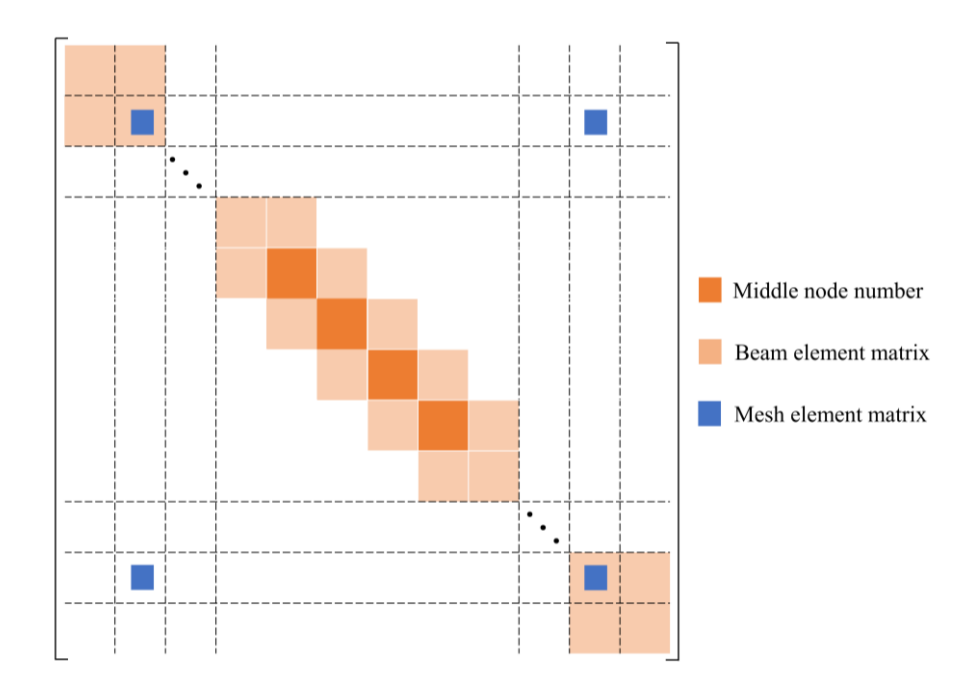


Fig.2-20 The diagram of overall assembly matrice

Additionally, the specific forms of the damping matrix, stiffness matrices and Force are shown below:

$$\mathbf{K}_{sys} = \mathbf{K}_{B} + \mathbf{K}_{b} + \mathbf{K}_{m} + \omega_{c}^{2} \mathbf{K}_{Centrifugal} + \mathbf{K}_{Coriolis}$$

$$\mathbf{C}_{sys} = \mathbf{C}_{R} + \mathbf{C}_{b} + \mathbf{C}_{m} + 2\omega_{c} \mathbf{G}_{Coriolis} + \sum_{i=shaft}^{n} \omega_{i} \mathbf{G}_{di}$$

$$\mathbf{F}_{sys} = \mathbf{F}_{T} + \mathbf{F}_{g} + \mathbf{F}_{c} + \mathbf{F}_{me}$$
(2-41)

where $\mathbf{F}_T/\mathbf{F}_g/\mathbf{F}_c/\mathbf{F}_{me}$ denote the torque term, the gravity term, the centrifugal force term (for the first-stage planet gear), and the meshing excitation term, respectively. $\mathbf{K}_B/\mathbf{K}_b/\mathbf{K}_m/\mathbf{K}_{Centrifugal}/\mathbf{K}_{Coriolis}$ denote the beam element stiffness matrix, the bearing support stiffness matrix, the meshing stiffness matrix, the stiffness matrix

resulting from the centrifugal acceleration term, and the stiffness matrix generated by the Koehler effect of the velocity term correction term, respectively. In contrast to the stiffness matrix, $\mathbf{C}_b/\mathbf{C}_m/\mathbf{C}_{Coriolis}$ denote the bearing support damping matrix, the meshing damping matrix, the damping matrix resulting from the Coefficients acceleration term. Furthermore, \mathbf{C}_R denotes the Rayleigh damping matrix of the whole system, which is usually related to the system mass matrix and the system stiffness matrix, and is calculated by the formula shown below:

$$\mathbf{C}_{R} = \alpha \mathbf{M}_{sys} + \beta \mathbf{K}_{sys}$$

$$\alpha = 2(\xi_{2} / \omega_{2} - \xi_{1} / \omega_{1}) / (1 / \omega_{2}^{2} - 1 / \omega_{1}^{2})$$

$$\beta = 2(\xi_{2} \omega_{2} - \xi_{1} \omega_{1}) / (\omega_{2}^{2} - \omega_{1}^{2})$$
(2-42)

where α and β are the scaling factors corresponding to the front of the mass and stiffness matrices. ω_1 and ω_2 are the first and second order natural frequency values of the system. ξ_1 and ξ_2 are the damping ratio coefficients, which in this paper take the value of 0.07.

In addition, the gyro matrix G_{di} for the concentrated mass points such as the sun gear, the planet gear and the ring gear is shown below.

where the gyro matrix is an anti-symmetric matrix, J_p is the polar moment of inertia, and it should be noted that it is preceded by a multiplication by the angular velocity of the axis represented by the node.

2.5 Brief summary

This chapter presents the mechanical models, quasi-static and dynamic model, for a two-stage parallel compound gear system based on common error types in gear transmission and the calculation formulas for the meshing phases in planetary gear systems. The main contents are as follows:

(1) A unified and concise modeling method suitable for the two-stage parallel compound gear system is proposed, based on the structural characteristics of

different gear trains. Unlike previous literature, this method combines fixed and moving coordinate systems and introduces a formula for calculating the meshing displacement of differential gear systems. This approach simplifies the modeling process by avoiding the complexities associated with coordinate transformations, establishing a static model, which provides a reference for modeling the dynamic model.

(2) Based on the moving coordinate systems, in order to address the incompleteness of dynamic equations arising from neglecting coupling and Coriolis accelerations due to the rotation of the carrier, complete formulas for the absolute acceleration of various components in the first-stage gear system are derived. According to the modeling process of static model and incorporates additional projection vectors generated by velocity terms, thereby the lumped mass dynamic model of the compound gear system in the moving coordinate system of the first-stage is developed. By employing the finite element method and node position diagrams, the flexibility of the shafts is taken into account, leading to the establishment of a comprehensive dynamic model for the entire two-stage parallel compound gear system.

Chapter 3 Study on the Static Characteristics of the Double-helical Two-Stage Parallel Compound Marine Gear Transmission System

3.1 Preface

Based on the translational-torsional static model, this chapter primarily analyzes its static characteristics. Formulas for calculating the load sharing ratio (LSR) and global transmission error (GTE) are provided. The effects of planet pinhole position error and eccentricity errors on LSR and GTE are examined. Additionally, the influence of different configurations of the sun (fixed vs. floating) on the LSR is explored. Finally, the influence of eccentricity errors on the orbit is investigated, the conclusion that the shape of the axis trajectory is related to the number of teeth of gears with eccentricity errors is obtained.

3.2 Study on load sharing ratio and transmission error

In quasi-static, load sharing ratio (LSR) and global transmission error (GTE) from input to output element are basic characteristics. In this section, the content of a two-stage double helical differential closed planetary gear train is presented. Different errors, such as planet positioning error or eccentricity, were considered and the influence of the errors on the LSR and GTE was analysed. A two-stage double-helical planetary gear train for ships is studied in the following, with its basic gear parameters and phase relationship of every stage shown in Tab.3-1. The input speed is 600rpm and the input torque is 5000N.m.

Tab.3-1 Parameters of the two-stage double-helical planetary gear train studied

| Stage | | First Stage | ; | Second Stage | | |
|---------------------------------------|-----------|-------------|------|--------------|--------|------|
| Element | Sun | Planet | Ring | Sun | Planet | Ring |
| Teeth number, Z | 41 | 88 | 217 | 85 | 60 | 205 |
| Normal module, m_n (mm) | 6 | | | | | |
| Normal pressure angle, α_n (°) | | | 2 | 0 | | |
| Helix angle, β (°) | | | 2 | 5 | | |
| Number of planets (N) | 3 | | | 5 | | |
| Planets spacing angle (°) | 120 72 | | | | | |
| Mesh Phasing condition | ESSP ESIP | | | | | |

For every planet in a planetary gear system, it bears the contact force from sun and ring, and the torque generated by these contact forces must be equal. So once the balance of every element is reached, the input torque will be split into every planet gear. The LSR of planet i is obtained as follows:

$$LSR_i = F_i / (\sum_{i=1}^{N} F_i)$$
 (3-1)

where F_i is contact force in planet i, and the ideal value of LSR_i is 1/N, which depends on the number of planet gear.

The transmission error is the difference between the ideal angular position and real angular position.

$$TE_i = \theta_{real} - \theta_{ideal} \tag{3-2}$$

Therefor, for GTE, the transmision error is shown.

$$GTE = \theta_{real} - \theta_{in} / TR \tag{3-3}$$

where TR is the transmission ratio from input element to output element, as shown in following equation. $TR = 1 + (Z_r^1/Z_s^1) + (Z_r^1/Z_s^1) \times (Z_r^2/Z_s^2)$

3.2.1 Load sharing ratio and transmission error analysis without error in fixed sun configuration

3.2.1.1 Load sharing ratio results

The mesh phasing in first stage is ESSP, the ideal mean LSR is 1/3, and the phase difference is $2\pi/3$. The mesh phasing in second stage is ESIP, the ideal LSR is 1/5, and the phase difference is 0. The LSR result of 1st stage without any error of overall system are presented in Fig.3-1. For 2nd stage, the LSR result is perfect and equal 0.2 because of mesh phasing, this result it is not shown in the figure.

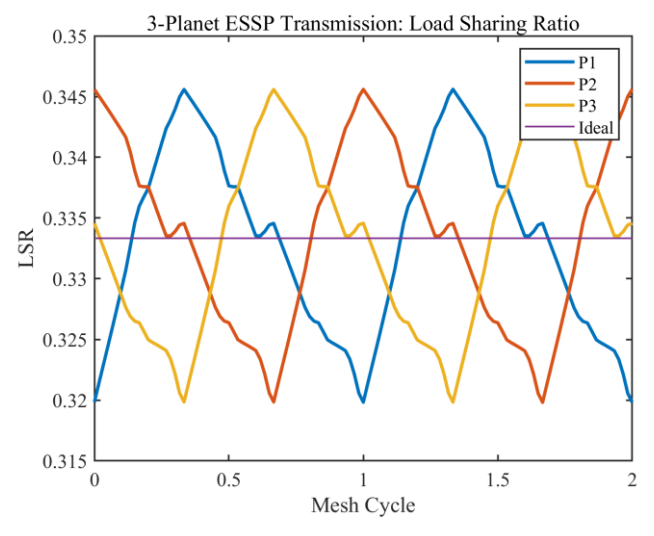


Fig.3-1 LSR results of 1st stage without errors

As shown in Fig.3-1, the calculated LSR value fluctuates due to the variation of the gear stiffness and the different force balance this produces between the different gears. In addition, the LSR result in the first stage has the same phase difference as that exhibited by the planet meshes.

3.2.1.2 Transmission error results

For two stages, there are two mesh frequencies and their formulas are shown as follows:

$$f_m^1 = (f_s^1 - f_c^1) \times Z_s^1, \quad f_m^2 = (f_s^2) \times Z_s^2$$
 (3-4)

Fig.3-2 shows the transmission error result in the time domain of output element within 1 cycle and its frequency spectrum in the frequency domain without any error. The mesh frequency in 2nd stage and its first 6th harmonics have a bigger influence on the output element than the mesh frequency in the first stage. The literature [151] shows that for one stage planetary gear system, in terms of the overall transmission error, the nominal IP gear set shows all harmonics of gear mesh frequency, and the SP gear set shows only the multiples of number of planet gear. Compared to that, the excitation frequency of output element can be seen as a superposition of excitation frequency in each stage, with different mesh phasing (SP and IP).

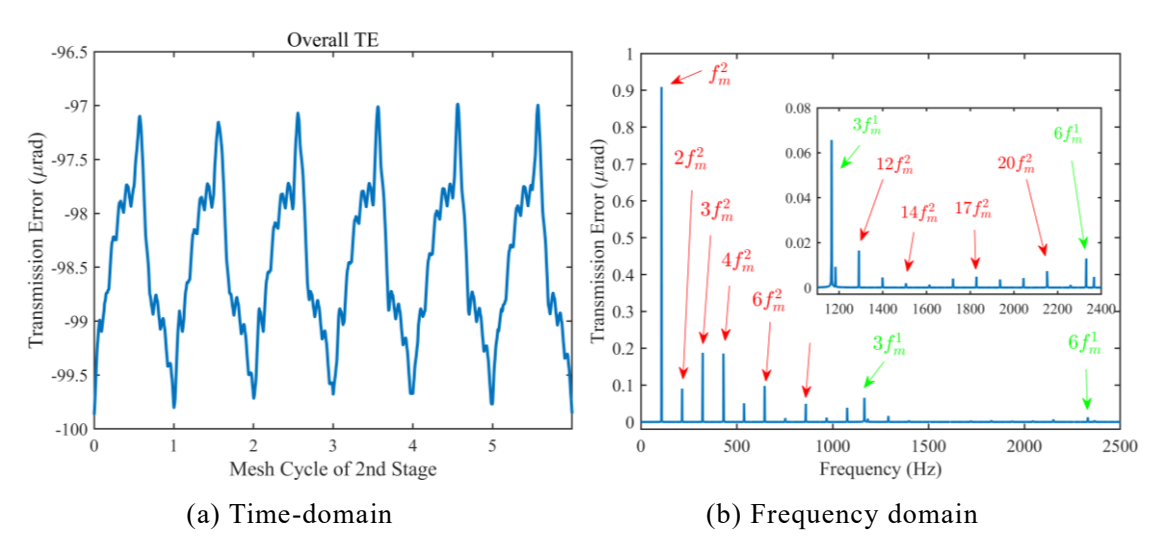


Fig.3-2 The transmission error results of output element in fixed sun configuration

3.2.2 Load sharing ratio and transmission error analysis considering error in fixed sun configuration

In order to study the influence of the same error value on the LSR, a K factor is defined as the ratio of the actual load carried and the ideal load carried by this

planet to its nominal sharing value:

$$K_i = LSR_i / (1/N) \tag{3-5}$$

 K_i >1 indicates that planet i carries more load than the ideal load. On the other hand, in order to clearly show the effect on the planet load sharing, only errors on planet #1 will be considered in the analysis, so that the cause of the loading or unloading of the different paths can be more easily interpreted.

3.2.2.1 Influence of the planet pinhole positional error on load sharing ratio and global transmission error

First, as reported in the scientific literature, the radial component of the planetary position error has a negligible influence on the load sharing of planetary transmissions when the pressure angles of the sun-planet and planet-ring contacts are equal. In the case where the pressure angles are not equal, Iglesias et al. [114] conclude that, although not negligible, the radial component of the error has a much smaller impact on the LSR than the tangential component. In the present work, because the pressure angles coincide, only the tangential component of the positioning error on the load distribution is studied.

Tab.3-2 shows the five case studies used, with different error values, where it can be seen that both the LSR and the relative LSR decrease as the error value increases, leading to a worse distribution of the load and therefore a worse transmission performance.

| Error | e _t | 1st stage $LSR_I(\%)$ K_I | | | LSR | K_{I} | |
|---------------|----------------|-----------------------------|-------|--------|-------|---------|-------|
| Configuration | (µm) | max | min | | max | min | |
| 1 | 5 | 28.91 | 26.54 | 0.8318 | 22.16 | 22.08 | 1.106 |
| 2 | 10 | 23.25 | 21.11 | 0.6654 | 24.31 | 24.16 | 1.212 |
| 3 | 15 | 17.60 | 15.67 | 0.4991 | 26.47 | 26.24 | 1.318 |
| 4 | 20 | 11.95 | 10.23 | 0.3327 | 28.63 | 28.32 | 1.423 |
| 5 | 30 | 0.0064 | 0 | 0.0002 | 32.94 | 32.48 | 1.647 |

Tab.3-2 LSR value with different tangential error value in planet

In order to clearly demonstrate the loading situation of each planet over time, Fig.3-3 shows the load distribution when a tangential error of 30 and 10 micrometres respectively is applied to planet # 1 of each stage. In the first case (stage 1) it can be seen that planet 1 is almost totally unloaded, while in the second figure (stage 2) the error leads to an overloading of planet 1. From a durability point of view, it should be noted that errors that advance the loading of the planet

are more dangerous, since the increase in stresses is higher in the defective planet that individually absorbs the excess load imbalance. When the planet suffers a discharge, it is the rest of the planets that must absorb the imbalance, distributing it over a larger number of gears and not generating such high stresses.

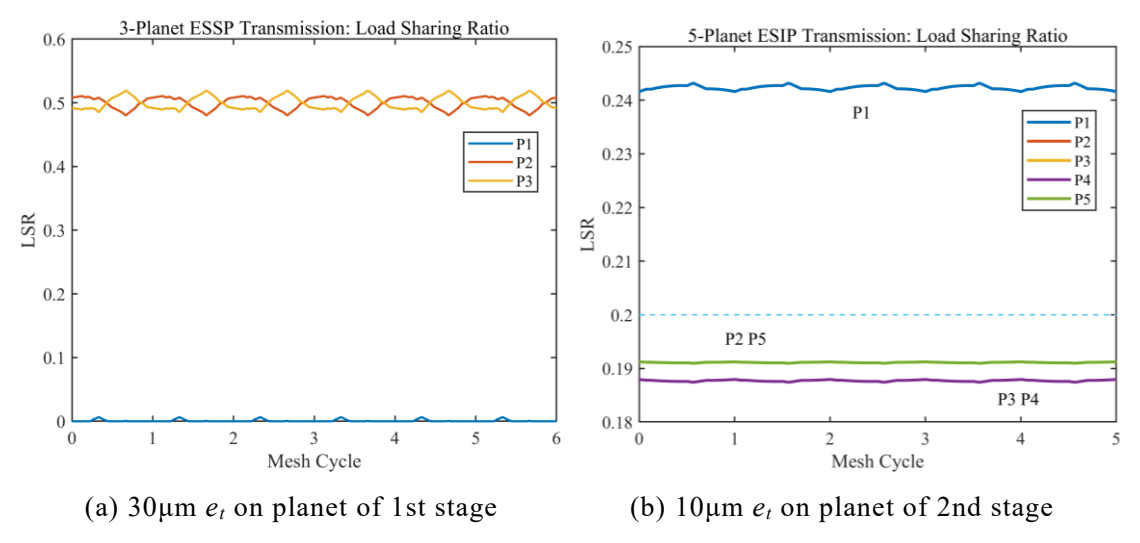


Fig.3-3 The LSR results with tangential error on planet #1 in every stage

Corresponding to the case shown in Fig.3-3 (a), Fig.3-4 shows the results in time and frequency of the TE with 30µm tangential error on planet #1 in the 1st stage. Compared with the case shown in Fig.3-2, it can be seen that the main excitation frequency does not change, which means that the main excitation frequency of the output element is still the meshing frequency of each stage, but the residual multiples of the meshing frequencies of the 1st stage appear, as shown in Fig.3-4 (b).

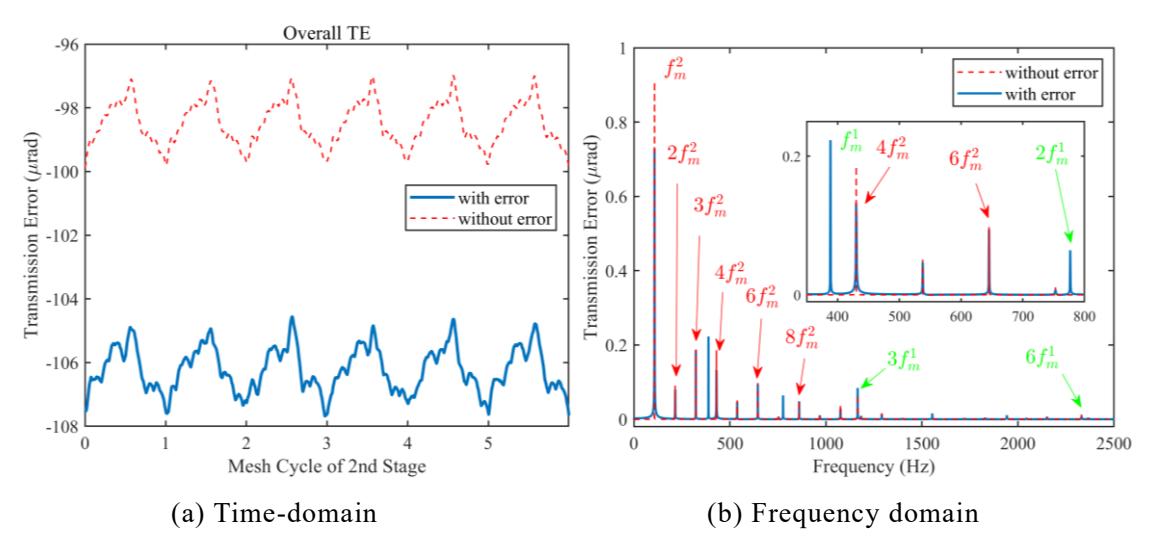


Fig.3-4 The overall transmission error with 30 µm tangential error on planet #1 in 1st stage

On the other hand, and in correspondence with the case shown in Fig.3-3 (b), when the tangential error of 10 µm is considered only in the 2nd stage planet, the TE time and frequency results are shown in Fig.3-5. As shown in Fig.3-5 (b), the TE main excitation frequency does not change, and it can be seen how the tangential error introduced in the 2nd stage planet does not substantially modify the signal.

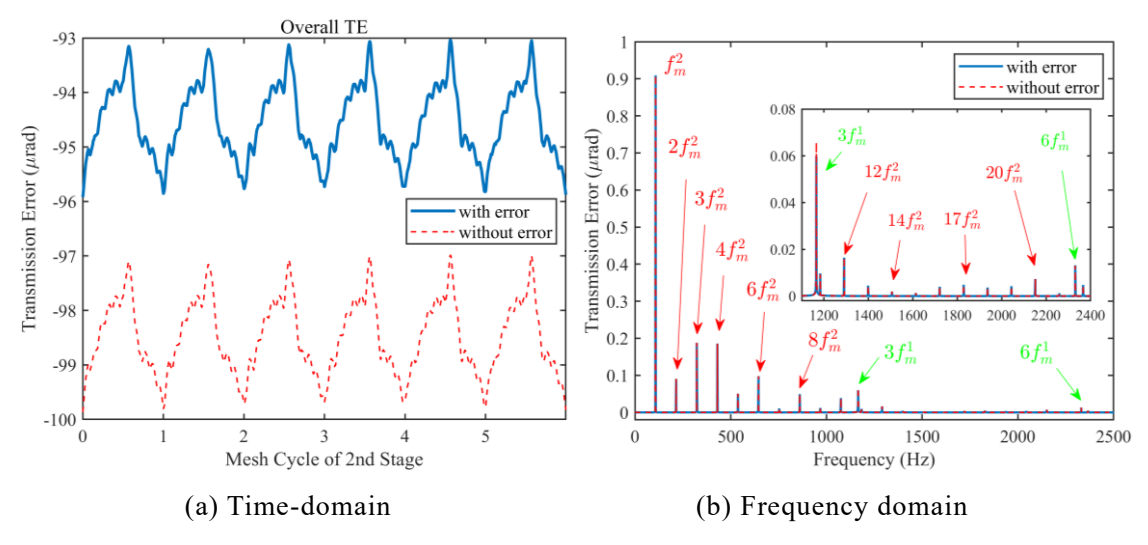


Fig.3-5 The overall transmission error with 10 µm tangential error on planet #1 in 2nd stage

Comparing Fig.3-4 and Fig.3-5, in terms of GTE, for the sequential mesh phase stage, the tangential error activates some new frequencies. On the other hand, for the stage with the contacts in phase, the tangential error does not produce any new frequencies.

3.2.2.2 Influence of the planet eccentricity error on load sharing ratio and globa l transmission error

Secondly, the eccentricity error on planet 1 of each stage is chosen as an example to study the influence of the eccentricity error on the global TE. Tab.3-2 shows the LSR and its relative value with eccentricity error at planet 1 of each stage.

| - | | | 1st stage | | | 2nd stage | | |
|------------------------|-----------------------------|---------|-----------|------------|---------|-----------|--------------|--|
| Error Configuration | e _{runout} (μm) | LSR1(%) | | may(V.) | LSR1(%) | | may (V.) | |
| | (1) | max | min | $max(K_1)$ | max | min | $\max (K_1)$ | |
| 1 | 5 | 40.21 | 26.55 | 1.206 | 22.15 | 17.85 | 1.108 | |
| 2 | 10 | 45.86 | 21.11 | 1.376 | 24.31 | 15.69 | 1.216 | |
| 3 | 15 | 51.51 | 15.67 | 1.545 | 26.46 | 13.54 | 1.323 | |

Tab.3-3 Error configuration for run out error in planet gear

| 4 | 20 | 57.16 | 10.23 | 1.715 | 28.62 | 11.38 | 1.431 |
|---|----|-------|-------|-------|-------|-------|-------|
| 5 | 30 | 68.47 | 0 | 2.054 | 32.93 | 07.07 | 1.647 |
| 6 | 50 | 91.16 | 0 | 2.735 | 41.55 | 0 | 2.077 |

In order to visualize the LSR changes, Fig.3-6 shows the shape of LSR, and Fig.3-6 (a) and (b) are the LSR results of two stages, respectively. In this figure, it can be seen how the eccentricity error corresponds to a projection of the error value in its radial and tangency components. The harmonic wave reaches its maximum when the projection is carried out on the tangential component, which has the greatest influence on the load distribution, and its minimum when the projection is carried out on the radial component, whose effect on the load distribution of a transmission as the one studied (same pressure angles) is zero.

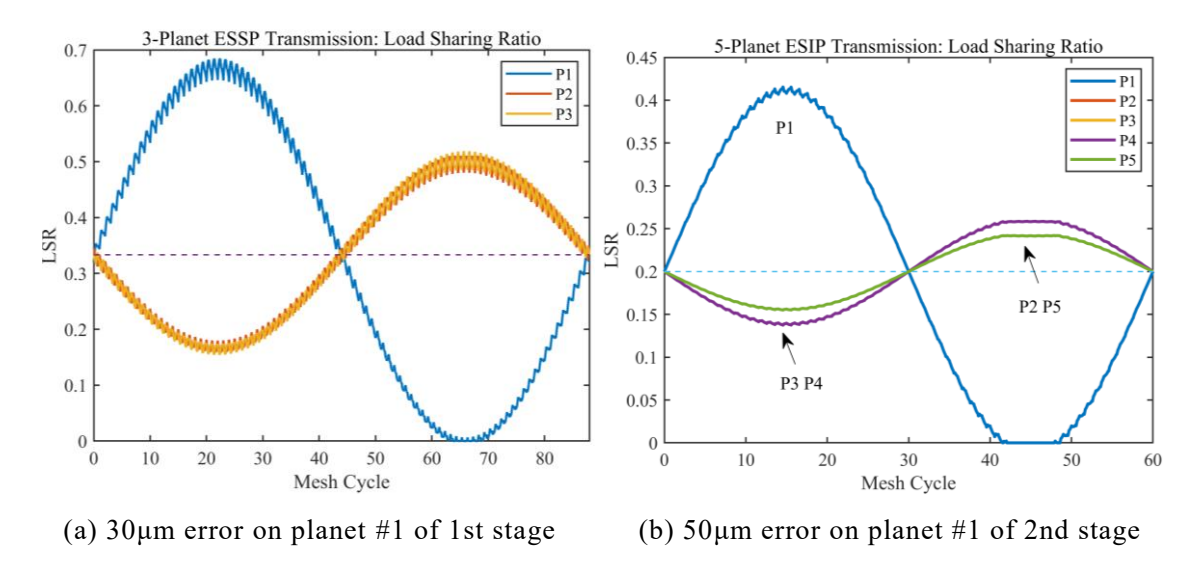


Fig.3-6 The LSR results with eccentricity error on planet in every stage

For 1st stage, corresponding to Fig.3-6 (a), Fig.3-7 shows the time and corresponding frequency result of overall TE. As shown in Fig.3-7 (a), 1 repeat cycle equal 24.37 times of mesh cycle of 2nd stage and there must is error frequency. Corresponding, not only are the error frequency (f_e) appearing, but some new major excitation frequencies such as $f_m^1 - f_e$, $f_m^1 + f_e$, $2f_m^1 - f_e$, $2f_m^1 + f_e$ are also appearing. These new frequencies appear around the meshing frequency of 1st stage. Except the influence of error, only the 1th meshing frequency of 2nd stage decrease a little value, and there is almost no change for the other frequency. Therefore, in terms of the global TE, the frequency of runout error of planet in 1st stage has a bigger effect than other primary frequencies.

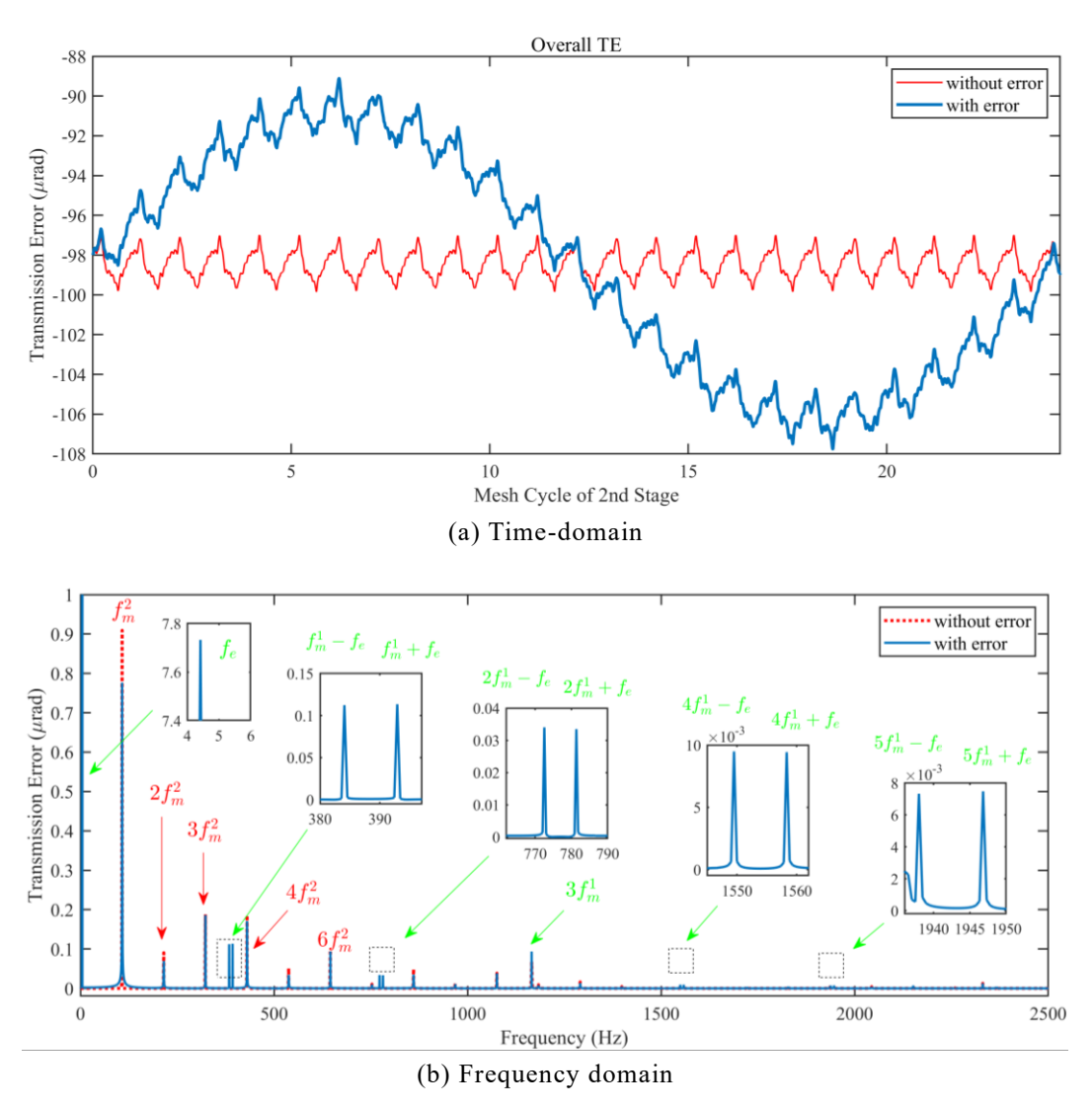
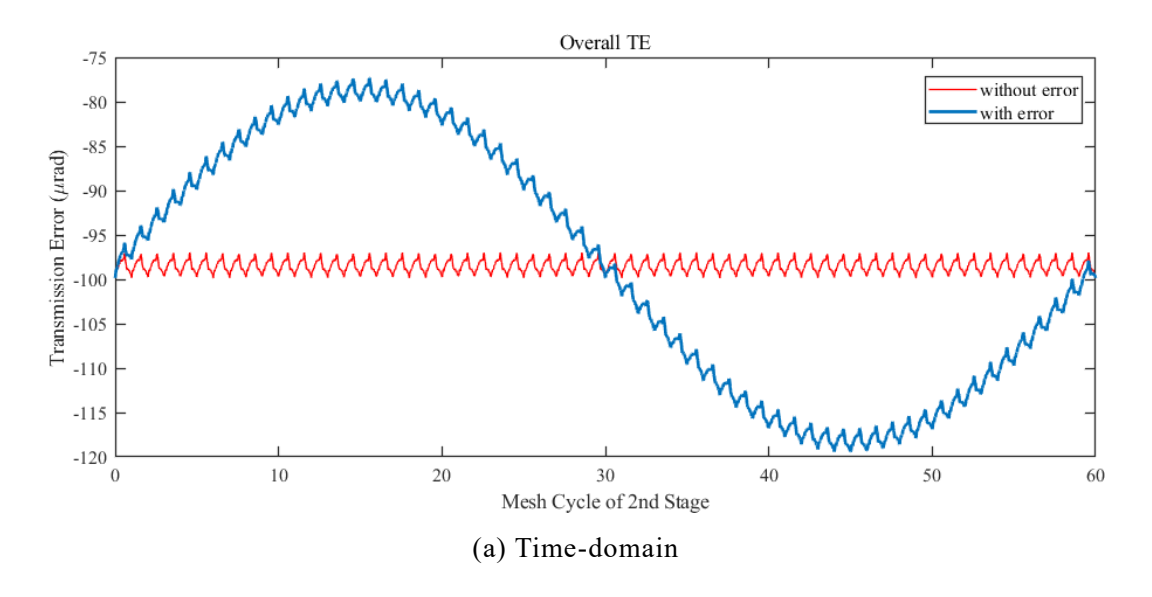


Fig.3-7 The overall transmission error with 30μm eccentricity error on planet #1 in 1st stage



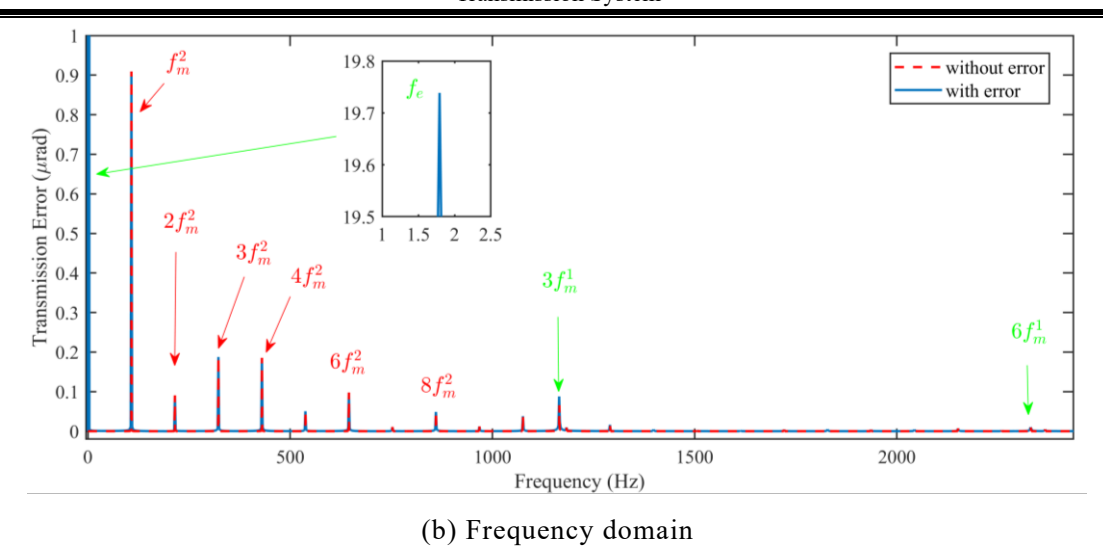


Fig.3-8 The overall transmission error with 50 µm eccentricity error on planet #1 in 2nd stage

According to the case shown in Fig.3-6 (b), for an eccentricity error of $50\mu m$ in the 2nd stage, the time record and frequency content of the global TE are shown in Fig.3-8. As shown in Fig.3-8 (b), the eccentricity error frequency (f_e) coincides with the rotation frequency of the 2nd stage planet, as the planet holder is fixed. On the other hand, in the spectral content the only variation is in the error frequency, while all other frequencies remain unchanged.

As shown in Fig.3-7 and Fig.3-8, for the planetary stages with different meshing phases, by comparing the frequency spectrum, it can be known that the eccentricity error of the planet gear has a greater impact on the overall TE, because error of planet activates its own rotation frequency in this model.

3.2.3 Influence of different supporting configuration of sun on load sharing ratio

One way to improve the load sharing behaviour of planetary drives is to increase the flexibility or buoyancy of the central elements (sun, planet carrier or corona). In this study, the buoyancy of the sun has been established to assess the influence of this configuration on the load sharing.

For the first stage, with sequential phase shift, the improvement in the LSR value with floating versus fixed sun can be seen in Fig.3-9a). In Fig.3-9b), for the second stage, it can be seen how the change from fixed to floating configuration causes a homogenisation of the LSR, decreasing notably the impact of the introduced eccentricity error.

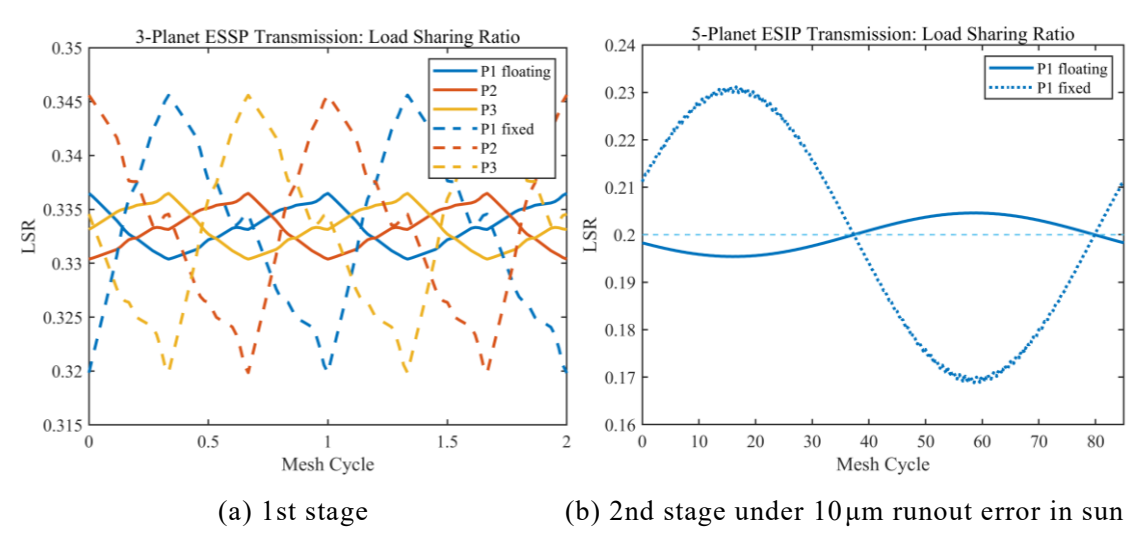


Fig.3-9 The LSR of the transmission with floating sun configuration

For the in-phase transmission of the 2nd stage, the load sharing on each planet is the same, since there are no errors or transmission paths with different stiffness. In order to evaluate the benefit of the configuration change, Fig.3-9b) shows the LSR of planet 1 when considering an error of 10 µm of eccentricity in the sun, both for fixed and floating configuration. As can be seen in the figure, the fixed configuration shows that each planet can transmit at certain times up to 23% of the load under the fixed sun configuration, but under the floating configuration the maximum load is 20.45%. It can therefore be concluded that the floating configuration can improve the load sharing characteristics of the planetary drive whether under in-phase or out-of-phase meshing conditions.

3.3 Study on eccentricity error

Eccentricity error is a common error arising from various factors, including manufacturing defects, assembly inaccuracies, and improper pin hole arrangement during gear installation. This subsection primarily investigates the impact of eccentricity error on the axis trajectory, utilizing the quasi-static model established in the previous chapter to investigate its effects on certain time-varying parameters and the trajectory.

3.3.1 Analysis of system states considering eccentricity error

3.3.1.1 Calculation of time-varying meshing stiffness considering eccentricity error

To describe the effect of the eccentricity error, an example meshing pair diagram of sun and planet is shown in Fig.2-2. Due to the existence of eccentricity

distances e_s and e_p , the actual centers of rotation (see Fig.2-2) are time-varying, and the gear center distance $O_s(t)O_p(t)$ and the transverse working pressure angle $\alpha_{\rm wt}$ are also time-varying. Therefore, the meshing process becomes a dynamic process, and the parameters related to the gear centre distance are all time-varying parameters. A modelling method considering the eccentricity error is introduced.

As shown in Fig.2-2, the actual gear centre distance during the meshing process varies with time because of the eccentricity, and it is given as follows:

$$\overline{O_s(t)O_p(t)} = \sqrt[2]{\frac{[\overline{O_sO_p} + e_s \cos(\omega_s t + \lambda_s) - e_p \cos(\omega_p t + \lambda_p)]^2}{+[e_s \sin(\omega_s t + \lambda_s) - e_p \sin(\omega_p t + \lambda_p)]^2}}$$
(3-6)

where e_s , e_p , λ_s , λ_p , ω_s and ω_p are the amplitudes, initial phase angles and angular speeds of the eccentricity error of the sun and planet, respectively.

Then, the time-varying transverse working pressure angle is obtained as:

$$\alpha_{wt}(t) = \cos^{-1}[(R_{bs} + R_{bp}) / \overline{O_s(t)O_p(t)}]$$
 (3-7)

where R_{bs} and R_{bp} are the radius of the base circles, respectively.

Next, the contact ratios, including the transverse contact ratio and overlap ratio are also obtained as shown the equation (3-8), and the transverse ratio becomes time-varying.

$$\varepsilon_{\alpha}(t) = \frac{1}{2\pi} [Z_{s}(\tan \alpha_{ats} - \tan \alpha_{wt}(t)) + Z_{p}(\tan \alpha_{atp} - \tan \alpha_{wt}(t))],$$

$$\varepsilon_{\beta} = \frac{B \sin \beta}{\pi m_{n}},$$

$$\varepsilon = \varepsilon_{\alpha}(t) + \varepsilon_{\beta}$$
(3-8)

where α_{ats} , Z_s , α_{atp} and Z_p correspond to the tip circle pressure angle and tooth number of the sun and planet, respectively. m_n , B and β are the normal module, width and helix angle, respectively.

The variation in contact ratios caused by the eccentricity error could result in a change in the number of teeth meshing pairs during the meshing process; therefore, the meshing stiffness could be impacted. Based on Maatar's work [152], the calculation equation of the time-varying meshing stiffness under considering the eccentricity error and associated factors is improved in this study. Therefore, the mesh stiffness of a double-helical gear can be regarded as the sum of the mesh stiffness of two individual helical gears, which is given by the following method

First, the calculation equation of the instantaneous average meshing stiffness is shown below.

$$k_{mean}(t) = 2BC_{\gamma}(t) \tag{3-9}$$

where B is the gear tooth width, and C_{γ} is the meshing stiffness per helical gear width, which is mainly affected by the time-varying transverse contact ratio shown in Equation (3-8) and is calculated by the following equation.

$$C_{\nu}(t) = (0.75\varepsilon_{\alpha}(t) + 0.25) \times (0.8\cos\beta/q)$$
 (3-10)

Based on ISO6336-1-2019, q is obtained by.

$$q = 0.04723 + \frac{0.15551}{Z_{n1}} + \frac{0.25791}{Z_{n2}} - 0.00635x_1 - 0.11654 \frac{x_1}{Z_{n1}} - 0.00193x_2 - 0.24188 \frac{x_2}{Z_{n2}} + 0.00529x_1^2 + 0.00182x_2^2$$
(3-11)

where x_1 and x_2 are the modification coefficients of a pair of meshing gears, respectively. Z_n is the equivalent tooth, which can be calculated by the formula $Z_n = Z/\cos^3 \beta$.

Then, the length of the instantaneous time-varying meshing line for the s-pi meshing pair and the r-pi meshing pair are calculated according to following equations based on the contact ratio.

$$L_{spi}(\tau) = L_{msp} \left(1 + \sum_{k=1}^{\infty} (A_k \cos(2\pi(\tau - \varphi_{spi})) + B_k \sin(2\pi(\tau - \varphi_{spi}))) \right)$$

$$L_{rpi}(\tau) = L_{mrp} \left(1 + \sum_{k=1}^{\infty} (A_k \cos(2\pi(\tau - \varphi_{rpi} - \varphi_{sr})) + B_k \sin(2\pi(\tau - \varphi_{rpi} - \varphi_{sr}))) \right)$$
(3-12)

where τ is dimensionless time, $\tau = t/T_m$, and T_m is the meshing time. A_k , B_k and L_m are calculated by

$$A_{k}(t) = \frac{1}{2\pi^{2}k^{2}\varepsilon_{\alpha}(t)\varepsilon_{\beta}} \left[\cos(2\pi k\varepsilon_{\alpha}(t)) + \cos(2\pi k\varepsilon_{\beta}) - \cos(2\pi k(\varepsilon_{\alpha}(t) + \varepsilon_{\beta})) - 1\right]$$

$$B_{k}(t) = \frac{1}{2\pi^{2}k^{2}\varepsilon_{\alpha}(t)\varepsilon_{\beta}} \left[\sin(2\pi k\varepsilon_{\alpha}(t)) + \sin(2\pi k\varepsilon_{\beta}) - \sin(2\pi k(\varepsilon_{\alpha}(t) + \varepsilon_{\beta}))\right]$$

$$L_{m}(t) = b \times \varepsilon_{\alpha}(t) / \cos(\beta_{b})$$
(3-13)

in which, β_b is the base circle pressure angle of the helical gear.

In addition, φ_{spi} and φ_{rpi} are the mesh phasing of two adjacent meshes, for instance s-p1 and s-p2. Furthmore, the φ_{spi} and φ_{rpi} is related to the teeth number and planet number in a plenatary gear train, which are expressed as follows, and the detailed calculation equations are described in the literatures [115,153].

$$\varphi_{spi} = -dec(\kappa_1(\frac{Z_s\phi_{pi}}{2\pi})), \ \varphi_{rpi} = dec(\kappa_1(\frac{Z_r\phi_{pi}}{2\pi})). \tag{3-14}$$

where, dec() indicates the fractional part of the result of the bracket, and $\kappa_1 = \pm 1$ represents the counterclockwise and clockwise directions of the input torque of the sun gear.

The φ_{sr} is the meshing phase difference between the same planet gear mesh with the sun and the ring. Fig.3-10 is the meshing process diagram, A is the start point and B is end point for sun-planet meshing, and C is the start point and D is end point for ring-planet meshing.

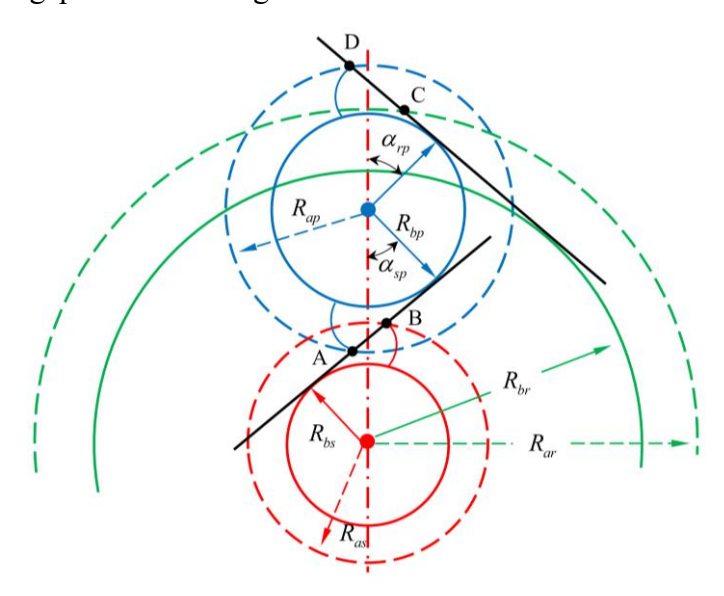


Fig.3-10 Schematic of the meshing phase difference φ_{sr}

The tooth pitch is the distance rotated during one meshing cycle, as shown in Fig.3-10, the same tooth (blue line) of the planet gear starts from contact the sun gear to ends meshing with the ring gear, i.e., the distance from point A to point D, this distance should be compared with the tooth pitch to get how many times it is the tooth pitch. Therefore, according to the Fig.3-10 the calculation equation of the meshing phase difference between external and internal meshing pairs is shown as Equation (3-15) in this way, and more detail can be found in detail in the literature [153].

$$\varphi_{sr} = dec(\frac{AB + BC + CD}{p_{bt}}) \tag{3-15}$$

where p_{bt} is the tooth pitch of the base circle.

Therefore, the time-varying meshing stiffness is derived by.

$$k_{spi}(\tau) = k_{mean} L_{spi}(\tau),$$

$$k_{rpi}(\tau) = k_{mean} L_{rpi}(\tau).$$
(3-16)

3.3.1.2 Kinematic relationship analysis of compound gear train considering ecc entricity error

During the installation and manufacturing of planetary gear systems, various errors inevitably occur, which can be classified into time-invariant errors and time-varying errors. Considering the run-out in the case of time-varying errors (errors that change values and direction depending upon the rotational position of the gears, such as eccentricity and run-out), the analysis must be performed at a predetermined number of carrier rotational rounds $n_{CI/0}$. In other words, the carrier must rotate in integer rounds and carry planets to return the initial position. For instance, if the run-out error is only on planet #1 in an epicyclic planetary gear train, the carrier must rotate into an integer round and planet #1 with respect to the carrier must also rotate into an integer round. Therefore, based on the kinematic conditions of the studied compound planetary gear train, rotation relationship equations are shown as follows.

$$n_{S1/C1} \cdot Z_{S1} = -n_{P1/C1} \cdot Z_{P1}$$

$$n_{R1/C1} \cdot Z_{R1} = n_{P1/C1} \cdot Z_{P1}$$

$$n_{R1/C1} = n_{R1/0} + n_{0/C1}$$

$$n_{R1/0} = n_{S2/0}$$

$$n_{S2/0} \cdot Z_{S2} = -n_{R2/0} \cdot Z_{R2}$$

$$(3-17)$$

Based on Equation (3-17), considering run-outs on all the members (sun, planet and ring) in the 1st stage, the number of rotational rounds for carrier in the 1st stage rotations required to fully capture the effects of eccentricity errors is derived as

$$n_{C1/0} = -\left[\frac{Z_{P1}}{Z_{R1}} \left(\frac{Z_{S2}}{Z_{R2} + Z_{S2}}\right)\right] \cdot n_{P1/C1}$$

$$n_{C1/0} = -\left[\left(\frac{Z_{S2}}{Z_{R2} + Z_{S2}}\right)\right] \cdot n_{R1/C1}$$

$$n_{C1/0} = \left[\frac{Z_{S1}}{Z_{R1}} \left(\frac{Z_{S2}}{Z_{R2} + Z_{S2}}\right)\right] \cdot n_{S1/C1}$$
(3-18)

According to Equation (3-18), if the eccentricity error is on planet #1 in the 1st stage, the carrier in the 1st stage must rotate $Z_{P1} \times Z_{S2}$ rounds, and planet #1 with respect to the carrier simultaneously rotates $Z_{R1} \times (Z_{R2} + Z_{S2})$ rounds. If the the eccentricity error is on sun in the 1st stage, the carrier in the 1st stage must rotate $Z_{S1} \times Z_{S2}$ rounds, and sun with respect to the carrier simultaneously rotates

 $Z_{R1} \times (Z_{R2} + Z_{S2})$ rounds. If there are errors on both meshing gears, the rotational rounds should be the least common multiple of the result for each condition. Furthermore, the rotation count of the input sun gear can be derived based on the relationship between the number of revolutions of the carrier and the transmission ratio.

3.3.2 Analysis of meshing parameters in compound Gear train considering eccentricity error

Some paremeters and meshing stiffness with the eccentricity error was presented in 3.3.1.1 subsection, so it is necessary to analyse these parameters. In this subsection, the center idstance, meshing angle and the contact ratio with eccentricity error are compared to that without error, and so does the meshing stiffness. Furthmore, the predetermined number of carrier rotational rounds with eccentricity error is also given in this section.

The meshing stiffnesses of planetary gear train without and with eccentricity error are compared and analyzed to study the effect of eccentricity error on meshing stiffness in this section. In general, the meshing stiffnesses k_{spi} and k_{rpi} are described in detail in the literatures [152][153], but the eccentricity error affecting the shape of the meshing stiffness is not included. Therefore, if the meshing stiffness where the effect of eccentricity error is considered, the wave of the meshing stiffness is influenced not only by the meshing frequency but also by the frequency of eccentricity error.

The basic and design parameters of the planetary gear train, eccentricity error and bearings are shown in Tab.3-4 to Tab.3-6. According to the mesh phasing equations shown in the literature [115] and Tab.3-4, the mesh phasing relationships for the two stages are equally spaced sequential phasing (ESSP) and equally spaced in phasing (ESIP), respectively. Moreover, because the basic parameters of all planets in each stage shown in Tab.3-4 are absolutely same in the study, the eccentricity error of the planets is considered only on one planet, i.e., planet #1 in each stage, and the remaining planets are perfect. On the other hand, in this simulation case the equivalent radius of pitch circle (R_c) shown in Fig.2-9 is about 422mm.

Tab.3-4 Basic design parameters of the compound gear train

| Stage | F | irst Stage | ; | Second Stage | | | |
|--|-----------------------------|------------|--------|---------------|--------|--------|--|
| Element | Sun Planet Ring | | | Sun | Planet | Ring | |
| Teeth number, Z | 40 | 80 | 200 | 80 | 60 | 200 | |
| Width, B (mm) | 65 | 65 | 65 | 70 | 70 | 70 | |
| Radius of pitch circle, R_i (mm) | 132.41 | 287.98 | 711.68 | 281.36 | 188.68 | 662.02 | |
| Ideal transverse contact ratio, ε_{α} (-) | 1.3045-1.4116 1.3253-1.39 | | | | | 934 | |
| Ideal overlap ratio, ε_{β} (-) | 1.4 | 573-1.45 | 73 | 1.5694-1.5694 | | | |
| Ideal overall contact ratio, ε_{γ} (-) | 2.7618-2.8690 2.8948-2.9629 | | | | | 629 | |
| Normal module, m_n (mm) | 6 | | | | | | |
| Normal pressure angle, α_n (°) | 20 | | | | | | |
| Helix angle, β (°) | 25 | | | | | | |
| Helix angle of base circle, β_b (°) | 23.40 | | | | | | |
| Normal addendum coefficient, h_{an} (-) | 1 | | | | | | |
| Normal tip clearance coefficient, c_n (-) | 0.25 | | | | | | |
| Total transmission ratio, $i(-)$ | 18.5 | | | | | | |
| Number of planets (N) | 3 5 | | | | | | |
| Planets spacing angle (°) | 120 72 | | | | | | |
| Mesh phasing condition | ESSP ESIP | | | | | | |

Tab.3-5 The values of the error and other parameters

| Stage | First Stage | | | Second Stage | | |
|--|-------------|--------|------|--------------|--------|------|
| Element | Sun | Planet | Ring | Sun | Planet | Ring |
| Eccentricity error amplitude, e_{ei} (μm) | 5 | 5 | 5 | 5 | 5 | 5 |
| Initial phase of the error, λ_i (°) | 0 | 180 | 0 | 0 | 180 | 0 |
| Rotational angular speed, f_i (rad/s) | 62.83 | 30.67 | 7.77 | 7.77 | 11.59 | 3.30 |

Tab.3-6 The bearing stiffness values used in the studied model

| Stage | First Stage | | | | Second Stage | | | |
|-------------------|-------------|--------|--------|---------|--------------|--------|--------|---------|
| Element | Sun | Planet | Ring | Carrier | Sun | Planet | Ring | Carrier |
| $K_{bx}(N/m)$ | 1.0e10 | 1.1e11 | 1.1e11 | 1.1e11 | 1.1e10 | 2.2e11 | 1.5e11 | 1.0e12 |
| $K_{by}(N/m)$ | 1.0e10 | 1.1e11 | 1.1e11 | 1.1e11 | 1.1e10 | 2.2e11 | 1.5e11 | 1.0e12 |
| $K_{bt} (Nm/rad)$ | 0 | 0 | 0 | 0 | 0 | 0 | 0 | 1.0e13 |

According to Tab.3-4 and Tab.2-1, the specific mesh phasing value shown in equations (3-14) and (3-15) in this case is calculated in Tab.3-7, it is seen that the calculation results are also agreement with the mesh phasing relationship in two stages (ESSP and ESIP).

| Stage | Fir | rst Stage (N=3) Second Stage (N=5) | | | |) | | |
|--|-----|------------------------------------|--------|---|---|---|---|---|
| Sun-planet (φ_{spi} , $i=1,,N$) | 0 | 0.333 | 0.667 | 0 | 0 | 0 | 0 | 0 |
| Ring-planet (φ_{rpi} , $i=1,,N$) | 0 | -0.667 | -0.333 | 0 | 0 | 0 | 0 | 0 |
| Sun-planet \$i\$ -ring (\emptyset_{m}) | | 7.013e-4 3.679e-4 | | | 4 | | | |

Tab.3-7 The mesh phasing value of the studied planetary gear train

Firstly, as mentioned above, several parameters (such as the center distance, meshing angle and contact ratio) of two meshing gears for the first stage during the meshing process in this proposed model are time-varying. For instance, the centre distance, meshing angle and contact ratio of sun-planet #1 under different combinations of gear errors can be seen in Fig.3-11. Compared with the constant center distance, it is drawn from Fig.3-11 (a) that the constant center distance in the previous model is approximately 422.042 mm, while the time-varying center distance for the modified model fluctuates from 422.032 mm to 422.205 mm under the same small error amplitude such as 5 microns. Furthermore, the meshing angle (also called the working pressure angle) and contact ratio vary with time (see Fig.3-11 (b) and (c)) because of the time-varying center distance. By comparing the results shown in Fig.3-11, it can be found that these meshing parameters are affected by eccentricity error configurations such as single gear error and double gear errors.

Secondly, the meshing stiffness of the sun and planet #1 (S-P1) in the 1st stage are taken as an example to show the influence of eccentricity error, and the eccentricity error is in planet #1. Therefore, a comparison of the meshing stiffness results without and with the eccentricity error in this subsection is shown in Fig.3-12, and an enlarged shape of the meshing stiffness for a perfect meshing pair (red line in Fig.3-12) can be seen in Fig.3-13, which is a detailed supplement to Fig.3-12.

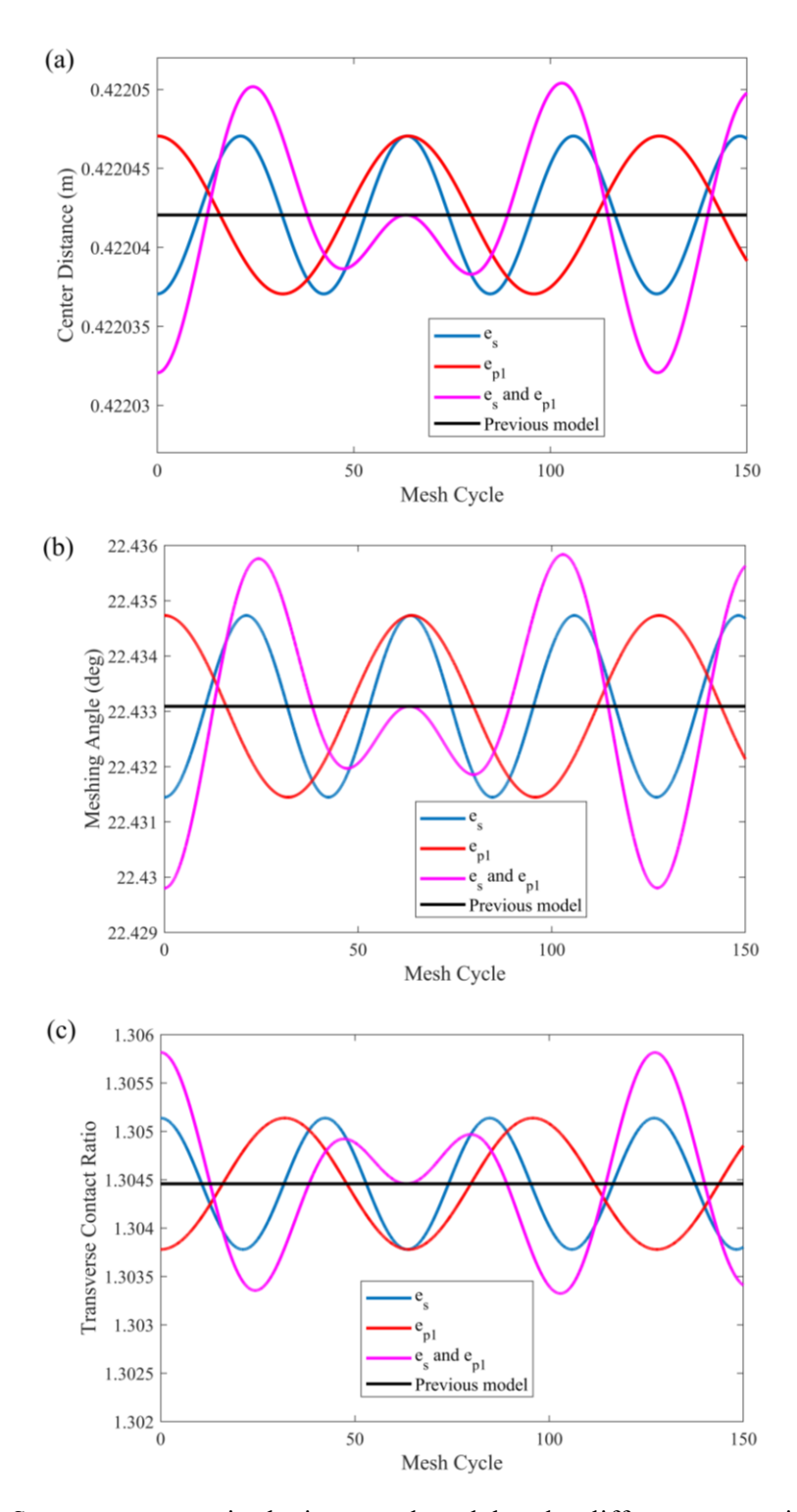


Fig.3-11 Some parameters in the improved model under different eccentricity error configuration: blue line represents error on only sun, red line represents error on only planet #1, pink line represents error both on sun and planet #1 and the black line is the constant center distance without error

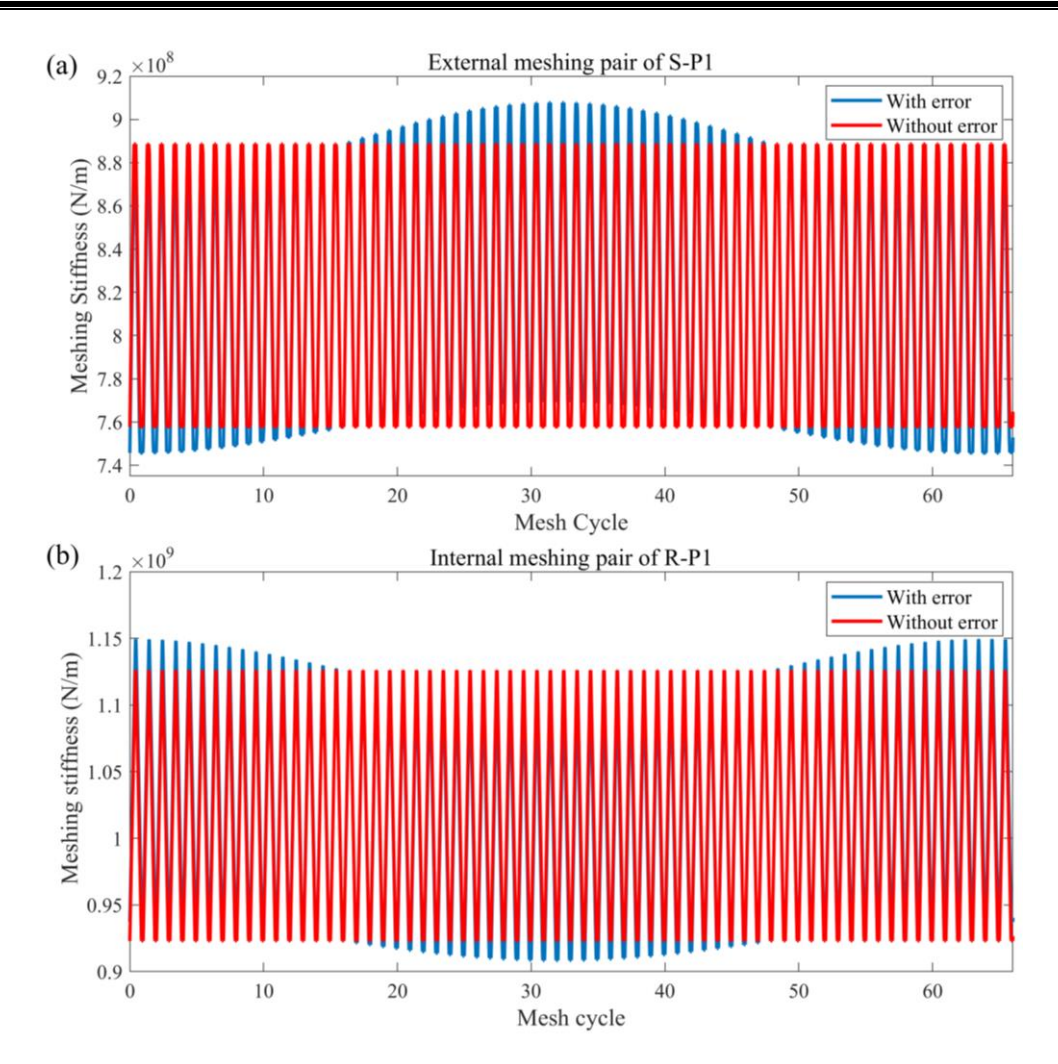


Fig.3-12 Meshing stiffness for a helical gear pair in the 1st stage without and with eccentricity error only on planet #1: (a) external meshing pair of sun-planet #1 and (b) internal meshing pair of sun-planet #1

Finally, as shown in Fig.3-13, there are two fluctuation periods, namely, the short-term period and the long-term period. The former is the gear meshing period, and the latter is the rotational period of the shaft, i.e., the eccentricity error period. It is seen from Fig.3-13 that two pairs of teeth and three pairs of teeth alternately contact each other because the contact ratio is between 2 and 3. In addition, it is worth mentioning that the size of the contact ratio shown in Fig.3-11 (c) also affects the contact region of 3 pairs of teeth or 2 pairs of teeth (region between the blue dashed lines shown in Fig.3-13).

Therefore, for the meshing gear pair with geometric eccentricity, the mesh stiffness is definitely affected, which verifies the validity of the proposed meshing stiffness in this subsection.

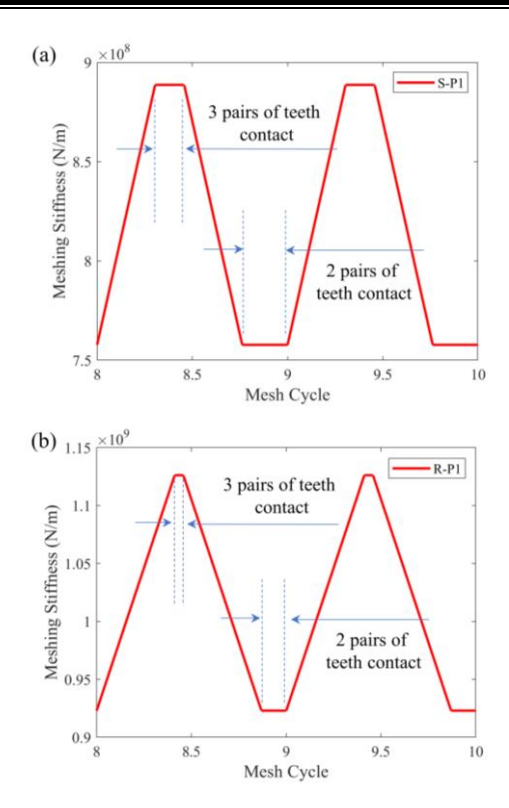


Fig.3-13 Detailed meshing stiffness for helical gear pair in 1st stage without eccentricity error: (a) external meshing pair of sun-planet #1 and (b) internal meshing pair of sun-planet #1

3.3.3 Influence of eccentricity error on orbit

As shown in Tab.3-4, the mesh phasing of the two stages is ESSP and ESIP, respectively. Based on gear parameters, the influence of eccentricity error on the orbit (also called transverse displacement) is investigated in this section. In general, a planetary gear system includes three central components (a sun, a ring and a carrier) and N planet. Moreover, sun gear which represents central components, and planets are chosen to study the influence of eccentricity error on orbit in this study.

3.3.3.1 Orbits without considering eccentricity error

First, the simulation results of the components need to be shown and analyzed to verify the accuracy of the established model. For this purpose, Fig.3-14 (a) and (b) show the floating trajectories without any error in the moving coordinate of the sun gear in the 1st stage and the corresponding force analysis for and proposed model, respectively. In order to verify whether the calculation contact force value shown in Fig.3-14 (b) in this studied model is equal to the nominal ones, every contact force value of the three planets (blue line) shown in Fig.3-14 (b) is

calculated and its mean value equals to one-third of the contact force calculated from the input torque divide by the radius of base circle. Furthermore, although the transmission is complex, the torque assumed by each stage is in accordance with the transmission ratio. In this case, the input torque of the second stage is the torque assumed by the ring gear in 1st stage, i.e., the input torque of the second stage equals the input torque multiple of the transmission ratio Z_{R1}/Z_{S1} from the sun in 1st stage to the ring gear in 1st stage, which is shown as follows:

$$T_{\text{input}}^2 = T_{\text{input}} \times \left(\frac{Z_{R1}}{Z_{S1}}\right) \tag{3-19}$$

Fig.3-14 (c) and (d) are the trajectories without any error under 10 mesh cycles in terms of the global coordinate and partial detailed drawing. It can be drawn from the Fig.3-14 (a) that the orbit of the sun gear in moving coordinate (MC) approximates a triangle and the three branches are the same, which well matches the results in a star planetary gear system. By analyzing the modelling method, one reason is that the reference coordinate of 1st stage is the moving coordinate that is attached to the carrier in 1st stage. Hence, the epicyclic planetary gear train becomes a star planetary gear system. Another reason is that the mesh phasing of 1st stage is the sequential phase, and the force wave from each planet is absolutely the same except for a forward or a backward phase. Therefore, three forces from each planet cannot form an equilateral triangle at the one time, and an additional resultant force always appears shown as a red arrow in Fig.3-14 (b). In addition, the planets are evenly distributed through the force diagram shown in Fig.3-14 (b), and the gear parameters shown in Tab.3-4. Moreover, it also can be concluded from Fig.3-14 (c) and (d) that the trajectory of the global coordinate rotates by an angle after one mesh cycle, and the orbit of the sun in global coordinate is predicted to a ring shape until the sun rotates a certain number of rounds so that the orbit of one mesh cycle coincides with the orbit of the first mesh cycle in accordance with this trend, as shown in Fig.3-14(e) and (f).

Likewise, for the 2nd stage, the orbit in global coordinate (GC) and force analysis diagram are seen in Fig.3-15. It is clearly shown from Fig.3-15 (a) that the orbit of the sun in the 2nd stage is fixed due to the displacement response could be seen zero, and Fig.3-15 (b) presents an equilateral pentagon composed of five equal forces (F_{sp1} , F_{sp2} , F_{sp3} , F_{sp4} and F_{sp5} shown in the figure) from each planet appears because of equally spaced in phase. Compared to the mesh phasing, and planet gear distribution conditions of the two stages, as shown in Fig.3-14 (b) and Fig.3-15 (b), how is the orbit of the sun gear (which presents the central gears) formed with two kinds of common mesh phasing in this subsection is explained in detail.

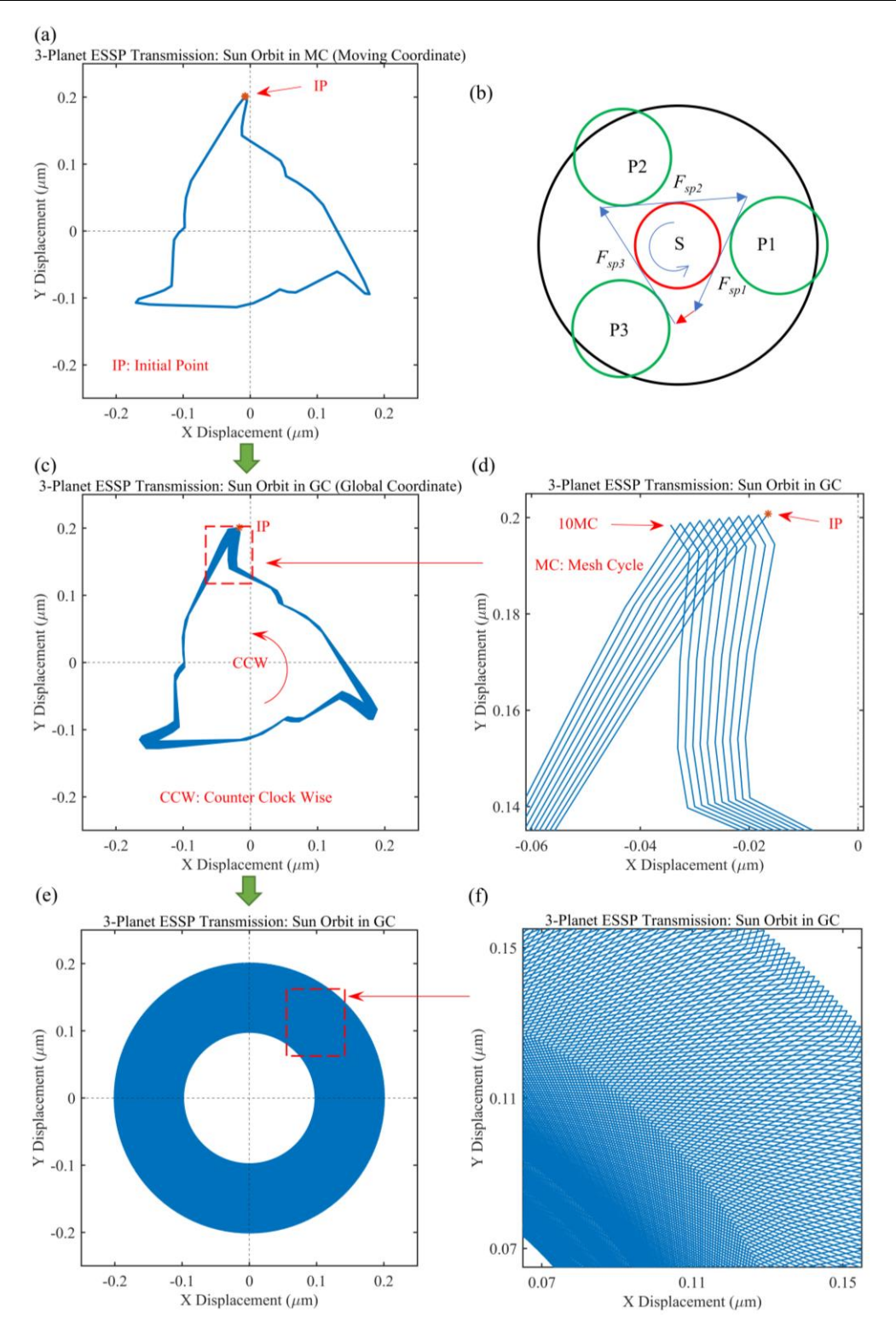


Fig.3-14 Sun gear in the 1st stage without eccentricity error: (a) orbit in moving coordinate under one mesh cycle, (b) force analysis diagram, (c) orbit in global coordinate under ten mesh cycles, (d) partial enlarged drawing of figure (c), (e) orbit in global coordinate under sun rotates for N rounds, and (f) partial enlarged drawing of figure (e)

On the other hand, five contact forces of the sun-planet in the 2nd stage from this model (blue line in Fig.3-15 (b)) multiply by the base circle of sun in 2nd stage equal the input torque of second stage shown in the equation (3-19). Combining Fig.3-14 (b), Fig.3-15 (b) and equation (3-19), it is indicated that the calculation value from this model is equal to the nominal ones.

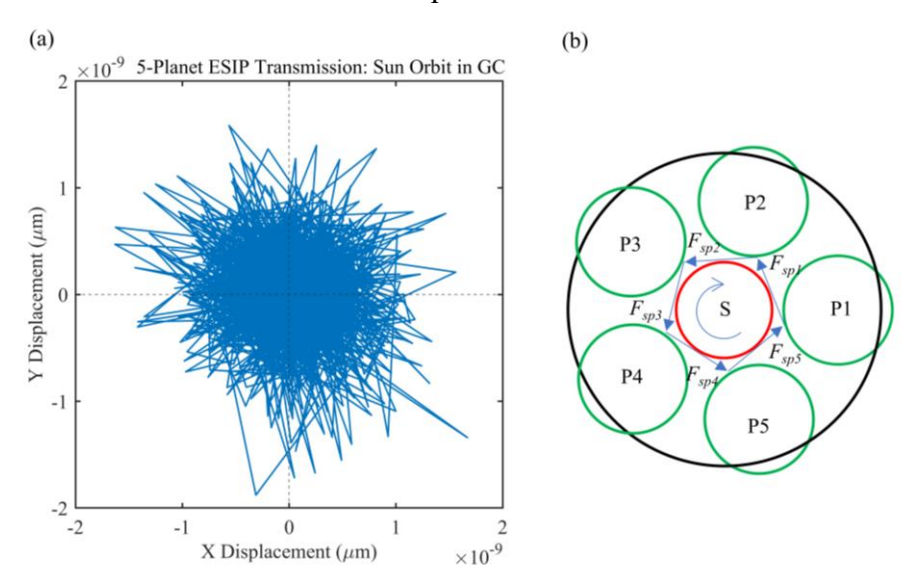


Fig.3-15 Sun gear in the 2nd stage without eccentricity error: (a) orbit in global coordinate and (b) force analysis diagram

Regarding to the orbits of the planet in two stages, Fig.3-16 (a) and Fig.3-17 (a) show the response, respectively. Correspondingly, the force analysis diagrams can be also seen in Fig.3-16 (b) and Fig.3-17 (b), respectively.

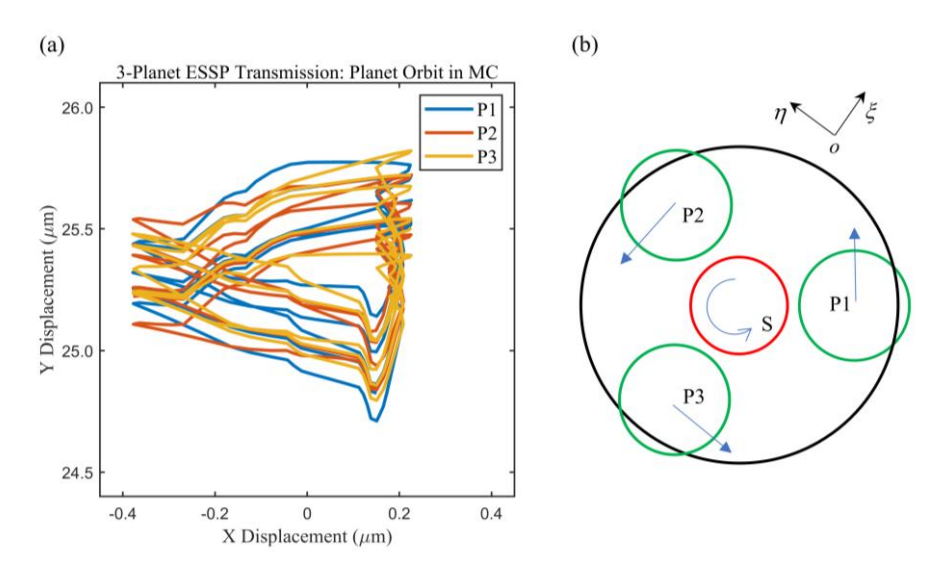


Fig.3-16 Planet gear in the 1st stage without eccentricity error: (a) orbit in moving coordinate and (b) force analysis diagram

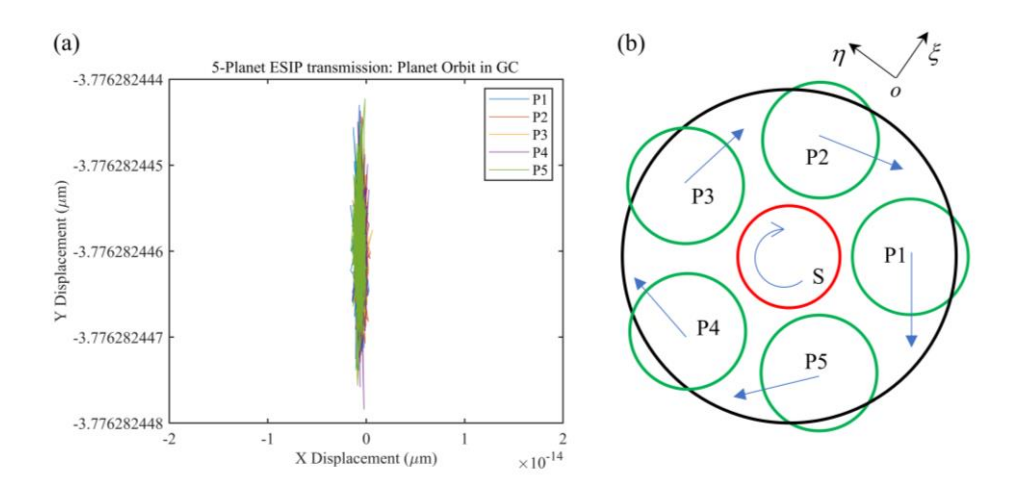


Fig.3-17 Planet gear in the 2nd stage without eccentricity error: (a) orbit in moving coordinate and (b) force analysis diagram

Taking Fig.3-16 (b) as an example, the reference coordinate of the planet is always the radial and tangential direction although its coordinate moves with the carrier (also see Fig.2-5 and Fig.2-6). Because the rotation direction of sun is counter clock wise, so the combined force (blue arrow) of the planet from the sun and ring is the same as that in the tangential positive direction as shown in Fig.3-16 (b). Therefore, the Y displacement for the orbit of each planet in the 1st stage (see Fig.3-16 (a)) is positive, and the X displacement is approximately 0. In the same way, because the combined force direction of the planets in the 2nd stage is opposite to the positive direction shown in Fig.3-17 (b), the Y displacement at the equilibrium position should be negative, which coincides with the results shown in Fig.3-17 (a).

3.3.3.2 Orbit considering eccentricity error

(1) Analysis of orbit of the sun considering eccentricity error

Based on the parameters in Tab.3-4, when the error is only on the sun in the 1st stage, the displacement response of the sun gear in MC is shown in Fig.3-18 (a), the corresponding orbit in GC is shown in Fig.3-18 (b), and Fig.3-18 (c) is an enlarged version of Fig.3-18 (b). As shown in Fig.3-18 (a), IP is the initial point, No.1 presents the first loop, and No.40 presents the last loop, which returns the IP, thus, there are 40 loops in total and each loop shape is from the shape without error shown as Fig.3-14 (a). At the same time, one mesh cycle time is the time between two adjacent loops shown in the Fig.3-18 (a). The reason why there are 40 loops in MC is that the number of sun gear is 40, and 40 teeth must fully complete contact because of eccentricity error. Compared to the orbit in the MC, the orbit in Fig.3-18 (b) and (c) is complex and it is drawn that the orbit in MC

could more simply explain the phenomenon (teeth number loop), however, the MC is a reference coordinate, and the orbit in the GC is realistic and has a certain periodicity, as shown in Fig.3-18 (c).

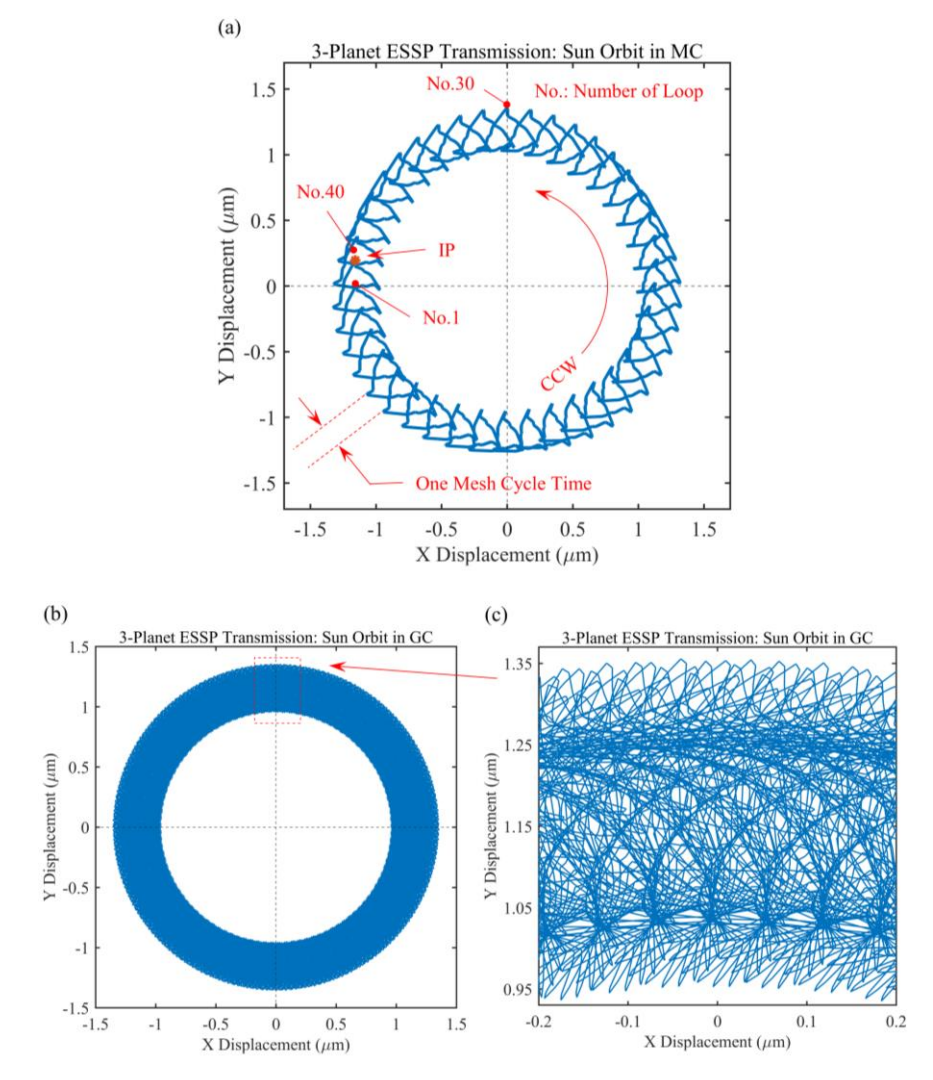


Fig.3-18 Orbit of the sun gear with eccentricity error in 1st stage: (a) moving coordinate, (b) global coordinate and, (c) enlarged version of (b)

Correspondingly, the orbit of the planets in 1st stage which mesh to sun gear with an error is shown in Fig.3-19. Orbit in MC (Fig.3-19 (a)) is not very clear, so the orbit in GC (Fig.3-19 (b), (c) and (d)) is marked to study results of the planet, which is different from the results shown in Fig.3-18 (a). It is shown from Fig.3-19 (b) and (c) that orbit of planets are same, and there is only a delay and advance phase which is same to the mesh phasing. Hence it can be conclused from Fig.3-19 (b) and (c) that the eccentricity error does not affect the mesh phasing (ESSP), and there are also 40 loops in Fig.3-19 (d), which matches well with Fig.3-18 (a).

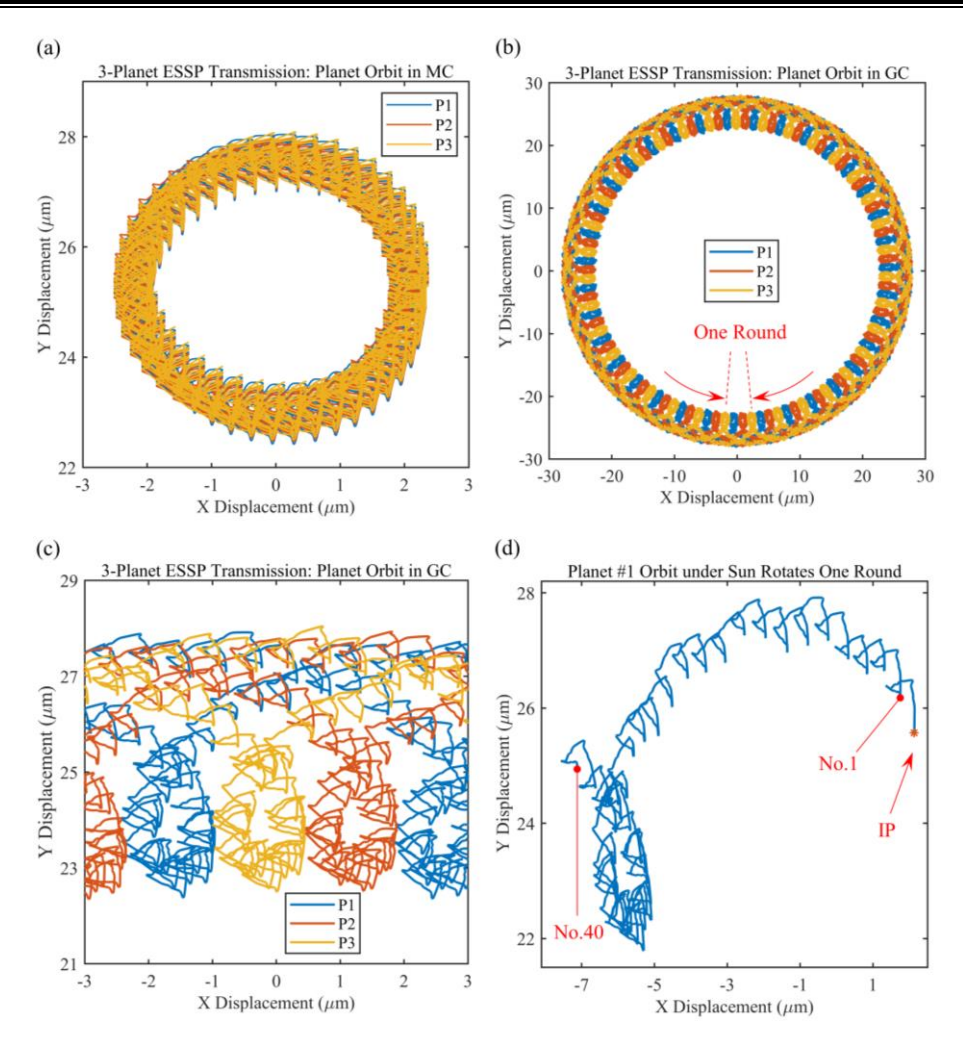


Fig.3-19 Orbit of planet meshes with the sun gear with eccentricity error: (a) MC, (b) GC, (c) enlarged version of (b), and (d) orbit of planet #1 when the sun rotates one round

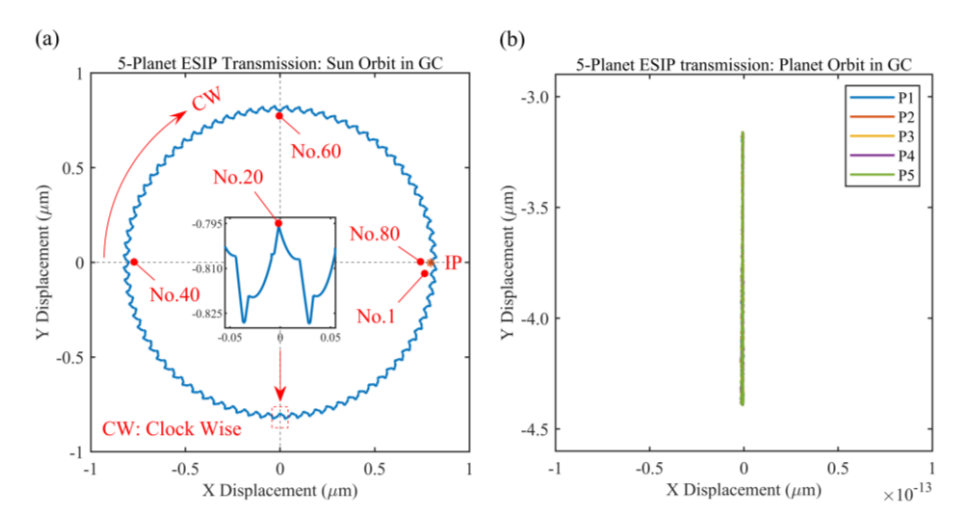


Fig.3-20 Orbit of the sun with eccentricity error in the 2nd stage: (a) orbit of sun in global coordinate, and (b) orbit of planets in global coordinate

It is concluded from this studied case that the orbit of the sun includes N loops, and these loops are related to the number of teeth of the sun despite whether the mesh phasing is sequential phase or in phase.

(2) Analysis of orbit of the planet #1 considering eccentricity error

In this subsection, the eccentricity error is only on planet #1 in each stage is investigated. For the first stage, Fig.3-21 is the orbit of the planet #1. The fluctuation (blue line) of the orbit in the MC is much greater than that without error because of the large fluctuation of meshing stiffness. Fig.3-21 (b) shows 35 rounds, and Fig.3-21 (c) shows 80 loops during 1 round, which is in good agreement with the calculation results. On the one hand, it verifies the model.

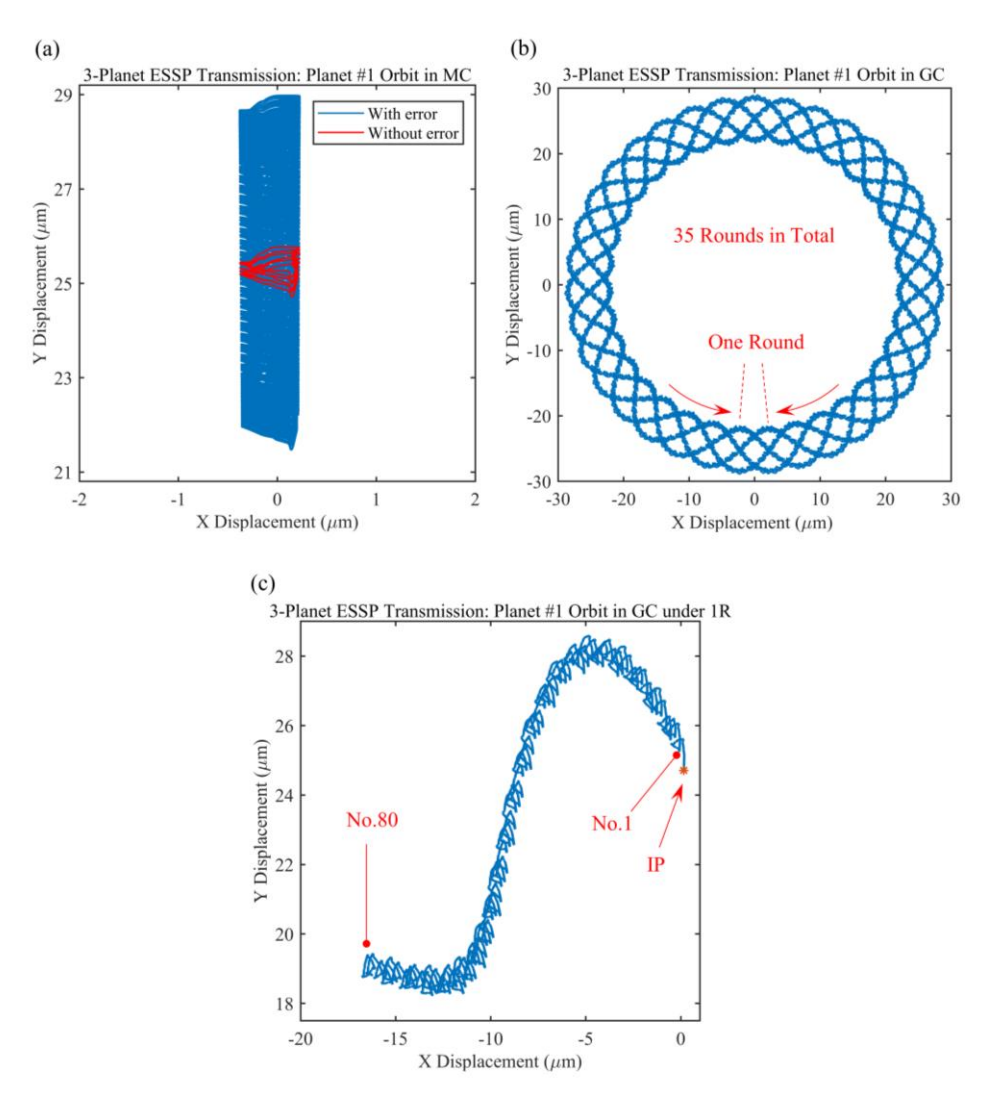


Fig.3-21 Orbit of planet #1 gear in the 1st stage: (a) orbit in moving coordinate without and with eccentricity error, (b) orbit in global coordinate with eccentricity error and (c)

orbit in global coordinate with eccentricity error when the planet #1 rotates 1 round

Correspondingly, Fig.3-22 is the orbit of the sun gear which meshes with planet #1 gear with the single eccentricity error in the 1st stage.

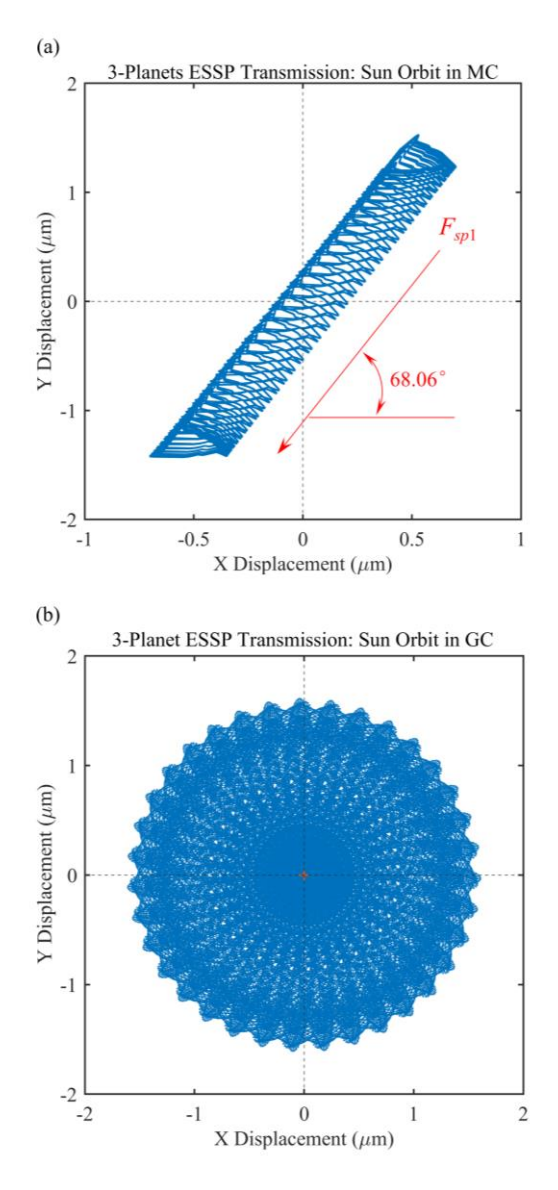


Fig.3-22 Orbit of the corresponding sun gear which meshes with planet #1 gear with eccentricity error in the 1st stage:(a) orbit in moving coordinate, and (b) orbit in global coordinate

For the 2nd stage, the condition of Fig.3-23 (a) is similar to those in Fig.3-21 (a). Moreover, combining Fig.3-22 (a) and Fig.3-23 (b), the sharp angles formed by the trend line of the orbit and the horizontal coordinate (X axis) are 68.06 degrees and 68.12 degrees, respectively. The force direction of F_{sp1} (compression direction of the spring shown in Fig.2-5 and Fig.2-6) in two stages is theoretically

at an angle of 90- α_t from the position direction of the X axis in global reference, which equals 68.1198 degrees. Therefore, the angles match well with the theoretical angle. On the other hand, the above result verifies the accuracy of the model.

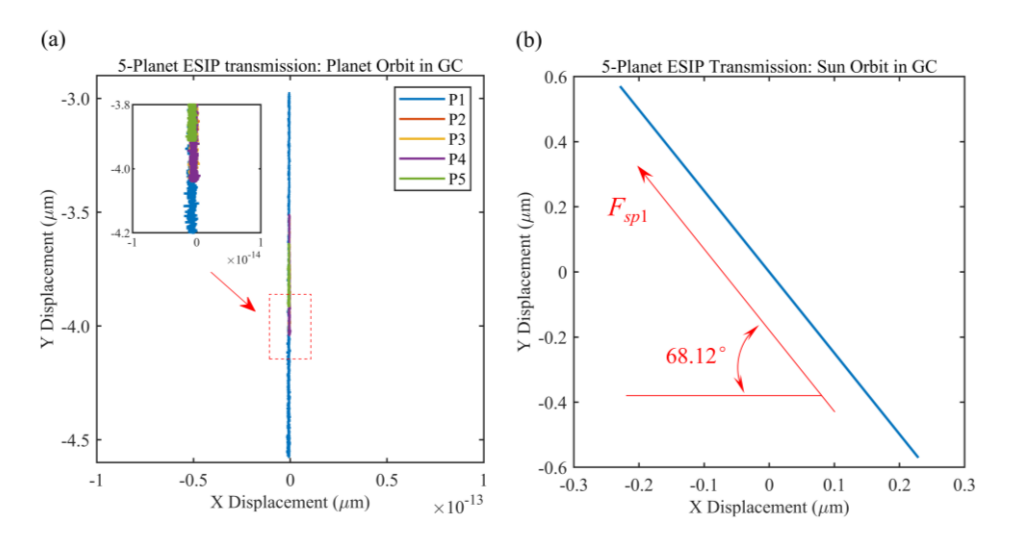


Fig.3-23 Orbit of planet #1 gear with eccentricity error in the 2nd stage: (a) orbit in moving coordinate, and (b) orbit in global coordinate

(3) Analysis of orbit of the sun and planet #1 considering eccentricity error

For the 1st stage with the mesh phasing of the ESSP, when there are eccentricities on both the sun and planet #1, the center trajectory results of the sun gear and planet #1 in MC and GC are shown in Fig.3-24 and Fig.3-25, respectively.

It is observed from the orbit in MC that there are 80 loops in total, and by combining the conditions of the single error shown in Fig.3-18 (a) and Fig.3-22 (a), it also can be drawn that in both error cases, the part of the reason for orbit orbital shape in the MC is that partly affected by the direction of the force F_{sp1} , which is also observed from Fig.3-19 (b), Fig.3-22 (a) and Fig.3-25 (b). Therfore, influenting factors for the orbit of sun gear shown in Fig.3-24 are the teeth number and the derection of the meshing force with planet #1. Furthermore, the beautiful orbit in GC shown in Fig.3-24 (b) is a combination of the Fig.3-24 (a) rotate a certain small angle each time. According to Equation (3-18), the loop number is the product of the meshing period and the least common multiple of the tooth number of the two meshing gears. The least common multiple of the tooth number of sun and planet #1 is 80, so there are 80 loops for the orbit in the MC of the sun gear when the IP returns to itself for the first time, as shown in Fig.3-24 (a).

Fig.3-24 (b) shows a complex drawing, but there are 70 rounds when the IP returns to itself for the first time; that is, because the sun with respect to carrier needs rotates 70 rounds. Similarly, the planet with respect to carrier needs rotates 35 rounds, as shown in Fig.3-25.

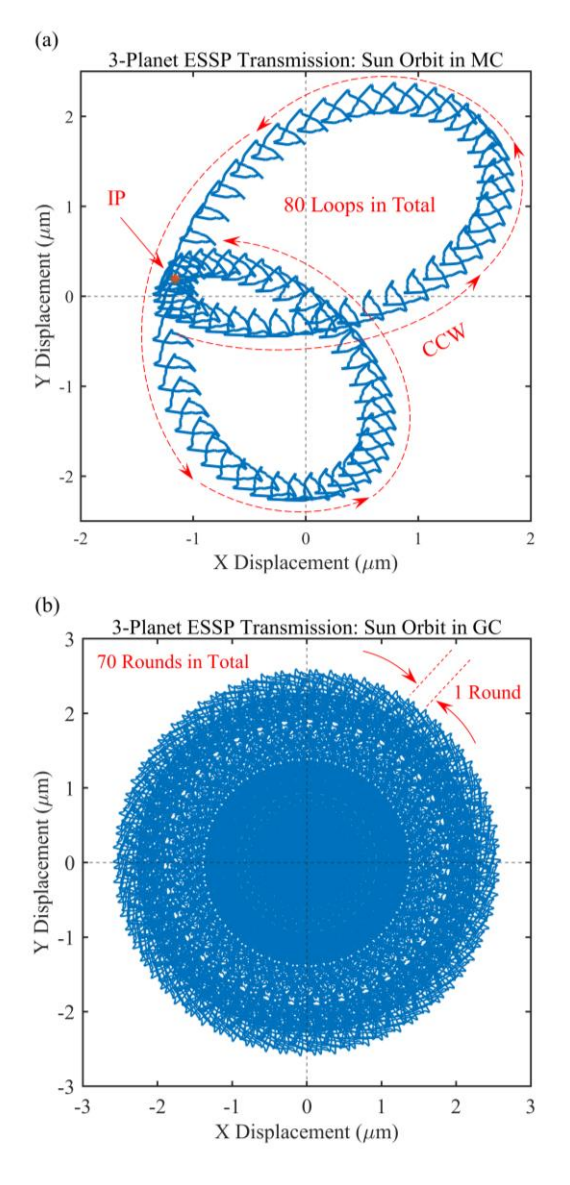


Fig.3-24 Orbit of the sun gear with eccentricity error on both the sun and planet #1 gear in the 1st stage (a) orbit in moving coordinate, and (b) orbit in global coordinate

In addition, comparing to Fig.3-19 (b) and (c), it is observed from Fig.3-25 (b) that shape of the orbit is a little skewed, which corresponds the conclusion in Fig.3-24 (a), and it is again proved that the orbit is partly affected by the meshing

force.

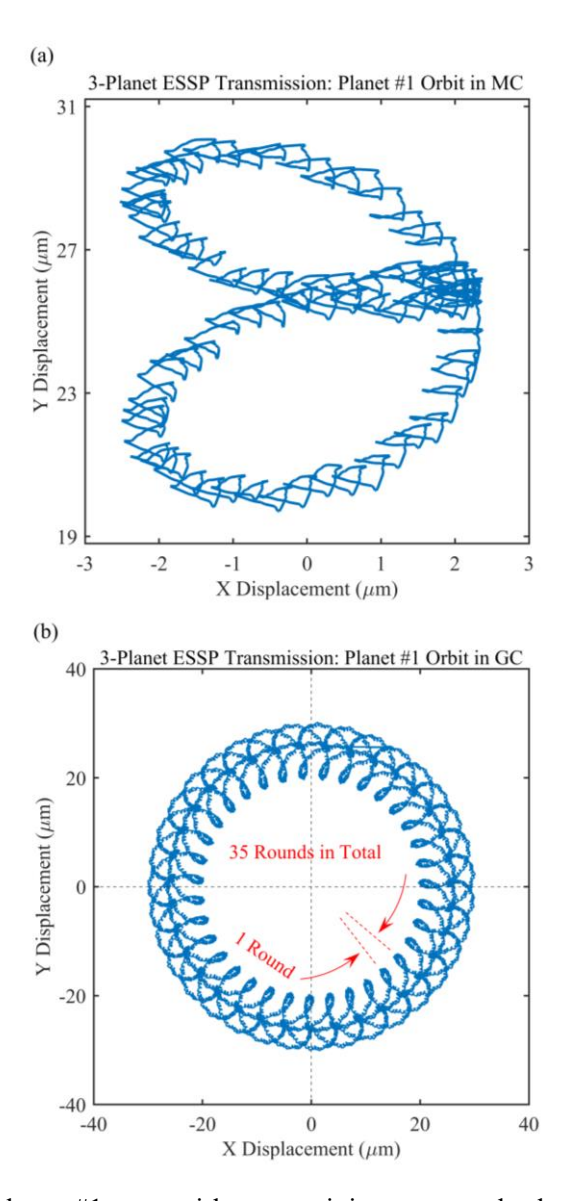


Fig.3-25 Orbit of the planet #1 gear with eccentricity error on both sun and planet #1 gear in the 1st stage (a) orbit in moving coordinate, and (b) orbit in global coordinate

For the 2nd stage with the ESIP, when there are eccentricity errors on both the sun and the planet #1, the center trajectory of the sun is shown in Fig.3-26. It is drawn from Fig.3-26 that the ornit of the sun is composed of 240 loops in total, counting clockwise from the IP to the number of rounds returned to the IP for the first time, and because the least common multiple of 80 (sun teeth number) and 60 (planet #1 teeth number) is 240. Hence for the same reason, the conclusion in the 2nd stage is the same as that in the 1st stage. Furthermore, the shape of orbit

for sun in 2nd stage is both affected by the results in Fig.3-20(a) and Fig.3-23(b), this conclusion is also same as that in 1st stage.

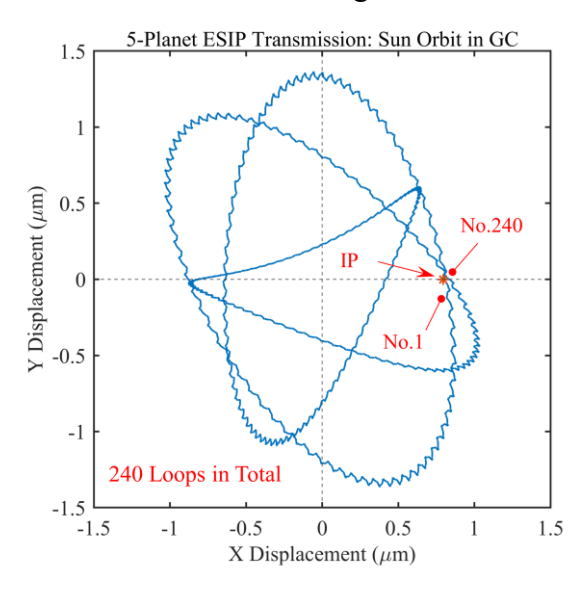


Fig.3-26 Orbit of the sun gear with eccentricity error on both the sun and planet #1 gear in the 2nd stage

3.4 Brief summary

In this chapter, the transmission behavior of a two stages compound gear trains with double-helical gears has been studied in depth. As a fundamental novelty of the study, special attention has been paid to the meshing phase shift between each of the sun-planet and planet-ring contacts, which in the example transmission used presented two types: sequentially phased for the first stage and in phase for the second stage. These meshing phase conditions, as has been demonstrated, strongly determine the load sharing and vibration characteristics of the transmission, as they have a strong impact on the transmission error.

Firstly, the static characteristics of the transmission, including the load sharing ratio and the transmission error, were analyzed. The influence of different errors on the load sharing ratio and transmission error was then studied. The main conclusions of the study are as follows:

- (1) It is shown that the load sharing ratio is strongly conditioned by the phase configuration of the gears, especially with sequentially out-of-phase transmission. The frequency domain results also show that the excitation frequency of the output component is the joint action of the excitation frequency of each stage.
- (2) The tangential error at different mesh phase shift conditions will produce different effects on the global TE: sequential phase shifts change the frequency content, while an in-phase configuration does not activate any new frequencies.

- (3) For the stage with sequential phase shift, the eccentricity error generates new excitation frequencies. For the in-phase stage there is a relevant change that coincides with the error frequency, but the eccentricity error in the planetary gears does not generate new excitation frequencies.
- (4) Compared to the fixed sun configuration, the floating sun configuration improves the load sharing, more markedly in the case of sequentially phased configurations, but also absorbing the effect of possible errors when the transmission is in phase.

Secondly, the influences of eccentricity error on the contact ratio, meshing stiffness, orbit, etc., are discussed and analyzed. The main conclusions are given as follows:

- (1) Parameters, including the center distance, working pressure angle, contact ratio and meshing stiffness wave, are strongly affected by the eccentricity error. The frequency of meshing stiffness considering eccentricity error is composed of the meshing frequency (short-term frequency) and rotating frequency (long-term frequency).
- (2) The orbit shape of one gear with eccentricity error is related to its tooth number, and each loop is based mainly on the orbit shape without error, especially for the case of the ESSP.
- (3) The orbit shape of two meshing gears with both eccentricities is greatly affected by the least common multiple (LCM) of two teeth number, regardless of the mesh phasing. Moreover, the orbits of two meshing pairs in MC or GC are also influenced partly by the direction of the meshing force.

Chapter 4 Study on the Dynamic Characteristics of the Double-helical Two-Stage Parallel Compound Marine Gear Transmission System

4.1 Preface

The previous chapter examined the static characteristics of the two-stage parallel compound gear system, validating the modeling strategy. In contrast to the static model, the dynamic model incorporates additional inertia terms, particularly concerning absolute acceleration. In order to address the time-varying characteristics of the overall stiffness matrix in the established dynamic model, this chapter introduces an improved Newmark- β numerical method suitable for solving time-varying stiffness matrices and large degree-of-freedom equations. The dynamic model is further validated through comparisons of dynamic and static vibration responses, investigating the effects of gravity, centrifugal forces, and providing theoretical explanations. Additionally, the coupling relationship between the two-stage gear systems is analyzed.

4.2 Improved Newmark- β numerical solution method

Regarding to the dynamic equation of the whole compound gear system shown in Equation (2-40), the key question is how to get the solution fast and accurately. Due to the meshing force in the dynamic model of this paper is a nonlinear force, the meshing stiffness matrix and the meshing damping matrix are also time-varying. Based on the above form of the meshing force, the Newmark- β method is not suitable for directly adopting the Newmark- β solution method because it is appropriate to the dynamic equation of a fixed stiffness and less suitable for the nonlinear time-varying engagement stiffness. Therefore, for this reason, the method is improved to used to be suitable for solving the time-varying nonlinear meshing force dynamics equation.

Assuming that the time step in the solution process is dt, the basic principle of the Newmark- β method is to divide the effective load by the effective stiffness, so that the displacement at the time moment t+dt can be expressed as:

$$\mathbf{K}_{E}\mathbf{q}_{t+dt} = \mathbf{F}_{t+dt} \tag{4-1}$$

where \mathbf{K}_E represents the equivalent stiffness matrix and \mathbf{F}_{t+dt} represents the external force at the moment of t+dt. The acceleration and velocity at the moment

of t+dt can be calculated from the displacement at the moment of t+dt as well as the acceleration and velocity at the moment of t. The method can be used to calculate the acceleration and velocity at the moment of t+dt. However, in this method, there is not a relative error accuracy as in the Runge-Kutta method, which is not directly usable for the dynamic model of this paper due to the presence of nonlinear meshing forces. For this reason, the Newmark- β method is improved in this section, and the relative error ϵ is set in order to eliminate the accumulation of errors in the original method as well as to improve the accuracy of the solution. Fig.4-1 shows the main computational flow of this improved numerical solution method.

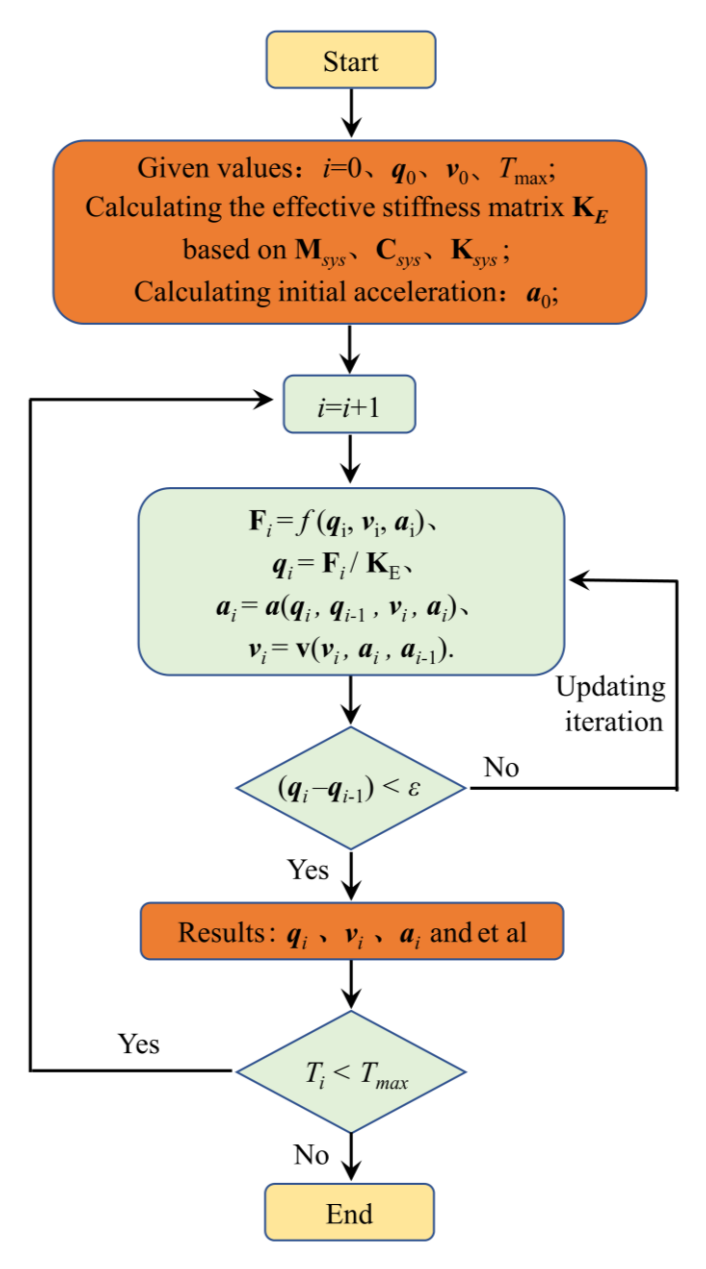


Fig.4-1 The flowchart of the improved Newmark- β method

As shown in Fig.4-1, the initial displacement q_0 and initial velocity v_0 are first given, and the initial acceleration a_0 is calculated according to the equation. starting from the second time step, the displacement q calculated at each step is first compared with the displacement at the previous moment, and if the difference is less than or equal to the relative error ϵ , the calculation of the next time step is carried out; if it does not meet the relative error ϵ , the calculated displacement, velocity, and acceleration will be used as the initial values. Re-effective external force, re-calculate the iteration, get the new displacement, velocity, acceleration until it meets the relative error, end the iteration process or reach the maximum number of iterations.

4.3 Analysis of dynamic vibration response results

In this subsection, based on the dynamic equations and the improved Newmark-beta numerical method, the accuracy of the established dynamic model is validated by comparing dynamic vibration response results with static results. The fundamental parameters of the gears remain consistent with those in the static study, while other parameters, such as gear mass and moment of inertia, are presented in the following table.

| Stage | First stage | | | Second stage | | |
|---|-------------|--------|-------|--------------|--------|-------|
| Component | Sun | Planet | Ring | Sun | Planet | Ring |
| Mass, m (kg) | 127 | 421 | 333.4 | 501.5 | 293 | 393 |
| Mement of inertia, J (kg.m ²) | 23.798 | 25.8 | 225.0 | 40.687 | 8.398 | 224.5 |

Tab. 4-1 Basic parameters of gear in the compound gear train

4.3.1 Comparison of sun orbit between dynamic model and quasistatic model

The transmission effect of a planet gear system can be expressed by the axial trajectory, and at the same time the axial trajectory influences the motion state between each meshing pair. Therefore, the orbit is firstly analyzed in this subsection to verify the accuracy of the dynamic modeling method of this two-stage parallel compound planetary gear system. In the modeling process, the coordinate system of the planet gear in each planetary gear system is selected as radial-tangential coordinate system, so the axial trajectories of the sun (representing the central component) and the planet in each stage are selected for comparative analysis. Fig.4-2 shows the axial trajectory of the sun in the first

stage, where Fig.4-2 (a) and (b) correspond to the vibration response results of the quasi-static and dynamic models, respectively.

From the modeling process of the dynamics, it can be seen that the first stage is modeled using a moving coordinate system, and the second stage is a global coordinate system. As a consequence, this means that the first stage becomes a fixed-axis planetary gear system, so that position of each planet with respect to the sun is fixed. Therefore, at the same time, the first stage is in a sequential phase so that at every moment of time, combined force of sun about the planets has an additional force, thus causing the trajectory of the sun not to be fixed but to have a trajectory radius. Meanwhile the orbit diagram of sun illustrated in Fig.4-2 (b) show that the result is in a fixed-axis gear system, although it is not as precise as the quasi-static result of a triangle as shown in Fig.4-2 (a), whose reason is the complexity of the dynamic model compared to the static model. However, it is still a good indication that the vibration response of the sun derived from the dynamic model is correct.

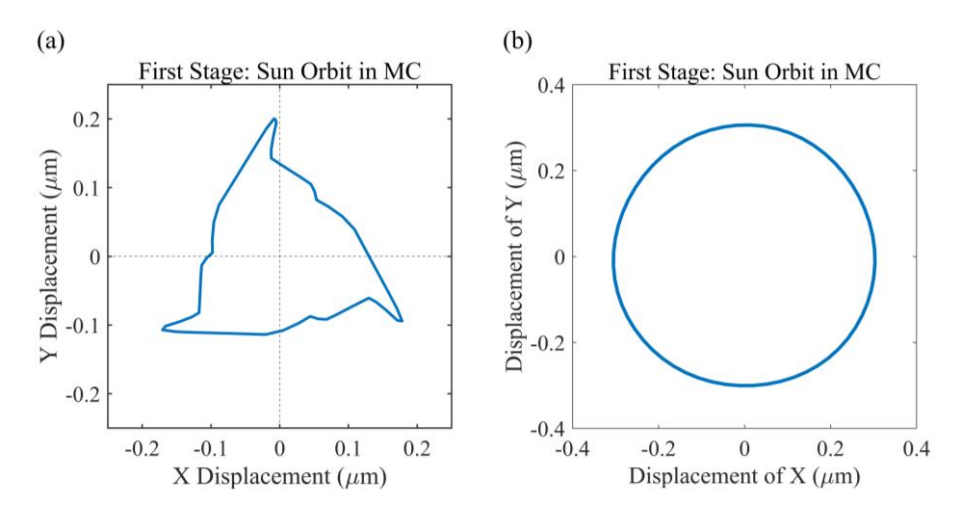


Fig.4-2 Orbit of sun in first stage: (a) results of quasi-static model [154], (b) results of dynamic model

Similarly, Fig.4-3 illustrates the comparison of vibration responses of the sun gear in second stage between the dynamic and static models. The results indicate that the sun gear in second stage remains fixed, primarily due to its in-phase engagement, resulting in zero resultant force at all times. Based on Fig.4-2 and Fig.4-3, the consistent results from both dynamic and static models provide preliminary evidence for the accuracy of the dynamic model.

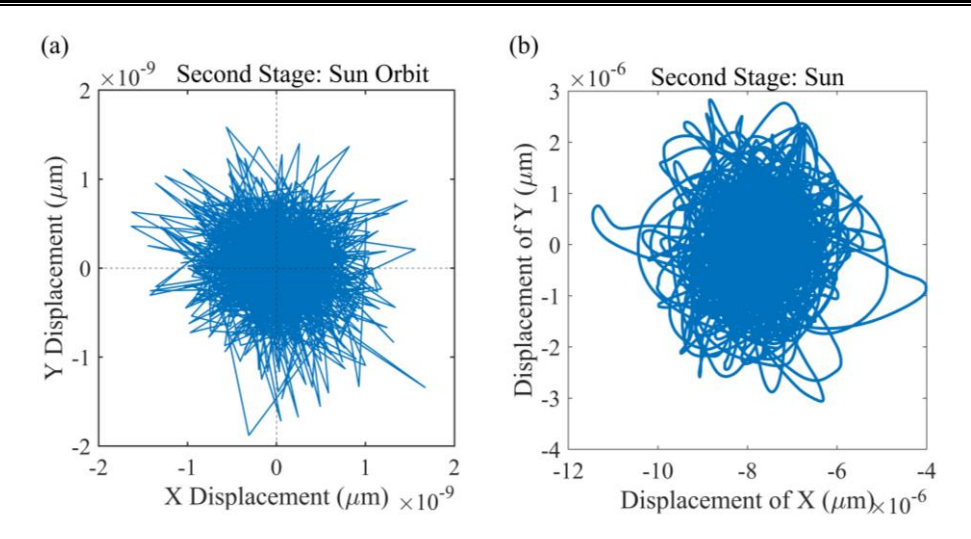


Fig.4-3 Orbit of sun in second stage: (a) result of quasi-static model [154], (b) results of dynamic model

4.3.2 Comparison of planets orbit between dynamic model and quasistatic model

Due to the direction of rotational speed input to the sun in first stage is anticlockwise, as well as based on the schematic shown in Fig.2-11, it can be seen that the tangential direction of the planet in the first stage is the same as the direction of the combined force coming from the sun and ring, and so the tangential displacement of the planet should be positive.

Fig.4-4 (a) and (b) are the vibration response diagrams of the planets in the first stage calculated by the static and dynamic models, respectively. From Fig.4-4 (a) and (b), it can be seen initially that the results of the tangential displacements of the individual planet are positive and consistent with direction of the combined force. The results of the vibration displacements of each planet are consistent in the moving coordinate system, which are consistent to the force analysis. Meanwhile the results calculated by the dynamic model in Fig.4-4 (b) show that the dynamic equilibrium point of the planets in the tangential direction is larger than the static equilibrium point in Fig.4-4 (a), which is because there are more forces to be taken into account in the dynamics (similar to inertial forces in the form of ma) than in the statics.

Therefore, although the results of the tangential displacement vibration response calculated by the dynamics model are greater than those of the statics, the accuracy of the dynamics model calculations is illustrated by combining the axial trajectory plots in Fig.4-4 (a) and (b). Fig.4-4 (c) demonstrates the axial trajectory results of Fig.4-4 (b) transformed into the axial trajectory results in the

fixed coordinate system XOY. Since the meshing phases of the first-stage is sequential phases, which can be seen from Fig.4-4 (c), the vibration response of the planet conforms to the meshing phases. It is concluded that the axial trajectory results calculated by the dynamic model for the first-stage planets are relatively correct.

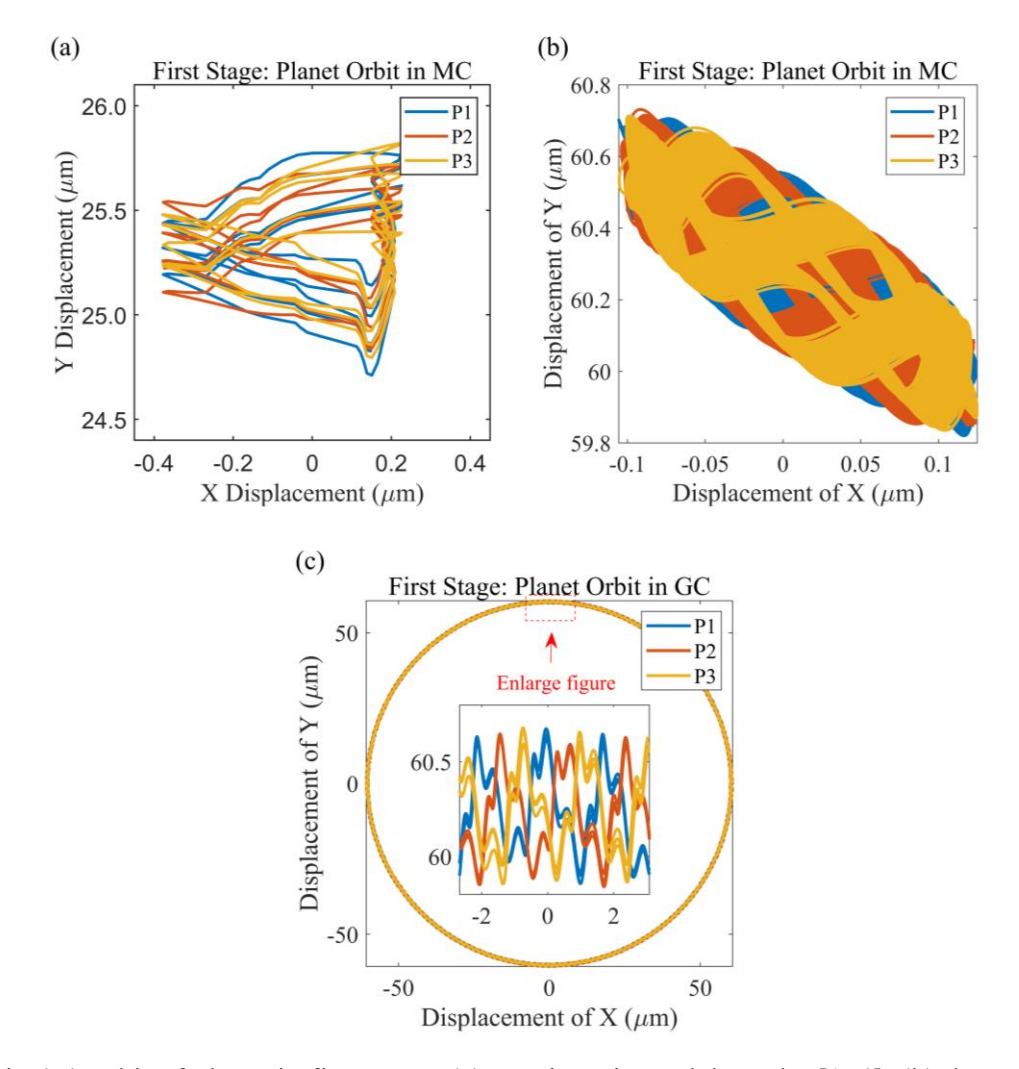


Fig.4-4 Orbit of planet in first stage: (a) quasi-static model results [154], (b) dynamic model results in moving coordinate and (c) dynamic model results in global coordinate

In the same way as the first stage, Fig.4-5 (a) and (b) shows the comparative results of the transverse vibration displacements in the radial-tangential coordinate system of the planet in the second stage. As shown in Fig.4-5 (a) and (b), it can be seen that the values of tangential displacements of the planets calculated by the dynamic and static model are all negative, the displacements magnitude of each planet is basically the same. The difference of the displacements is that the values of the dynamic tangential displacements are larger

than those of the static ones, which is same as that in first stage. Analyzing the cause, it can be seen that the input direction of the second stage is clockwise, as shown in Fig.4-5 (d). Furthermore, the combined direction of the meshing force from the sun and the ring is opposite to the positive direction of its tangential coordinate system. Hence, the results of the tangential displacements shown in Fig.4-5 (a) and (b) are consistent with the analysis of the forces.

Therefore, according to the comparative analysis of the basic axial trajectory diagrams of the sun and planets in two-stage from Fig.4-2 to Fig.4-5, it can be seen that the results of the dynamic and static calculations show a consistent trend which demonstrates that the consideration of the various additional forces in the dynamic modeling process is adequate. In addition, the proposed modeling methodology on this studied two-stage parallel compound planetary gear system fits with the expected performance accurately.

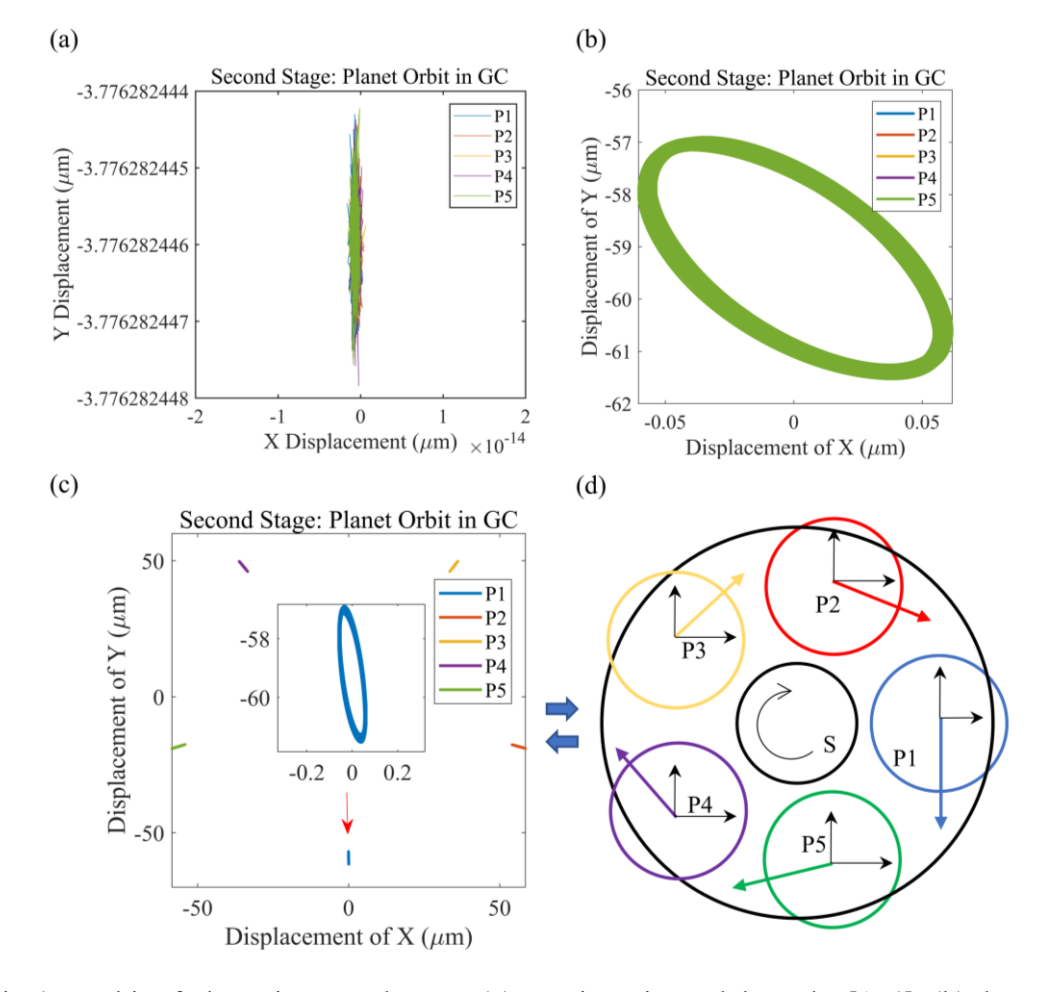


Fig.4-5 Orbit of planet in second stage: (a) quasi-static model results [154], (b) dynamic model results in radius-tangential coordinate, (b) dynamic model results in horizontal-vertical coordinate, (d) force analysis diagram of planets in horizontal-vertical coordinate

4.3.3 Comparison of the load sharing ratio between dynamic model and quasi-static model

In the previous subsection, the basic vibration response results in the dynamic model were analyzed and compared, and basic consistent conclusions were obtained. In the planet gear system, another important parameter is the meshing force. In the dynamic model studied in this paper, the dynamic meshing force is not only affected by the vibration displacement, but also by the vibration velocity. Therefore, the next step is to calculate the magnitude of the load sharing ratio (LSR) based on the meshing force, and to validate the dynamic model by looking at LSR of the dynamic model.

Fig.4-6 shows the LSR of individual planet gear in first stage calculated by the quasi-static and dynamic models. By comparing Fig.4-6 (a) and (b), it is found that the LSR calculated by the two models are in accordance with the sequential phasing due to the existence of the sequential phasing in the first stage. Secondly, the magnitude of variation of LSR calculated by the dynamic model shown in Fig.4-6 (b) is larger than that in the static results. This is also due to the fact that there are more forces in the dynamic model than in the static one, and the dynamic results are more in line with the load conditions of the actual equipment operation. Thus, the accuracy of the dynamic model is once again demonstrated by the comparison of the meshing force results.

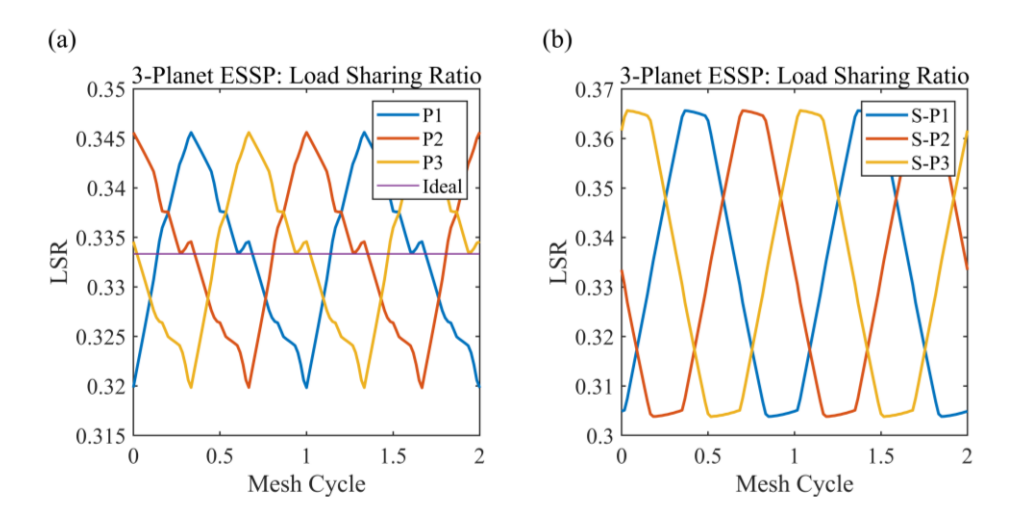


Fig.4-6 Load sharing ratio of first stage: (a) quasi-static model results [155], and (b) dynamic model results

4.3.4 Vibration angular displacement in dynamic model

In this subsection, the axial torsional vibration angular displacements of the

two-stage were analyzed by stipulating that the counterclockwise direction is defined as positive (manifested as positive vibration angular displacement values), while the clockwise direction is defined as negative (manifested as negative vibration angular displacement values), and that the input direction of sun gear in first-stage is counterclockwise.

Fig.4-7 shows the vibration angular displacements of the sun, planet and ring in the first stage. As can be seen from the Fig.4-7, the directions of their vibration angular displacements are all in accordance with the direction of rotation, indicating the reliability of the results calculated by the dynamic model.

Similarly, the results of the vibration angular displacements of each component of the second stage are shown in Fig.4-8. Due to the direction of sun of the second stage is clockwise, which is same as the ring in first stage, so it does not give. Correspondingly, the vibration angular displacements of the planet and ring exhibits a positive value. Fig.4-8 illustrates that the calculations for the second stage are also correct.

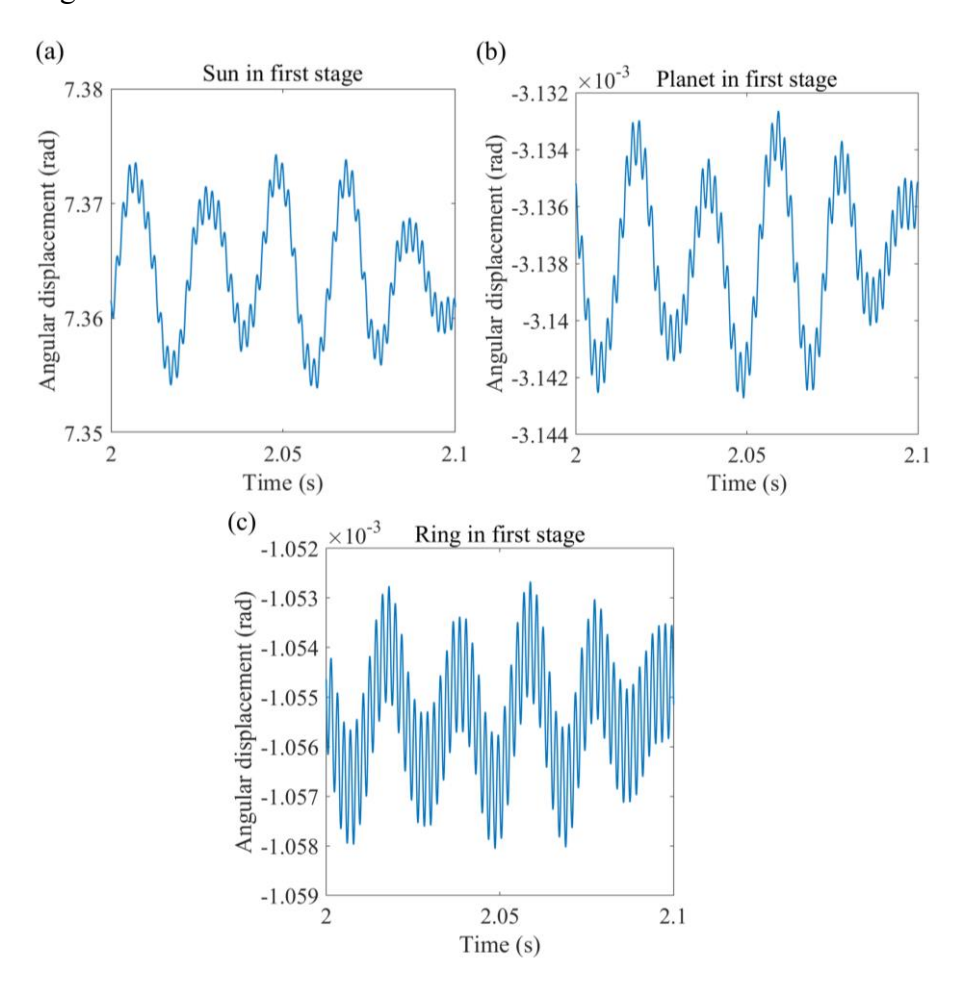


Fig.4-7 Vibration angular displacement results in first stage: (a) sun, (b) planet, (c) ring

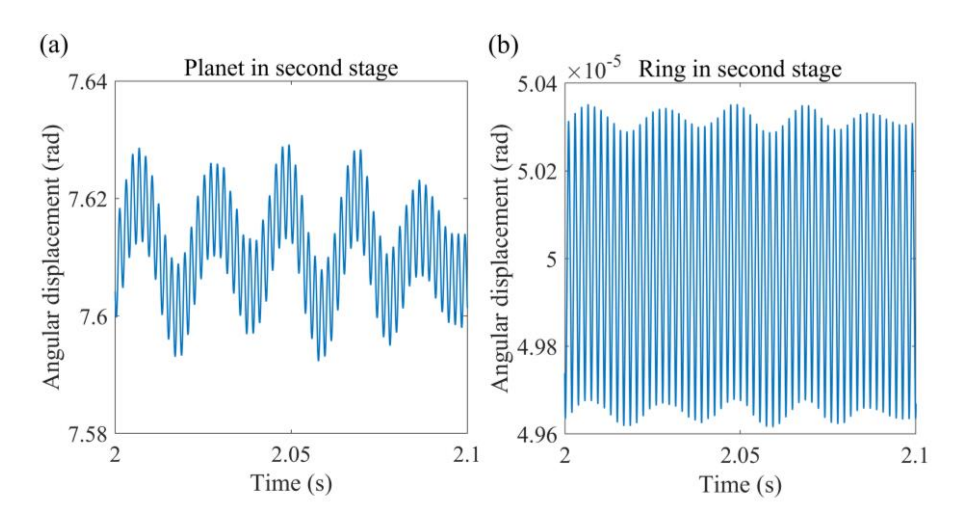


Fig.4-8 Vibration angular displacement results in second stage: (a) planet, (b) ring

Through the analysis results of transverse vibration displacement and torsional vibration angular displacement, we conclude that the established dynamic model of the two-stage parallel compound planetary gear system accurately reflects the vibration behaviour of each component in the two stages, so the model can effectively capture the angular displacement characteristics of each component due to rotation. The successful construction of this accurate dynamic model provides a reliable model basis for further gear dynamic analysis.

4.4 Influence of the gravity force and centrifugal force on dynamic vibration characteristics

From the analysis of the modelling process in Chapter 2, it can be seen that the external force terms of the whole two-stage parallel compound system mainly come from torque, gravity (which contains time-varying and time-invariant terms), centrifugal force (mainly for the first stage of the planet), etc. Different forces determine different vibration response results, and the influence on the vibration response can not be ignored, so the following is a comparative analysis of the contribution of the influence of the different forces on the vibration characteristics (orbit trajectory). The following comparative analysis investigates the influence law of different forces on the axial trajectory. Here the benchmark axis trajectory, is the external force term only exists in the case of torque.

4.4.1 Influence of the gravity force on dynamic vibration characteristics

Since the object of this study is a large marine transmission system, involving

a great mass and inertia, the gravity item can not be ignored obtaining an appreciable value. For second stage, gravity item is a constant item. However, for the first stage, gravity needs to be projected onto the moving coordinate, thus turning the time-invariant gravity item G into a time-varying gravity item G(t). The gravity term can be expressed in two stages as:

$$\begin{cases} G_{jx}^{(1)}(t) = -m_{j}g \sin(\omega_{c}t) \\ G_{jy}^{(1)}(t) = -m_{j}g \cos(\omega_{c}t) \end{cases}$$

$$\begin{cases} G_{pix}^{(1)}(t) = -m_{p}g \sin(\omega_{c}t + 2\pi(i-1)/n_{p}) \\ G_{pix}^{(1)}(t) = -m_{p}g \cos(\omega_{c}t + 2\pi(i-1)/n_{p}) \end{cases}$$

$$\begin{cases} G_{piy}^{(2)}(t) = 0 \\ G_{jx}^{(2)}(t) = -m_{p}g \sin(2\pi(i-1)/n_{p}) \end{cases}$$

$$\begin{cases} G_{pix}^{(2)}(t) = -m_{p}g \sin(2\pi(i-1)/n_{p}) \\ G_{piy}^{(2)}(t) = -m_{p}g \cos(2\pi(i-1)/n_{p}) \end{cases}$$

where superscripts 1, 2 represent the first and second stage, respectively, j represents components other than planets, and n_p represents the number of planets.

Based on the above equations, the orbits (axial trajectories) of the components in the second stage system are analyzed firstly. Fig.4-9 is a schematic diagram of the transverse vibration response of the planets in the second stage when gravity is considered.

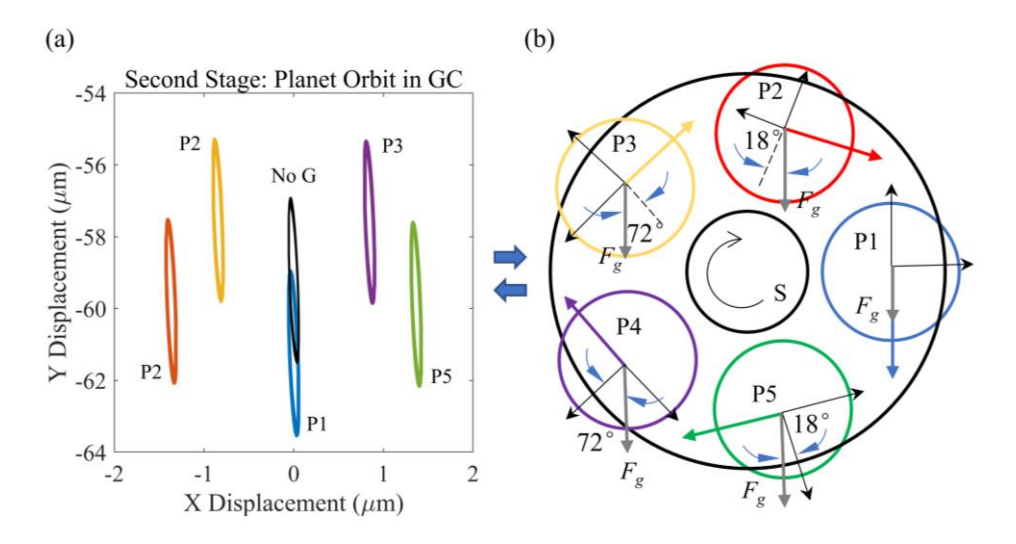


Fig.4-9 The planets in second stage under considering gravity: (a) orbit diagram, and (b) force analysis diagram

Fig.4-9 (a) is the trajectory diagram in the radial tangential coordinate system,

where it can be seen from Fig.4-9 (a) that the black trajectory describes the movement of the five planets when gravity is not taken into account, and each of them exhibiting an analogous. The other five colors correspond to the trajectories of the five planets when gravity is taken into account, respectively. From Fig.4-9 (a), it can initially be seen that the presence of gravity makes the axial trajectory of each planet change greatly. Taking the Planet #1 as an example, the trajectory of Planet #1 along the direction of gravity has decreased by half the distance of the original trajectory length. The decrease ratio reaches about 50%, which illustrates that gravity has a great influence on the trajectory of planets. In addition, the trajectories of the remaining four planets are distributed on both sides of Planet #1, showing a symmetrical trend.

Fig.4-9 (b) corresponds to the force analysis diagram of each planet when gravity is considered, where the grey part is the sign of gravity. For the Planet #2 and Planet #5 combinations, by analyzing the magnitude of the angle between the direction of gravity and their radial, the angle of their acute angle with the gravity is 18°. However, the component of gravity in their radial direction is that one along the positive direction, and the other one along the opposite direction. As a consequence, it is indicated that the component of gravity in magnitude are equal in their radial direction, but the directions are opposite. Similarly, for the combination of Planet #3 and Planet #4, the angle is 72°, the conclusion is same. Therefore, the orbits of Planet #2 and Planet #5, and Planet #3 and Planet #4 in Fig.4-9 (a) show a symmetric distribution (in the radial direction) on both sides of Planet #1.

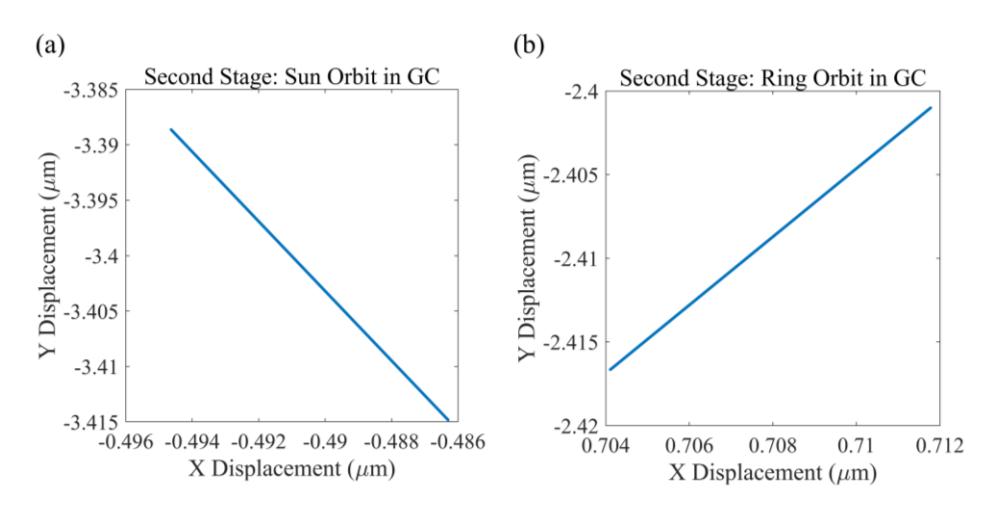


Fig.4-10 Orbit diagrams in second stage under considering gravity: (a) sun, and (b) ring

Correspondingly, Fig.4-10 is the diagrams of the axial trajectories of the sun and ring when gravity is taken into account, and the change in the trajectories of the individual planets due to the presence of gravity causes the force for the

central gear at each moment to no longer be a force of equal magnitude, and therefore the central gear is no longer fixed. Therefore, the trajectories of the central gears are mainly affected by the direction of the trajectories of the five planets, with Fig.4-9 (b) and Fig.4-10 it can be seen that the sun is mainly affected by the trajectory of the planet #4, and the ring is mainly affected by the trajectory of the planet #3. But the presence of gravity all makes the displacement of each central gear in the Y-direction decreased, which matches well with the direction of gravity. For the components of the first stage, gravity becomes a time-varying excitation with the carrier rotation speed ω_c as the variable. Accordingly, Fig.4-11 shows the axial trajectories of the sun and the planets in the first stage when gravity is considered.

Compared with Fig.4-2 (b), the radius of the axial trajectory of the sun in the moving coordinate system grows from about $0.3\,\mu\mathrm{m}$ to $17\,\mu\mathrm{m}$, which is about more than 50 times larger. Moreover, based on the fact that the period of time-varying gravity is $2pi/(\omega_c)$, it is known that one period of the gravity cycle is 750 times the meshing period of the first-stage, therefore the axial trajectory in the gravity case should be obtained by rotating the axial trajectory along a certain central point in one meshing cycle shown in Fig.4-2 (b), which can be verified in the trajectory diagram of the sun shown in Fig.4-11 (a) as well as in the enlarge diagram shown in Fig.4-11 (a), whose trajectory consists precisely of 700 circles, indicating that from Fig.4-11 (a) it can be concluded that the results of the vibration response computed by this dynamical model are fully in accordance with those obtained from the kinematic theory.

The axial trajectory of planets in first stage is shown in Fig.4-11 (b). In this graph, it can be observed that the trajectory radius exhibits a value around 40 µm. It is worth highlighting the difference in this value when the gravity is taken into account respect when it is not. the maximum trajectory radius when gravity is not taken into account just reaches 1 µm, as displayed in Fig.4-4 (b), reflecting the significant increase of this value. On the other hand, it can be seen from Fig.4-11 (b) that the coordinates of the centre of the planet trajectory, which are (0,60.3), demonstrate the model accuracy as this value coincides with the centre of the trajectory when gravity is not taken into account (Fig.4-4 (b)). The gravity item is a periodic function in the moving coordinate system. Therefore, the effect of gravity is not directly visible from the axial trajectories in the dynamic coordinate system illustrated in Fig.4-11 (a) and (b). Furthermore, Fig.4-11 (c) and (d) show the results of the vibration response of the sun and planets on the global coordinate system (XOY), respectively. It can be seen from Fig.4-11 (c) and (d) that those trajectories are located in the negative Y-axis, asserting the validity of the gravity

effect on the vibration response in this model.

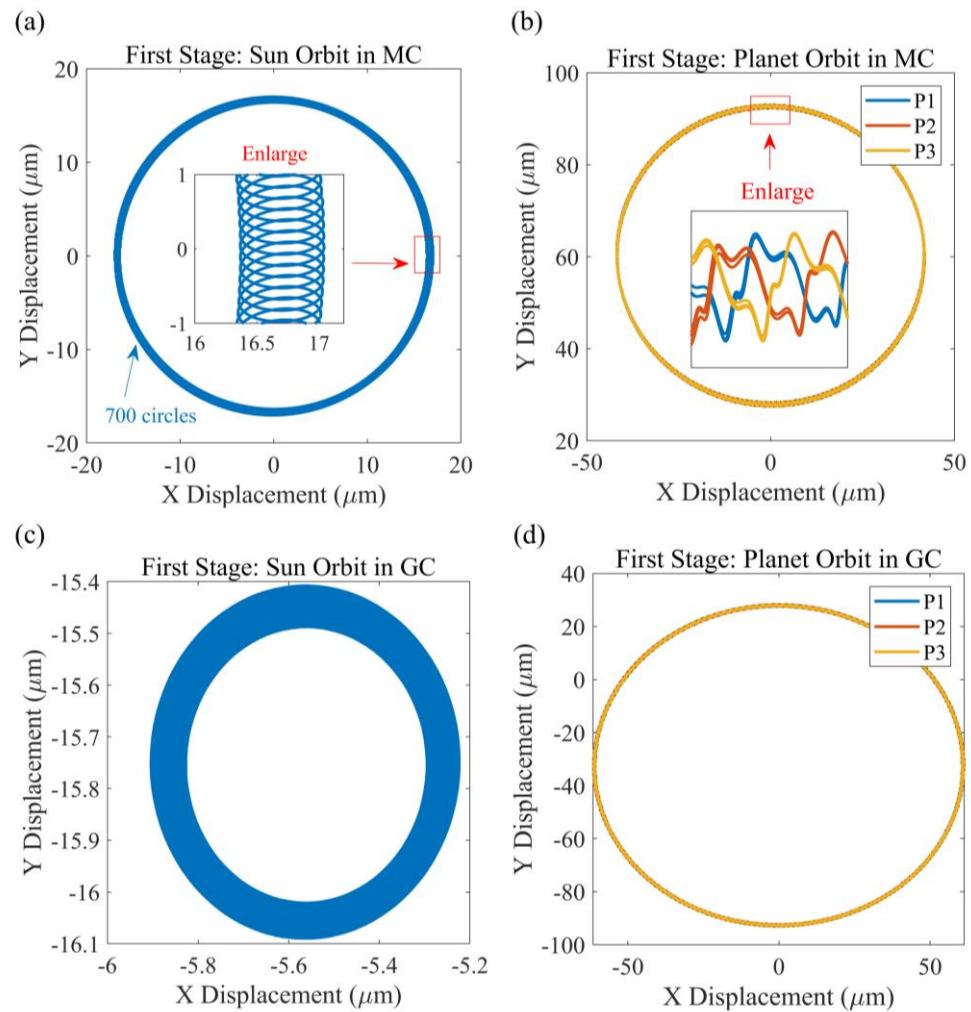


Fig.4-11 The trajectories of the components in the first stage: (a) sun in moving coordinate system, (b) planet in moving coordinate system, (c) sun in global coordinate system, (d) planet in the global coordinate system

Secondly, the presence of gravity has a significant effect on the vibration response displacement, which in turn affects the meshing displacement and hence the engagement force. Therefore, it is necessary to analyze the effect of the presence of gravity on the engagement force. The effect of gravity is illustrated using the load sharing ratio (LSR). The LSR of each planet in the first stage under the influence of gravity is shown in Fig.4-12 (a). Fig.4-12 (b) is a partial enlargement of Fig.4-12 (a), reflecting the effect of meshing phases. From Fig.4-12 (a) and (b), comparing to the case when the gravity force is not taken into account, it can be seen that the variation of LSR is very significant, and the variation of the load borne by each planet varies from 30.5%-36.5% to 23.9%-

44.7%. The maximum LSR variation rate reaches 22.466%. As can be seen in Fig.4-12 (a) and (b), the LSR by the individual planet comprise two cycles, and excepting the short cycle with the meshing cycle, it exists a long cycle with 700 times the meshing cycle, which corresponds to the 700 circles on in Fig.4-11 (a). Fig.4-12 (c) shows the force analysis diagram. It can be observed that the direction of gravity in the static coordinate system is always in the negative direction of the Y-axis. However, in the moving coordinate system, the gravity force has the same effect on each meshing force. Thus, for each planet, gravity becomes an excitation that affects the magnitude of the engagement force. The excitation period is the rotation period of the carrier, which corresponds exactly to the long period of 700 times the engagement period in LSR. Therefore, this is the cause of cyclic variation of the LSR displayed in Fig.4-12 (a).

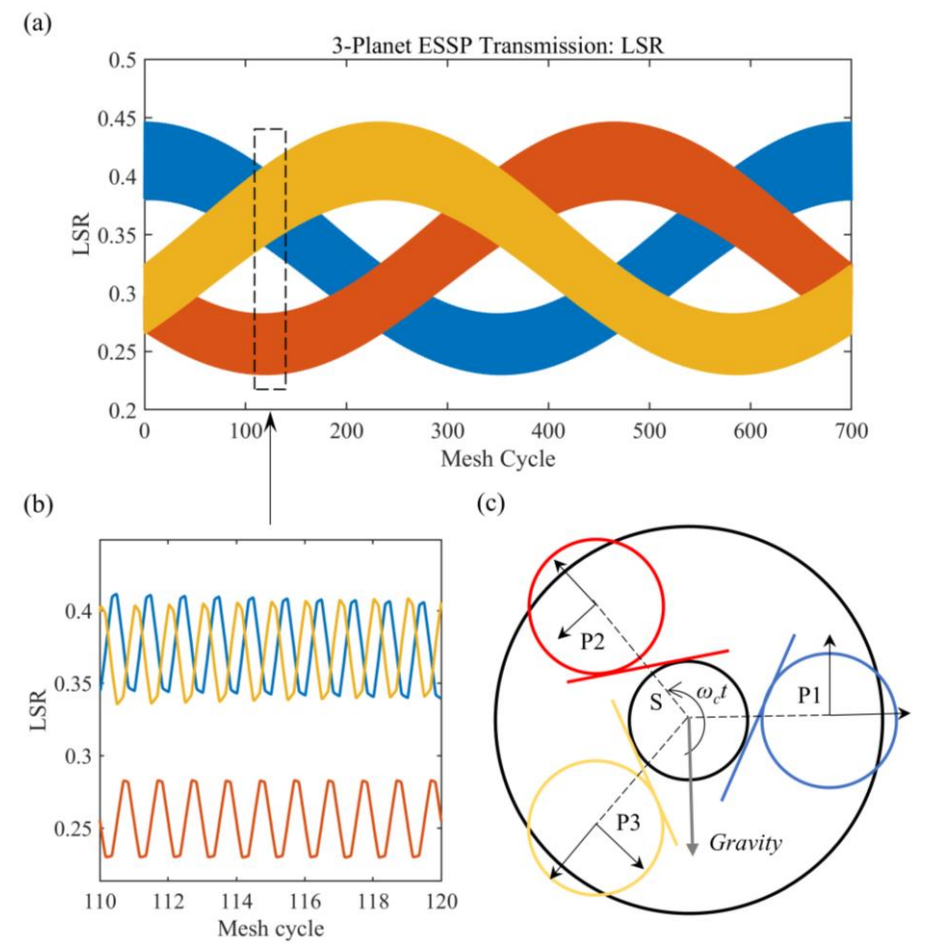


Fig.4-12 The load sharing ratio characteristics in first stage under considering gravity: (a) LSR, and (b) enlarge drawing of (a), and (c) force analysis diagram.

According to the results of this subsection, it can be concluded that the constant gravity in the static coordinate system has a non-negligible effect on the vibration response of the components in this parallel compound gear system. In

particular, it has a very interesting effect on the uniform load transmission characteristics of the first stage.

4.4.2 Influence of the centrifugal force on dynamic vibration characteristics

The centrifugal force exists only in the first stage, so it only has a direct effect on the axial trajectory of the planets, which may lead to affect the axial trajectory of the sun and ring. This subsection analyses the axial trajectory of the planet first in stage to verify the accuracy of the dynamics model.

Fig.4-13 (a) shows the axial trajectory of the planet in the first stage at 2400 rpm, 2700 rpm, 3000 rpm, 3300 rpm and 3600 rpm. It can be observed a trend between the rotational speed and radius displacement of the central point for planet trajectory. An increment in the rotational speed supposes a gradual shift of the planet of the planet trajectory in the radius direction as a result of the gradual increase in the centrifugal force direction. Fig.4-13 (b) shows the change rule of trend of the midpoint of the trajectory in the radial direction with the increase of rotational speed, from which it can be seen that the rate of change of the central point shows an upward trend with the proportional increase of rotational speed.

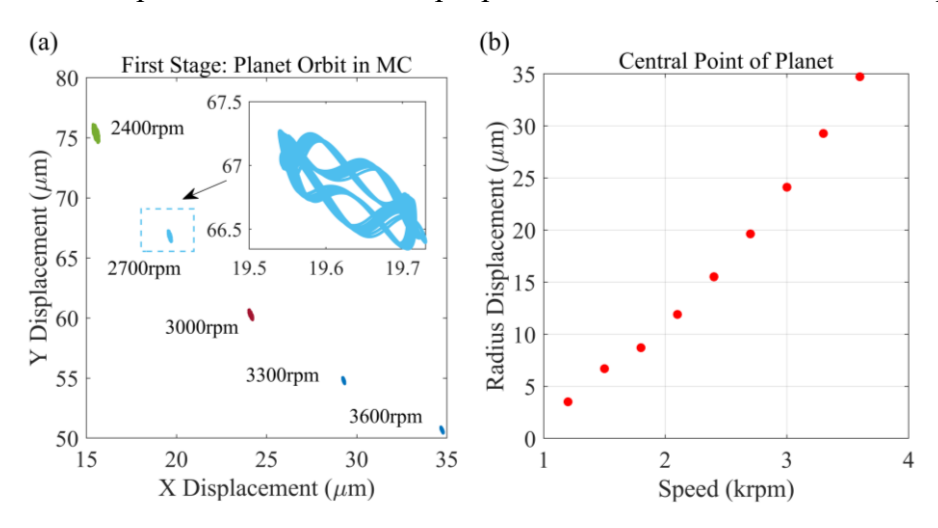


Fig.4-13 Planet in first stage: (a) trajectory at different speeds, (b) radial displacement centre versus speed

Nextly, the influence of on the load sharing ratio is presented, and Fig.4-14 is the results diagrams. Fig.4-14 (a) shows a schematic diagram of the LSR of the first-stage when the centrifugal force is considered, while Fig.4-14 (b) shows a schematic diagram considering the centrifugal force with respect to the direction of the meshing line. From Fig.4-14 (a), the LSR barely changed comparing to the case when the centrifugal force is not considered. As shown in Fig.4-14 (b), the

direction of the meshing force is constant with the positional direction angle with respect to the x-axis on the moving coordinate system. The centrifugal force always points outward along the radial direction, the angle α between the centrifugal force and the direction of the meshing line is always kept fixed, so the effect of the meshing force is the same for each S-Pi meshing force. Regarding LSR, centrifugal force has no effect on the LSR. Although, the centrifugal force has no effect on the LSR, it does have an effect on the meshing force shown in Fig.4-14 (b). Fig.4-14 (c) and (d) are meshing force of S-P meshing considering 2400 rpm and 3600 rpm, respectively. It is concluded that the high speed causes a decrease of meshing force of S-P, which may cause an increase of meshing force of R-P, resulting in an unexpected working condition.

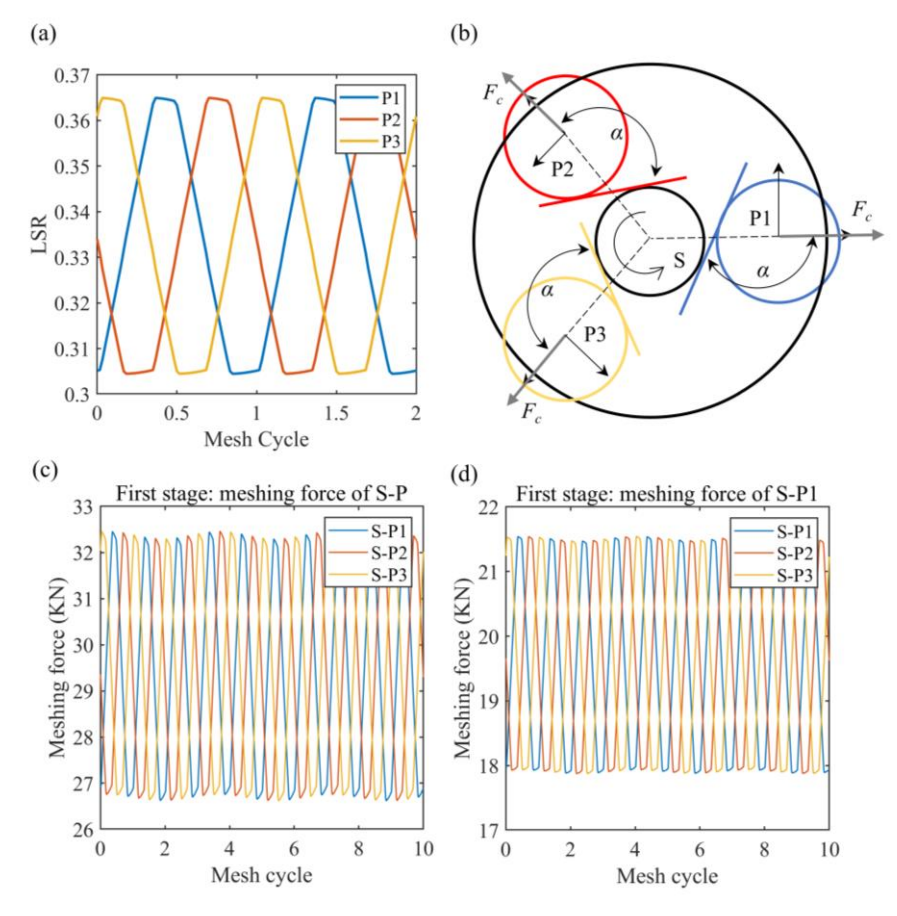


Fig.4-14 Transmission characteristics of the first stage considering centrifugal force: (a) LSR, (b) force analysis diagram, (c) (d) meshing force under 2400rpm and 3600 rpm

4.5 Analysis of coupling relationship between two stages

Based on the transmission structure diagram of the two-stage parallel compound gear system, the transmission between the two stages is relatively complex, existing a coupling relationship. This subsection, therefore, focuses on

investigating the coupling between the two stages by analyzing the frequency components. Moreover, the transmission error is only taken into account in this study case, and so do the excitation of gravity and centrifugal force.

Fig.4-15 shows the waterfall spectrum of the transverse vibration displacement of the planets in a two-stage. It can be seen that for the first stage the main excitation frequency is its own meshing frequency f_{m1} , but there are also meshing frequencies f_{m2} of the second stage and their multiplicative frequencies, and their amplitudes are quite large, especially for $0.5f_{m2}$, f_{m2} , and $1.5f_{m2}$. However, for the second stage, the meshing frequency f_{m2} of the second stage and its harmonics are the main frequencies. Although the meshing frequency f_{m1} of the first stage is also present in the second stage, the amplitude of the vibration acceleration is very low compared to that of f_{m1} , but it also indicates the presence of the meshing frequency f_{m1} of the first stage in the second stage.

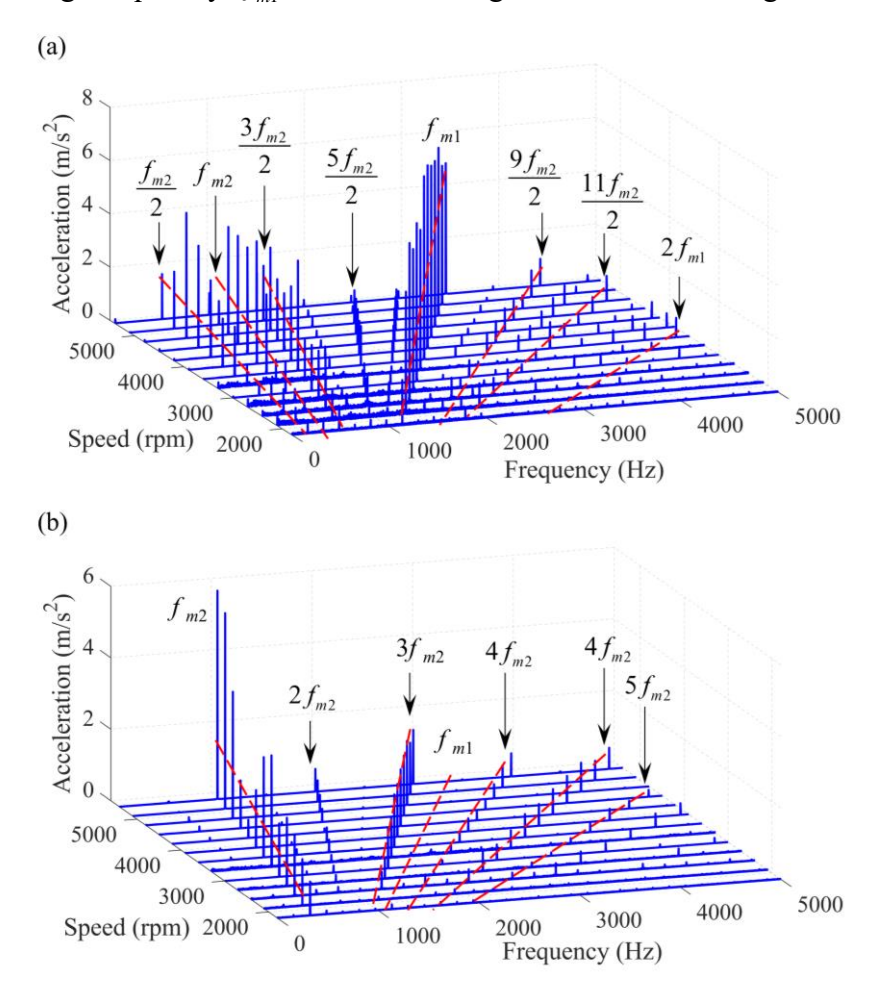


Fig.4-15 The spectrum waterfall of planets in both stage: (a) first stage, and (b) second stage

The coupling relationship between the two stages is illustrated by the Fig.4-15 diagram, in which a rich frequency content in the first stage (high speed stage) compared to the second stage is highlighted. In addition, the meshing frequency of the second stage has a greater influence on the vibration of the first stage. On the contrary the meshing frequency of the first stage has a relatively low influence on the vibration of the second stage. Therefore, in this study case, it is showed that the vibration of the differential stage (high-speed stage) should be focussed on in comparison to the second stage, even the second stage carries more torque.

4.5.1 Influence of indexing error on the coupling relationship

In order to study the ability of the established dynamic model to represent the error, in this subsection, the spectrum under a certain speed considering errors is analyzed in detail.

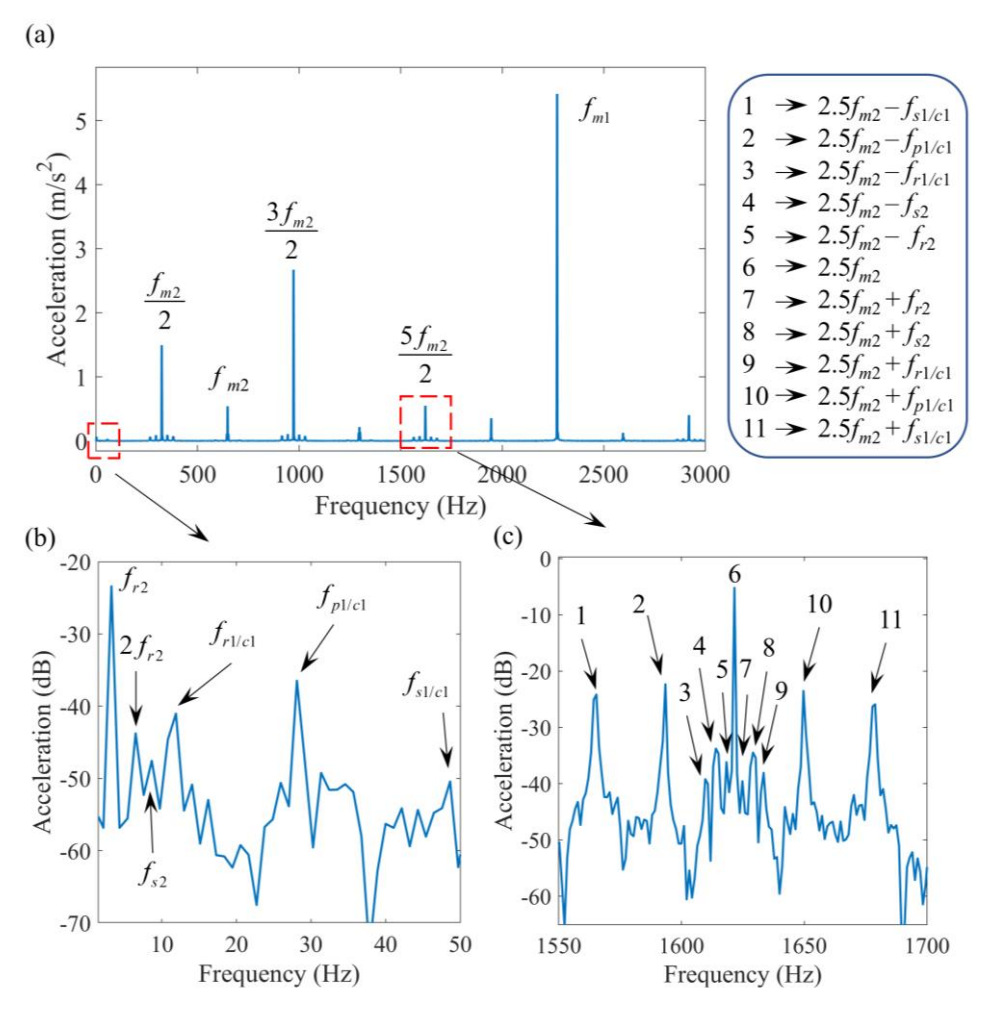


Fig.4-16 Spectrum of planet in first stage under indexing error: (a) 0-3000Hz, (b) 0-50Hz, (c) 1550-1700Hz

Fig.4-16 and Fig.4-17 show the two-dimensional spectrum diagrams of the transverse vibration acceleration of the planet, when the pitch error is considered, in each stage within 0 to 3000 Hz at 3600 rpm operating condition, respectively. The local detailed diagram is also included. The error frequency of each component can be identified from both Fig.4-16 (b) and Fig.4-17 (b). Correspondingly, the obvious modulation phenomenon, even if the amplitude is very small, can be observed from both sides of the main excitation frequency of the examples of Fig.4-16 (c) and Fig.4-17 (c).

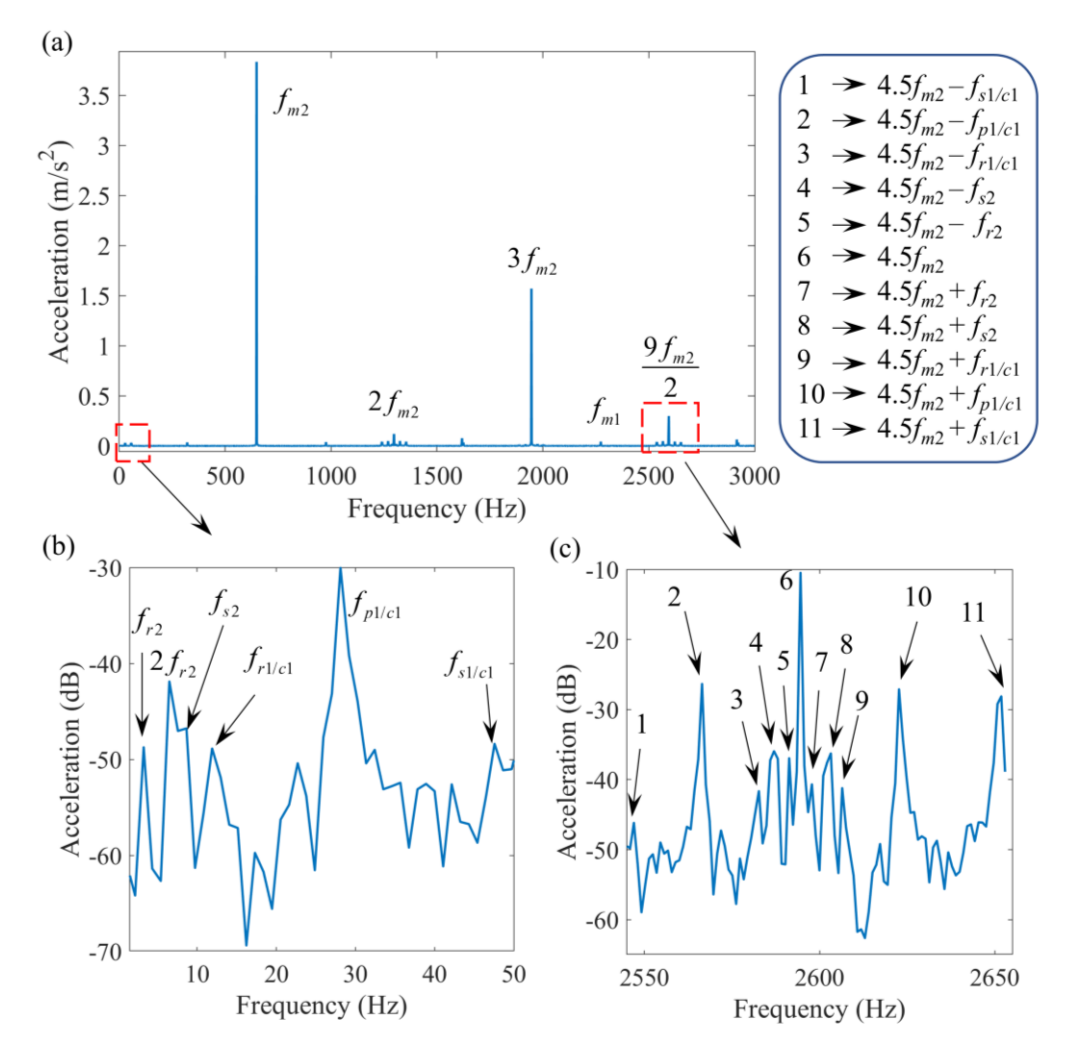


Fig.4-17 The spectrum of planet in second stage under indexing error: (a) 0-3000Hz, (b) 0-50Hz, (c) 2550-2650Hz

4.5.2 Influence of run-out error on the coupling relationship

Another time-varying error (run out error) is considered in the dynamic model of the two-stage parallel compound gear train to study the influence of eccentricity error. With the consideration of eccentricity error, Fig.4-18 (a) and

Fig.4-19 (a) are the spectral plots of the planet in the two-stage, and Fig.4-18 (b)(c) and Fig.4-19 (b)(c) are the local detail plots, respectively. It can be seen from the spectral plots that among the excitation frequencies of the first-stage, the frequencies related to the meshing frequency of the second-stage, such as $f_{m2}/2$, f_{m2} , $3f_{m2}/2$, $2f_{m2}$ and etc., has a significant influence. On the other hand, compared with the case of the existence of the pitch error, the amplitude of the vibration acceleration at these frequencies in the presence of the eccentricity error is generally a little bit larger than that at the case of the indexing error.

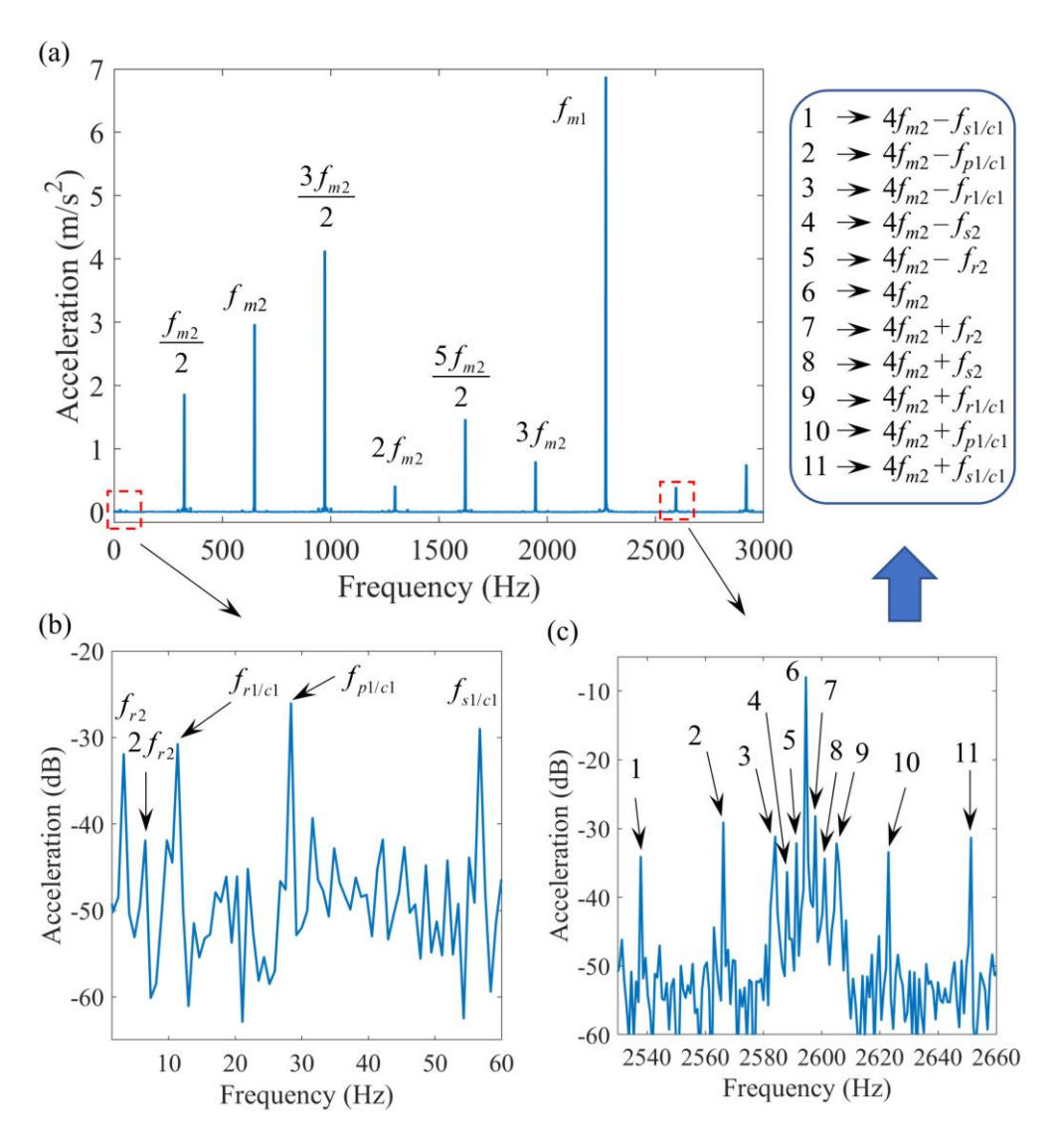


Fig.4-18 The spectrum of planet in first stage under run out error: (a) 0-3000Hz, (b) 0-60Hz, (c) 2540-2660Hz

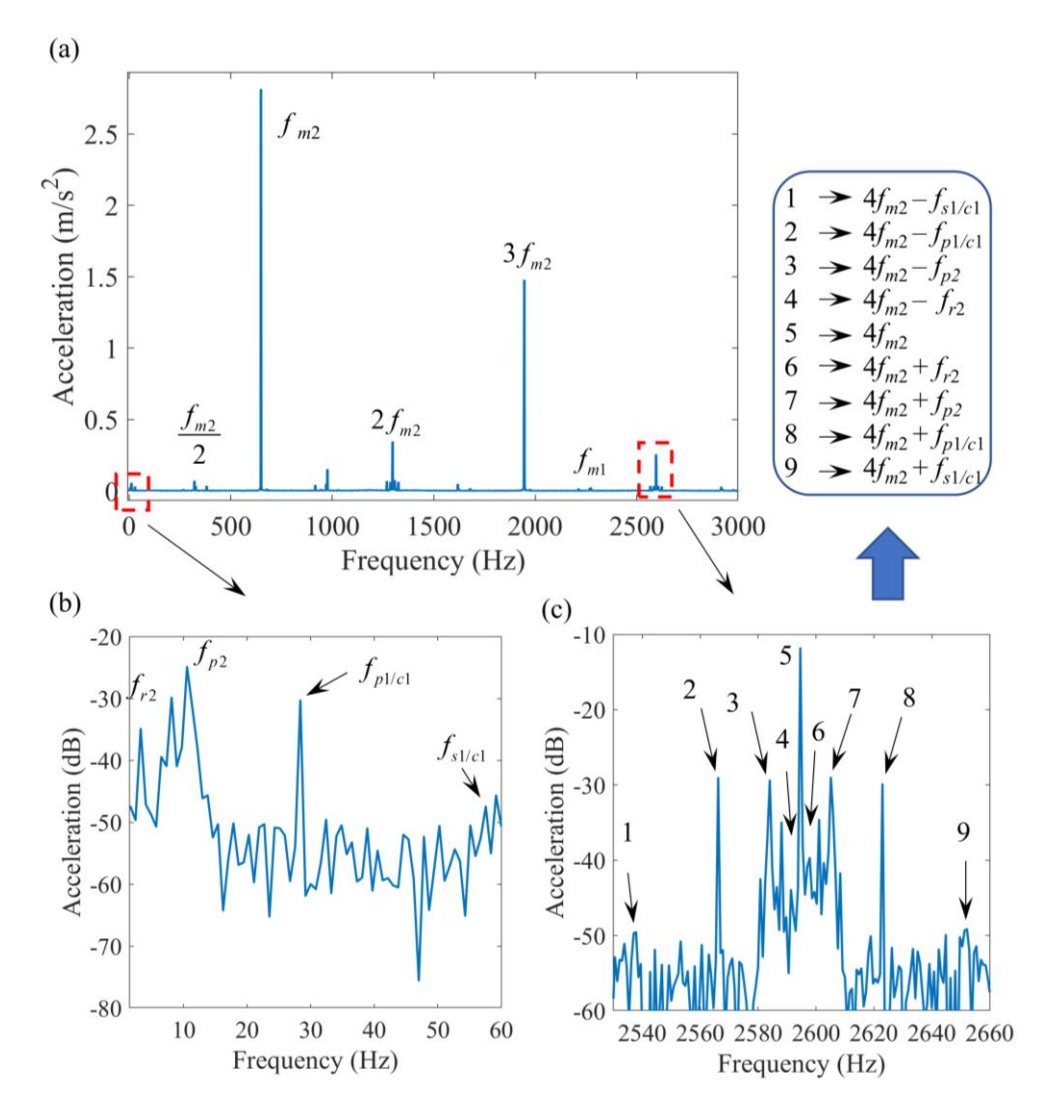


Fig.4-19 The spectrum of planet in second stage under run out error: (a) 0-3000Hz, (b) 0-60Hz, (c) 2540-2660Hz

In conclusion, the proposed dynamic model can easily capture the error frequency even if the error amplitude is relatively small according to the analysis from Fig.4-16 to Fig.4-19.

4.6 Brief summary

In this chapter, aiming to the dynamic characteristics of the two-stages parallel compound planetary gear system is studied based on the established dynamic model in Chapter 2. Firstly, an improved Newmark- β method is proposed to solve the time-varying nonlinear equation. Next, the dynamic model was verified by comparing the vibration results with that of quasi-static model, also torsional vibration displacement direction matched well to the direction of

components. The dynamic response and the influence of main excitation were discussed, and the main conclusion are shown as follow:

- (1) For second stage, the presence of constant gravity item causes the vibration displacement to move to the direction of gravity. For first stage, the time-varying gravity has an interesting influence on the load sharing ratio of the first stage, and the long cycle time of LSR has a good agreement with the rotation cycle of gravity. Furthermore, when gravity is considered, the orbit of sun includes 700 circles, coinciding with the number of mesh cycle of LSR, which is also 700. Therefore, the study of gravity effects proved the accuracy of the established dynamic model.
- (2) For first stage, the study of centrifugal force shows that it does not have a significant impact to LSR due to the angle formed by direction of centrifugal force and the fact that meshing line direction is always same for each planet. In addition, the simulation results of LSR corresponds with theoretical analysis.
- (3) In this study case, the coupling relationship exists two stages, comparing to the second stage, the high-speed stage, i.e. first stage, has a abundant frequency component. The influence of meshing frequency and its harmonics frequencies, such as $0.5f_{m2}$, f_{m2} , and $1.5f_{m2}$, of second stage affect strongly the vibration the first stage. Furthermore, the established dynamic model can observe the modulation phenomenon when the error exists.

Chapter 5 Nonlinear Dynamic Model and Analysis of the Double-helical Two-stage Parallel Compound Marine Gear Transmission System

5.1 Preface

In this chapter, a pure torsional nonlinear model of a two-stage parallel conforming wheel system is firstly established by considering the time-varying meshing stiffness, damping and meshing error excitation, and the effects of the bifurcation parameters such as the damping ratio coefficient on the nonlinear characteristics are analysed, and the key conclusion that the stable response state of the system is related to the least common multiple of the excitation period of the two-stage wheel system is obtained. Then, based on the pure torsional model, the translational-torsional coupled nonlinear model is extended and the its nonlinear characteristics are investigated. The reason of motion state of translational-torsional and its relationship with pure torsional nonlinear model are revealed.

5.2 Pure torsional nonlinear dynamic model

In this subsection, a torsional dynamic model of a two-stage double-helical planetary gear train is developed, and the vibration characteristics and coupling relationship are studied. Firstly, a purely torsional model was established based on the structure diagram and different mesh phasing. Then, the runout error is taken into account. Finally, according to frequency spectrum analysis, the coupling relationship of two stages is studied. It is shown that the runout error of the planet in different stages has a different impact on the torsional vibration of transmission error. It also shows that the coupling relationship exists and affects each other between the two stages, and the excitation frequency for the output element of two stages can be composed of a series of the mesh frequencies of each stage, the meshing frequency of high stage (1st stage) is dominated in two stages.

5.2.1 Pure torsional modeling

The dynamic model schematic of the studied compound double-helical planetary gear system is shown in Fig.5-1. The model is obtained based on the following several assumptions:

- 1). Each gear body is assumed to be rigid, and the flexibilities of the teeth of each gear are replaced by a spring-damper unit along the meshing line.
- 2). Each component is assumed to move in the torsional direction, i.e., they only have 1 degree of freedom.
 - 3). Each planet gear is absolutely same and assigned around the sun gear.

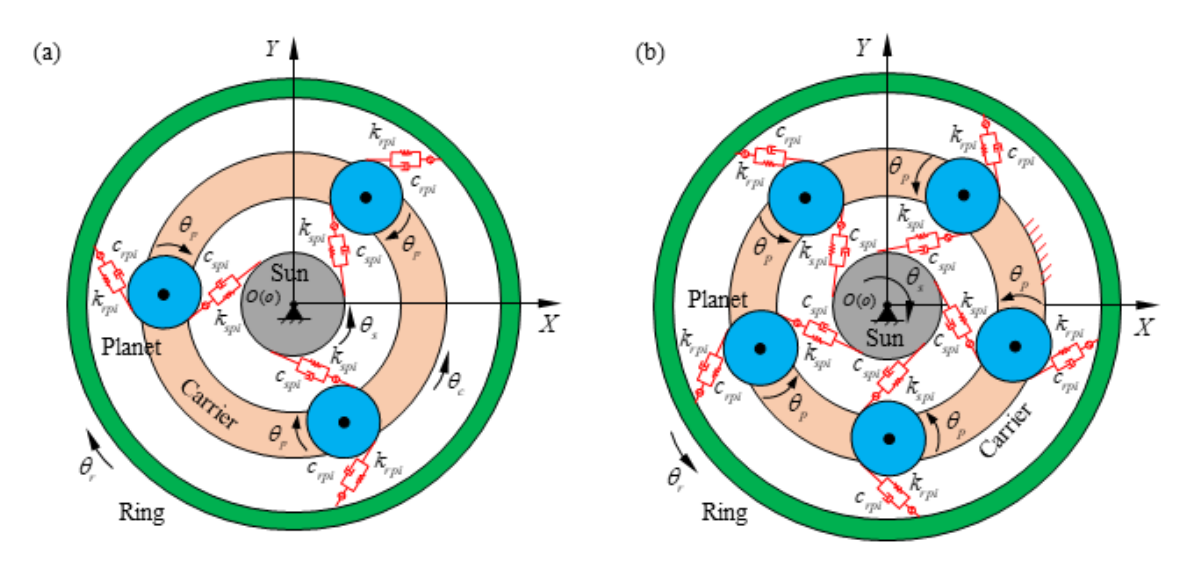


Fig.5-1 Pure torsional model

5.2.2 Relative displacements

Here, defining angular displacement $\theta_{i}^{(m)}$ (i = s, r, c and pn (n = 1, 2, ..., N), m=1 and 2) as the only motion of each component in each stage, which is obtained in a global coordinate system. It is noted that the upper right number 1 is stage 1, number 2 is stage 2 and it is assumed that counter clockwise direction is positive. Therefore, for the mesh between sun or ring and each planet i in the first stage, the equivalent meshing displacements in their contact direction are defined as shown in Equation (5-1).

$$\delta_{spi}^{(1)} = (R_{bs}^{(1)}\theta_{zs}^{(1)} + R_{bpi}^{(1)}\theta_{zpi}^{(1)} - R_{bc}^{(1)}\theta_{zc}^{(1)})\cos(\beta_b^{(1)}) - e_{spi}^{(1)}(t)$$

$$\delta_{rpi}^{(1)} = (R_{br}^{(1)}\theta_{zr}^{(1)} - R_{bpi}^{(1)}\theta_{zpi}^{(1)} - R_{bc}^{(1)}\theta_{zc}^{(1)})\cos(\beta_b^{(1)}) - e_{rpi}^{(1)}(t)$$
(5-1)

where, R_{bi} (i = s, r, c and p_n (n = 1, 2, ..., N)), β_b and e_{spi} are the radius of base circle, helix angle of base circle and transmission error and, respectively.

In same way, the equivalent meshing displacements in their contact direction of second stage are defined as shown in Equation (5-2).

$$\delta_{spi}^{(2)} = (-R_{bs}^{(2)}\theta_{zs}^{(2)} - R_{bpi}^{(2)}\theta_{zpi}^{(2)})\cos(\beta_{b}^{(2)}) - e_{spi}^{(2)}(t)$$

$$\delta_{rpi}^{(2)} = (-R_{br}^{(2)}\theta_{zr}^{(2)} + R_{bpi}^{(2)}\theta_{zpi}^{(2)})\cos(\beta_{b}^{(2)}) - e_{rpi}^{(2)}(t)$$
(5-2)

Moreover, defining the relative angular displacements between connected members in two stages as $\delta_{rs}^{(1,2)}$ and $\delta_{cr}^{(1,2)}$, which are shown in Equation (5-3). It should be pointed out that a torsional spring is used to connect two members.

$$\delta_{rs}^{(1,2)} = \theta_{zr}^{(1)} - \theta_{zs}^{(2)}, \qquad \delta_{cr}^{(1,2)} = \theta_{zc}^{(1)} - \theta_{zr}^{(2)}$$
 (5-3)

5.2.3 Equations of motion

According to Lagrange equation [156][157], the equations of motion of two stages can be derived, are shown in Equation (5-4).

$$\begin{split} J_{zs}^{(1)}\theta_{zs}^{(1)} + \sum_{i=1}^{n} (k_{spi}^{(1)}\delta_{spi}^{(1)} + c_{spi}^{(1)}\dot{\delta}_{spi}^{(1)})R_{bs}^{(1)}\cos(\beta_{b}^{(1)}) &= T_{in} \\ J_{zpi}^{(1)}\theta_{zpi}^{(1)} + (k_{spi}^{(1)}\delta_{spi}^{(1)} + c_{spi}^{(1)}\dot{\delta}_{spi}^{(1)} - k_{rpi}^{(1)}\delta_{rpi}^{(1)} - c_{rpi}^{(1)}\dot{\delta}_{rpi}^{(1)})R_{bpi}^{(1)}\cos(\beta_{b}^{(1)}) &= 0 \\ J_{zr}^{(1)}\theta_{zr}^{(1)} + \sum_{i=1}^{n} (k_{rpi}^{(1)}\delta_{rpi}^{(1)} + c_{rpi}^{(1)}\dot{\delta}_{rpi}^{(1)})R_{br}^{(1)}\cos(\beta_{b}^{(1)}) + k_{rs}^{(1,2)}\delta_{rs}^{(1,2)} &= 0 \\ J_{zce}^{(1)}\theta_{zc}^{(1)} - \sum_{i=1}^{n} (k_{spi}^{(1)}\delta_{spi}^{(1)} + c_{spi}^{(1)}\dot{\delta}_{spi}^{(1)} + k_{rpi}^{(1)}\delta_{rpi}^{(1)} + c_{rpi}^{(1)}\dot{\delta}_{rpi}^{(1)})R_{bc}^{(1)}\cos(\beta_{b}^{(1)}) + k_{cr}^{(1,2)}\delta_{cr}^{(1,2)} &= 0 \\ J_{zs}^{(2)}\theta_{zs}^{(2)} - \sum_{i=1}^{n} (k_{spi}^{(2)}\delta_{spi}^{(2)} + c_{spi}^{(2)}\dot{\delta}_{spi}^{(2)})R_{bs}^{(2)}\cos(\beta_{b}^{(2)}) - k_{rs}^{(1,2)}\delta_{rs}^{(1,2)} &= 0 \\ J_{zpi}^{(2)}\theta_{zpi}^{(2)} - (k_{spi}^{(2)}\delta_{spi}^{(2)} + c_{spi}^{(2)}\dot{\delta}_{spi}^{(2)})R_{br}^{(2)}\cos(\beta_{b}^{(2)}) - k_{rs}^{(1,2)}\delta_{rpi}^{(2)})R_{bpi}^{(2)}\cos(\beta_{b}^{(2)}) &= 0 \\ J_{zr}^{(2)}\theta_{zr}^{(2)} - \sum_{i=1}^{n} (k_{rpi}^{(2)}\delta_{rpi}^{(2)} + c_{rpi}^{(2)}\dot{\delta}_{rpi}^{(2)})R_{br}^{(2)}\cos(\beta_{b}^{(2)}) - k_{cr}^{(1,2)}\delta_{cr}^{(1,2)} &= -T_{out} \\ J_{zr}^{(2)}\theta_{zr}^{(2)} - \sum_{i=1}^{n} (k_{rpi}^{(2)}\delta_{rpi}^{(2)} + c_{rpi}^{(2)}\dot{\delta}_{rpi}^{(2)})R_{br}^{(2)}\cos(\beta_{b}^{(2)}) - k_{cr}^{(1,2)}\delta_{cr}^{(1,2)} &= -T_{out} \\ J_{zr}^{(2)}\theta_{zr}^{(2)} - \sum_{i=1}^{n} (k_{rpi}^{(2)}\delta_{rpi}^{(2)} + c_{rpi}^{(2)}\dot{\delta}_{rpi}^{(2)})R_{br}^{(2)}\cos(\beta_{b}^{(2)}) - k_{cr}^{(1,2)}\delta_{cr}^{(1,2)} &= -T_{out} \\ J_{zr}^{(2)}\theta_{zr}^{(2)} - \sum_{i=1}^{n} (k_{rpi}^{(2)}\delta_{rpi}^{(2)} + c_{rpi}^{(2)}\dot{\delta}_{rpi}^{(2)})R_{br}^{(2)}\cos(\beta_{b}^{(2)}) - k_{cr}^{(1,2)}\delta_{cr}^{(1,2)} &= -T_{out} \\ J_{zr}^{(2)}\theta_{zr}^{(2)} - \sum_{i=1}^{n} (k_{rpi}^{(2)}\delta_{rpi}^{(2)} + c_{rpi}^{(2)}\dot{\delta}_{rpi}^{(2)})R_{br}^{(2)}\cos(\beta_{b}^{(2)}) - k_{cr}^{(1,2)}\delta_{cr}^{(2)} &= -T_{out} \\ J_{zr}^{(2)}\theta_{zr}^{(2)} - \sum_{i=1}^{n} (k_{rpi}^{(2)}\delta_{rpi}^{(2)} + c_{rpi}^{(2)}\dot{\delta}_{rpi}^{(2)})R_{br}^{(2)}\cos(\beta_{b}^{(2)}) - k_{$$

in which, J_i is moment of inertia of each part except the carrier in 1st stage, and J_{zce} represents equivalent moment of inertia of the carrier in 1st stage, which is different with moment of inertia of the carrier, is shown as $J_{zce}=J_c+n\times m_{pi}\times R_c^2$. k_{jpi} and c_{jpi} are the meshing stiffness and corresponding meshing damping. It is assumed that each pair of gears (S-Pi and R-Pi) is meshing at the initial moment, but as the gear rotates, the mesh may separate, so the mesh displacement is a piecewise function as follows

$$\delta_{jpi} = \begin{cases} \delta_{jpi}, & \delta_{jpi} > 0 \\ 0, & else \\ \delta_{jpi} + b, \delta_{jpi} < -b \end{cases}$$
 (5-5)

5.2.4 Torsional results and discuss

For the simulation study, the two-stage planetary gear train with the basic parameters is studied. Tab.5-1 lists the basic parameters of whole system.

Tab.5-1 Parameters of the two-stage double-helical planetary gear train studied

| Stage | First Stage | | | Second Stage | | | |
|---------------------------|-------------|--------|------|--------------|--------|------|--|
| Element | Sun | Planet | Ring | Sun | Planet | Ring | |
| Teeth number | 38 | 76 | 190 | 80 | 55 | 190 | |
| Normal module (mm) | 6 | | | | | | |
| Normal pressure angle (°) | 20 | | | | | | |
| Helix angle (°) | 25 | | | | | | |
| Number of planets (N) | 3 5 | | | | | | |
| Planets spacing angle (°) | 120 72 | | | | | | |
| Mesh phasing | ESSP ESIP | | | | | | |

The different stages have different mesh frequencies, but there is a relationship between two stages, which is $f_m^1 = \psi f_m^2$, and $\psi = 3.375$ depends on teeth number.

5.2.4.1 Stability time-domain response analysis

The Newmark- β method is adapted to solve the dynamic equations, shown in Equation (5-4). In order to obtain a stable solution, the results of the first 8 seconds are removed.

In 1st stage, the time-domain stationary response curves of each element (sun, planet, ring) without any meshing error, are shown in Fig.5-2 - Fig.5-4 under a constant 1200 rpm input speed and a constant 72400 Nm load torque. Here, the result of the angular displacement is a linear curve with respect to time, the slope of the angular displacement is velocity, and the only difference is the positive or negative values. Therefore, taking the angular velocity (negative value) of the planet as an example, i.e., its rotation direction (clockwise) is opposite to the definition of the positive direction. Moreover, the angular displacement of the part rotating in the positive direction increases linearly and vice versa.

As shown in Fig.5-2 - Fig.5-4, the angular speed of the sun is more stable and less fluctuating, the ideal angular speed is 125.66 rad/s and angular acceleration is between -40 rad/s² and 40 rad/s². Angular velocity of planet fluctuates between -52.2 rad/s and -52.4 rad/s, and the ideal angular speed is -52.28 rad/s. Angular velocity of ring fluctuates between -16.75 rad/s and -16.66 rad/s, and the ideal angular speed is -16.39 rad/s, therefore, the angular speed agrees well with ideal value. Moreover, the acceleration fluctuation of the planet gear is more severe than that of the sun and the ring gear.

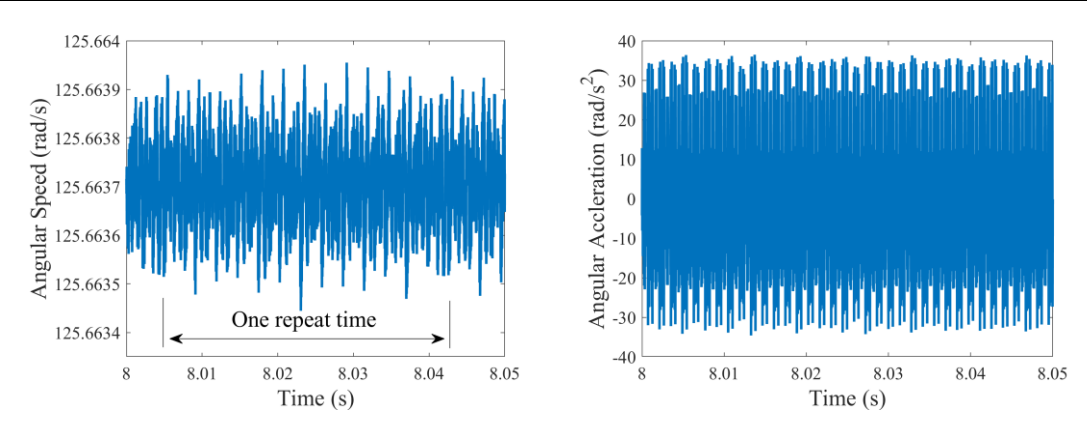


Fig.5-2 Stationary response of sun in 1st stage: (a) angular velocity, (b) angular acceleration

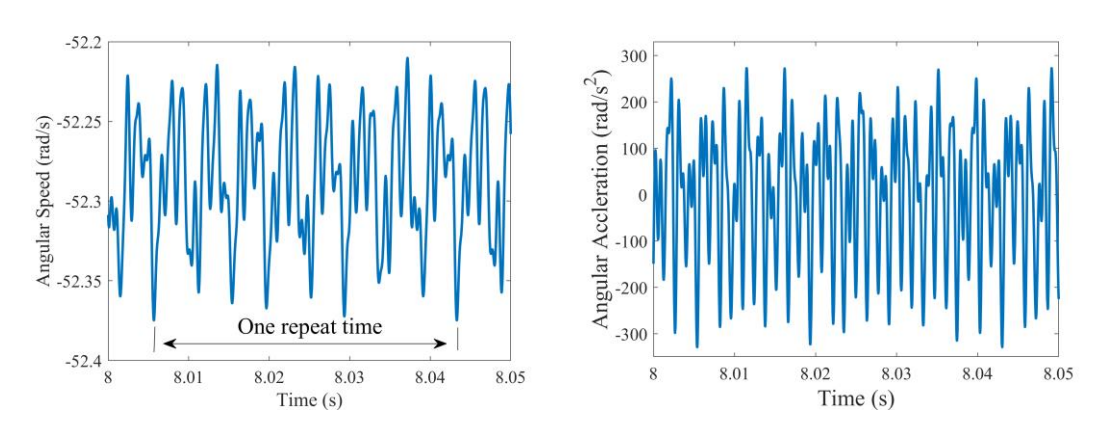


Fig.5-3 Stationary response of planet in 1st stage: (a) angular velocity, (b) angular acceleration

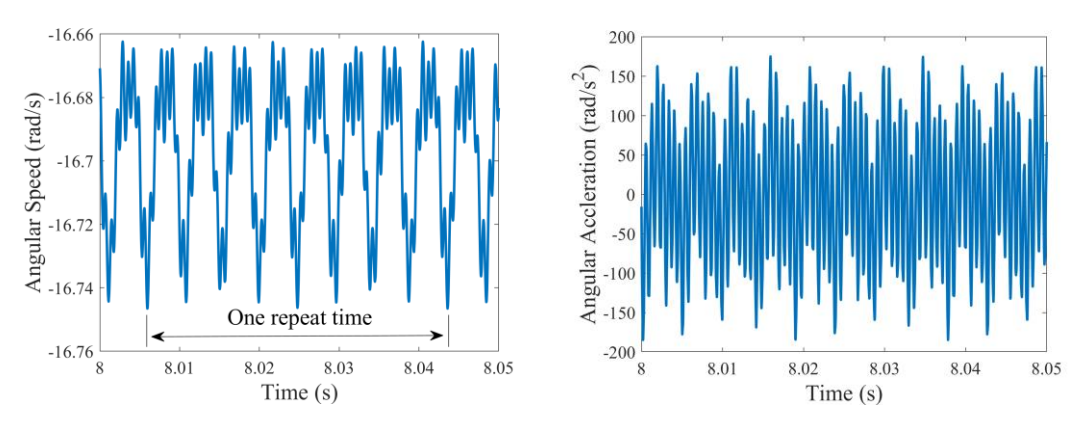


Fig.5-4 Stationary response of ring gear in 1st stage: (a) angular velocity, (b) angular acceleration

Similarly, in 2nd stage, the time-domain stationary response curves are shown in Fig.5-5 to Fig.5-7. As shown in Fig.5-5 to Fig.5-7, it can be known that

the direction of the angular displacement and magnitude of average angular velocity for each component corresponds to the theoretical rotation direction and theoretical value.

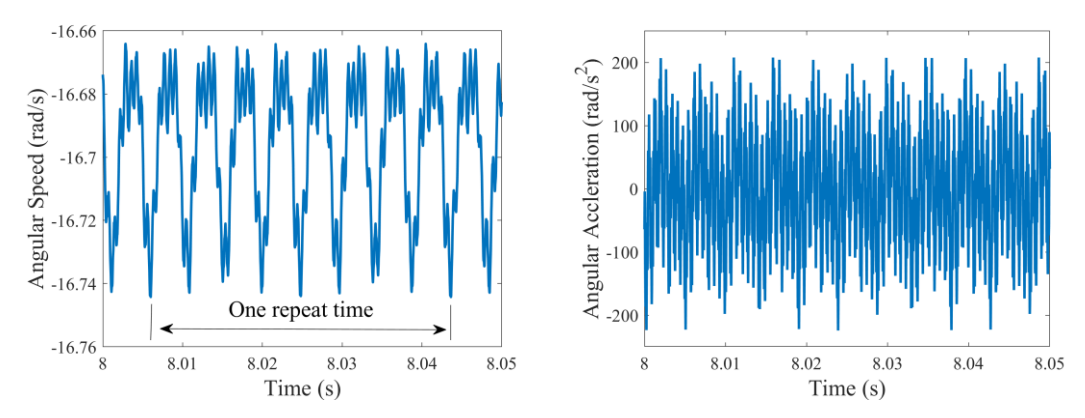


Fig.5-5 Stationary response of sun in 2nd stage: (a) angular velocity, (b) angular acceleration

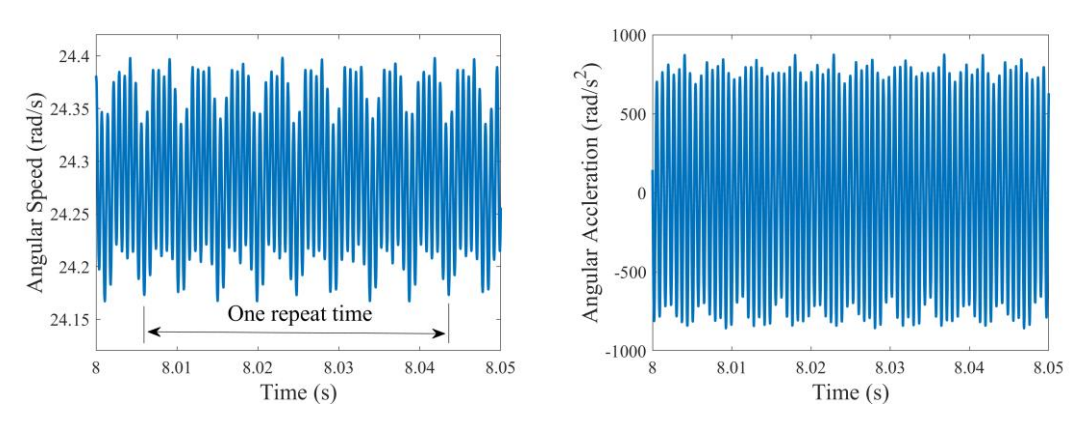


Fig.5-6 Stationary response of planet in 2nd stage: (a) angular velocity, and (b) angular acceleration

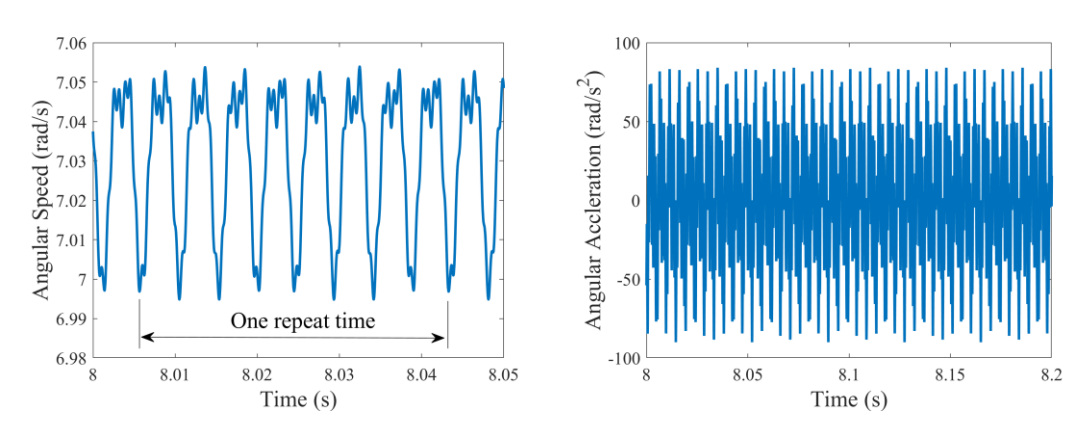


Fig.5-7 Stationary response of ring in 2nd stage: (a) angular velocity, (b) angular acceleration

According to the curves of the angular displacement and the calculated velocity value, as shown in the above Figures, it is noted that the mean calculated velocity values agree well with ideal angular velocity value.

5.2.4.2 Frequency-domain Analysis

It is critical to study coupling properties of the two-stage due to the structure diagram, shown in

Fig.1-7. In order to study the coupling characteristics, the acceleration of the planet in each stage is chosen to study the coupling characteristics. The reason is that the planet meshes with both the sun and the ring simultaneously, which causes the excitation of the planet to be complicated and it could reflect the main excitation frequency of each stage.

Without error

Fig.5-8 is the acceleration in the frequency domain under input speed 1200rpm. It is observed from Fig.5-8(a) that meshing frequency and its frequency multiplication, such as $f_{\rm m}^{\rm l}$ and $2f_{\rm m}^{\rm l}$, is the main excitation frequency. Moreover, the meshing frequency of the 2nd stage also appears. Excepting that, the modulations of $f_{\rm m}^{\rm l}$ and $f_{\rm m}^{\rm l}$, also become the main excitation frequencies, particularly the peak at $f_{\rm m}^{\rm l} + f_{\rm m}^{\rm l}$.

As shown in Fig.5-8(b), there is some different situation. Although main excitation frequencies include it own meshing frequency and harmonic frequencies, it is clear that frequencies related to meshing frequency of the 1st stage, not only appear but also are the dominant frequency such as $2f_{\rm m}^{\rm 1}$, which is similar to Fig.5-8(a). Overall, influence of the other frequencies which is related to $2f_{\rm m}^{\rm 1}$, cannot be ignored.

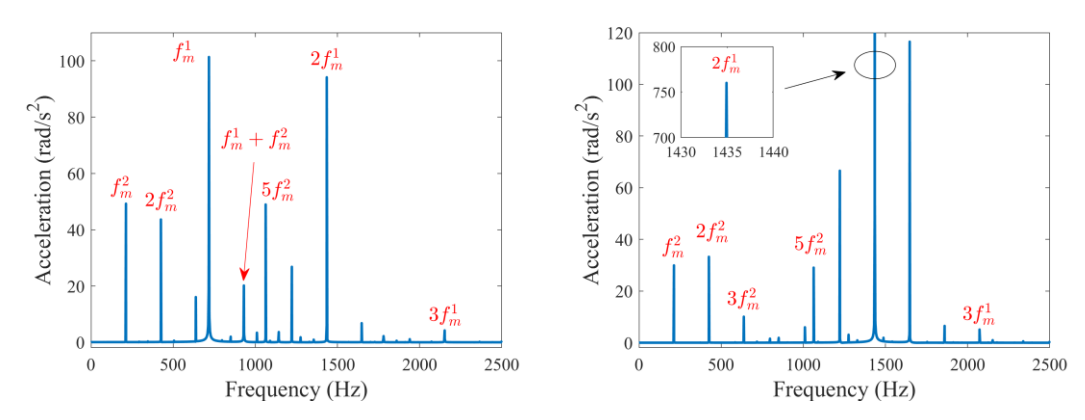


Fig.5-8 Angular acceleration frequency spectrum of planet in each stage: (a) 1st stage, (b)

2nd stage

Run out error

Next, the influence of run out error on the coupling is studied. As shown in Fig.5-9(a), sideband effects appear on either side of the location corresponding to the meshing frequency in angular acceleration frequency spectrum of the planet in 1st stage. Also, the same phenomenon occurs in the 2nd stage, shown in Fig.5-9(b), because the ring gear of the 1st stage is the input of the 2nd stage. The runout error of the planet in 1st stage excites some frequencies of 2nd stage, although its magnitude is small.

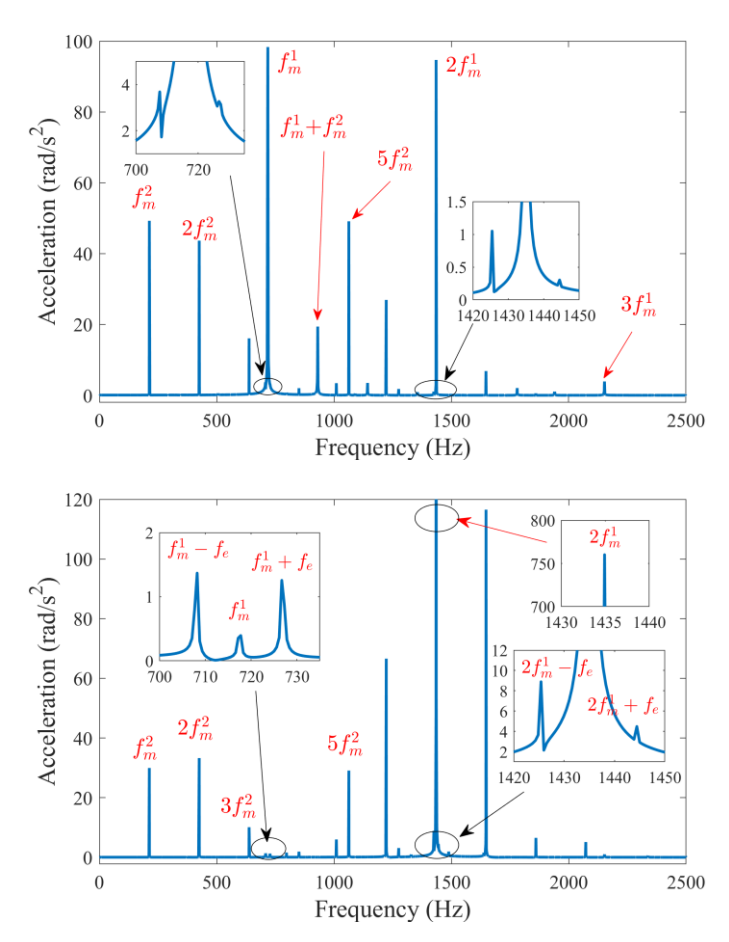


Fig.5-9 Angular acceleration frequency spectrum of planet #1 in 1st stage with runout error: (a) 1st stage, (b) 2nd stage

When the runout error is in planet of 2nd stage, the corresponding figure is given in Fig.5-10. The exciting frequency almost does not change. Comparing with the results of Fig.5-8, the runout error of the planet in the 2nd stage does not change coupling relationship.

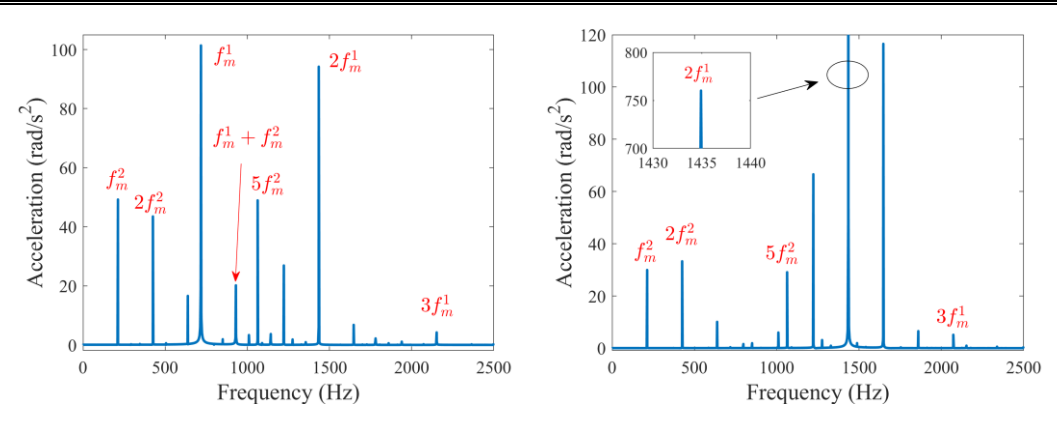


Fig.5-10 Acceleration frequency spectrum of planet #1 in 2nd stage with runout error: (a)

1st stage, (b) 2nd stage

5.2.5 Dimensionless equations of motion

Banse on the Equation (5-4), the general displacement is introduced in this subsection to study the nonlinear dynamic characteristics of the established model, and the general displacement is meshing displacement and relative displacement shown as follows:

$$\mathbf{q} = \begin{cases} \delta_{sp1}^{(1)}, \delta_{sp2}^{(1)}, \delta_{sp3}^{(1)}, \delta_{rp1}^{(1)}, \delta_{rp2}^{(1)}, \delta_{rp3}^{(1)}, \delta_{sp1}^{(2)}, \delta_{sp2}^{(2)}, \delta_{sp3}^{(2)}, \delta_{sp4}^{(2)}, \\ \delta_{sp5}^{(2)}, \delta_{rp1}^{(2)}, \delta_{rp2}^{(2)}, \delta_{rp3}^{(2)}, \delta_{rp4}^{(2)}, \delta_{rp5}^{(2)}, \delta_{rs}^{(1,2)}, \delta_{cr}^{(1,2)} \end{cases}^{T}$$

$$(5-6)$$

Therefore, the new equation of motion is rewritten as follows bansed on the meshing displacement, relative displacement formulars and Equation (5-4):

$$\ddot{\delta}_{spi}^{(1)} + \cos^{2}(\beta_{b}^{(1)}) \left\{ \left(\frac{1}{M_{se}^{(1)}} + \frac{1}{M_{ce}^{(1)}} \right) \sum_{i=1}^{m} (k_{spi}^{(1)}(t) \delta_{spi}^{(1)} + c_{spi}^{(1)} \dot{\delta}_{spi}^{(1)}) \right. \\
+ \frac{1}{M_{pe}^{(1)}} (k_{spi}^{(1)}(t) \delta_{spi}^{(1)} + c_{spi}^{(1)} \dot{\delta}_{spi}^{(1)} - k_{rpi}^{(1)}(t) \delta_{rpi}^{(1)} - c_{rpi}^{(1)} \dot{\delta}_{rpi}^{(1)}) \\
+ \frac{1}{M_{ce}^{(1)}} \sum_{i=1}^{m} (k_{rpi}^{(1)}(t) \delta_{rpi}^{(1)} + c_{rpi}^{(1)} \dot{\delta}_{rpi}^{(1)}) \right\} - \cos(\beta_{b}^{(1)}) \frac{1}{M_{ce}^{(1)}} K_{cr}^{(1,2)} \delta_{cr}^{(1,2)} \\
= \frac{T_{in}^{(1)} / R_{bs}^{(1)} \cos(\beta_{b}^{(1)})}{M_{se}^{(1)}} - \ddot{e}_{spi}^{(1)}(t)$$
(5-7)

$$\begin{split} \ddot{\mathcal{S}}_{pl}^{(1)} + \cos^{2}(\beta_{b}^{(1)}) \{ (\frac{1}{M_{re}^{(1)}} + \frac{1}{M_{ce}^{(1)}}) \sum_{i=1}^{m} (k_{rpl}^{(1)}(t) \delta_{rpl}^{(1)} + c_{rpl}^{(1)} \dot{\delta}_{rpl}^{(1)}) \\ - \frac{1}{M_{pe}^{(1)}} (k_{spl}^{(1)}(t) \delta_{spl}^{(1)} + c_{spl}^{(1)} \dot{\delta}_{spl}^{(1)} - k_{rpl}^{(1)}(t) \delta_{rpl}^{(1)} - c_{rpl}^{(1)} \dot{\delta}_{rpl}^{(1)}) \\ + \frac{1}{M_{ce}^{(1)}} \sum_{i=1}^{m} (k_{spl}^{(1)}(t) \delta_{spl}^{(1)} + c_{spl}^{(1)} \dot{\delta}_{spl}^{(1)}) \} + \cos(\beta_{b}^{(1)}) (\frac{1}{M_{re}^{(1)}} K_{rs}^{(1,2)} \delta_{rs}^{(1,2)}) \\ - \frac{1}{M_{ce}^{(1)}} K_{cr}^{(1,2)} \delta_{cr}^{(1,2)}) = -\ddot{e}_{rpl}^{(1)}(t) \\ \ddot{\mathcal{S}}_{spl}^{(2)} + \cos^{2}(\beta_{b}^{(2)}) \{ \frac{1}{M_{se}^{(2)}} \sum_{i=1}^{m} (k_{spl}^{(2)}(t) \delta_{spl}^{(2)} + c_{spl}^{(2)} \dot{\delta}_{spl}^{(2)}) + \frac{1}{M_{pe}^{(2)}} (k_{spl}^{(2)}(t) \delta_{spl}^{(2)} + c_{spl}^{(2)} \dot{\delta}_{spl}^{(2)}) \\ - k_{rpl}^{(2)}(t) \delta_{rpl}^{(2)} - c_{rpl}^{(2)} \dot{\delta}_{rpl}^{(2)}) \} + \cos(\beta_{b}^{(2)}) \frac{1}{M_{se}} K_{rs}^{(1,2)} \delta_{rs}^{(1,2)} = -\ddot{e}_{spl}^{(2)}(t) \\ \ddot{\mathcal{S}}_{rpl}^{(2)} + \cos^{2}(\beta_{b}^{(2)}) \{ \frac{1}{M_{re}^{(2)}} \sum_{i=1}^{m} (k_{rpl}^{(2)}(t) \delta_{rpl}^{(2)} + c_{rpl}^{(2)} \dot{\delta}_{rpl}^{(2)}) - \frac{1}{M_{re}^{(2)}} k_{spl}^{(2)}(t) \delta_{spl}^{(2)} \\ + c_{spl}^{(2)} \dot{\delta}_{spl}^{(2)} - k_{rpl}^{(2)} \dot{\delta}_{rpl}^{(2)} - c_{rpl}^{(2)} \dot{\delta}_{rpl}^{(2)}) \} + \cos(\beta_{b}^{(2)}) \frac{1}{M_{re}^{(2)}} K_{rr}^{(1,2)} \delta_{rr}^{(1,2)} \delta_{rr}^{(1,2)} \\ + c_{spl}^{(2)} \dot{\delta}_{spl}^{(2)} - k_{rpl}^{(2)} (t) \delta_{rpl}^{(2)} - c_{rpl}^{(2)} \dot{\delta}_{rpl}^{(2)}) \} + \cos(\beta_{b}^{(2)}) \frac{1}{M_{re}^{(2)}} K_{rr}^{(1,2)} \delta_{rr}^{(1,2)} \\ + c_{spl}^{(2)} \dot{\delta}_{spl}^{(2)} - k_{rpl}^{(2)} \dot{\delta}_{spl}^{(2)} - c_{rpl}^{(2)} \dot{\delta}_{rpl}^{(2)}) \} + \cos(\beta_{b}^{(2)}) \frac{1}{M_{re}^{(2)}} K_{rr}^{(1,2)} \delta_{rr}^{(1,2)} \\ + \cos(\beta_{b}^{(2)}) \frac{1}{M_{re}^{(2)}} \sum_{i=1}^{m} (k_{spl}^{(i)}(t) \delta_{spl}^{(i)} + c_{spl}^{(i)} \dot{\delta}_{spl}^{(i)}) + c_{rpl}^{(i)} \dot{\delta}_{rpl}^{(i)}) \\ + \cos(\beta_{b}^{(1)}) \frac{1}{M_{re}^{(2)}} \sum_{i=1}^{m} (k_{spl}^{(i)}(t) \delta_{spl}^{(i)} + c_{spl}^{(i)} \dot{\delta}_{spl}^{(i)}) + k_{rpl}^{(i)} \dot{\delta}_{spl}^{(i)}) \\ + \cos(\beta_{b}^{(1)}) \frac{1}{M_{re}^{(2)}} \sum_{i=1}^{m} (k_{spl}^{(i)}(t) \delta_{spl$$

in which, M_{je} , $M_{je}=J_{zj}/(R_{bj})^2$, (j=s,r,c,p). c_{spi} and c_{rpi} are the meshing damping for the sun or ring mesh with the planet i, respectively.

Normally, the Equations (5-7)-(5-12) could be simplified into dimensionless Equations (5-13)-(5-18) in order to eliminate the effect between different orders of magnitude in the process of solving through introducing the dimensionless time

parameter $\tau = \omega_d t$ and dimensionless displacement parameter b_c . The frequency shown in the dimensionless time parameter is given as $\omega_d = \sqrt{k_{spm}/(m_{eq})}$, in which $m_{eq} = M_s^{(1)} M_p^{(1)} M_{ce}^{(1)} / (M_s^{(1)} M_p^{(1)} + M_s^{(1)} M_{ce}^{(1)} + M_p^{(1)} M_{ce}^{(1)})$.

$$\ddot{\bar{S}}_{spi}^{(1)} + \cos^{2}(\beta_{b}^{(1)}) \left\{ \left(\frac{1}{M_{se}^{(1)}} + \frac{1}{M_{ce}^{(1)}} \right) \sum_{i=1}^{m} (\bar{k}_{spi}^{(1)}(t) \bar{\delta}_{spi}^{(1)} + \bar{c}_{spi}^{(1)} \dot{\bar{\delta}}_{spi}^{(1)} \right) \\
+ \frac{1}{M_{pe}^{(1)}} (\bar{k}_{spi}^{(1)}(t) \bar{\delta}_{spi}^{(1)} + \bar{c}_{spi}^{(1)} \dot{\bar{\delta}}_{spi}^{(1)} - \bar{k}_{rpi}^{(1)}(t) \bar{\delta}_{rpi}^{(1)} - \bar{c}_{rpi}^{(1)} \dot{\bar{\delta}}_{rpi}^{(1)} \right) \\
+ \frac{1}{M_{ce}^{(1)}} \sum_{i=1}^{m} (\bar{k}_{rpi}^{(1)}(t) \bar{\delta}_{rpi}^{(1)} + \bar{c}_{rpi}^{(1)} \dot{\bar{\delta}}_{rpi}^{(1)}) \right\} - \cos(\beta_{b}^{(1)}) \frac{1}{M_{ce}^{(1)}} \bar{K}_{cr}^{(1,2)} \bar{\delta}_{cr}^{(1,2)} \\
= \frac{T_{in}^{(1)} / R_{bs}^{(1)} \cos(\beta_{b}^{(1)})}{M_{se}^{(1)} b_{c} \omega_{d}^{2}} - \dot{\bar{e}}_{spi}^{(1)}(t)$$
(5-13)

$$\ddot{\bar{\delta}}_{rpi}^{(1)} + \cos^{2}(\beta_{b}^{(1)}) \left\{ \left(\frac{1}{M_{re}^{(1)}} + \frac{1}{M_{ce}^{(1)}} \right) \sum_{i=1}^{m} (\bar{k}_{rpi}^{(1)}(t) \bar{\delta}_{rpi}^{(1)} + \bar{c}_{rpi}^{(1)} \dot{\bar{\delta}}_{rpi}^{(1)}) \right. \\
\left. - \frac{1}{M_{pe}^{(1)}} (\bar{k}_{spi}^{(1)}(t) \bar{\delta}_{spi}^{(1)} + \bar{c}_{spi}^{(1)} \dot{\bar{\delta}}_{spi}^{(1)} - \bar{k}_{rpi}^{(1)}(t) \bar{\delta}_{rpi}^{(1)} - \bar{c}_{rpi}^{(1)} \dot{\bar{\delta}}_{rpi}^{(1)}) \right. \\
\left. + \frac{1}{M_{ce}^{(1)}} \sum_{i=1}^{m} (\bar{k}_{spi}^{(1)}(t) \bar{\delta}_{spi}^{(1)} + \bar{c}_{spi}^{(1)} \dot{\bar{\delta}}_{spi}^{(1)}) \right\} + \cos(\beta_{b}^{(1)}) \left(\frac{1}{M_{re}^{(1)}} \bar{K}_{cr}^{(1,2)} \bar{\delta}_{cr}^{(1,2)} - \frac{1}{M_{ol}^{(1)}} \bar{K}_{cr}^{(1,2)} \bar{\delta}_{cr}^{(1,2)} \right) = -\ddot{e}_{rpi}^{(1)}(t) \tag{5-14}$$

$$\begin{split} & \ddot{\overline{\delta}}_{spi}^{(2)} + \cos^{2}(\beta_{b}^{(2)}) \{ \frac{1}{M_{se}^{(2)}} \sum_{i=1}^{m} (\bar{k}_{spi}^{(2)}(t) \bar{\delta}_{spi}^{(2)} + \bar{c}_{spi}^{(2)} \dot{\bar{\delta}}_{spi}^{(2)}) + \frac{1}{M_{pe}^{(2)}} (\bar{k}_{spi}^{(2)}(t) \bar{\delta}_{spi}^{(2)} \\ & + \bar{c}_{spi}^{(2)} \dot{\bar{\delta}}_{spi}^{(2)} - \bar{k}_{rpi}^{(2)}(t) \bar{\delta}_{rpi}^{(2)} - \bar{c}_{rpi}^{(2)} \dot{\bar{\delta}}_{rpi}^{(2)}) \} + \cos(\beta_{b}^{(2)}) \frac{1}{M_{spi}^{(2)}} \bar{K}_{rs}^{(1,2)} \bar{\delta}_{rs}^{(1,2)} = -\ddot{\bar{e}}_{spi}^{(2)}(t) \end{split}$$

$$(5-15)$$

$$\ddot{\bar{\delta}}_{rpi}^{(2)} + \cos^{2}(\beta_{b}^{(2)}) \left\{ \frac{1}{M_{re}^{(2)}} \sum_{i=1}^{m} (\bar{k}_{rpi}^{(2)}(t) \bar{\delta}_{rpi}^{(2)} + \bar{c}_{rpi}^{(2)} \dot{\bar{\delta}}_{rpi}^{(2)}) - \frac{1}{M_{pe}^{(2)}} (\bar{k}_{spi}^{(2)}(t) \bar{\delta}_{spi}^{(2)} + \bar{c}_{rpi}^{(2)} \dot{\bar{\delta}}_{rpi}^{(2)}) - \frac{1}{M_{pe}^{(2)}} (\bar{k}_{spi}^{(2)}(t) \bar{\delta}_{spi}^{(2)} + \bar{c}_{rpi}^{(2)} \dot{\bar{\delta}}_{rpi}^{(2)}) \right\} + \cos(\beta_{b}^{(2)}) \frac{1}{M_{re}^{(2)}} \bar{K}_{cr}^{(1,2)} \bar{\delta}_{cr}^{(1,2)}$$

$$= \frac{T_{out}^{(2)} / R_{br}^{(2)} \cos(\beta_{b}^{(2)})}{M_{re}^{(2)} b_{s} \omega_{s}^{2}} - \ddot{e}_{rpi}^{(2)}(t)$$
(5-16)

$$\dot{\bar{\delta}}_{rs}^{(1,2)} + \cos(\beta_{b}^{(1)}) \frac{1}{M_{re}^{(1)}} \sum_{i=1}^{m} (\bar{k}_{rpi}^{(1)}(t) \bar{\delta}_{rpi}^{(1)} + \bar{c}_{rpi}^{(1)} \dot{\bar{\delta}}_{rpi}^{(1)})
+ \cos(\beta_{b}^{(2)}) \frac{1}{M_{se}^{(2)}} \sum_{i=1}^{m} (\bar{k}_{spi}^{(2)}(t) \bar{\delta}_{spi}^{(2)} + \bar{c}_{spi}^{(2)} \dot{\bar{\delta}}_{spi}^{(2)})
+ (\frac{1}{M_{re}^{(1)}} + \frac{1}{M_{se}^{(2)}}) \bar{K}_{rs}^{(1,2)} \bar{\delta}_{rs}^{(1,2)} = 0
\dot{\bar{\delta}}_{cr}^{(1,2)} - \cos(\beta_{b}^{(1)}) \frac{1}{M_{ce}^{(1)}} \sum_{i=1}^{m} (\bar{k}_{spi}^{(1)}(t) \bar{\delta}_{spi}^{(1)} + \bar{c}_{spi}^{(1)} \dot{\bar{\delta}}_{spi}^{(1)} + \bar{k}_{rpi}^{(1)}(t) \bar{\delta}_{rpi}^{(1)} + \bar{c}_{rpi}^{(1)} \dot{\bar{\delta}}_{rpi}^{(1)})
+ \cos(\beta_{b}^{(2)}) \frac{1}{M_{re}^{(2)}} \sum_{i=1}^{m} (\bar{k}_{rpi}^{(2)}(t) \bar{\delta}_{rpi}^{(2)} + \bar{c}_{rpi}^{(2)} \dot{\bar{\delta}}_{rpi}^{(2)})
+ (\frac{1}{M_{ce}^{(1)}} + \frac{1}{M_{re}^{(2)}}) \bar{K}_{cr}^{(1,2)} \bar{\delta}_{cr}^{(1,2)} = \frac{T_{out}^{(2)} / R_{br}^{(2)}}{M_{re}^{(2)} b_{c} \omega_{d}^{2}}$$
(5-18)

It should be noted that the dimensionless parameters including displacement, velocity, acceleration and other relative parameters such as stiffness, damping, frequency used in Equations (5-13)-(5-18) are defined as Equation (5-19).

$$\overline{X} = X / b_c, \overline{X} = X / (b_c \omega_d), \overline{X} = X / (b_c \omega_d^2),
\overline{b} = b / b_c, \overline{k} = k / \omega_d^2, \overline{c} = c / \omega_d.$$
(5-19)

5.3 Nonlinear dynamic characteristics analysis of the pure torsional model

5.3.1 Contact separation specification

Tooth contact separation is easily affected by the backlash and meshing displacement, causing multi-meshing states, which will result in the dynamic instability of the gear system. Therefore, the teeth contact separation specification is explained by using a time-domain diagram between the meshing displacement and backlash, as shown in the Fig.5-11. It is shown from Fig.5-11 that the meshing displacement $\bar{\delta}$ is horizontal axis, and two vertical dotted lines named as $\bar{b}=0$ and $\bar{b}=-1$ divide the horizontal axis into three parts. Moreover, if the meshing displacement is greater than 0, the drive-contact exist. if the meshing displacement is less than 0, but greater than backlash value, the tooth doesn't contact. Then, if it is the rest of the case, causing the drive-contact. Therefore, there are in total three meshing states such as drive side contact, contact separation and the back side contact, which are shown in meshing state diagram and marked as DC region, CS region and BC region in Fig.5-11, respectively. In addition, the red circle, green circle and blue circle marked as 1, 2 and 3 presents that the

system undergoes one, two and three states, respectively.

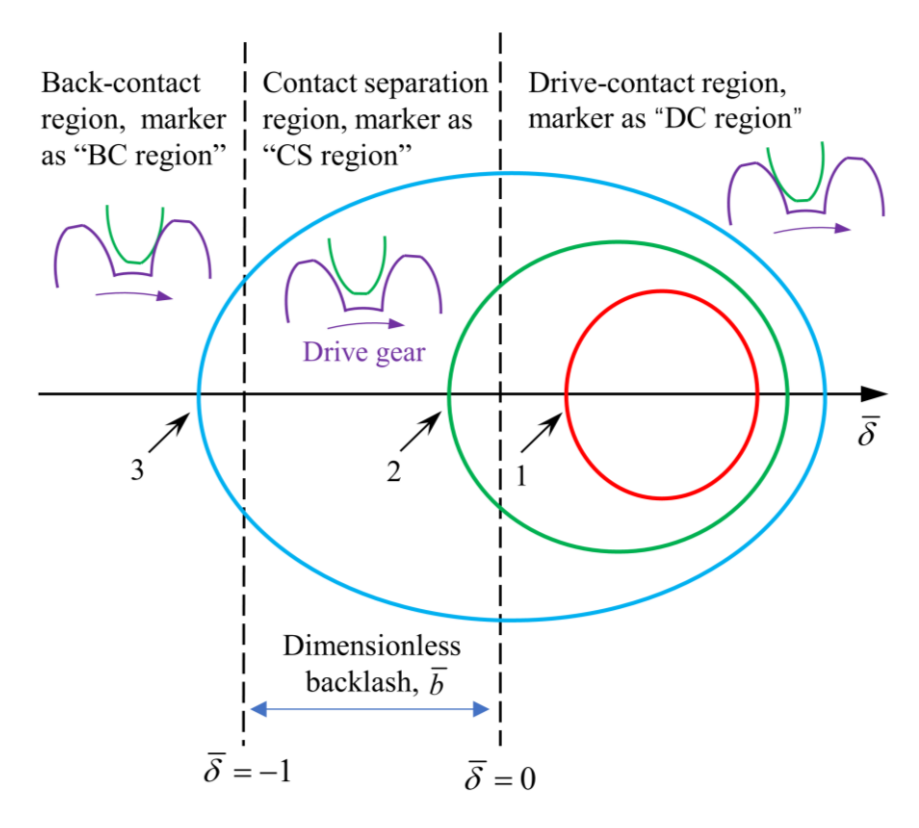


Fig.5-11 The diagram of the tooth separation based on the meshing displacement and backlash

Based on the comparison of the meshing displacement and backlash shown in Fig.5-11, the contact separation state of the meshing teeth under certain parameter value can be clearly judged.

In the following study case, the ordinary differential equations, shown as Equations (5-13)-(5-18), were solved by the fourth-order Runge-Kutta method. The result data corresponding to the first 500 response periods are removed in order to move out the transient results influence and capture the data corresponding to the steady response. Moreover, the influence laws of parameters on the dynamic response were revealed by means of bifurcation diagrams, time-history diagrams, Poincaré maps, and phase orbit diagrams in order to get an initial understanding of the non-linear dynamic behavior according to the basic equations.

The gear basic parameters are listed in Tab.5-2, the other parameters such as normal module, normal pressure angle and et al are same as the parameters in Tab.5-1. The calculated mesh phasing values used in meshing stiffness and damping are shown in Table. Moreover, some stiffness values are given in Table.

Fig.5-12 presents the meshing stiffness of external and internal meshing gear

pairs, it can be seen that stiffness value of internal meshing pairs is larger than that of external meshing in a meshing period, and reason is that the overall contact ratio ϵ_{γ} for internal gear pairs is large, which corresponds to the calculated results shown in Tab.5-2. It is shown from Fig.5-12(c) that the two meshing periods has a certain relationship, $T_{m2} = AT_{m1}$, A = 3.5 based on the transmission relationship, which corresponds to the teeth number given in Tab.5-2, in this study case. The relationship shown in Fig.5-12(c) will also be discussed in the following content.

Tab.5-2 Basic design parameters of the compound planetary gear train

| Stage | First stage Second stag | | | stage | | |
|--|----------------------------|-------|-------|----------|--------|-------|
| Component | S | P | R | S | P | R |
| Teeth, Z | 40 | 80 | 200 | 80 | 60 | 200 |
| Radius of pitch circle, R_i (mm) | 165.5 | 248.3 | 662.0 | 264.8 | 198.6 | 662.0 |
| Transverse contact ratio, ε_{α} (-) | 1.4882-1.5884 1.4938-1 | | | 4938-1.5 | 1.5282 | |
| Overlap ratio, ε_{β} (-) | 1.3452-1.3452 1.5694-1.569 | | | 694 | | |
| Overall contact ratio, ε_{γ} (-) | 2.8335-2.9336 3.0632-3.1 | | | 276 | | |
| Overall transmission ratio, $i(-)$ | 15 | | | | | |
| Dimensionless displacement, b_c (μ m) | 5 | | | | | |

Tab.5-3 The mesh phasing values of the two stages

| Stage | - | First s | tage | - | S | econ | d sta | ge |
|--|---|---------|------|---|---|------|-------|----|
| Sun-planet (φ_{spi}) | 0 | 1/3 | 2/3 | 0 | 0 | 0 | 0 | 0 |
| Ring-planet (φ_{rpi}) | 0 | -2/3 | -1/3 | 0 | 0 | 0 | 0 | 0 |
| Sun-planet <i>i</i> -ring (φ_{sr}) | | 0 | | | | 0 | | |

Tab.5-4 The values of some stiffness

| Parameter name | Value | Parameter name | Value |
|--------------------------------|----------------------|--------------------------------|----------------------|
| $k_{mspi}^{(1)}$, (N/m) | 2.28×10 ⁹ | $k_{mrpi}^{(1)}$, (N/m) | 2.57×10° |
| $k_{mspi}^{(2)}, (N/m)$ | 2.68×10 ⁹ | $k_{mrpi}^{(2)}$, (N/m) | 2.93×10° |
| $K_{rs}^{(1,2)}$, $(N.m/rad)$ | 1.0×10^{10} | $K_{cr}^{(1,2)}$, $(N.m/rad)$ | 1.0×10^{10} |

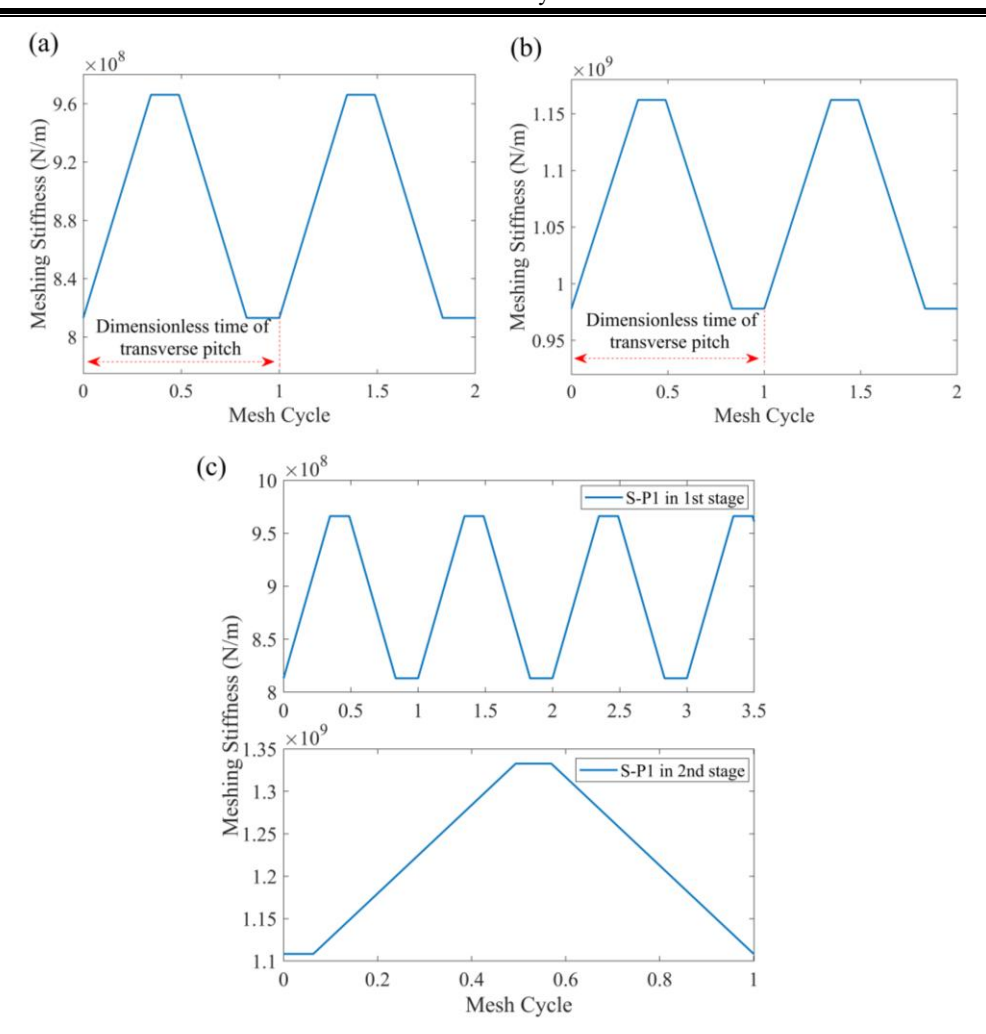


Fig.5-12 Meshing stiffness of (a) the external meshing gear pairs in first stage, (b) the internal meshing gear pairs in first stage, (c) the compared results for the meshing periods relationship in two stages

5.3.2 Influence of the damping ratio coefficient on the dynamic response

The bifurcation diagram is a diagram that allows researchers to visually view the vibration responses of a transmission system as the variation of the bifurcation factors such as speed, damping ratio coefficient. The damping ratio is a critical parameter to adjust the damping of the whole system, and it is crucial to analyze the impact of damping ratio on the dynamic response.

Fig.5-13 is the bifurcation diagram of the dimensionless displacement $\overline{\delta}_{rpi}^{(1)}$ of the two-stage compound planetary gear system, and the damping ratio ξ is the bifurcation parameter under the dimensionless excitation frequency of $\Omega_m^{(1)} = 3.96$,

dimensionless backlash of $\bar{b}=1$, and the initial conditions of $\bar{\delta}_{rpi}^{(1)}=0$, $\dot{\bar{\delta}}_{rpi}^{(1)}=0$. It can be seen from the Fig.5-13 that different vibration response condition including different motions changes with the damping ratio changes. Moreover, it is also concluded that the studied compound planetary gear train has an abundant nonlinear dynamic behavior because of the exist of the nonlinear factors such as meshing stiffness, meshing damping, and backlash. The bifurcation characteristics of other dimensionless meshing displacements have been obtained in the same way, and they have same variation tendency as the $\bar{\delta}_{rpi}^{(1)}$, and these plots are not presented for brevity.

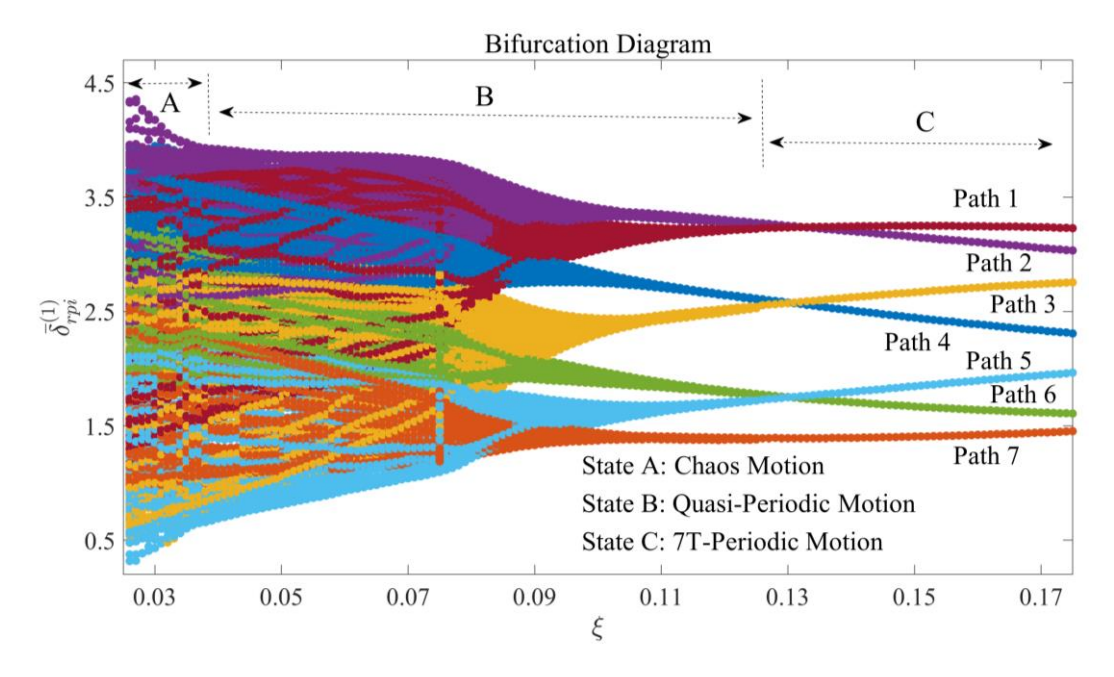


Fig.5-13 Bifurcation diagram for $\bar{\delta}_{rpi}^{(1)}$ versus $\xi = [0.026, 0.175]$ under 350 steady state periods. (To clearly distinguish references to color in this figure, the reader is referred to

the online version of this article)

Generally speaking, it is drawn that the bifurcation diagram can be divided into two kinds of state motion, periodic and non-periodic motion. Fig.5-13 mainly includes three regions marked by A, B and C by means of the state motion, which are chaos, quasi-periodic and 7T-periodic motion, respectively. From the Fig.5-13, it is very clear that there are 7 routes that gradually transition from chaos to stable periodic motion, and various law of each route is same, the reason why 7 routes appear will be explained in the following content.

Next, the specific vibration response and influence law of damping ratio coefficient on vibration response are analyzed and discussed based on the Fig.5-13.

The system presented a chaotic motion shown in Fig.5-13 when the damping coefficient at low values,i.e., $\xi \le 0.038$. Specifically, for instance, when $\xi = 0.026$, the whole system presented a chaos motion, marked as stage A in Fig.5-13, and the nonlinear characteristic diagrams such as Poincaré map, Phase trajectory and time history are shown in Fig.5-14. Fig.5-14(a) shows that the distribution of the points is haphazard, which illustrates a chaos motion. The phase trajectory in the phase trajectory shown in Fig.5-14(b) is disordered and fills the whole phase space, and it can be seen that the system experiences two meshing state shown as DC and CS region marked in Fig.5-14(b), including tooth contact separation, but the contact separation part is small. The phase trajectory in is disordered and fills the whole phase space. Correspondingly, Fig.5-14(c) shows that the curve is a very irregular fluctuation from one cycle to another cycle.

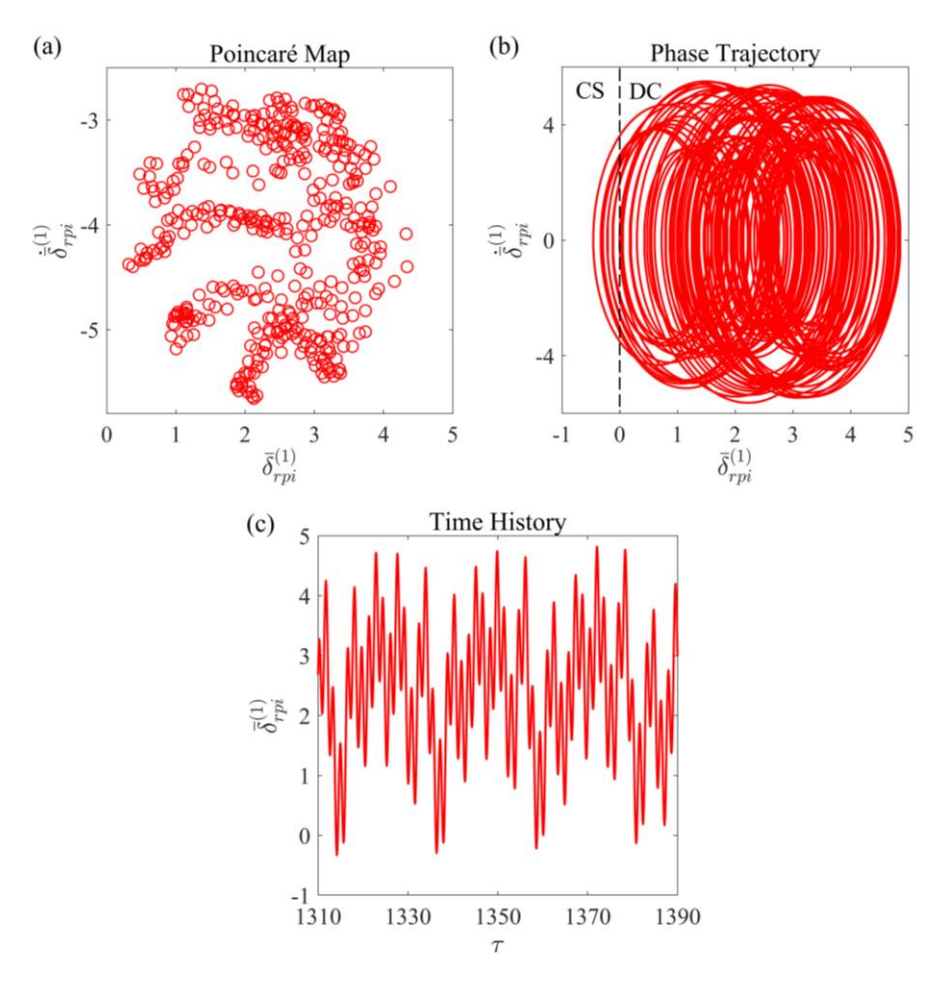


Fig. 5-14 The chaotic motion at $\xi = 0.026$: (a) the Poincaré map diagram, (b) the phase trajectory diagram, (c) the time history diagram.

The unstable quasi-periodic motion gradually changes to a stable quasi-periodic motion as the ξ increase between 0.039 and 0.125, i.e., $\xi \in [0.039, 0.125]$,

which is marked by B in Fig.5-13. The evolution of the entire process will be shown as the Fig.5-15 - Fig.5-17. It is seen from the Poincaré map shown in Fig.5-15(a) to Fig.5-17(a) that 7 relatively regular circles gradually form as the damping ratio coefficient ξ increases, and the dynamic behavior of the compound planetary gear system exhibits an obvious quasi-periodic motion. Moreover, although the vibration response results shown in Fig.5-15(c) to Fig.5-17(c) do not look exactly same, it can be drawn that them repeat themselves through every 14 waveforms, which is associated with 7 circles in Poincaré map. It also showed from time history diagram that the vibration response is complex. Correspondingly, Fig.5-15 (b) to Fig.5-17 (b) show that the phase diagram is getting clearer, and the tooth contact separation part (BC region showed as Fig.5-15 (b) to Fig.5-17 (b)) gradually become smaller and finally is zero, which shows that the meshing state of the system gradually becomes completely driveside contact as the damping ratio coefficient ξ further increases.

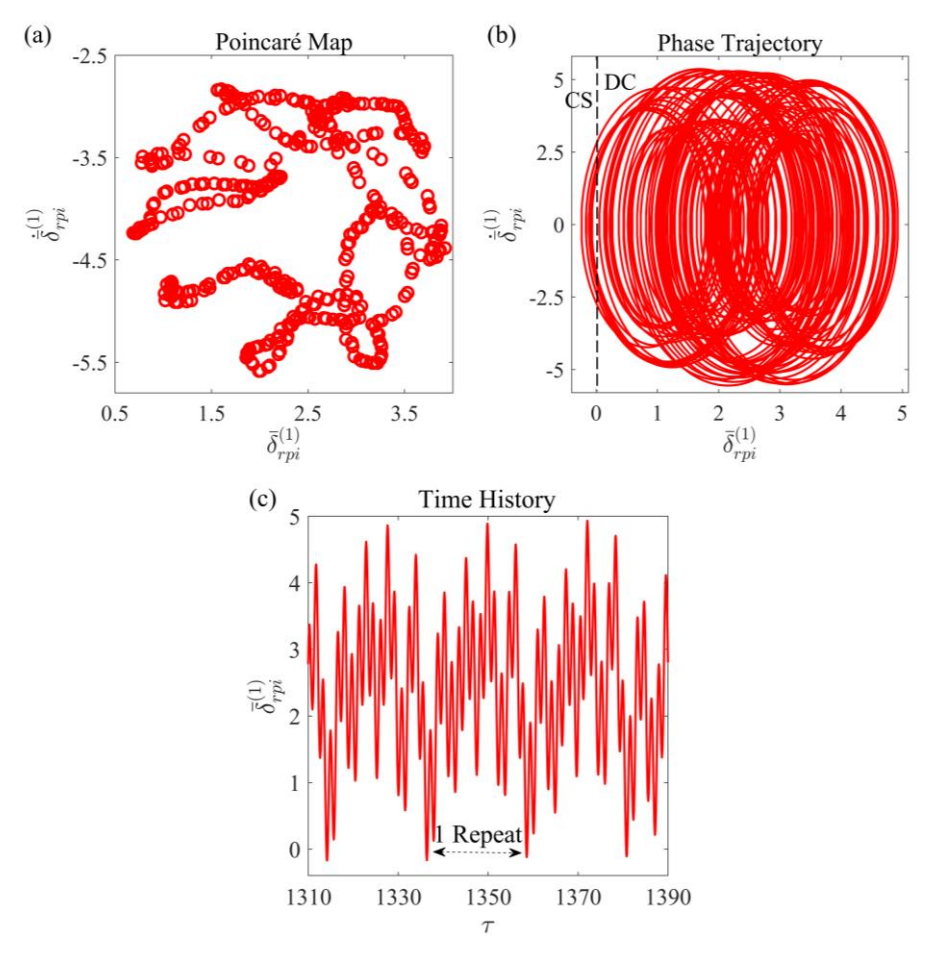


Fig.5-15 The chaotic motion at $\xi = 0.040$: (a) the Poincaré map diagram, (b) the phase trajectory diagram, (c) the time history diagram.

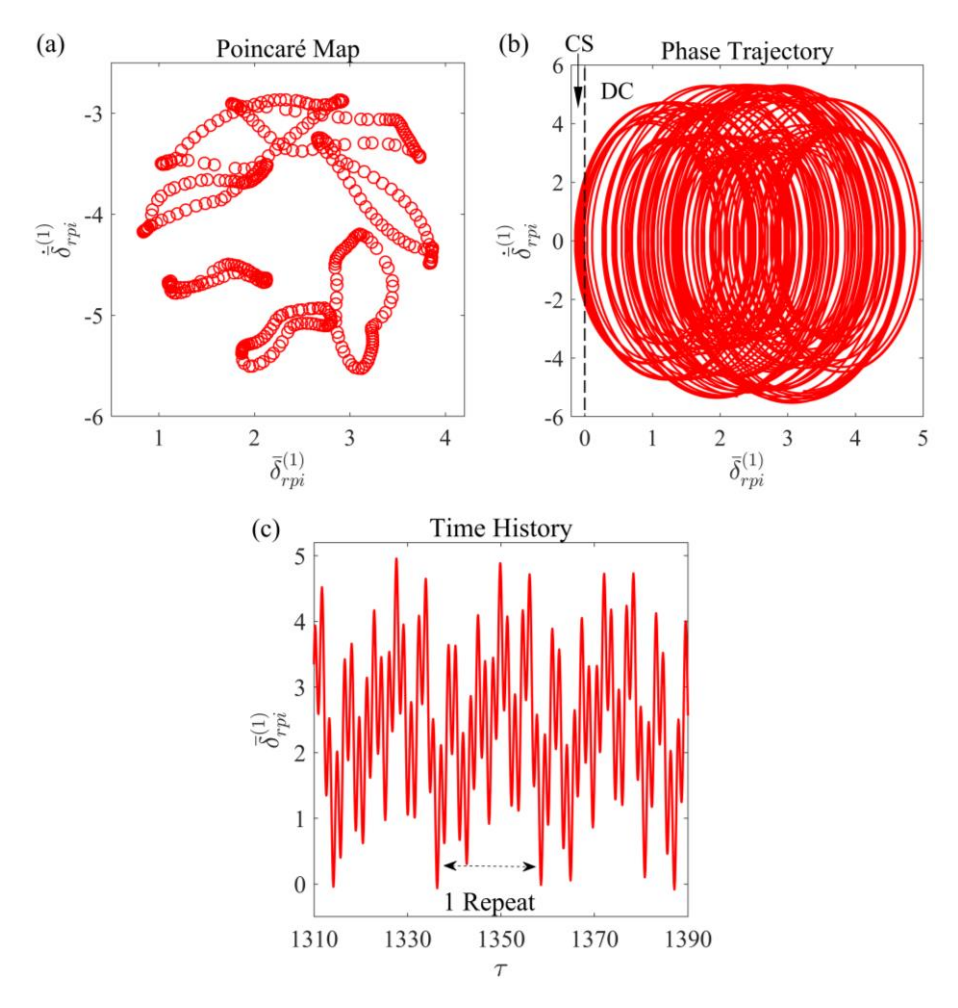


Fig. 5-16 The chaotic motion at $\xi = 0.051$: (a) the Poincaré map diagram, (b) the phase trajectory diagram, (c) the time history diagram.

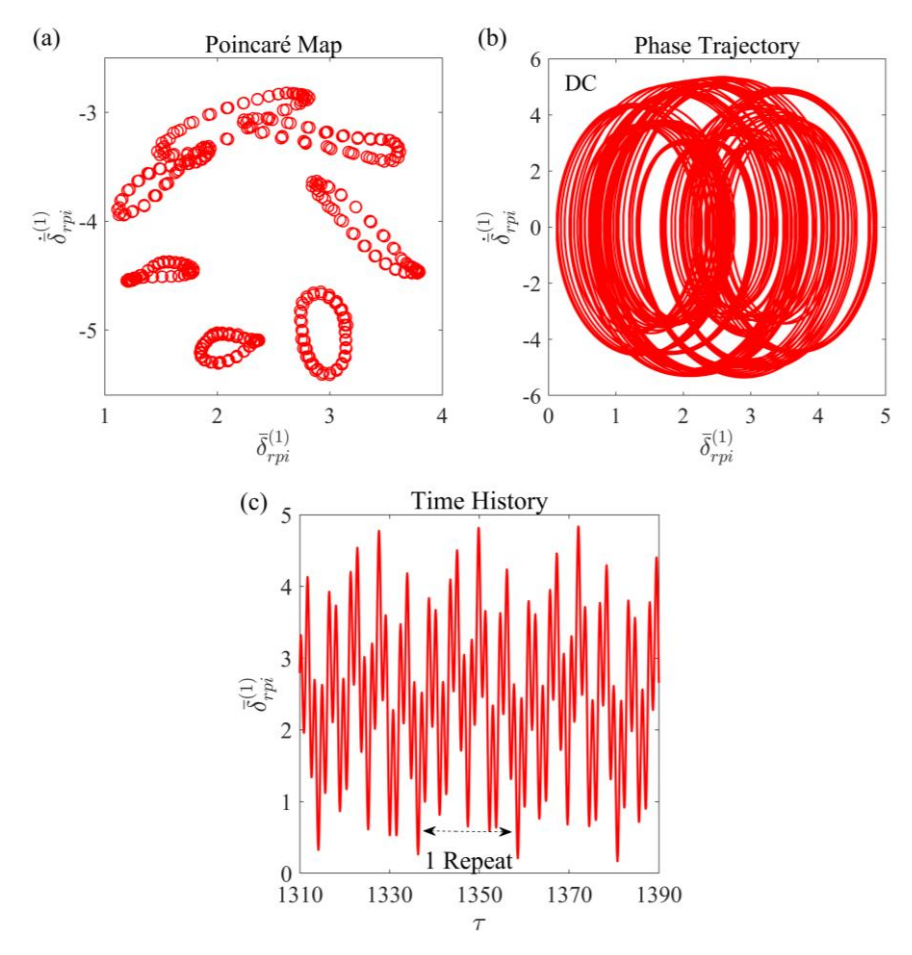


Fig.5-17 The chaotic motion at $\xi = 0.076$: (a) the Poincaré map diagram, (b) the phase trajectory diagram, (c) the time history diagram.

Sequentially, when the damping ratio coefficient ξ further continues to increase, the quasi-periodic motion becomes more and more obvious. For example, the numerical results are shown in Fig.5-18 when the damping ratio is 0.090, the time history diagram shown in Fig.5-18(c) showed that motion is an obvious quasi-periodic motion due to similar 7 times regular fluctuation but have differences between two adjacent repeat cycle. Comparing to the Fig.5-17(b), Fig.5-18(b) are similar to 7T-periodic motion, and every cycle is composed of many single circles. Moreover, it should be noted that the DC region only appears in Fig.5-17(b) and Figure Fig.5-18(b) proving that there is only one meshing state in the system, that is the drive-contact meshing state. It could be seen that Fig.5-18(a) includes seven sets of points, each set is composed of a finite number of points, as shown the detailed figure in Fig.5-18(a), which proved the quasi-periodic motion.

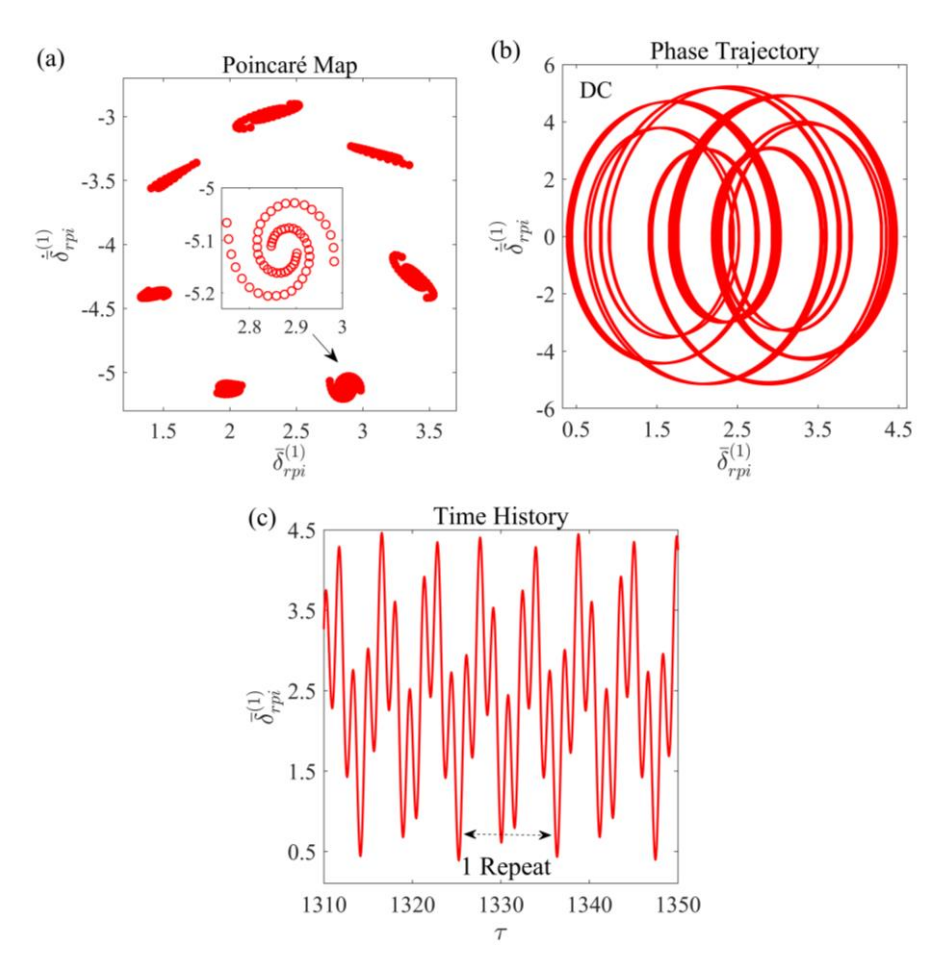


Fig. 5-18 The chaotic motion at $\xi = 0.090$: (a) the Poincaré map diagram, (b) the phase trajectory diagram, (c) the time history diagram.

Finally, for the damping ratio coefficient $\xi > 0.125$, The system starts to experience a stable state, i.e., 7T-periodic motion, as marked by C in Fig.5-13 until the damping ratio coefficient reaches 0.175. An exampled result is shown in Fig.5-19, in which the damping ratio coefficient is 0.151. As appeared in Fig.5-19(a) and Fig.5-19(b), there are 7 discrete points in the Poincaré map, and also 7 circles in the phase space. Moreover, the time history diagram indicates that the vibration response repeats itself every 7 periods, and the response result is almost same.

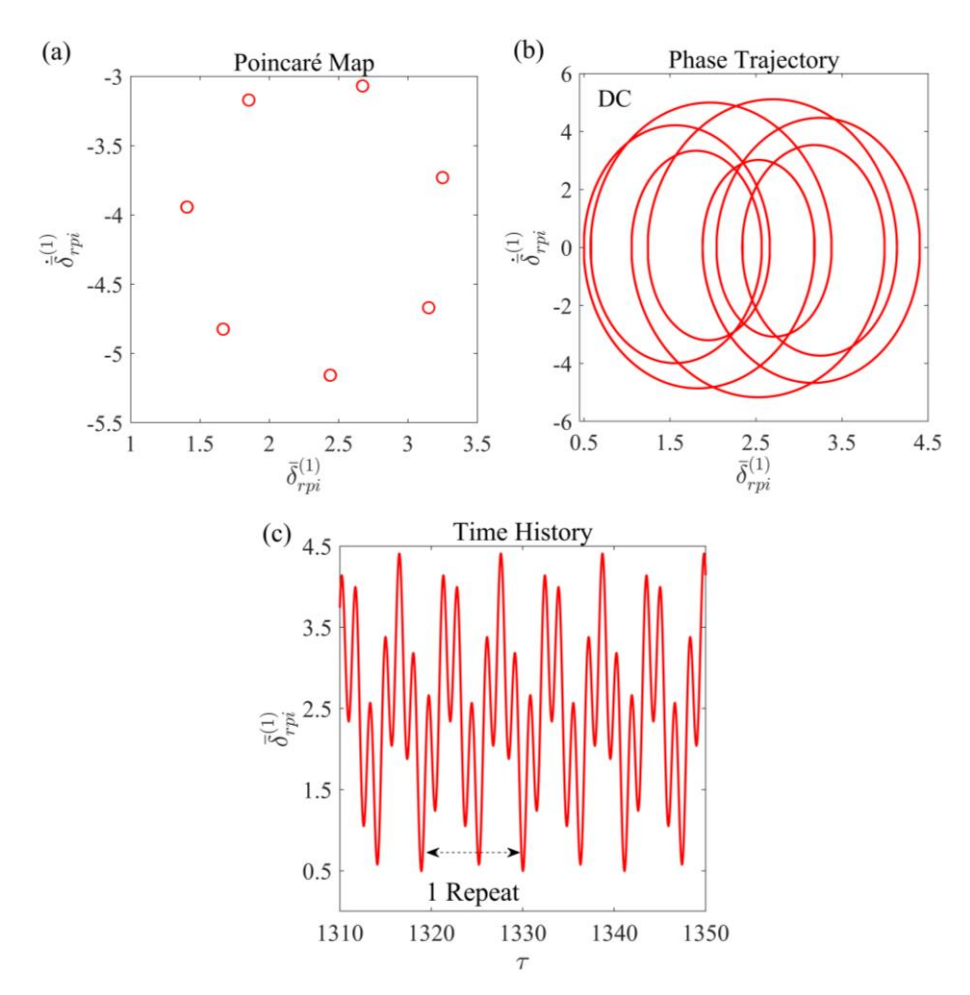


Fig. 5-19 The chaotic motion at $\xi = 0.151$: (a) the Poincaré map diagram, (b) the phase trajectory diagram, (c) the time history diagram.

It is found from the above bifurcation and corresponding diagrams that the final stable state motion is 7T-periodic motion, which corresponds to the seven paths shown in Fig.5-13, and the single periodic motion or 2T-periodic motion doesn't appear. At the same time, the quasi-periodic motion also is related to the 7T-periodic motion, in other word, the 7T-periodic motion is the most basic

motion state for the other motions.

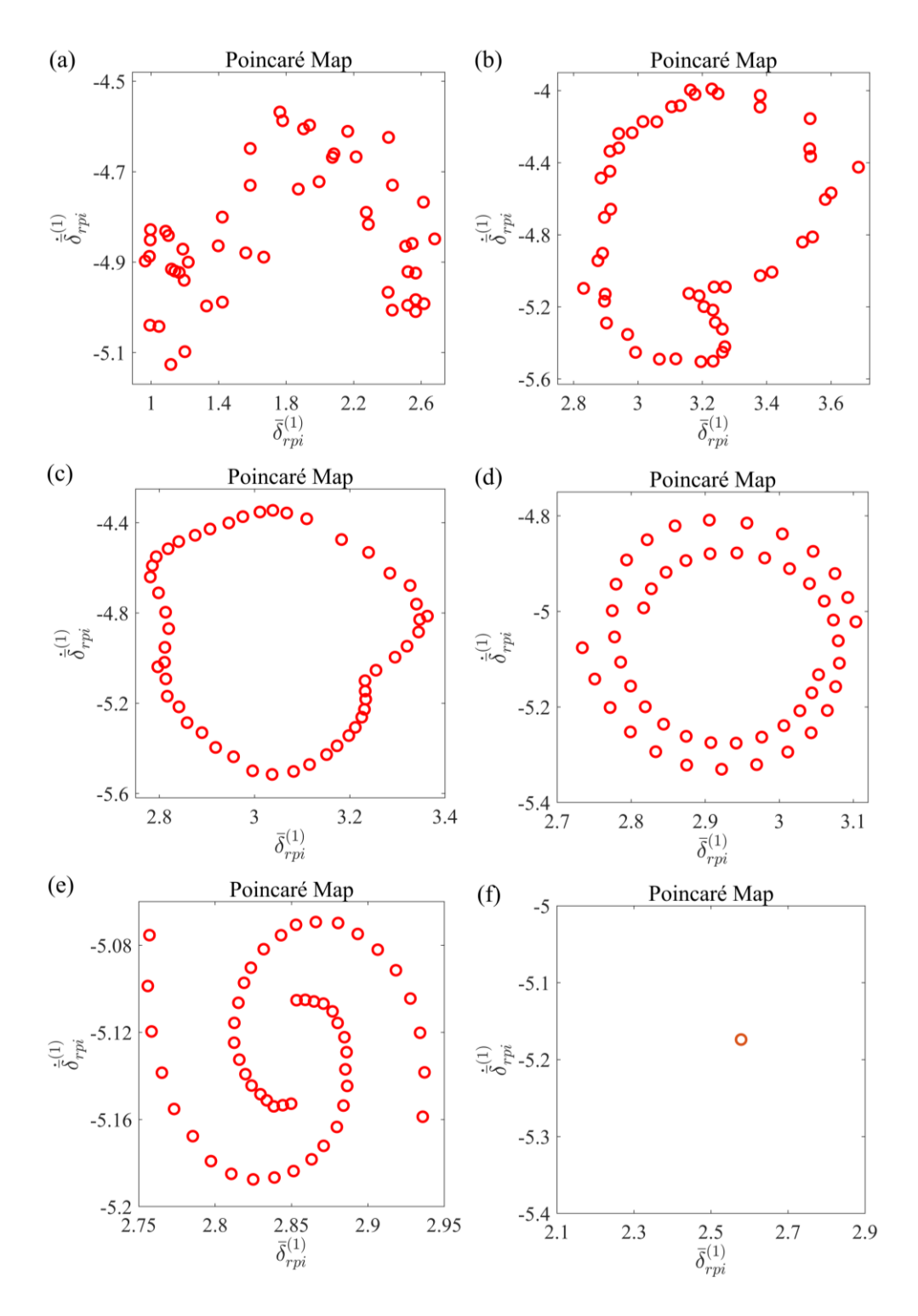


Fig.5-20 Poincaré map diagrams for $\bar{\delta}_{pi}^{(1)}$ versus ξ : (a) ξ =0.025, (b) ξ =0.039, (c) ξ =0.060,

(d) ξ =0.081, (e) ξ =0.093, (f) ξ =0.130.

The reason can be explained by using the meshing stiffness of two stages shown in Fig.5-12(c), because the excitation of the studied compound planetary gear system has two, and the meshing cycle of 2nd stage is 3.5 times of that of 1st stage, which means these two excitations want to return the same phase for the first time, the system must round 7 mesh cycles of the 1st stage, i.e., the lease common multiple(LCM) 7 = LCM(1,3.5). Therefore, the final basic stable motion is 7T-periodic motion, which is associated with the LCM(1,3.5). This understanding is important to the nonlinear behavior for the compound planetary gear system, and it could provide a basic understanding and guidance for the complex structural planetary gear system. Furthermore, by means of bifurcation, there are two main kinds of bifurcation ways, Doubling-Periodic and Hopf bifurcation. Fig.5-13 showed that the system experienced chaos, quasi-periodic and 7T-periodic motion, and Fig.5-20 presented the detailed Hopf bifurcation process from chaos to 7T-periodic motion through Poincaré map, and the Poincaré map of one path is only showed for brief. It is found from Fig.5-20 (a)-(c) that disorder unstable points became to a stable circle, which means that quasiperiodic motion forms. As the ξ increases, the stable circle broken, and gradually diverges inward, but it is still quasi-periodic motion only the ring became smaller shown as in Fig.5-20(d)-(e) until finally all the points come together, and then single periodic motion (i.e., 7T-periodic motion) is obtained.

Finally, it also could be drawn that the damping ratio coefficient ξ has an important influence on the nonlinear characteristics of the studied two stages compound planetary gear system.

5.3.3 Influence of damping ratio coefficient and input speed on the dynamic response

Compared to the common parameter, rotational speed, the value of the damping ratio coefficient ξ is fixed before designing a planetary gear system due to the gearbox structure. Combining the conclusion of damping ratio coefficient, and in order to choose the proper parameters of $\Omega_m^{(1)}$ and ξ , the influence of speed $\Omega_m^{(1)}$ and damping ratio coefficient ξ on the nonlinear dynamics is here jointly studied in this subsection. Fig.5-21 presents the corresponding three bifurcation diagrams with ξ =0.075, 0.100 and 0.125, respectively.

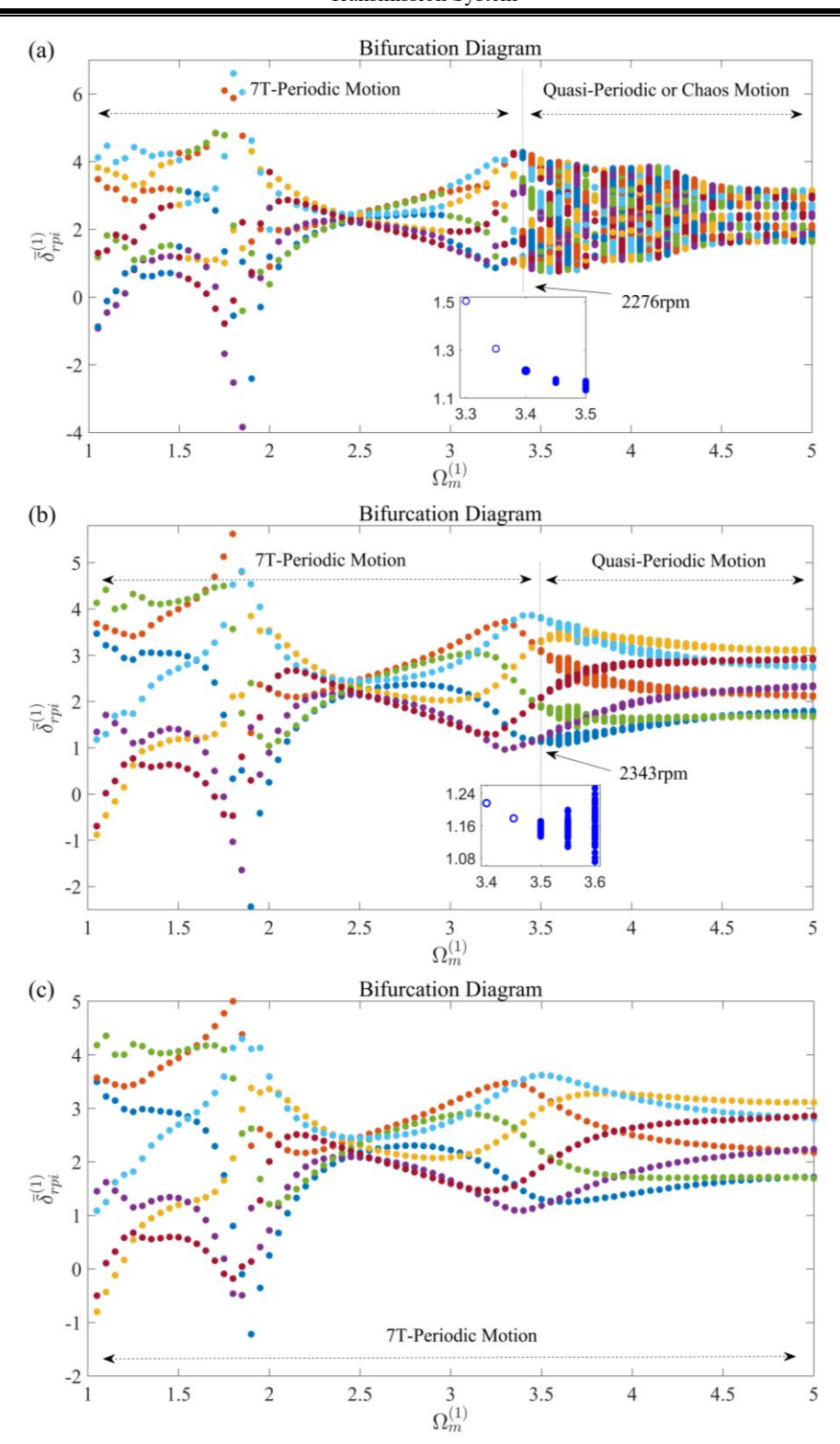


Fig.5-21 Bifurcation diagram for $\bar{\delta}_{pi}^{(1)}$ versus speed $\Omega_m^{(1)}$ with different ξ : (a) ξ =0.075, (b) ξ =0.100, (c) ξ =0.125.

By comparing Fig.5-21 (a)–(c), the results present that the stability of the studied two-stage compound planetary gear train exhibits an increasingly stable motion trend as the ξ increases. Specifically, when ξ increase from 0.075 to 0.1, the non-periodic motion (chaos or quasi-periodic motion) shown in Fig.5-21 (a) transfers to quasi-periodic motion in Fig.5-21 (b), and the bifurcation point between 7T-periodic motion and quasi-periodic motion also move from 2276rpm to 2343rpm, which increases the periodic region. If the ξ continues to change to 0.125, the whole dynamic response area completely becomes 7T-periodic motion (stable motion). In other words, unstable non-periodic motion disappears and more expected stable periodic motion appears. Moreover, Fig.5-21 also indicated that the maximum response amplitude ranges from [-3.86,6.6] to [-2.43,5.62] and finally to [-1.21,5] as ξ increases. Hence, it can be revealed that the nonlinear behavior of the studied compound planetary gear system is highly sensitive to the damping ratio coefficient ξ , and a higher value of damping ratio coefficient ξ on suppressing non-periodic motion and improving periodic motion is very useful. It is demonstrated that proper ξ can let the gear system have an expected narrow interval of the chaos motion, causing enhancing reliability and extending life time.

5.3.4 Influence of the meshing error amplitude on the dynamic response

Because the meshing error is composed of a series of errors, and the amplitude could be changed due to differences in manufacturing and assembly conditions. Fig.5-22 (a) is the bifurcation of the dimensionless displacement versus the meshing error amplitude, and Fig.5-22 (b) is the detailed drawing of the one path shown in Fig.5-22 (a).

It is seen that there are three motion states marked as A, B and C as the variation of the \bar{E} , which are 7T-periodic motion, 14T-periodic motion and quasi-periodic motion, respectively. The bifurcation way between state A and B is the doubling-periodic bifurcation, which is different to Hopf bifurcation.

It is also concluded from this study case that the motion starts to becomes non-periodic motion after \bar{E} reaches 2.5, the reason is that some teeth start to disengage as \bar{E} increases, causing the motion state to become complicated than steady periodic motion. Corresponding to Fig.5-22 (a), Poincaré map diagram and phase diagram representing the three motion states are shown in the Fig.5-23, respectively.

According to the results in Fig.5-22 and Fig.5-23, 7T-periodic, 14T-periodic and quasi-periodic motion are proved clearly. Furthermore, it is drawn from phase trajectory that the three meshing state shown as blue circle in Fig.5-11 when meshing error amplitude is greater than 1.2, and the DC region become smaller as the meshing error amplitude increases, indicating that the processing accuracy should be improved as far as possible to avoid tooth contact separation and so on.

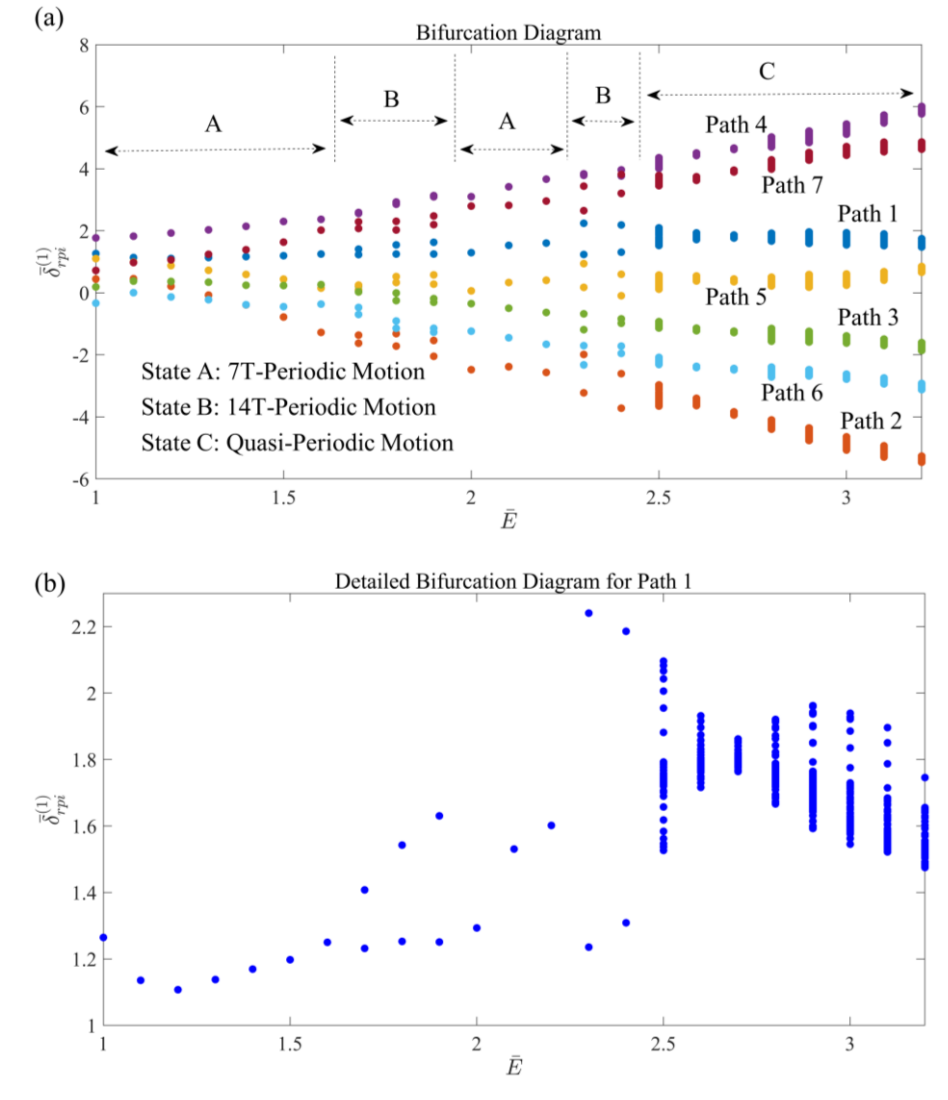


Fig.5-22 Bifurcation diagram for $\bar{\delta}^{(1)}_{rpi}$ versus meshing error amplitude \bar{E}

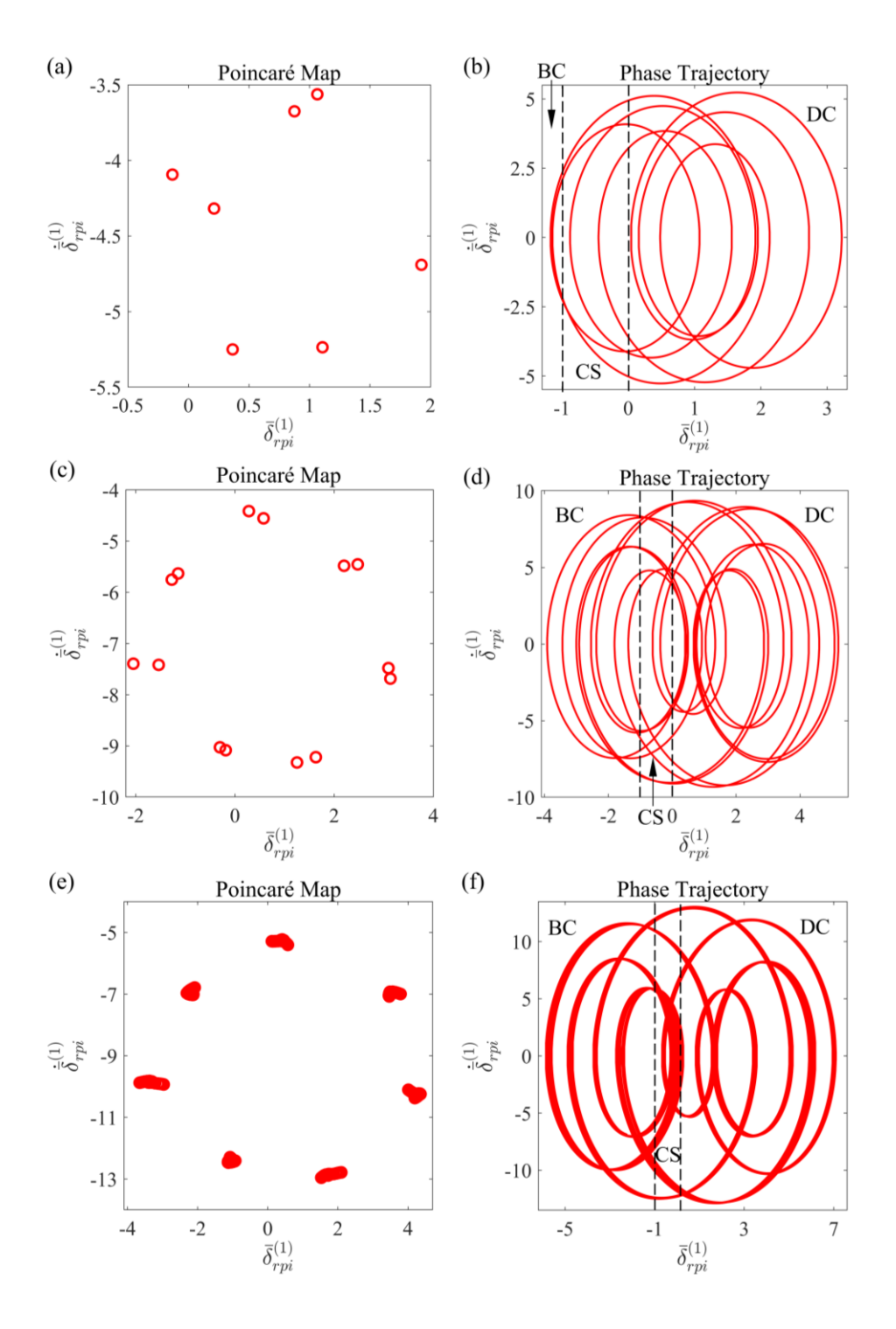


Fig.5-23 Poincaré map diagram and phase diagram for three states shown in Fig.5-22:

(a)(b)
$$\overline{E} = 1.2$$
, (c)(d) $\overline{E} = 1.9$, (e)(f) $\overline{E} = 2.5$

5.4 Translational-torsional nonlinear dynamic model

Based on the schematic diagrams of the dynamics models in Fig.2-11, Fig.2-12 and the pure torsion model in the previous subsection, this subsection develops a translational-torsional coupled multi-degree-of-freedom nonlinear dynamics model for this compound planetary gear system and analyses its nonlinear dynamics properties.

5.4.1 Relative displacement

In this study, the choice of coordinate system in the two-stage planetary gear system is still referred to the moving coordinate of first stage and fixed coordinate of the second level. Each component is modelled by considering three degrees of freedom, i.e., two lateral and one rotational degrees of freedom. The relative displacements of the interconnected components are still presented by a torsional stiffness, and the meshing displacements for S-P and R-P of the two stages are calculated as follows:

$$\begin{split} \delta_{spi}^{(1)} &= (x_s^{(1)} \sin \psi_{spi}^{(1)} + y_s^{(1)} \cos \psi_{spi}^{(1)} - \xi_{pi}^{(1)} \sin \alpha_{sp}^{(1)} - \eta_{pi}^{(1)} \cos \alpha_{sp}^{(1)} \\ &+ R_{bs}^{(1)} \theta_{zs}^{(1)} + R_{bpi}^{(1)} \theta_{zpi}^{(1)} - R_{bc}^{(1)} \theta_{zc}^{(1)}) \cos \beta_b^{(1)} - e_{spi}^{(1)}(t) \\ \delta_{rpi}^{(1)} &= (y_r^{(1)} \cos \psi_{rpi}^{(1)} - x_r^{(1)} \sin \psi_{rpi}^{(1)} + \xi_{pi}^{(1)} \sin \alpha_{rp}^{(1)} - \eta_{pi}^{(1)} \cos \alpha_{rp}^{(1)} \\ &+ R_{br}^{(1)} \theta_{zr}^{(1)} - R_{bpi}^{(1)} \theta_{zpi}^{(1)} - R_{bc}^{(1)} \theta_{zc}^{(1)}) \cos \beta_b^{(1)} - e_{rpi}^{(1)}(t) \\ \delta_{spi}^{(2)} &= (x_s^{(2)} \sin \psi_{spi}^{(2)} - y_s^{(2)} \cos \psi_{spi}^{(2)} - \xi_{pi}^{(2)} \sin \alpha_{sp}^{(2)} + \eta_{pi}^{(2)} \cos \alpha_{sp}^{(2)} \\ &- R_{bs}^{(2)} \theta_{zs}^{(2)} - R_{bpi}^{(2)} \theta_{zpi}^{(2)}) \cos \beta_b^{(2)} - e_{spi}^{(2)}(t) \\ \delta_{rpi}^{(2)} &= (-y_r^{(2)} \cos \psi_{rpi}^{(2)} - x_r^{(2)} \sin \psi_{rpi}^{(2)} + \xi_{pi}^{(2)} \sin \alpha_{rp}^{(2)} + \eta_{pi}^{(2)} \cos \alpha_{rp}^{(2)} \\ &- R_{br}^{(2)} \theta_{zr}^{(2)} + R_{bpi}^{(2)} \theta_{zpi}^{(2)}) \cos \beta_b^{(2)} - e_{rpi}^{(2)}(t) \end{split}$$

where the formulae for the angles, etc. shown in Equation (5-20) are as defined in Chapter 2.

The relative displacements of the carrier with its pin on the planet i in the radial and tangential directions of the planet gear are:

$$\delta_{cpix}^{(1)} = \xi_{pi}^{(1)} - x_c^{(1)} \cos \phi_{pi}^{(1)} - y_c^{(1)} \sin \phi_{pi}^{(1)}$$

$$\delta_{cpiy}^{(1)} = \eta_{pi}^{(1)} + x_c^{(1)} \sin \phi_{pi}^{(1)} - y_c^{(1)} \cos \phi_{pi}^{(1)}$$
(5-21)

where R_c is the distance from the centre of the planet carrier pin to the centre of the planet carrier.

Also, the relative angular displacements between the connecting parts in the

two stages system are shown below:

$$\delta_{cr}^{(1,2)} = u_c^{(1)} / R_{bc}^{(1)} - u_r^{(2)} / R_{br}^{(2)}$$

$$\delta_{rs}^{(1,2)} = u_r^{(1)} / R_{br}^{(1)} - u_s^{(2)} / R_{bs}^{(2)}.$$
(5-22)

5.4.2 Equation of motion

The translational-torsional coupled dynamics model of this studied gear system is established based on the force equilibrium relationship. The general displacement vectors of the system are shown below:

$$\mathbf{q} = \begin{cases} x_s^{(1)}, y_s^{(1)}, u_s^{(1)}, x_r^{(1)}, y_r^{(1)}, u_r^{(1)}, x_c^{(1)}, y_c^{(1)}, u_c^{(1)}, x_{pi}^{(1)}, y_{pi}^{(1)}, u_{pi}^{(1)}, \\ x_s^{(2)}, y_s^{(2)}, u_s^{(2)}, x_r^{(2)}, y_r^{(2)}, u_r^{(2)}, x_{pi}^{(2)}, y_{pi}^{(2)}, u_{pi}^{(2)}, \\ \end{cases}$$
(5-23)

Finally, the set of dynamic equations for the whole system is shown below:

(1) Sun gear in first stage:

$$m_{s}^{(1)}(\ddot{x}_{s}^{(1)} - 2\omega_{c}^{(1)}\dot{y}_{s}^{(1)} - \omega_{c}^{(1)2}x_{s}^{(1)}) + \sum_{i=1}^{n} F_{spi}^{(1)}a_{1i} + F_{bsx} = F_{gsx}^{(1)}$$

$$m_{s}^{(1)}(\ddot{y}_{s}^{(1)} + 2\omega_{c}^{(1)}\dot{x}_{s}^{(1)} - \omega_{c}^{(1)2}y_{s}^{(1)}) + \sum_{i=1}^{n} F_{spi}^{(1)}a_{2i} + F_{bsy} = F_{gsy}^{(1)}$$

$$M_{se}^{(1)}\ddot{u}_{s} + a_{3}\sum_{i=1}^{n} F_{spi}^{(1)} = (T_{in}/R_{bs}^{(1)})$$
(5-24)

(2) Ring gear in first stage:

$$m_r^{(1)}(\ddot{x}_r^{(1)} - 2\omega_c^{(1)}\dot{y}_r^{(1)} - \omega_c^{(1)2}x_r^{(1)}) - \sum_{i=1}^n F_{rpi}^{(1)}a_{8i} + F_{brx}^{(1)} = F_{bgx}^{(1)}$$

$$m_r^{(1)}(\ddot{y}_r^{(1)} + 2\omega_c^{(1)}\dot{x}_r^{(1)} - \omega_c^{(1)2}y_r^{(1)}) + \sum_{i=1}^n F_{rpi}^{(1)}a_{9i} + F_{bry}^{(1)} = F_{bgy}^{(1)}$$

$$M_{re}^{(1)}\ddot{u}_r^{(1)} + a_3\sum_{i=1}^n F_{rpi}^{(1)} + (1/R_{br}^{(1)})K_{rs}^{(1,2)}\delta_{rs}^{(1,2)} = 0$$
(5-25)

(3) Planet gear in first stage:

$$m_{pi}^{(1)}(\ddot{\xi}_{pi}^{(1)} - 2\omega_{c}^{(1)}\dot{\eta}_{pi}^{(1)} - \omega_{c}^{(1)2}\xi_{pi}^{(1)}) + (-a_{4}F_{spi}^{(1)} + a_{6}F_{rpi}^{(1)}) + F_{bpx}^{(1)} = F_{gpix}^{(1)} + F_{cpi}^{(1)}$$

$$m_{pi}^{(1)}(\ddot{\eta}_{pi}^{(1)} + 2\omega_{c}^{(1)}\dot{\xi}_{pi}^{(1)} - \omega_{c}^{(1)2}\eta_{pi}^{(1)}) + (-a_{5}F_{spi}^{(1)} - a_{7}F_{rpi}^{(1)}) + F_{bpy}^{(1)} = F_{gpiy}^{(1)}$$

$$M_{pi}^{(1)}\ddot{u}_{pi}^{(1)} + a_{3}(F_{spi}^{(1)} - F_{pi}^{(1)}) = 0$$

$$(5-26)$$

(4) Carrier in first stage:

$$\begin{split} & m_c^{(1)}(\ddot{x}_c^{(1)} - 2\omega_c^{(1)}\dot{y}_c^{(1)} - \omega_c^{(1)2}x_c^{(1)}) + \sum_{i=1}^n (-F_{bpx}^{(1)} \, \mathrm{c} \, \phi_{pi}^{(1)} + F_{bpy}^{(1)} \, \mathrm{s} \, \phi_{pi}^{(1)}) + F_{bcx}^{(1)} = F_{gcx}^{(1)} \\ & m_c^{(1)}(\ddot{y}_c^{(1)} + 2\omega_c^{(1)}\dot{x}_c^{(1)} - \omega_c^{(1)2}y_c^{(1)}) + \sum_{i=1}^n (-F_{bpx}^{(1)} \, \mathrm{s} \, \phi_{pi}^{(1)} - F_{bpy}^{(1)} \, \mathrm{c} \, \phi_{pi}^{(1)}) + F_{bcy}^{(1)} = F_{gcy}^{(1)} \quad (5-27) \\ & M_{ce}^{(1)}\ddot{u}_c^{(1)} - (R_c^{(1)} / R_{bc}^{(1)}) \sum_{i=1}^n F_{bpy}^{(1)} + (1/R_{bc}^{(1)}) K_{cr}^{(1,2)} \delta_{cr}^{(1,2)} = 0 \end{split}$$

(5) Sun gear in second stage:

$$m_s^{(2)} \ddot{x}_s^{(2)} + \sum_{i=1}^m F_{spi}^{(2)} a_{10i} + F_{bsx}^{(2)} = 0$$

$$m_s^{(2)} \ddot{y}_s^{(2)} - \sum_{i=1}^m F_{spi}^{(2)} a_{11i} + F_{bsy}^{(2)} = F_{gs}^{(2)}$$

$$M_{se}^{(2)} \ddot{u}_s^{(2)} - a_{12} \sum_{i=1}^m F_{spi}^{(2)} - (1/R_{bs}^{(2)}) K_{rs}^{(1,2)} \delta_{rs}^{(1,2)} = 0$$
(5-28)

(6) Ring gear in second stage:

$$\begin{split} & m_r^{(2)} \ddot{x}_r^{(2)} - \sum_{i=1}^m F_{rpi}^{(2)} a_{17i} + F_{brx}^{(2)} = 0 \\ & m_r^{(2)} \ddot{y}_r^{(2)} - \sum_{i=1}^m F_{rpi}^{(2)} a_{18i} + F_{bry}^{(2)} = F_{gr}^{(2)} \\ & M_{re}^{(2)} \ddot{u}_r^{(2)} - a_{12} \sum_{i=1}^m F_{rpi}^{(2)} - (1/R_{br}^{(2)}) K_{cr}^{(1,2)} \delta_{cr}^{(1,2)} = (-T_{out}/R_{br}^{(2)}) \end{split}$$
(5-29)

(7) Planet gear in second stage:

$$m_{pi}^{(2)} \ddot{\xi}_{pi}^{(2)} + (-a_{13}F_{spi}^{(2)} + a_{15}F_{rpi}^{(2)}) + F_{bpix}^{(2)} = F_{gpix}^{(2)}$$

$$m_{pi}^{(2)} \ddot{\eta}_{pi}^{(2)} + (+a_{14}F_{spi}^{(2)} + a_{16}F_{rpi}^{(2)}) + F_{bpiy}^{(2)} = F_{gpiy}^{(2)}$$

$$M_{pie}^{(2)} \ddot{u}_{pi}^{(2)} + a_{12}(F_{rpi}^{(2)} - F_{spi}^{(2)}) = 0$$
(5-30)

where, in the above equation, the expressions for the engagement force and other symbols are shown below:

$$\begin{cases} F_{jpi}^{(k)} = k_{jpi}^{(k)} \delta_{jpi}^{(k)} + c_{jpi}^{(k)} \dot{\delta}_{jpi}^{(k)} \\ F_{bpn}^{(1)} = k_{bp}^{(1)} \delta_{cpin}^{(1)} + c_{bp}^{(1)} \dot{\delta}_{cpin}^{(1)} \\ F_{bjn}^{(1)} = k_{bj}^{(1)} \delta_{cpin}^{(1)} + c_{bj}^{(1)} \dot{\delta}_{cpin}^{(1)} \\ F_{bjn}^{(k)} = k_{bj}^{(1)} n_j^{(k)} + c_{bj}^{(k)} \dot{n}_j^{(k)} \\ F_{gix}^{(1)} = -m_j^{(1)} g \cdot \sin(\omega_c^{(1)} t) \\ F_{giy}^{(1)} = -m_j^{(1)} g \cdot \cos(\omega_c^{(1)} t) \\ F_{giy}^{(2)} = -m_j^{(2)} g \\ F_{giy}^{(2)} = -m_j^{(2)} g \\ F_{giy}^{(1)} = -m_j^{(1)} g \cdot \sin(\omega_c^{(1)} t + 2\pi (i - 1) / n_p), \\ F_{gpiy}^{(1)} = -m_j^{(1)} g \cdot \cos(\omega_c^{(1)} t + 2\pi (i - 1) / n_p), \\ F_{gpiy}^{(1)} = -m_j^{(2)} g \cdot \sin(\omega_c^{(1)} t + 2\pi (i - 1) / n_p), \\ F_{gpiy}^{(2)} = -m_{pi}^{(2)} g \cdot \sin(\omega_c^{(2)} t), F_{gpiy}^{(2)} = -m_{pi}^{(2)} g \cdot \cos(\omega_c^{(2)} t), F_{cpi}^{(1)} = m_{pi}^{(1)} R_c^{(1)} \omega_c^{(1)} 2, \\ g_{pix}^{(1)} = \sin \phi_{pi}^{(1)}, c \phi_{pi}^{(1)} = \cos \phi_{pi}^{(1)}, a_{1i} = \cos(\beta_b^{(1)}) \sin \psi_{spi}^{(1)}, a_{2i} = \cos(\beta_b^{(1)}) \cos \psi_{spi}^{(1)}, \\ a_3 = \cos(\beta_b^{(1)}), a_4 = \cos(\beta_b^{(1)}) \sin \alpha_{sp}^{(1)}, a_5 = \cos(\beta_b^{(1)}) \cos \alpha_{sp}^{(1)}, \\ a_6 = \cos(\beta_b^{(1)}) \sin \alpha_{rp}^{(1)}, a_{7} = \cos(\beta_b^{(1)}) \cos \alpha_{rp}^{(1)}, a_{8i} = \cos(\beta_b^{(1)}) \sin \psi_{rpi}^{(1)}, \\ a_{9i} = \cos(\beta_b^{(1)}) \cos \psi_{rpi}^{(1)}, a_{10i} = \cos(\beta_b^{(2)}) \sin \psi_{spi}^{(2)}, a_{11i} = \cos(\beta_b^{(2)}) \cos \psi_{spi}^{(2)}, \\ a_{12} = \cos(\beta_b^{(2)}), a_{13} = \cos(\beta_b^{(2)}) \sin \alpha_{rp}^{(2)}, a_{16} = \cos(\beta_b^{(1)}) \cos \alpha_{rp}^{(2)}, \\ a_{17i} = \cos(\beta_b^{(2)}) \sin \psi_{rpi}^{(2)}, a_{18i} = \cos(\beta_b^{(2)}) \cos \psi_{rpi}^{(2)}. \end{cases}$$

5.4.3 Dimensionless equations of motion

Due to the presence of relative displacements in the above modelling process, the equations of motion for each of the above components are semi-positive definite, so some torsional relative displacements are first defined based on the pure torsional dynamics model and these torsional displacement variables are defined as follows:

$$\begin{cases} U_{spi}^{(1)} = (u_s^{(1)} + u_{pi}^{(1)} - u_c^{(1)}) \cos \beta_b^{(1)} - e_{spi}^{(1)} \\ U_{rpi}^{(1)} = U_{src}^{(1)} - U_{spi}^{(1)} - e_{spi}^{(1)} - e_{rpi}^{(1)} \\ U_{src}^{(1)} = (u_s^{(1)} + u_r^{(1)} - 2u_c^{(1)}) \cos \beta_b^{(1)} \\ U_{spi}^{(2)} = (-u_s^{(2)} - u_{pi}^{(2)}) \cos \beta_b^{(2)} - e_{spi}^{(2)} \\ U_{rpi}^{(2)} = U_{sr}^{(2)} - U_{spi}^{(2)} - e_{spi}^{(2)} - e_{rpi}^{(2)} \\ U_{sr}^{(2)} = (-u_s^{(2)} - u_r^{(2)}) \cos \beta_b^{(2)} \\ U_{rs}^{(2)} = (-u_s^{(2)} - u_r^{(2)}) \cos \beta_b^{(2)} \\ U_{rs}^{(1,2)} = u_r^{(1)} - (R_{br}^{(1)} / R_{bs}^{(2)}) u_s^{(2)} \\ U_{cr}^{(1,2)} = u_c^{(1)} - (R_{bc}^{(1)} / R_{br}^{(2)}) u_s^{(2)} \end{cases}$$

Therefore, the above relative torsional displacements are introduced into the generalised coordinates of equation (5-23), along with the displacement scale parameter b_c and the time parameter $\tau=\omega_d t$, both of which are defined in the same way as in the purely torsional nonlinear model, thus transforming the generalised coordinates dimensionlessly, and hence the new generalised displacement vector obtained is shown below:

$$\overline{\mathbf{q}} = \begin{cases} \overline{x}_{s}^{(1)}, \overline{y}_{s}^{(1)}, \overline{x}_{r}^{(1)}, \overline{y}_{r}^{(1)}, \overline{x}_{c}^{(1)}, \overline{y}_{c}^{(1)}, \overline{\xi}_{pi}^{(1)}, \overline{\eta}_{pi}^{(1)}, \overline{U}_{spi}^{(1)}, \overline{U}_{src}^{(1)}, \\ \overline{x}_{s}^{(2)}, \overline{y}_{s}^{(2)}, \overline{x}_{r}^{(2)}, \overline{y}_{r}^{(2)}, \overline{\xi}_{pi}^{(2)}, \overline{\eta}_{pi}^{(2)}, \overline{U}_{spi}^{(2)}, \overline{U}_{sr}^{(2)}, \overline{U}_{rs}^{(1,2)}, \overline{U}_{cr}^{(1,2)} \end{cases} \end{cases}^{T}$$

$$(5-32)$$

Based on the new generalised coordinates and the set of kinetic equations for each component, the dimensionless form of the kinetic equations for the new translational-torsional model is shown below:

(1) Dimensionless equations for the sun in first stage in the support direction:

$$\ddot{\bar{x}}_{s}^{(1)} = 2\Omega_{cd}\dot{\bar{y}}_{s}^{(1)} + \Omega_{cd}^{2}\bar{x}_{s}^{(1)} - \sum_{i=1}^{n} a_{1i}\bar{F}_{spi-s}^{(1)}
-\bar{F}_{bs-sx}^{(1)} + \bar{F}_{gs}\sin(\Omega_{cd}\tau)
\ddot{\bar{y}}_{s}^{(1)} = -2\Omega_{cd}\dot{\bar{x}}_{s}^{(1)} + \Omega_{cd}^{2}\bar{y}_{s}^{(1)} - \sum_{i=1}^{n} a_{2i}\bar{F}_{spi-s}^{(1)}
-\bar{F}_{bs-sy}^{(1)} + \bar{F}_{gs}\cdot\cos(\Omega_{cd}\tau)$$
(5-33)

(2) Dimensionless equations for the ring in first stage in the support direction:

$$\ddot{\bar{x}}_{r}^{(1)} = 2\Omega_{cd}\dot{\bar{y}}_{r}^{(1)} + \Omega_{cd}^{2}\bar{x}_{r}^{(1)} + \sum_{i=1}^{n} a_{8i}\bar{F}_{rpi-r}^{(1)} - \bar{F}_{br-rx}^{(1)} + \bar{F}_{gr}\cdot\sin(\Omega_{cd}\tau)$$

$$\ddot{\bar{y}}_{r}^{(1)} = -2\Omega_{cd}\dot{\bar{x}}_{r}^{(1)} + \Omega_{cd}^{2}\bar{\bar{y}}_{r}^{(1)} - \sum_{i=1}^{n} a_{9i}\bar{F}_{rpi-r}^{(1)} - \bar{F}_{br-ry}^{(1)} + \bar{F}_{gr}\cdot\cos(\Omega_{cd}\tau)$$

$$(5-34)$$

(3) Dimensionless equations for the planet in first stage in the support direction:

$$\begin{split} \ddot{\xi}_{pi}^{(1)} &= 2\Omega_{cd}\dot{\bar{\eta}}_{pi}^{(1)} + \Omega_{cd}^{2}\bar{\xi}_{pi}^{(1)} + a_{4}\bar{F}_{spi-p}^{(1)} - a_{6}\bar{F}_{rpi-p}^{(1)} - \bar{F}_{bp-px}^{(1)} \\ &+ \bar{F}_{gpi}^{(1)} \cdot \sin(\Omega_{cd}\tau + \phi_{pi}^{(1)}) + F_{cpi}^{(1)} \\ \ddot{\bar{\eta}}_{pi}^{(1)} &= -2\Omega_{cd}\dot{\bar{\xi}}_{pi}^{(1)} + \Omega_{cd}^{2}\bar{\eta}_{pi}^{(1)} + a_{5}\bar{F}_{spi-p}^{(1)} + a_{7}\bar{F}_{rpi-p}^{(1)} - \bar{F}_{bp-py}^{(1)} \\ &+ \bar{F}_{gpi}^{(1)} \cdot \cos(\Omega_{cd}\tau + \phi_{pi}^{(1)}) \end{split} \tag{5-35}$$

(4) Dimensionless equations for the carrier in first stage in the support direction:

$$\ddot{\bar{x}}_{c}^{(1)} = 2\Omega_{cd}\dot{\bar{y}}_{c}^{(1)} + \Omega_{cd}^{2}\bar{x}_{c}^{(1)} + \sum_{i=1}^{n} (\bar{F}_{cp-cx}^{(1)} c \phi_{pi}^{(1)} - \bar{F}_{cp-cy}^{(1)} s \phi_{pi}^{(1)})
- \bar{F}_{bc-cx}^{(1)} + \bar{F}_{gc}^{(1)} \cdot \sin(\Omega_{cd}\tau)
\ddot{\bar{y}}_{c}^{(1)} = -2\Omega_{cd}\dot{\bar{x}}_{c}^{(1)} + \Omega_{cd}^{2}\bar{\bar{y}}_{c}^{(1)} + \sum_{i=1}^{n} (\bar{F}_{cp-cx}^{(1)} s \phi_{pi}^{(1)} + \bar{F}_{cp-cy}^{(1)} c \phi_{pi}^{(1)})
- \bar{F}_{bc-cy}^{(1)} + \bar{F}_{gc}^{(1)} \cdot \cos(\Omega_{cd}\tau)$$
(5-36)

(5) Dimensionless equations for relative torsional displacements in the first stage:

$$\ddot{\overline{U}}_{spi}^{(1)} = (a_3 / M_{se}^{(1)})(\overline{T}_{in} / R_{bs}^{(1)}) - (a_3^2 / M_{se}^{(1)}) \sum_{i=1}^{n} \overline{F}_{spi}^{(1)} - (a_3^2 / M_{pie}^{(1)})(\overline{F}_{spi}^{(1)} - \overline{F}_{rpi}^{(1)})
- (a_3 / M_{ce}^{(1)})(R_c^{(1)} / R_{bc}^{(1)}) \sum_{i=1}^{n} \overline{F}_{bp}^{(1)} + (1 / R_{bc}^{(1)2})(a_3 / M_{ce}^{(1)}) \overline{K}_{cr}^{(1,2)} \overline{U}_{cr}^{(1,2)}
- \ddot{\overline{e}}_{spi}^{(1)}(t)
\ddot{\overline{U}}_{src}^{(1)} = (a_3 / M_{se}^{(1)})(\overline{T}_{in} / R_{bs}^{(1)}) - (a_3^2 / M_{se}^{(1)}) \sum_{i=1}^{n} \overline{F}_{spi}^{(1)} - (a_3^2 / M_{re}^{(1)}) \sum_{i=1}^{n} \overline{F}_{rpi}^{(1)}
- (1 / R_{br}^{(1)2})(a_3 / M_{re}^{(1)}) \overline{K}_{rs}^{(1,2)} \overline{U}_{cr}^{(1,2)} - (2a_3 / M_{ce}^{(1)})(R_c^{(1)} / R_{bc}^{(1)}) \sum_{i=1}^{n} \overline{F}_{bp}^{(1)}
+ (1 / R_{bc}^{(1)2})(2a_3 / M_{ce}^{(1)}) \overline{K}_{cr}^{(1,2)} \overline{U}_{cr}^{(1,2)}$$
(5-37)

(6) Dimensionless equations for the sun in second stage in the support direction:

$$\frac{\ddot{x}_{s}^{(2)} = -\sum_{i=1}^{n} a_{10i} \bar{F}_{spi-s}^{(2)} - \bar{F}_{bs-sx}^{(2)}}{\ddot{y}_{s}^{(2)} = \sum_{i=1}^{n} a_{11i} \bar{F}_{spi-s}^{(2)} - \bar{F}_{bs-sy}^{(2)} + \bar{F}_{g}^{(2)}}$$
(5-38)

(7) Dimensionless equations for the planet in second stage in the support direction:

$$\ddot{\xi}_{pi}^{(2)} = a_{13} \bar{F}_{spi-p}^{(2)} - a_{15} \bar{F}_{ppi-p}^{(2)} - \bar{k}_{bp-px}^{(2)} + \bar{F}_{gpi}^{(2)} \sin(\phi_{pi}^{(2)})
\ddot{\eta}_{pi}^{(2)} = -a_{14} \bar{F}_{spi-p}^{(2)} - a_{16} \bar{F}_{ppi-p}^{(2)} - \bar{k}_{bp-py}^{(2)} + \bar{F}_{gpi}^{(2)} \cos(\phi_{pi}^{(2)})$$
(5-39)

(8) Dimensionless equations for the ring in second stage in the support direction:

$$\frac{\ddot{x}_r^{(2)}}{\ddot{x}_r^{(2)}} = \sum_{i=1}^m a_{17i} \bar{F}_{rpi-r}^{(2)} - \bar{F}_{br-rx}^{(2)}
\ddot{y}_r^{(2)} = \sum_{i=1}^m a_{18i} \bar{F}_{rpi-r}^{(2)} - \bar{F}_{br-ry}^{(2)} + \bar{F}_{gr}^{(1)}$$
(5-40)

(9) Dimensionless equations for relative torsional displacements in the second stage:

$$\begin{split} \ddot{\overline{U}}_{spi}^{(2)} &= -(a_{12}^2 / M_{se}^{(2)}) \sum_{i=1}^{m} \overline{F}_{spi}^{(2)} - (1 / R_{bs}^{(2)} / R_{br}^{(1)}) (a_{12} / M_{se}^{(2)}) \overline{K}_{rs}^{(1,2)} \overline{U}_{rs}^{(1,2)} \\ &+ (a_{12}^2 / M_{pie}^{(2)}) (\overline{F}_{rpi}^{(2)} - \overline{F}_{spi}^{(2)}) - \ddot{e}_{spi}^{(2)} (\tau) \\ \ddot{\overline{U}}_{sr}^{(2)} &= -(a_{12}^2 / M_{se}^{(2)}) \sum_{i=1}^{m} \overline{F}_{spi}^{(2)} - (1 / R_{bs}^{(2)} / R_{br}^{(1)}) (a_{12} / M_{se}^{(2)}) \overline{K}_{rs}^{(1,2)} \overline{U}_{rs}^{(1,2)} \\ &- (a_{12}^2 / M_{re}^{(2)}) \sum_{i=1}^{m} \overline{F}_{rpi}^{(2)} - (a_{12} / M_{re}^{(2)}) (1 / R_{br}^{(2)} / R_{bc}^{(1)}) \overline{K}_{cr}^{(1,2)} \overline{U}_{cr}^{(1,2)} \\ &- (a_{12} / M_{re}^{(2)}) (-\overline{T}_{out} / R_{br}^{(2)}) \end{split}$$

(10) Dimensionless equations for the relative torsional displacements of the connected parts in the two stages:

$$\begin{split} & \ddot{\overline{U}}_{rs}^{(1,2)} = -(a_3 / M_{re}^{(1)}) \sum_{i=1}^{m} \overline{F}_{rpi}^{(1)} - (1 / R_{br}^{(1)2}) (1 / M_{re}^{(1)}) \overline{K}_{rs}^{(1,2)} \overline{U}_{rs}^{(1,2)} \\ & - (R_{br}^{(1)} / R_{bs}^{(2)}) (a_{12} / M_{se}^{(2)}) \sum_{i=1}^{m} \overline{F}_{spi}^{(2)} - (1 / R_{bs}^{(2)2}) (1 / M_{se}^{(2)}) \overline{K}_{rs}^{(1,2)} \overline{U}_{rs}^{(1,2)} \\ & \ddot{\overline{U}}_{cr}^{(1,2)} = (1 / M_{ce}^{(1)}) (R_{c}^{(1)} / R_{bc}^{(1)}) \sum_{i=1}^{m} \overline{F}_{bp}^{(1)} - (1 / R_{bc}^{(1)2}) (1 / M_{ce}^{(1)}) \overline{K}_{cr}^{(1,2)} \overline{U}_{cr}^{(1,2)} \\ & - (R_{bc}^{(1)} / R_{br}^{(2)}) (a_{12} / M_{re}^{(2)}) \sum_{i=1}^{m} \overline{F}_{rpi}^{(2)} - (1 / R_{br}^{(2)2}) (1 / M_{re}^{(2)}) \overline{K}_{cr}^{(1,2)} \overline{U}_{cr}^{(1,2)} \\ & - (R_{bc}^{(1)} / R_{br}^{(2)}) (1 / M_{re}^{(2)}) (-\overline{T}_{out} / R_{br}^{(2)}) \end{split}$$

Some of the simplified formulas in Eqs.(5-33)-(5-42) above and the dimensionless physical quantities used in this subsection are defined below:

$$\begin{split} \overline{F}_{spi-s}^{(j)} &= \overline{k}_{spi-s}^{(j)} \overline{\delta}_{spi}^{(j)} + \overline{c}_{spi-s}^{(j)} \dot{\overline{\delta}}_{spi}^{(j)}, \overline{k}_{spi-s}^{(j)} = \frac{k_{spi}^{(j)}}{m_s^{(j)} \omega_d^2}, \overline{c}_{spi-s}^{(j)} = \frac{c_{spi}^{(j)}}{m_s^{(j)} \omega_d}, \\ \overline{F}_{spi-p}^{(j)} &= \overline{k}_{spi-p}^{(j)} \overline{\delta}_{spi}^{(j)} + \overline{c}_{spi-p}^{(j)} \dot{\overline{\delta}}_{spi}^{(j)}, \overline{k}_{spi-p}^{(j)} = \frac{k_{spi}^{(j)}}{m_{pi}^{(j)} \omega_d^2}, \overline{c}_{spi-p}^{(j)} = \frac{c_{spi}^{(j)}}{m_{pi}^{(j)} \omega_d}, \\ \overline{F}_{rpi-r}^{(j)} &= \overline{k}_{rpi-r}^{(j)} \overline{\delta}_{rpi}^{(j)} + \overline{c}_{rpi-r}^{(j)} \dot{\overline{\delta}}_{rpi}^{(j)}, \overline{k}_{rpi-r}^{(j)} = \frac{k_{rpi}^{(j)}}{m_r^{(j)} \omega_d^2}, \overline{c}_{rpi-r}^{(j)} = \frac{c_{rpi}^{(j)}}{m_r^{(j)} \omega_d}, \\ \overline{F}_{rpi-p}^{(j)} &= \overline{k}_{rpi-p}^{(j)} \overline{\delta}_{rpi}^{(j)} + \overline{c}_{rpi-p}^{(j)} \dot{\overline{\delta}}_{rpi}^{(j)}, \overline{k}_{rpi-p}^{(j)} = \frac{k_{rpi}^{(j)}}{m_{pi}^{(j)} \omega_d^2}, \overline{c}_{rpi-p}^{(j)} = \frac{c_{rpi}^{(j)}}{m_{pi}^{(j)} \omega_d}, \\ \overline{F}_{spi}^{(j)} &= \overline{k}_{spi}^{(j)} \overline{\delta}_{spi}^{(j)} + \overline{c}_{rpi}^{(j)} \dot{\overline{\delta}}_{spi}^{(j)}, \overline{k}_{spi}^{(j)} = \frac{k_{rpi}^{(j)}}{\omega_d^2}, \overline{c}_{rpi}^{(j)} = \frac{c_{rpi}^{(j)}}{\omega_d}, \\ \overline{F}_{rpi}^{(j)} &= \overline{k}_{rpi}^{(j)} \overline{\delta}_{rpi}^{(j)} + \overline{c}_{rpi}^{(j)} \dot{\overline{\delta}}_{rpi}^{(j)}, \overline{k}_{rpi}^{(j)} = \frac{k_{rpi}^{(j)}}{\omega_d^2}, \overline{c}_{rpi}^{(j)} = \frac{c_{rpi}^{(j)}}{\omega_d}, \\ \overline{F}_{rpi}^{(j)} &= \overline{k}_{rpi}^{(j)} \overline{\delta}_{rpi}^{(j)} + \overline{c}_{rpi}^{(j)} \dot{\overline{\delta}}_{rpi}^{(j)}, \overline{k}_{rpi}^{(j)} = \frac{k_{rpi}^{(j)}}{\omega_d^2}, \overline{c}_{rpi}^{(j)} = \frac{c_{rpi}^{(j)}}{\omega_d}, \\ \overline{F}_{rpi}^{(j)} &= \overline{k}_{rpi}^{(j)} \overline{\delta}_{rpi}^{(j)} + \overline{c}_{rpi}^{(j)} \dot{\overline{\delta}}_{rpi}^{(j)}, \overline{k}_{rpi}^{(j)} = \frac{k_{rpi}^{(j)}}{\omega_d^2}, \overline{c}_{rpi}^{(j)} = \frac{c_{rpi}^{(j)}}{\omega_d}, \\ \overline{F}_{rpi}^{(j)} &= \overline{k}_{rpi}^{(j)} \overline{\delta}_{rpi}^{(j)} + \overline{c}_{rpi}^{(j)} \dot{\overline{\delta}}_{rpi}^{(j)}, \overline{k}_{rpi}^{(j)} = \frac{k_{rpi}^{(j)}}{\omega_d^2}, \overline{c}_{rpi}^{(j)} = \frac{c_{rpi}^{(j)}}{\omega_d}, \\ \overline{F}_{rpi}^{(j)} &= \overline{k}_{rpi}^{(j)} \overline{\delta}_{rpi}^{(j)} + \overline{c}_{rpi}^{(j)} \dot{\overline{\delta}}_{rpi}^{(j)}, \overline{k}_{rpi}^{(j)} = \frac{k_{rpi}^{(j)}}{\omega_d^2}, \overline{c}_{rpi}^{(j)} = \frac{c_{rpi}^{(j)}}{\omega_d}, \\ \overline{F}_{rpi}^{(j)} &= \overline{k}_{rpi}^{(j)} \overline{\delta}_{rpi}^{(j)} + \overline{c}_{rpi}^{(j)} \dot{\overline{\delta}}_{rpi}^{(j$$

$$\begin{split} & \overline{F}_{bl-\ln}^{(j)} = \overline{k}_{bl-\ln}^{(j)} \overline{n}_{l}^{(j)} + \overline{c}_{bl-\ln}^{(j)} \overline{n}_{l}^{(j)}, \overline{k}_{bl-l}^{(j)} = \frac{k_{bl}^{(j)}}{m_{l}^{(j)} \omega_{d}^{2}}, \overline{c}_{bl-l}^{(j)} = \frac{c_{bl}^{(j)}}{m_{l}^{(j)} \omega_{d}} \\ & \overline{F}_{bp}^{(1)} = \overline{k}_{bp}^{(1)} \overline{\delta}_{cpiy}^{(1)} + \overline{c}_{bp}^{(1)} \dot{\overline{\delta}}_{cpiy}^{(1)}, \overline{k}_{bp}^{(1)} = \frac{k_{bp}^{(j)}}{\omega_{d}^{2}}, \overline{c}_{bp}^{(1)} = \frac{c_{bp}^{(1)}}{\omega_{d}}, \\ & \overline{K}_{cr}^{(1,2)} = \frac{K_{cr}^{(1,2)}}{\omega_{d}^{2}}, \overline{K}_{rs}^{(1,2)} = \frac{K_{rs}^{(1,2)}}{\omega_{d}^{2}}, \overline{e} = \frac{e}{b_{c}}, \overline{b} = \frac{b}{b_{c}}, \\ & \overline{T}_{in} = \frac{T_{in}}{b_{c} \omega_{d}^{2}}, \overline{T}_{out} = \frac{T_{out}}{b_{c} \omega_{d}^{2}}, \overline{F}_{gl} = \frac{-m_{l} g}{m_{l} b_{c} \omega_{d}^{2}}, \overline{F}_{cl} = \frac{m_{l} \Omega_{cd}^{2} R_{c}^{(1)}}{m_{l} b_{c}}, \Omega_{cd} = \frac{\omega_{c}^{(1)}}{\omega_{d}}. \end{split}$$

where the parameters in the upper are labelled j=1,2. The remaining letters stand for l=s,r,p,c,n=x,y.

5.5 Nonlinear dynamics characteristics analysis of the translational-torsional model

The nonlinear dynamic behaviour of the model can be obtained by concentrating on the transverse and torsional displacements of the two-stage parallel compound gear system, and the dimensionless ordinary differential equations are solved by the numerical method, and the basic parameters of the gears as well as the other parameters in the case of the present study are still as shown in Tab.5-2 to Tab.5-4, again in order to eliminate the effect of transient response, the results within the first 300 response cycles were removed. By analysing the transverse response results, the meshing displacements on the meshing line and the meshing forces, the influence of various factors on the dynamic response of the system is investigated.

5.5.1 Influence of the damping ratio coefficient on the dynamic response

The analysis of Fig.5-13 in Section 5.3 reveals that the motion state of the entire two-stage parallel compound gear system changes with increasing damping ratio coefficient, transitioning from unstable chaotic motion to stable 7T periodic motion. Notably, the quasi-periodic motion is also based on the 7T periodic motion as its foundation. Furthermore, analysis indicates that the fundamental motion is the 7T periodic motion. In the case of the translational-torsional model, which incorporates equations in the lateral direction and additional excitations, the vibration state of the entire system is expected to differ. However, it is assumed that the motion state of system may still relate to that of the pure torsional model.

In this subsection, the damping ratio coefficient is selected as the bifurcation parameter, while the other parameters remain consistent with those of the pure torsional model. To differentiate from Fig.5-13 and for clarity, two ranges of the meshing damping ratio coefficient are chosen: 0.119-0.124 and 0.166-0.174, corresponding to portions of Stage B (quasi-periodic motion) and Stage C (7T periodic motion) in Fig.5-13. It is evident that the motion state in the 0.119-0.124 range approaches 7T periodic motion, while the motion state in the 0.166-0.174 range represents 7T periodic motion. Fig.5-24 depicts the bifurcation diagram of the dimensionless relative torsional displacement U_{spi} . The results indicate that, with increasing damping ratios, the motion state of the relative torsional displacement of system does not exhibit any significant changes, remaining in the quasi-periodic state, even when the meshing ratio spans a wide range. Compared to the results shown in Fig.5-13, the increase in meshing damping ratio coefficient does not lead to a more stable motion state, suggesting that in this study case, the increase in meshing damping ratio has little effect on the motion state of the twostage compound gear system, indicating that the damping ratio does not improve the dynamic behavior of system.

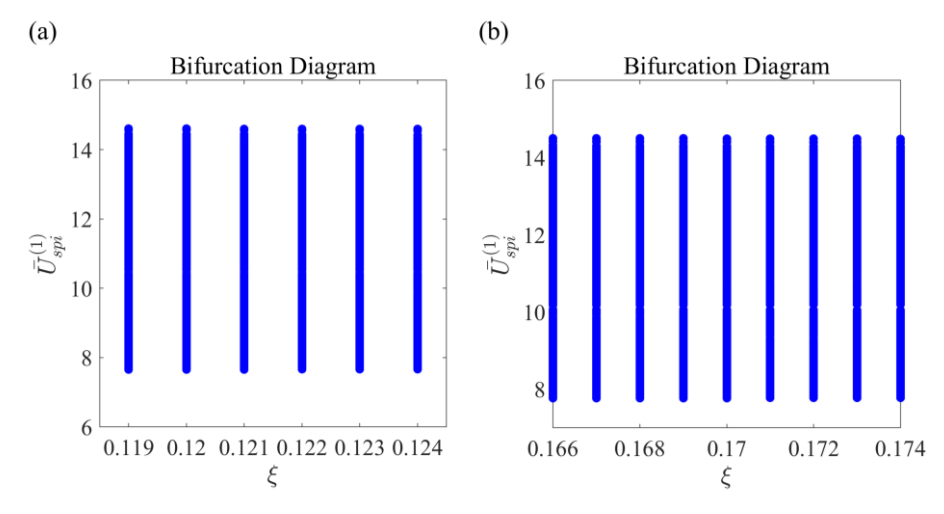


Fig.5-24 Bifurcation plots of dimensionless relative torsional displacements with different ranges of meshing damping ratios coefficient: (a) 0.119-0.124, (b) 0.166-0.174

To validate the motion state depicted in Fig.5-24, the maximum damping ratio coefficient 0.170 is selected while keeping other parameters constant. The corresponding Poincaré map and phase trajectory are shown in Fig.5-25. In Fig.5-25 (a), the Poincaré map clearly indicates a dense distribution of points without any discernible pattern. Correspondingly, Fig.5-25 (b) illustrates the phase trajectory, which is characterized by complex lines in the phase space, further confirming that the motion state of the relative torsional displacement is indeed quasi-periodic motion.

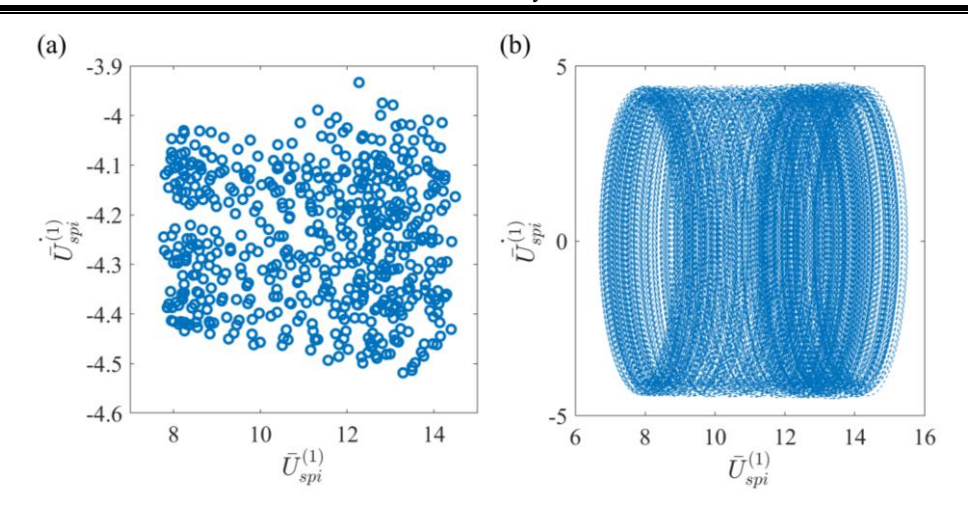


Fig.5-25 Meshing damping ratio coefficient of 0.170 in the case of (a) Poincaré map diagram, (b) phase-trajectory diagram

To verify whether the motion states of lateral vibration displacement $x_s^{(1)}$ and torsional vibration displacement differ, bifurcation diagrams for two ranges of meshing damping ratio coefficients are presented in Fig.5-26 (a) and (b). Similar to the results for relative torsional displacement, these bifurcation diagrams indicate that the motion state remains quasi-periodic, suggesting that both lateral vibration and relative torsion exhibit the same dynamic motion state.

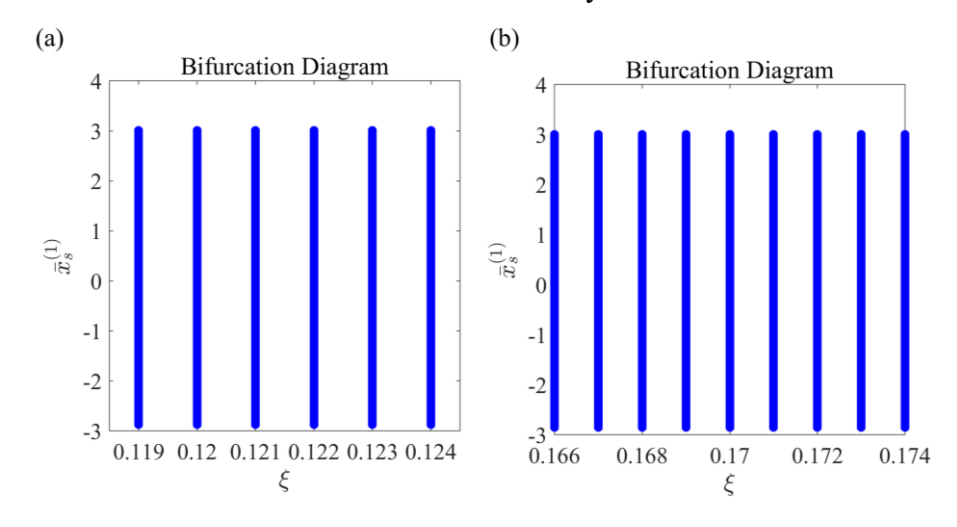


Fig.5-26 Bifurcation plots of dimensionless transverse vibration displacements with different ranges of meshing damping ratios coefficient: (a) 0.119-0.124, (b) 0.166-0.174

5.5.2 Influence of the speed on the dynamic response

Similarly, when the dimensionless rotational speed ranges from 1.2 to 3.5, the corresponding bifurcation diagram is shown in Fig.5-27. At a meshing

damping ratio of 0.17, the diagram reveals that even at the maximum damping ratio coefficient, as the rotational speed increases, results of the dimensionless lateral vibration displacement and relative torsional displacement does not change. Furthermore, there is no stable multi-periodic motion as observed. Therefore, similar to the meshing damping ratio coefficient, the rotational speed does not change the motion state of system.

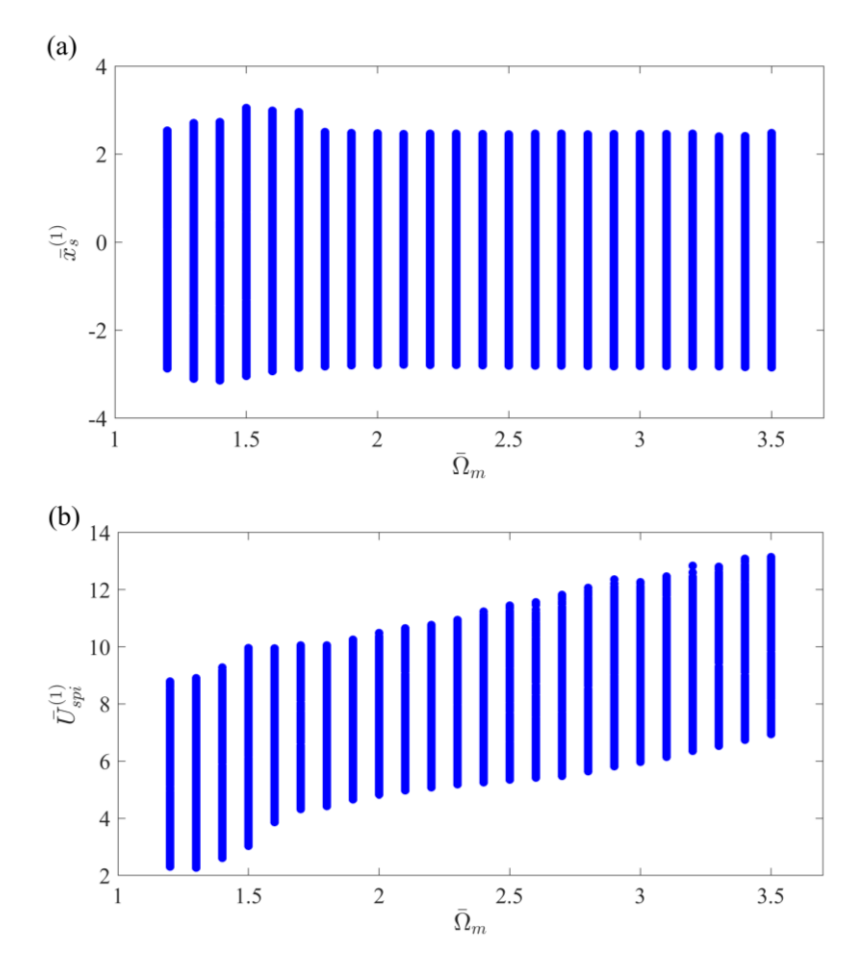


Fig.5-27 Bifurcation plots of dimensionless vibration displacements versus rotational speed: (a) transverse displacement, (b) relative torsional displacement

5.5.3 Analysis of the motion states in the translational-torsional coupled nonlinear model.

Based on the analyses in the previous two sections, it is evident that variations in the meshing damping ratio coefficient and rotational speed within reasonable limits do not significantly change the motion states of lateral and torsional vibrations displacement, which remain quasi-periodic, as demonstrated by bifurcation diagrams, Poincaré maps, and phase diagrams. This subsection

analyzes the underlying reasons for this phenomenon.

Compared to pure torsion nonlinear dynamic, the translational-torsional nonlinear dynamic model encompasses a more comprehensive consideration, with the key difference in the external force being that the constant gravitational term in the first stage becomes a time-varying excitation. Furthermore, the nonlinear analysis of the pure torsional model indicates that the stable motion ultimately manifests as a 7T periodic motion. This is attributed to the least common multiple of the two internal meshing stiffnesses' periods being seven, meaning that after seven cycles of the first-stage meshing period, the excitation of system returns to its initial position, initiating the subsequent repeating cycle. Therefore, it is inferred that the fundamental motion state in the translational-torsional model is still related to the 7T periodic motion observed in the pure torsional model.

To validate this hypothesis, the improved Newmark-beta method proposed in Chapter 4 is employed for re-solving the translational-torsional nonlinear model, as the built-in Runge-Kutta method in MATLAB is resource-intensive and slow, leading to computational limitations. In this analysis, factors such as gravity, gear backlash, and transmission errors are considered, with the primary parameters set to a rotational speed of 3000 rpm and a meshing damping ratio of 0.17 to compute the nonlinear dynamic response.

Fig.5-28 illustrates the phase trajectory and Poincaré map for one repeating cycle under these conditions. The Poincaré map indicates a discernible pattern, with the points roughly segmented into seven regions, each containing around 100 points, suggesting that the lateral vibration displacement of system exhibits approximately 700 periodic motion state. Additionally, while the trajectory lines in the phase plot are numerous, they display a recognizable periodic shape.

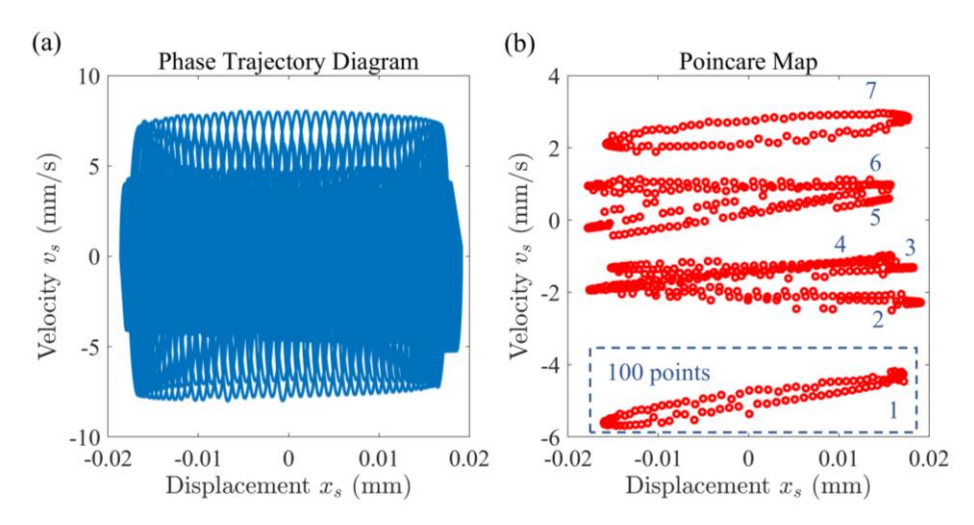


Fig.5-28 Transverse vibration of sun at 3000 rpm during one repetition cycle: (a) phase trajectory, (b) Poincare map diagram

Additionally, the phase trajectory and Poincaré map of the planet gear meshing with the sun are presented in Fig.5-29. Both the phase trajectory and Poincaré mapping clearly indicate that the motion state corresponds to a certain multiple time periodic motion, verifying the findings from Fig.5-28.

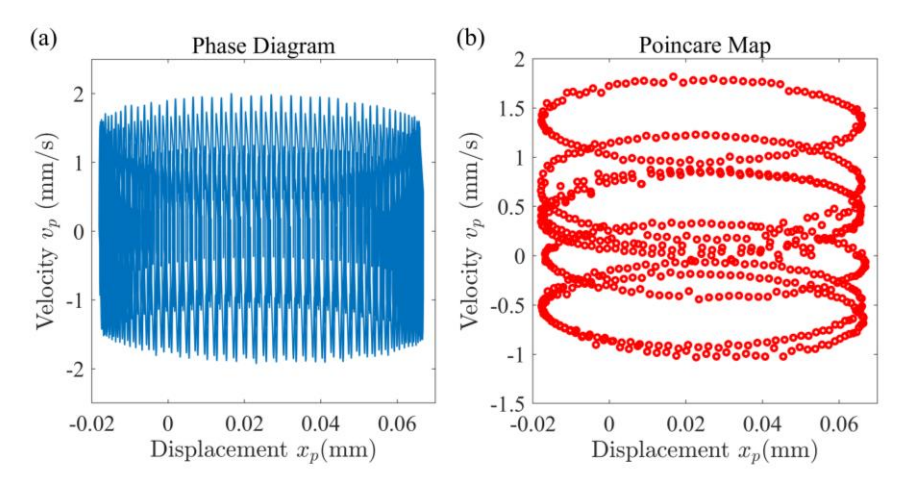


Fig.5-29 Transverse vibration of planet at 3000 rpm during one repetition cycle: (a) phase trajectory, (b) Poincare map diagram

Corresponding to Fig.5-28 and Fig.5-29, the time history of the lateral vibration of sun gear under the 3000rpm condition is shown in Fig.5-30. From the waveform in Fig.5-30 (a), it can be preliminarily inferred that the lateral vibration state exhibits a long-period behavior resembling a sine wave before repeating. Fig. 5-30 (b) and (c) reveal that the displacement values at the beginning point and end point of one long period are 0.00649419mm and 0.0065035mm, respectively, yielding a discrepancy of only 0.1434%. This confirms the computational accuracy of the improved Newmark-beta method and validates that the selected results indeed represent one complete repeating cycle. Furthermore, the enlarged view in Fig.5-30 (a) reveals the presence of a small cycle within the time history, which comprises seven peaks, as indicated by the black numbers (0-6) in the enlarged graph. This indicates that within one small cycle, there are seven excitation frequencies. After completing a small cycle, the peak at point 7 resets to point 0, initiating the next small cycle. Starting from the marked point #1 in Fig.5-30 (a), it is observed that the time history contains a total of 100 small cycles. Therefore, it can be concluded that the lateral vibration response of the composite planetary gear system experiences 700 distinct motion states within one complete cyclic period.

Moreover, it is known that the period of the first stage time-varying gravity is equal to the time taken for the carrier to complete one rotation, given by $t_c=1/f_c$. The meshing period of the first stage gear system is $t_m=1/f_m=1/(f_s-f_c)$. Hence, the gravitational period is an integer multiple of the meshing period, which is given

 $t_c/t_m=i\times Z_s=18.5\times 40=700$. The least common multiple of 700 and 7, as analyzed in the pure torsional nonlinear model, is still 700. This indicates that in the first stage gear system, the periods of the two meshing stiffnesses and the time-varying gravity item return to their initial positions simultaneously after 700 meshing cycles. This corresponds perfectly to the 700 peaks observed in the time history shown in Fig.5-30, elucidating that the fundamental motion in translational-torsional nonlinear dynamics is a 700T periodic motion, with all other motion states based on this foundation. Consequently, the most fundamental motion state can be classified as quasi-periodic, providing an explanation for the quasi-periodic or chaotic behaviors observed in the previous analyses. Thus, the analysis results in this subsection validate the relationship between the translational-torsional model and the pure torsional model, confirming the correctness of the hypothesis.

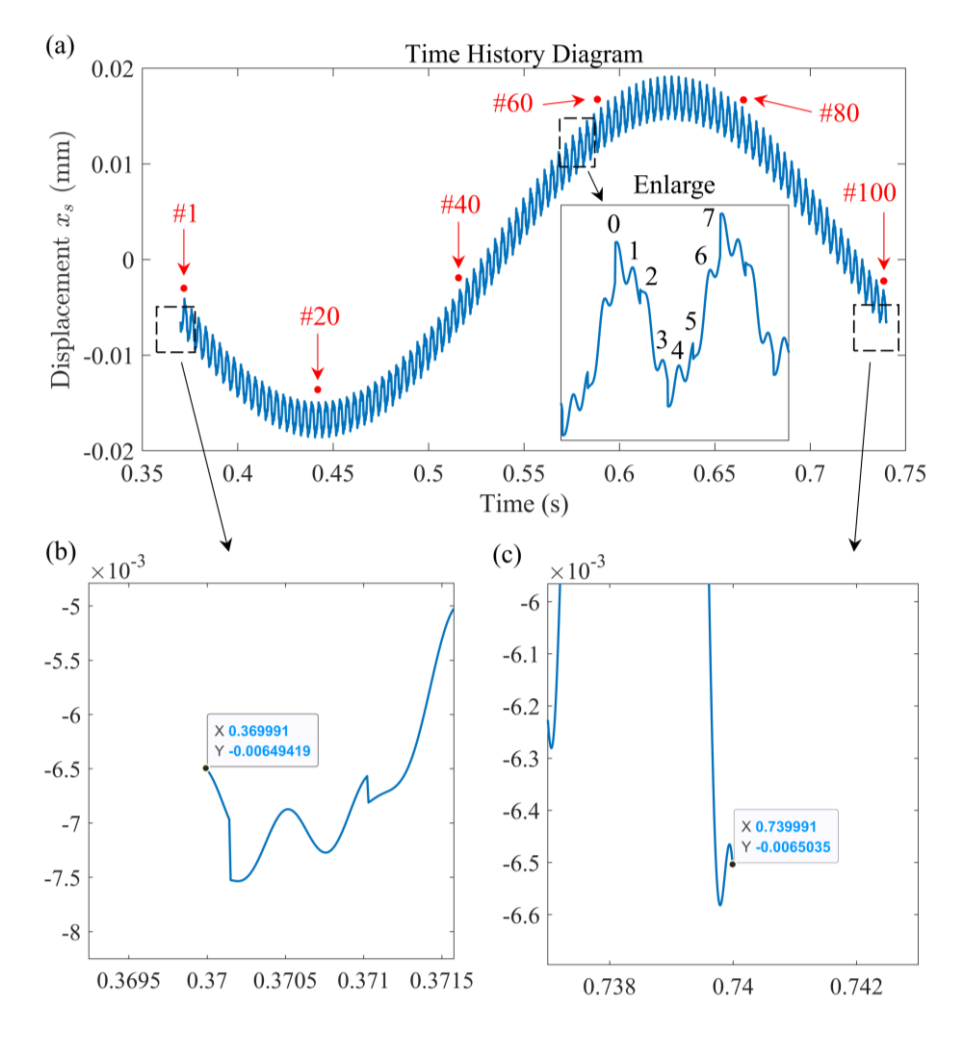


Fig.5-30 Transverse vibration displacements of the sun at 3000 rpm for one repetition cycle: (a) time history plot, (b) results at the initial point, and (c) results at the end point.

5.6 Brief summary

This chapter establishes the nonlinear dynamic model for a two-stage parallel compound gear system applied in ships, incorporating both a pure torsional model and a translational-torsional coupling model. It explores the nonlinear characteristics of this compound gear system and investigates the effects of various key parameters (such as meshing damping ratio, rotational speed, and meshing error amplitude) on its nonlinear motion states, leading to significant conclusions related to the parallel structure of the system. The specific findings are as follows:

- (1) For the pure torsional nonlinear dynamic model, as the meshing damping ratio increases within a reasonable range (0.03-0.17), the entire compound gear system exhibits a rich variety of motion states, with the behavior of system being highly sensitive to the damping ratio. Analysis of bifurcation diagrams indicates a transition from chaotic motion to quasi-periodic motion, and finally to stable 7-fold periodic motion. Poincaré maps, phase trajectories, and time histories confirm each state, revealing that the ultimate stable motion state of 7T periodic motion is linked to the least common multiple of the meshing stiffness excitations in the two-stage gear system.
- (2) In a low rotational speed range, the system demonstrates stable 7T periodic motion. Conversely, in a high rotational speed range, the system exhibits quasi-periodic or chaotic motion, indicating that higher speeds can induce instability. Additionally, as the meshing damping ratio increases from 0.075 to 0.1 to 0.125, chaotic motion in the high-speed range gradually transitions to quasi-periodic motion and ultimately to 7T periodic motion. Simultaneously, the amplitude range of the vibration response of the system decreases, further emphasizing that a higher meshing damping ratio enhances the stability of the motion state of system.
- (3) When the damping ratio and input speed are considered as bifurcation parameters, Poincaré maps reveal that the transition from instability to stability occurs via Hopf bifurcation. Additionally, when meshing error amplitude is treated as a bifurcation parameter, both Hopf bifurcation and doubling periodic bifurcation are observed. The nonlinear dynamic response transfers to increasingly stable periodic motion with increasing damping ratio coefficient and input speed. However, the opposite effect is noted for increasing meshing error amplitude, which leads to unstable motion states.
- (4) For the translational-torsional nonlinear model, changes in the damping ratio and rotational speed have minimal impact on the motion states of lateral vibration and relative torsional displacement, both of which exhibit quasi-periodic

motion. Compared to the stable 7T periodic motion of the pure torsional model, the fundamental motion state of the translational-torsional model is 700T periodic. This arises from the influence of time-varying gravity item, which introduces a gravitational term alongside the two meshing stiffnesses, with their least common multiple being 700. The analysis of the 7T periodic motion in the pure torsional model and the 700T periodic motion in the translational-torsional model illustrates the connection between the two models. It also demonstrates that the nonlinear study of the two-stage parallel compound gear system, starting from the pure torsional model and gradually exploring the translational-torsional model, validates the correctness of the approach. The comprehensive findings from both models effectively explain the complexity of the nonlinear dynamic behavior of the studied compound gear system.

Chapter 6 Analysis of the Dynamic Characteristics of the Double-helical Two-Stage Parallel Compound Marine Gear Transmission System Under Navigational Conditions

6.1 Preface

In the previous sections, this study employed a moving modeling approach, derived the absolute acceleration of the components in a two-stage parallel compound gear system within a fixed coordinate frame. Quasi-static and dynamic models were developed to analyze their mechanical characteristics. Additionally, both pure torsional and translational-torsional nonlinear models were established to investigate how key parameters influence the nonlinear characteristics of the compound gear system. However, when a ship moves on the sea surface, the gear transmission system undergoes spatial motion relative to the aforementioned fixed coordinate system. This results in the planetary gear transmission being affected by external non-inertial frames. Notably, previous literature on the dynamics of ship power systems under non-inertial frames is limited, highlighting the necessity for such research. Thus, in this chapter, considering that the sea surface is not always fixed during maritime operation, aiming to comprehensively analyze the dynamic characteristics of ships in wave environments by accounting for the motion of the marine itself. A dynamic model of the two-stage parallel compound gear system within an external non-inertial coordinate system is establish in this chapter. The dynamics of the power system of ship under these conditions are analyzed. The study of this chapter broadens the research scope of dynamic characteristics in operational states and enriches the content related to ship dynamics, ultimately providing guidance for the design of ship power systems.

6.2 Special ship motions in navigational states

6.2.1 Rocking motion

Due to the influence of factors such as waves and wind, ships experience rocking motion while operating at sea. Mechanical equipment like gear system, fixed to the hull, also undergoes this rocking motion, generating dynamic forces that significantly impact ship systems. Such motion must be considered when designing and analyzing the dynamic behavior of these mechanical components

to ensure their performance and reliability. Therefore, this subsection will analyze the dynamic characteristics of the entire compound gear system during the rocking motion of ship.

In this subsection, the rocking motion studied primarily refers to the lateral rocking of ship about the forward axis (z-axis), which is shown as Fig.6-1. While examining the rocking of hull, the rocking postion of ship must be considered, with its angular displacement, angular velocity, and angular acceleration represented by harmonic motion functions. In general, rocking is defined as the periodic angular displacement motion of the ship around its longitudinal axis, with a specified roll angle of ± 45 degrees and a period ranging from 3 to 14 seconds. Additionally, to describe the motion characteristics of a ship undergoing rocking motion, the following equations are given.

$$\theta_{zb} = A_{zb} \sin(\Omega_{zb}t),
\dot{\theta}_{zb} = A_{zb}\Omega_{zb} \cos(\Omega_{zb}t),
\ddot{\theta}_{zb} = -A_{zb}\Omega_{zb}^2 \sin(\Omega_{zb}t).$$
(6-1)

where, θ_{zb} , $\dot{\theta}_{zb}$, $\ddot{\theta}_{zb}$ are the angle displacement, velocity and acceleration, respectively. A_{zb} is the max rocking angle. Ω_{zb} is the angle velocity of the rocking motion, which is related to the period time of rocking motion, $\Omega_{zb} = 2\pi/T_{zb}$.

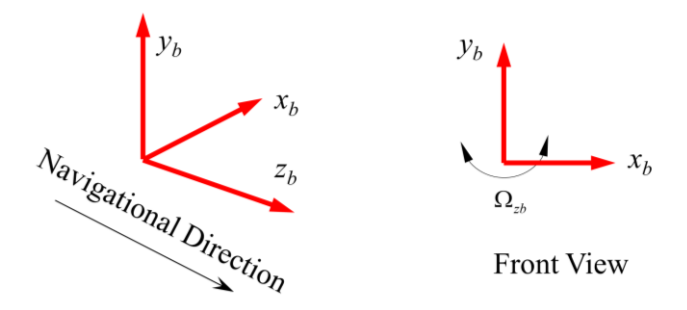


Fig.6-1 Rocking motion of ship

6.2.2 Picthing motion

Another form of motion closely related to ship navigation is pitch motion, caused by vertical wave profiles along the forward direction of ship, resulting in a fore-and-aft oscillation. As illustrated in Fig.6-2, the pitch motion (longitudinal oscillation) studied in this subsection primarily refers to the periodic angular displacement about the transverse axis (x-axis). In analyzing the pitch motion of ship, the harmonic motion functions are used to describe the angular displacement,

angular velocity, and angular acceleration. This approach effectively simplifies the analysis, enabling researchers to assess the impact of hull motion on mechanical equipment fixed to it more easily.

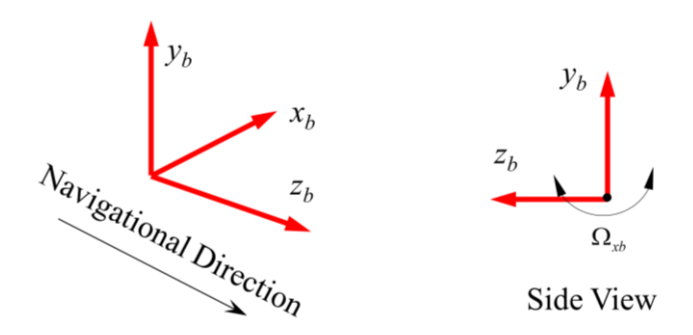


Fig.6-2 Pitching motion of ship

The pitch angle of the ship is ± 10 degrees, with a pitch period ranging from 4 to 10 seconds. Therefore, based on these standards, the motion characteristics of the ship during pitch motion can be expressed by the following equations.

$$\theta_{xb} = A_{xb} \sin(\Omega_{xb}i),$$

$$\dot{\theta}_{xb} = A_{xb}\Omega_{xb} \cos(\Omega_{xb}i),$$

$$\ddot{\theta}_{xb} = -A_{xb}\Omega_{xb}^{2} \sin(\Omega_{xb}i).$$
(6-2)

where, θ_{xb} , $\dot{\theta}_{xb}$, $\ddot{\theta}_{xb}$ are the angle displacement, velocity and acceleration, respectively. A_{xb} is the max picthing angle. Ω_{xb} is the angle velocity of the picthing motion, which is related to the period time of picthing motion, $\Omega_{xb} = 2\pi/T_{xb}$.

6.3 Dynamics model of the two-stage parallel compound marine gear transmission system in non-inertial reference frame

When the planetary gear system is fixed to a stationary base, the planet gears not only rotate about their own axes but also revolve with the carrier. In this moment, the planets exist within a non-inertial frame of reference frame associated with the carrier. To differentiate the non-inertial frame resulting from the motion of the ship (basic coordinate system), this study designates the moving coordinate system of the carrier as the internal non-inertial frame of the gear system, denoted by the subscript 'i'. Conversely, the coordinate system that accounts for the basic motion of the hull of ship is referred to as the external non-

inertial frame of the gear system, denoted by the subscript 'e'.

6.3.1 Kinematic analysis of components in two non-inertial frames

As described in Section 2.4.1 of Chapter Two, the planetary gear system inherently operates within a non-inertial frame (internal non-inertial frame), specifically the moving coordinate system of the carrier. This section considers the motion of the ship hull, introducing an additional external non-inertial frame. To facilitate modeling, the author has derived formulas for the absolute acceleration of various components within the internal non-inertial frame in Chapter Two. Therefore, before establishing the dynamic equations in this section, it is essential to derive the absolute absolute acceleration formulas for different components in both non-inertial frames.

Fig.6-3 illustrates the displacement vectors of the sun gear and planet gears in the two non-inertial frames. As shown in Fig.6-3, there are multi coordinate systems. Firstly, the coordinate system o_c - $x_cy_cz_c$ represents the moving coordinate system of the carrier (internal non-inertial frame), and the coordinate systems of sun and planets parallele to this coordinate system or at an angle with this coordinate system. While o_b - $x_by_bz_b$ denotes the coordinate system of the base movement (external non-inertial frame). The fixed coordinate system O-XYZ corresponds to the ground (inertial frame of the Earth). Aparting from the angular velocity vector ω_c of inernal non-inertial frame, the rotational angular velocity vector of the base coordinate system corresponding to the carrier moving coordinate system represented as Ω .

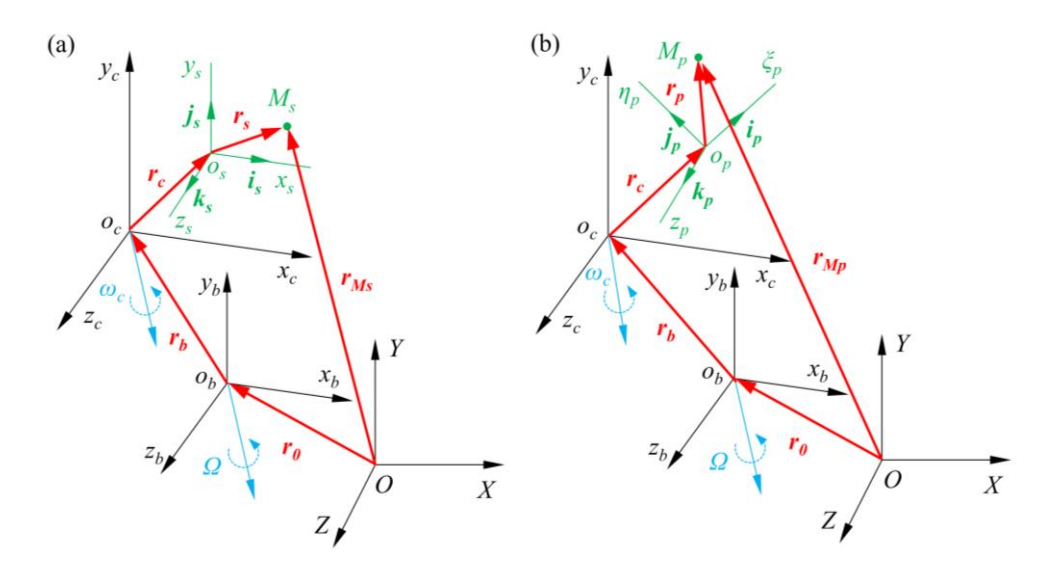


Fig.6-3 Displacement vectors for components in two non-inertial coordinates: (a) sun and (b) planet

In Fig.6-3 (a), the vector of the origin o_b of the ship coordinate system in the fixed coordinate system is denoted as \mathbf{r}_0 . The vector of the origin o_c of the carrier moving coordinate system in the ship coordinate system is represented as \mathbf{r}_b . The vector of the sun gear node M_s in the carrier moving coordinate system is given by $\mathbf{r}_c+\mathbf{r}_s$, while the vector of the sun gear node M_s in the fixed coordinate system is indicated as \mathbf{r}_{Ms} . The relationships between these displacement vectors are as follows:

$$\begin{cases}
\mathbf{r}_{Ms} = \mathbf{r}_{0} + \mathbf{r}_{b} + \mathbf{r}_{c} + \mathbf{r}_{s} \\
\mathbf{r}_{0} = \mathbf{x}_{0} \cdot \mathbf{i} + \mathbf{y}_{0} \cdot \mathbf{j} + \mathbf{z}_{0} \cdot \mathbf{k} \\
\mathbf{r}_{b} = \mathbf{x}_{b} \cdot \mathbf{i}_{b} + \mathbf{y}_{b} \cdot \mathbf{j}_{b} + \mathbf{z}_{b} \cdot \mathbf{k}_{b} \\
\mathbf{r}_{c} = \mathbf{0} \\
\mathbf{r}_{s} = \mathbf{x}_{s} \cdot \mathbf{i}_{c} + \mathbf{y}_{s} \cdot \mathbf{j}_{c} + \mathbf{z}_{s} \cdot \mathbf{k}_{c}
\end{cases} (6-3)$$

where, In the equations, x_b , y_b , z_b are constants, while x_0 , y_0 , z_0 , x_s , y_s , z_s are time-varying variables representing the displacement responses in their respective coordinate systems. i, j, k are constants unit vectors, and i_b , j_b , k_b , i_c , j_c , k_c are time-varying unit vectors. Meanwhile, the derivatives of the unit vectors in the external non-initial coordinate system and the internal non-initial coordinate system with respect to time are expressed as follows.

$$\frac{d\mathbf{i}_{b}}{dt} = \mathbf{\Omega} \times \mathbf{i}_{b}, \frac{d\mathbf{j}_{b}}{dt} = \mathbf{\Omega} \times \mathbf{j}_{b}, \frac{d\mathbf{k}_{b}}{dt} = \mathbf{\Omega} \times \mathbf{k}_{b}$$

$$\frac{d\mathbf{i}_{c}}{dt} = (\mathbf{\Omega} + \boldsymbol{\omega}_{c}) \times \mathbf{i}_{c}, \frac{d\mathbf{j}_{c}}{dt} = (\mathbf{\Omega} + \boldsymbol{\omega}_{c}) \times \mathbf{j}_{c}, \frac{d\mathbf{k}_{c}}{dt} = (\mathbf{\Omega} + \boldsymbol{\omega}_{c}) \times \mathbf{k}_{c}$$
(6-4)

Following the same calculation process as in Chapter Two, taking the one time and two times derivatives of the displacement vector \mathbf{r}_{Ms} with respect to time, respectively. The expressions for the absolute velocity and absolute acceleration of the node in the static coordinate system O-XYZ, presented as follows.

$$v_{as} = [v_{\theta} + \Omega \times r_{b} + \Omega \times (r_{c} + r_{s})] + [v_{s} + \omega_{c} \times (r_{c} + r_{s})]$$

$$= v_{es} + v_{is}$$

$$a_{as} = [a_{\theta} + \dot{\Omega} \times r_{b} + \Omega \times (\Omega \times r_{b})$$

$$+ 2\Omega \times v_{s} + \dot{\Omega} \times (r_{c} + r_{s}) + \Omega \times (\Omega \times (r_{c} + r_{s}))$$

$$+ \omega_{c} \times (\Omega \times (r_{c} + r_{s})) + \Omega \times (\omega_{c} \times (r_{s} + r_{c}))]$$

$$+ [a_{s} + 2\omega_{c} \times v_{s} + \dot{\omega}_{c} \times (r_{c} + r_{s}) + \omega_{c} \times (\omega_{c} \times (r_{c} + r_{s}))]$$

$$= a_{es} + a_{is}$$

$$(6-5)$$

in this equation, the subscript 'a' denotes absolute acceleration. The first eight terms represent the derived absolute acceleration components due to the external non-inertial system, denoted as a_{es} . The subsequent four terms reflect the absolute acceleration formula only present in the internal non-inertial system, denoted as a_{is} . Thus, the absolute acceleration in both non-inertial coordinate systems can be viewed as the sum of the derived acceleration components a_{es} asised from external non-inertial coordinate system and the derived acceleration components a_{is} asised from external non-inertial coordinate system.

Similarly, as illustrated in Fig.6-3 (b), the expressions for the absolute velocity and acceleration of the planets node in the fixed coordinate system O-XYZ are presented as follows:

$$\begin{aligned} \mathbf{v}_{ap} &= [\mathbf{v}_{0} + \mathbf{\Omega} \times \mathbf{r}_{b} + \mathbf{\Omega} \times (\mathbf{r}_{c} + \mathbf{r}_{p})] + [\mathbf{v}_{p} + \mathbf{\omega}_{c} \times (\mathbf{r}_{c} + \mathbf{r}_{p})] \\ &= \mathbf{v}_{ep} + \mathbf{v}_{ip} \\ \mathbf{a}_{ap} &= [\mathbf{a}_{0} + \dot{\mathbf{\Omega}} \times \mathbf{r}_{b} + \mathbf{\Omega} \times (\mathbf{\Omega} \times \mathbf{r}_{b}) + \dot{\mathbf{\Omega}} \times (\mathbf{r}_{c} + \mathbf{r}_{p}) + \mathbf{\Omega} \times (\mathbf{\Omega} \times (\mathbf{r}_{c} + \mathbf{r}_{p})) \\ &+ 2\mathbf{\Omega} \times \mathbf{v}_{p} + \mathbf{\omega}_{c} \times (\mathbf{\Omega} \times (\mathbf{r}_{c} + \mathbf{r}_{p})) + \mathbf{\Omega} \times (\mathbf{\omega}_{c} \times (\mathbf{r}_{c} + \mathbf{r}_{p}))] \\ &+ [\mathbf{a}_{p} + 2\mathbf{\omega}_{c} \times \mathbf{v}_{p} + \dot{\mathbf{\omega}}_{c} \times (\mathbf{r}_{p} + \mathbf{r}_{c}) + \mathbf{\omega}_{c} \times (\mathbf{\omega}_{c} \times (\mathbf{r}_{c} + \mathbf{r}_{p}))] \\ &= \mathbf{a}_{ep} + \mathbf{a}_{ip} \end{aligned}$$

$$(6-6)$$

It is noted that the $r_c \neq 0$ for planet.

In summary, based on equations (6-5) and (6-6) from this section, it is evident that the composition of absolute acceleration in the fixed coordinate system is more complex in the presence of external non-inertial systems compared to the case where only internal non-inertial systems exist. Consequently, the absolute acceleration in these two non-inertial coordinate systems must exhibit significant differences.

6.3.2 Dynamic model of the two-stage parallel compound marine gear transmission system in two non-inertial frames

The entire two-stage parallel compound gear system, assembled through coupling in the generalized coordinate system, forms a complete set of dynamic equations for the gear transmission system. Therefore, the matrix form of the dynamic equations for this compound gear train under both internal and external non-inertial systems is presented as follows.

$$\mathbf{M} \cdot \mathbf{A}_{a}(t) + \mathbf{C}(t) \cdot \dot{\mathbf{Q}}(t) + \mathbf{K}(t) \cdot \mathbf{Q}(t) = \mathbf{T} + \mathbf{G}(t) + \mathbf{F}_{me}(t)$$
(6-7)

Based on Section 6.3.1, kinematic analysis indicates that the absolute acceleration vectors of the components of the compound planetary gear system differ significantly when the ship is moving at constant velocity, or performing basic spatial maneuvers. During these fundamental movements, the components

are influenced by both internal and external non-inertial systems. An example of the absolute acceleration vector $A_a(t)$ in the equation (6-7) is presented as follows.

$$A_{a}(t) = [a_{isx} + a_{esx}, a_{isy} + a_{esy}, a_{isz} + a_{esz}, \ddot{\theta}_{sx}, \ddot{\theta}_{sy}, \ddot{\theta}_{sz}, ...$$

$$a_{irx} + a_{erx}, a_{iry} + a_{ery}, a_{irz} + a_{erz}, \ddot{\theta}_{rx}, \ddot{\theta}_{ry}, \ddot{\theta}_{rz}, ...$$

$$a_{icx} + a_{ecx}, a_{icy} + a_{ecy}, a_{icz} + a_{ecz}, \ddot{\theta}_{cx}, \ddot{\theta}_{cy}, \ddot{\theta}_{cz}, ...$$

$$a_{iox} + a_{eox}, a_{ioy} + a_{eoy}, a_{ioz} + a_{eoz}, \ddot{\theta}_{ox}, \ddot{\theta}_{oy}, \ddot{\theta}_{oz}, ...]^{T}$$

$$(6-8)$$

Here, the a_{ijk} , a_{ejk} represent the components of the absolute acceleration of the j component node in the internal and external non-inertial systems along the k direction.

Due to the composition of multiple terms in the absolute acceleration $A_a(t)$ within the two non-inertial coordinate systems, dynamic analysis requires decomposing the absolute acceleration vector into fundamental acceleration terms Q(t) in local coordinate systems and additional terms A(t) from the non-inertial systems. Some components related to displacement or velocity from the additional terms are incorporated into the overall stiffness and damping matrices. The remaining excitation component A'(t) is then moved to the right side of the equation, reformulating the dynamic equations. Consequently, equation (6-7) can be derived into equation (6-9) as follows

$$\mathbf{M} \cdot \ddot{\mathbf{Q}}(t) + \mathbf{C}(t) \cdot \dot{\mathbf{Q}}(t) + \mathbf{K}(t) \cdot \mathbf{Q}(t) = \mathbf{T} + \mathbf{G}(t) + \mathbf{F}_{me}(t) - \mathbf{M} \cdot \mathbf{A}'(t)$$
 (6-9)

- 6.4 Dynamic characteristics analysis of compound marine gear transmission system considering ship rocking motion
- 6.4.1 Calculation of generalized acceleration considering ship rocking motion

For the additional generalized vector during ship rocking motion, the rotational angular velocity Ω of the ship own coordinate system is first analyzed. According to Equation (6-1), the angular velocity vector Ω of the body-fixed coordinate system $(o_b$ - $x_by_bz_b)$ shown in Fig.6-3 can be expressed as follows

$$\mathbf{\Omega} = \Omega_{zb} \cdot \mathbf{k}_b \tag{6-10}$$

Based on the principles of rocking motion and motion analysis, the relationships between the unit vectors of the various coordinate systems are as follows.

$$\begin{cases} \mathbf{i} = \cos \theta_{zb} \cdot \mathbf{i}_{b} - \sin \theta_{zb} \cdot \mathbf{j}_{b} \\ \mathbf{j} = \sin \theta_{zb} \cdot \mathbf{i}_{b} + \cos \theta_{zb} \cdot \mathbf{j}_{b} \\ \mathbf{k} = \mathbf{k}_{b} \end{cases} \begin{cases} \mathbf{i}_{b} = \cos \theta_{c} \cdot \mathbf{i}_{c} - \sin \theta_{c} \cdot \mathbf{j}_{c} \\ \mathbf{j}_{b} = \sin \theta_{c} \cdot \mathbf{i}_{c} + \cos \theta_{c} \cdot \mathbf{j}_{c} \\ \mathbf{k}_{b} = \mathbf{k}_{c} \end{cases}$$

$$\begin{cases} \mathbf{i}_{b} = \cos(\theta_{c} + \phi_{p}) \cdot \mathbf{i}_{p} - \sin(\theta_{c} + \phi_{p}) \cdot \mathbf{j}_{p} \\ \mathbf{j}_{b} = \sin(\theta_{c} + \phi_{p}) \cdot \mathbf{i}_{p} + \cos(\theta_{c} + \phi_{p}) \cdot \mathbf{j}_{p} \\ \mathbf{k}_{b} = \mathbf{k}_{p} \end{cases}$$

$$(6-11)$$

Therefore, based on the analysis of absolute acceleration of components in both non-inertial reference frames outlined in section 5.3.1, the components of absolute velocity and absolute acceleration of each component in their respective local coordinate systems under the influence of both non-inertial frames are derived. The following formulas sequentially provide the calculations for the second-stage sun gear node and planet gear node. Notably, since the second-stage gear system does not have an internal non-inertial frame, it is only affected by the rocking motion of the ship, thus influenced solely by the external non-inertial frame

$$\begin{cases} \mathbf{v}_{G2\text{-}as} = (\dot{x}_s - \Omega_{zb} y_s) \mathbf{i}_c + (\dot{y}_s + \Omega_{zb} x_s) \mathbf{j}_c + \dot{z}_s \mathbf{k}_c \\ \mathbf{a}_{G2\text{-}as} = (\ddot{x}_s - 2\Omega_{zb} \dot{y}_s - \dot{\Omega}_{zb} y_s - \Omega_{zb}^2 x_s) \mathbf{i}_c \\ + (\ddot{y}_s + 2\Omega_{zb} \dot{x}_s + \dot{\Omega}_{zb} x_s - \Omega_{zb} y_s) \mathbf{j}_c + \ddot{z}_s \mathbf{k}_c \end{cases}$$
(6-12)

$$\begin{cases}
\mathbf{v}_{G2\text{-}as} = (\dot{x}_s - \Omega_{zb} y_s) \mathbf{i}_c + (\dot{y}_s + \Omega_{zb} x_s) \mathbf{j}_c + \dot{z}_s \mathbf{k}_c \\
\mathbf{a}_{G2\text{-}as} = (\ddot{x}_s - 2\Omega_{zb} \dot{y}_s - \dot{\Omega}_{zb} y_s - \Omega_{zb}^2 x_s) \mathbf{i}_c \\
+ (\ddot{y}_s + 2\Omega_{zb} \dot{x}_s + \dot{\Omega}_{zb} x_s - \Omega_{zb} y_s) \mathbf{j}_c + \ddot{z}_s \mathbf{k}_c
\end{cases}$$

$$\begin{cases}
\mathbf{v}_{G2\text{-}ap} = (\dot{\xi}_p - \Omega_{zb} y_p) \mathbf{i}_p + (\dot{\eta}_p + \Omega_{zb} (x_p + r_c)) \mathbf{j}_p + \dot{z}_s \mathbf{k}_s \\
\mathbf{a}_{G2\text{-}ap} = (\ddot{\xi}_p - 2\Omega_{zb} \dot{\eta}_p - \dot{\Omega}_{zb} \eta_p - \Omega_{zb}^2 (\xi_p + r_c)) \mathbf{i}_p \\
+ (\ddot{\eta}_p + 2\Omega_{zb} \dot{\xi}_p + \dot{\Omega}_{zb} (\xi_p + r_c) - \Omega_{zb}^2 \eta_p) \mathbf{j}_p + \ddot{z}_p \mathbf{k}_p
\end{cases}$$
(6-13)

In contrast to the second stage, the sun, carrier, ring, and planes in first stage are influenced by both non-inertial reference frames, resulting in significantly different expressions, as shown below.

$$\begin{cases} \boldsymbol{v}_{G1\text{-}as} = (\dot{x}_s - (\Omega_{zb} + \omega_c)y_s) \cdot \boldsymbol{i}_c + (\dot{y}_s + (\Omega_{zb} + \omega_c)x_s) \cdot \boldsymbol{j}_c + (\dot{z}_s + \dot{z}_b) \cdot \boldsymbol{k}_c \\ \boldsymbol{a}_{G1\text{-}as} = (\ddot{x}_s - 2(\omega_c + \Omega_{zb})\dot{y}_s - (\Omega_{zb} + \omega_c)^2 x_s) \cdot \boldsymbol{i}_c \\ + (\ddot{y}_s + 2(\omega_c + \Omega_{zb})\dot{x}_s - (\Omega_{zb} + \omega_c)^2 y_s) \cdot \boldsymbol{j}_c + \ddot{z}_s \cdot \boldsymbol{k}_c \end{cases}$$
(6-14)

$$\begin{cases} \mathbf{v}_{GI\text{-}ap} = (\dot{\xi}_{p} - (\omega_{c} + \Omega_{zb})\eta_{p})\mathbf{i}_{p} + (\dot{\eta}_{p} + (\omega_{c} + \Omega_{zb})(\xi_{p} + r_{c}))\mathbf{j}_{p} + (\dot{z}_{p} + \dot{z}_{b})\mathbf{k}_{p} \\ \mathbf{a}_{GI\text{-}ap} = (\ddot{\xi}_{p} - 2(\omega_{c} + \Omega_{zb})\dot{\eta}_{p} - (\omega_{c} + \Omega_{zb})^{2}(\xi_{p} + r_{c})) \cdot \mathbf{i}_{p} \\ + (\ddot{\eta}_{p} + 2(\omega_{c} + \Omega_{zb})\dot{\xi}_{p} - (\omega_{c} + \Omega_{zb})^{2}\eta_{p}) \cdot \mathbf{j}_{p} + \ddot{z}_{p} \cdot \mathbf{k}_{p} \end{cases}$$
(6-15)

Additionally, due to the presence of multiple coordinate systems in the dynamics equations and the continuously varying rotation angle of the carrier, the expressions for the components of gravitational force in each component local coordinate system are represented as follows.

$$\begin{cases}
G_{GIj} = m_{Gj}g \cdot (-\sin(\theta_{zb} + \theta_c) \cdot \boldsymbol{i}_c - \cos(\theta_{zb} + \theta_c) \cdot \boldsymbol{j}_c + 0 \cdot \boldsymbol{k}_c) \\
G_{GIp} = m_{Gj}g \cdot (-\sin(\theta_{zb} + \theta_c + \phi_p) \cdot \boldsymbol{i}_c - \cos(\theta_{zb} + \theta_c + \phi_p) \cdot \boldsymbol{j}_c + 0 \cdot \boldsymbol{k}_c)
\end{cases}$$

$$\begin{cases}
G_{G2j} = m_{Gj}g \cdot (-\sin(\theta_{zb}) \cdot \boldsymbol{i}_c - \cos(\theta_{zb}) \cdot \boldsymbol{j}_c + 0 \cdot \boldsymbol{k}_c) \\
G_{G2p} = m_{Gj}g \cdot (-\sin(\theta_{zb} + \phi_p) \cdot \boldsymbol{i}_c - \cos(\theta_{zb} + \phi_p) \cdot \boldsymbol{j}_c + 0 \cdot \boldsymbol{k}_c)
\end{cases}$$
(6-16)

in while, the subscript p denotes the planets in the planetary gear system, while the subscript j represents other components within the system. Furthermore, the digits 1 and 2 correspond to the first stage and second stage for the compound gear system, respectively.

6.4.2 Influence of ship rocking motion on the vibrational response of central components

Under ship rocking motion, the entire compound planetary gear system is influenced by multiple non-inertial reference frames, in contrast to a single intrinsic non-inertial frame. In this study, the chosen rocking period is 4 seconds, with a maximum rocking angle of 45°. Fig.6-4 illustrates the corresponding angular displacement results for the selected sway parameters

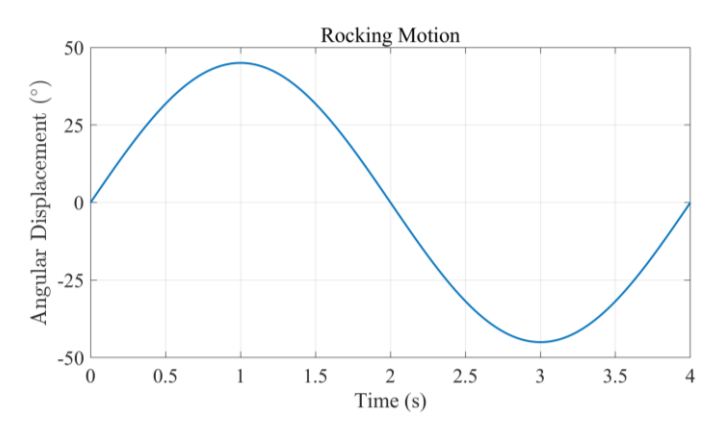


Fig.6-4 Sketch diagram of swinging motion

Utilizing the improved Newmark-beta method proposed in Chapter 4 to solve the dynamic equations of the entire compound gear system under two non-inertial reference frames, the vibrational displacement, velocity, and acceleration for each node are obtained. Accordingly, Fig.6-5 presents the lateral dynamic response of the carrier (representing the central component) in the first stage over one rocking period (4 seconds).

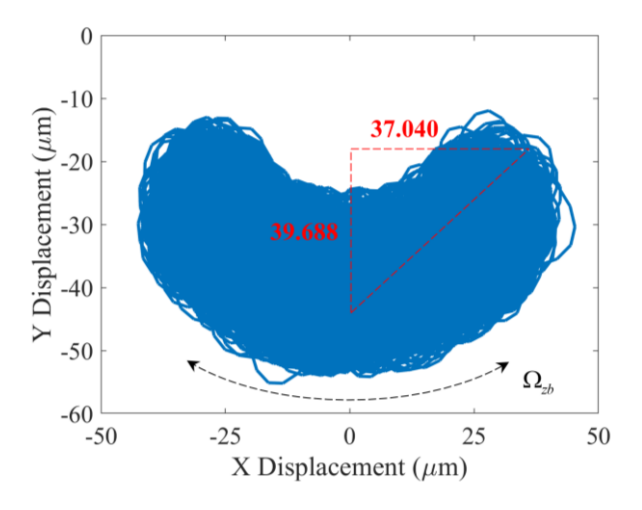


Fig.6-5 Orbit of carrier in the first stage

The axis trajectory shown in Fig.6-5 indicates that the central component undergoes lateral rocking motion in the *XOY* plane, following the rocking of the ship hull, as indicated by the dashed arrows. This phenomenon preliminarily suggests that the dynamic response of the derived equations aligns with the direction and trend of external forces on the ship. Further analysis of the data in Fig.6-5 reveals that the distance from the swing center to the midpoint of the vibrational response path (illustrated by the red dashed lines and annotations) indicates that the maximum lateral displacement of the carrier in first-stage during the rocking is 37.040 microns, while the maximum vertical displacement is 39.688 microns. These two distances are approximately equal, and simulations based on these values yield a swing angle of approximately 46.977°. This closely aligns with the theoretical swing angle of 45°, confirming the accuracy of the dynamic models established in this chapter under multiple non-inertial coordinate frames.

Fig.6-6 illustrates the lateral axis trajectory response of the sun in second stage over one sway cycle, along with a schematic analysis. Since the second stage lacks a moving coordinate system for the carrier, it is not affected by the non-inertial frame of the carrier in that stage. Consequently, the vibrational response occurs directly within the coordinate system of the ship hull sway, eliminating the need for coordinate transformations as required for the first-stage components.

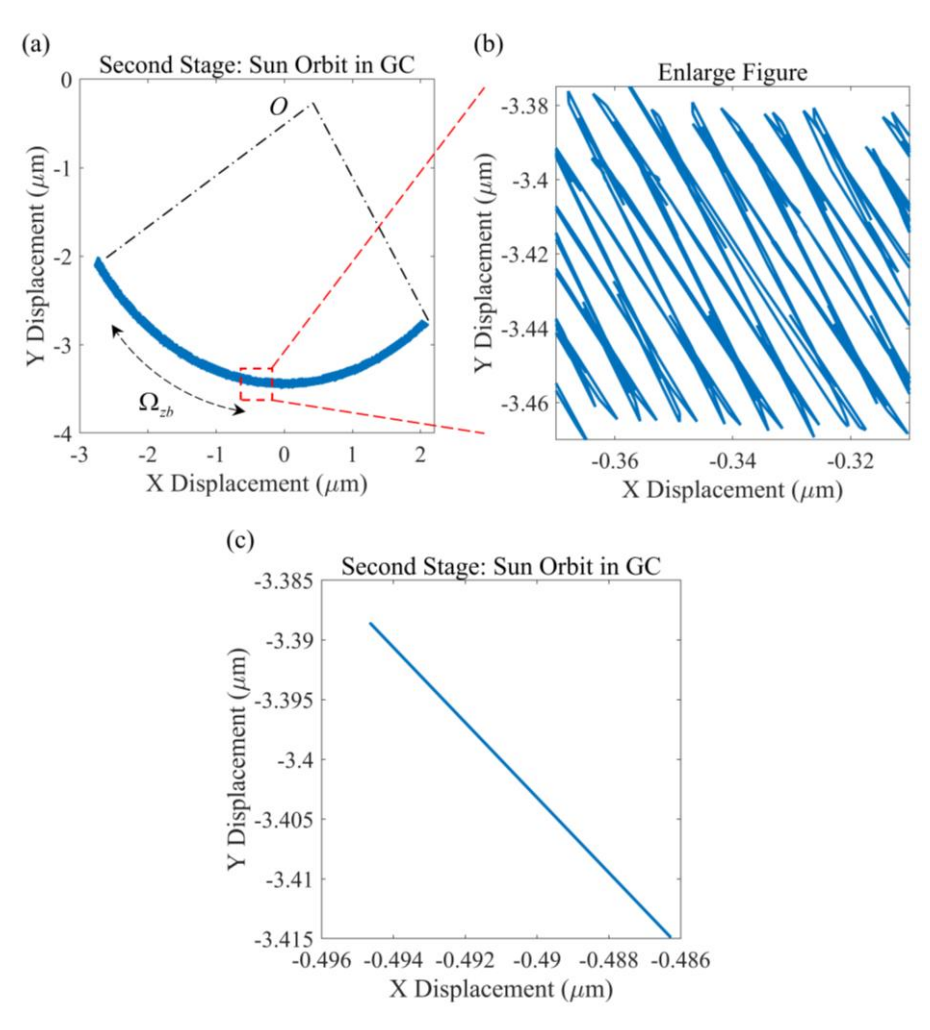


Fig.6-6 The transverse vibration displacement of sun in second stage

Fig.6-6 (a) also clearly shows that the trajectory of the sun moves periodically around point O. Fig.6-6 (b) provides a magnified view of this trajectory for a more detailed analysis. Fig.6-6 (c) illustrates the axis trajectory of the sun under the influence of gravity, without considering the swing motion. The trajectory shown in Fig.6-6 (c) effectively explains the vibrational response depicted in Fig.6-6 (b) and indirectly validates the observations in Fig.6-6 (a). Based on the trajectory analysis in Fig.6-6 (a), (b), and (c), it can be accurately predicted that the trajectory of central components, such as the ring, in the second-stage gear system under sway motion.

Corresponding to the sun gear in Fig.6-6, Fig.6-7 illustrates the axis trajectory of the ring in the second stage, both considering and neglecting sway

motion. Similar to Fig.6-6 (a), Fig.6-7 (a) clearly depicts the sway motion and the sway center point O. Fig.6-7 (b) provides a magnified view of Figure 6-5(a), while Fig.6-7 (c) shows the axis trajectory of the ring without considering sway motion. The trajectory displayed in Fig.6-7 (b) indicates that the ring path is composed of multiple segments similar to those in Fig.6-7 (c). Therefore, Fig.6-7 (b) and (c) indirectly validate the observed axis trajectory of the ring under sway motion.

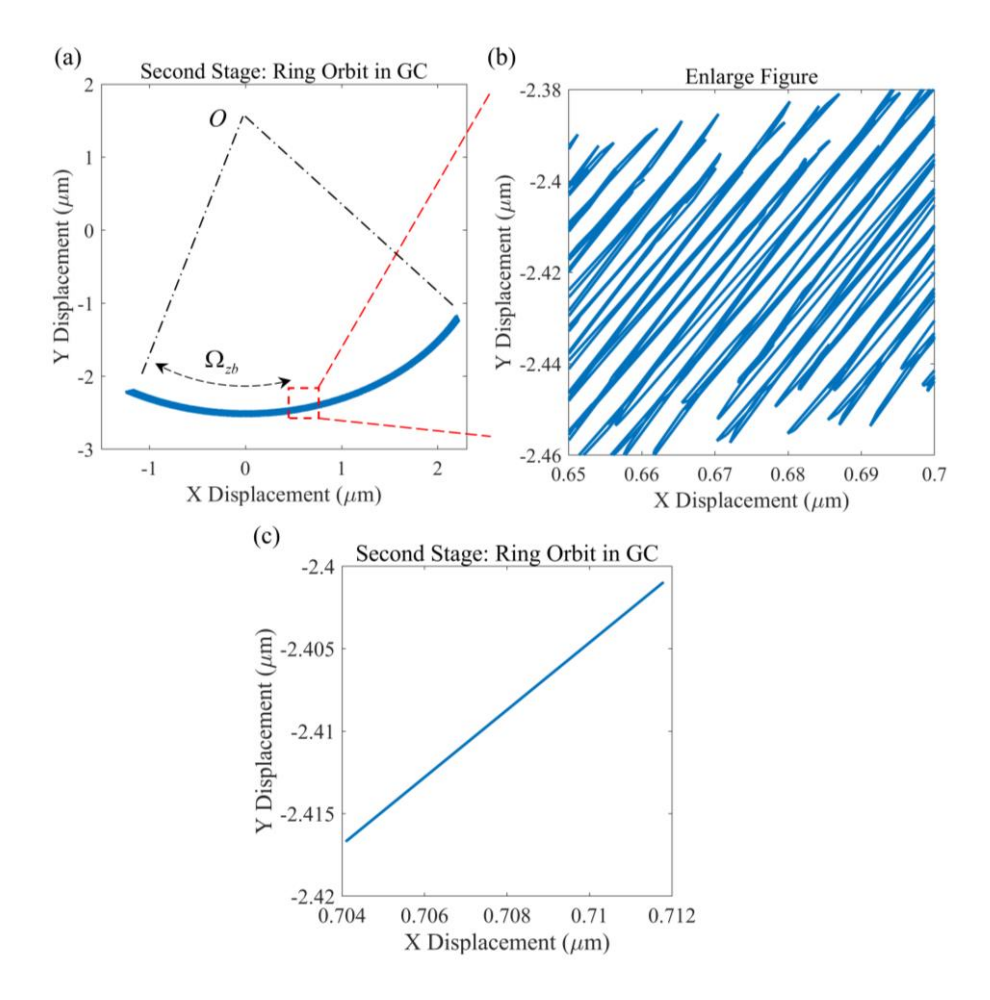


Fig.6-7 The transverse vibration displacement of ring in second stage

Moreover, an interesting phenomenon can be observed in Fig.6-6 (a) and Fig.6-7 (a), their axis trajectories are not symmetrically aligned about the vertical line X=0. This asymmetry can be explained by the trajectories illustrated in Fig.6-6 (c) and Fig.6-7 (c).

Therefore, the analysis of the vibrational response of the central components reveals that their motion trends in the fixed coordinate system are consistent with sway motion, highlighting the influence of ship rocking motion.

6.4.3 Influence of ship rocking motion on the vibration response of planets

Considering rocking motion, the first-stage planet gear not only follows the revolution of the carrier but also the motion of the ship hull. Consequently, under the influence of two angular velocities, the centrifugal force on the planet gear differs from that under a single angular velocity. In this study, the rocking motion angular velocity is 1.5708 rad/s, while the input speed of the compound gear system is 3300 rpm, resulting in a carrier angular velocity of 18.8496 rad/s. Based on equation (6-15), the centrifugal force formula for the first-stage planet gear can be expanded to $m_p r_c(\Omega_{zb} + \omega_c)^2$, which includes the effects of rocking motion. Although the rocking angular velocity Ω_{zb}^2 is relatively small compared to the carrier angular velocity ω_c^2 , an additional term $2\Omega_{zb}\omega_c$ also exists. Therefore, it is essential to investigate the impact of rocking motion on the vibration response of the first-stage planet gear in the radial coordinate direction. Figure 6-6 illustrates a comparative schematic of the axis trajectory of the first-stage planet gear in the inertial reference frame, both with and without considering rocking motion.

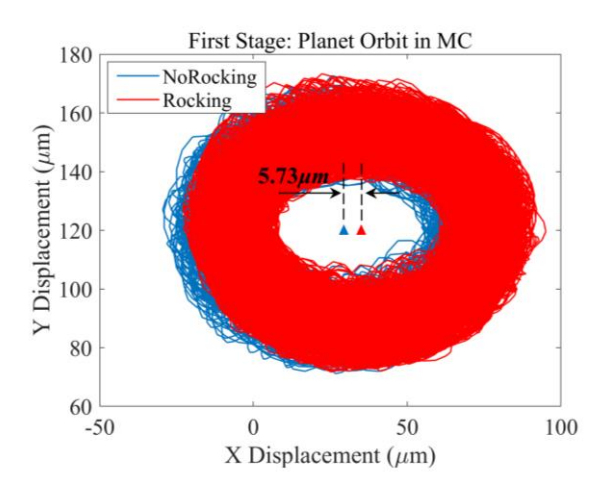


Fig.6-8 Comparison of the orbit of planets in first stage without and with consideration of the rocking motion

The results show that, after accounting for ship rocking motion, the midpoint of the radial displacement of the first-stage planet gear increases from 29.2481 microns to 34.9751 microns, resulting in a radial shift of 5.73 microns, approximately 19.58% greater than the original trajectory midpoint.

Rocking motion affects the components of the second stage system by transforming their movement into one influenced by an external non-inertial frame. As a result, the motion of the planets is described in a moving coordinate system, leading to the generation of an additional centrifugal force. Fig.6-9 illustrates a comparative schematic of the axis trajectory of the planets in second stage in the radial-tangential moving coordinate system, both with and without considering rocking motion

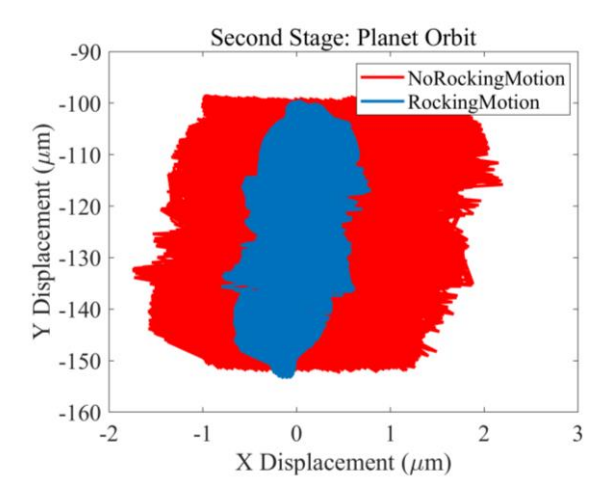


Fig.6-9 Comparison of the orbit of planets in second stage without and with consideration of the rocking motion

Fig.6-9 indicates that, compared to the axis trajectory without considering rocking motion (blue part), the presence of rocking motion significantly increases the trajectory range of the planet gear of second-stage in the radial direction (red part) by approximately 2-3 times. However, with a rocking angular velocity of only 1.5708 rad/s, the impact of centrifugal force on the trajectory remains limited. Therefore, it can be inferred that the observed changes in the trajectory are primarily due to the effects of rocking motion itself.

6.4.4 Influence of ship rocking motion on the motion state of the compound gear train

Building on the research from Chapters 4 and 5, the nonlinear dynamic behavior of the compound gear system used in ship within a internial non-inertial conditions has been established, detailing the fundamental cause of the 700T periodic motion. This chapter also analyze the motion state of the entire compound

gear system under the influence of rocking motion, which significantly changes the form of the dynamic equations. Fig.6-10 presents the phase trajectory and Poincaré map of the sun gear in first stage, demonstrating that the entire gear system exhibits a chaotic motion state under the influence of rocking motion.

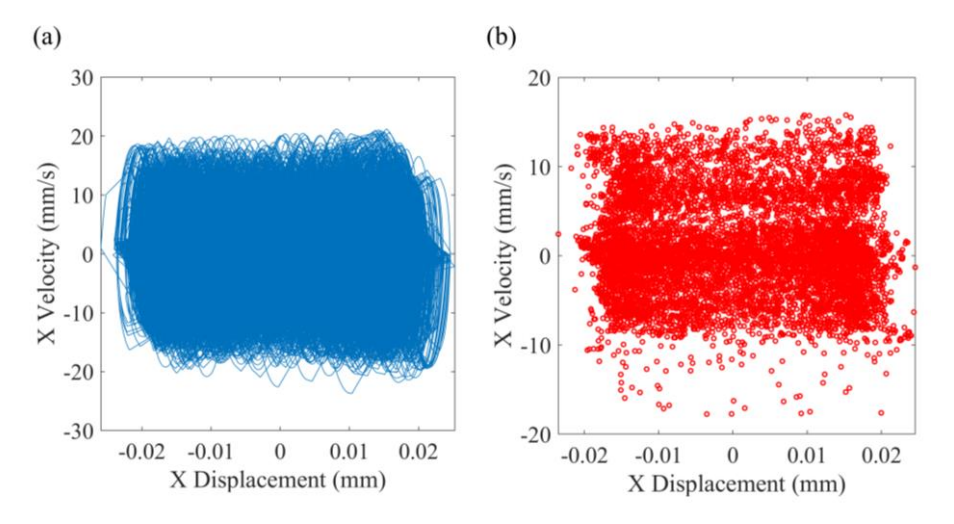


Fig.6-10 Transverse vibration of sun in first stage during one rocking cycle: (a) phase trajectory, (b) Poincare map diagram

Corresponding to the phase trajectory and Poincaré map, the variation of lateral displacement of the sun gear in first stage versus time is illustrated in Fig.6-11. Fig.6-11 (a) presents the complete time history over one rocking cycle, while Fig.6-11 (b) and (c) provide supplementary information. Based on Fig.6-10, Fig.6-11 (a), and Fig.6-11 (b), it is evident that the system is currently in a chaotic motion state. Furthermore, Fig.6-11 (c) highlights the numerous peaks within a repeating time, displaying no discernible pattern, thereby reinforcing the conclusion of chaotic behavior.

Therefore, this subsection concludes that the presence of rocking motion has transformed the fundamental 700T periodic motion of the compound gear system into a chaotic state. Although the motion is now chaotic, the range of displacement amplitude remains largely unchanged compared to the results in Chapter 4; it simply indicates that the motion has become more complex.

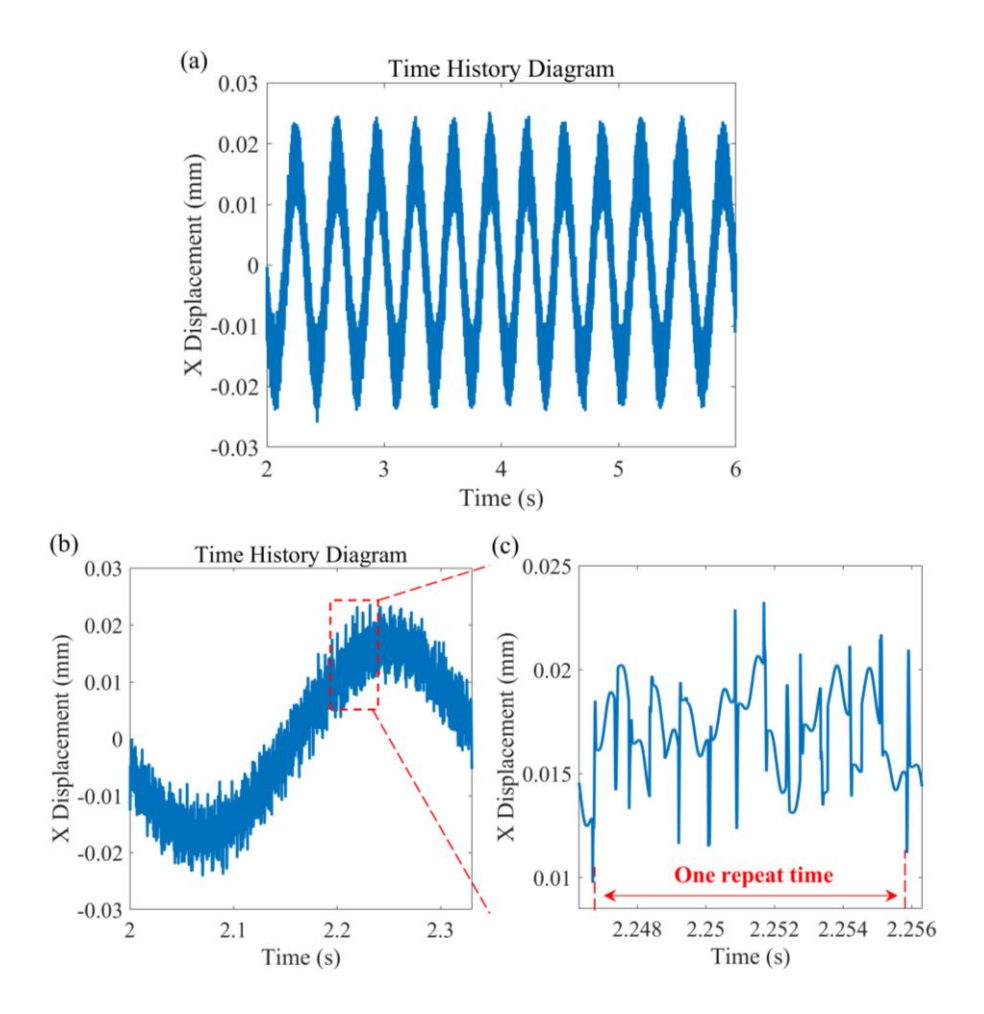


Fig.6-11 Transverse vibration displacements of the sun in first stage for one swinging cycle: (a) time history diagram, (b) local time history maps, (c) time history diagram over a short period of time

6.5 Dynamic characteristics analysis of compound marine gear transmission system considering ship pitching motion

6.5.1 Calculation of generalized acceleration considering ship pitching motion

For the pitch motion, the angular velocity vector Ω of the hull coordinate system $(o_b-x_by_bz_b)$ in Fig.6-2 can be expressed using the following formula.

$$\mathbf{\Omega} = \Omega_{xb} \cdot \mathbf{i}_b \tag{6-17}$$

According to the principles of pitching motion, the relationships between the unit vectors of various coordinate systems are as follows:

$$\begin{cases}
\mathbf{i} = \mathbf{i}_{b} \\
\mathbf{j} = \cos \theta_{xb} \cdot \mathbf{j}_{b} - \sin \theta_{xb} \cdot \mathbf{k}_{b} \\
\mathbf{k} = \sin \theta_{xb} \cdot \mathbf{j}_{b} + \cos \theta_{xb} \cdot \mathbf{k}_{b}
\end{cases}$$

$$\begin{cases}
\mathbf{i}_{b} = \cos \theta_{c} \cdot \mathbf{i}_{c} - \sin \theta_{c} \cdot \mathbf{j}_{c} \\
\mathbf{j}_{b} = \sin \theta_{c} \cdot \mathbf{i}_{c} + \cos \theta_{c} \cdot \mathbf{j}_{c} \\
\mathbf{k}_{b} = \mathbf{k}_{c}
\end{cases}$$

$$\begin{cases}
\mathbf{i}_{b} = \cos(\theta_{c} + \phi_{p}) \cdot \mathbf{i}_{p} - \sin(\theta_{c} + \phi_{p}) \cdot \mathbf{j}_{p} \\
\mathbf{j}_{b} = \sin(\theta_{c} + \phi_{p}) \cdot \mathbf{i}_{p} + \cos(\theta_{c} + \phi_{p}) \cdot \mathbf{j}_{p} \\
\mathbf{k}_{b} = \mathbf{k}_{p}
\end{cases}$$

$$(6-18)$$

Therefore, based on the analysis of the absolute acceleration of components in both internal and external non-inertial frames in section 6.3.1, expressions for the absolute velocity and acceleration of components within the compound gear system under the influence of both non-inertial frames have been derived. Utilizing the relationship equations between coordinate systems (6-18), the computational formulas for the second-stage and first-stage sun gear nodes (representing the central gear) and the planet gear nodes in their respective coordinate systems are presented as follows:

$$\begin{cases} \mathbf{v}_{G2\text{-}as} = \dot{x}_{s} \cdot \mathbf{i}_{c} + (\dot{y}_{s} - \Omega_{xb} z_{s} - \Omega_{xb} (z_{s0} + z_{b}) + \dot{z}_{b} \sin \theta_{xb}) \cdot \mathbf{j}_{c} \\ + (\dot{z}_{s} + \Omega_{xb} y_{s} + \dot{z}_{b} \cos \theta_{xb}) \cdot \mathbf{k}_{c} \\ \mathbf{a}_{G2\text{-}as} = \ddot{x}_{s} \cdot \mathbf{i}_{c} + (\ddot{y}_{s} - \dot{\Omega}_{xb} (z_{s} + z_{s0}) - \Omega_{xb}^{2} y_{s} - 2\Omega_{xb} \dot{z}_{s}) \cdot \mathbf{j}_{c} \\ + (\ddot{z}_{s} + \dot{\Omega}_{xb} y_{s} - \Omega_{xb}^{2} (z_{s} + z_{s0} + z_{b}) + 2\Omega_{xb} \dot{y}_{s}) \cdot \mathbf{k}_{c} \end{cases}$$

$$(6-19)$$

$$\begin{cases} \mathbf{v}_{G2\text{-}ep} = (\dot{x}_{p} + \dot{z}_{b} \sin(\phi_{p}) \sin \theta_{xb} - \Omega_{xb} \sin(\phi_{p})(z_{b} + z_{p})) \cdot \mathbf{i}_{p} \\ + (\dot{y}_{p} + \dot{z}_{b} \cos(\phi_{p}) \sin \theta_{xb} - \Omega_{xb} \cos(\phi_{p})(z_{b} + z_{p})) \cdot \mathbf{j}_{p} \\ + (\dot{z}_{p} + \dot{z}_{b} \cos \theta_{xb} + \Omega_{xb} \sin \phi_{p}(x_{p} + r_{c}) + \Omega_{xb} \cos \phi_{p} y_{p}) \cdot \mathbf{k}_{p} \end{cases}$$

$$\mathbf{a}_{G2\text{-}ep} = (\ddot{x}_{p} - \dot{\Omega}_{xb} z_{p} \sin \phi_{p} - \Omega_{xb}^{2}(x_{p} + r_{c}) \sin^{2} \phi_{p} \\ - \Omega_{xb}^{2} y_{p} \sin \phi_{p} \cos \phi_{p} - 2\Omega_{xb} \dot{z}_{p} \sin \phi_{p}) \mathbf{i}_{p}$$

$$+ (\ddot{y}_{p} - \dot{\Omega}_{xb} z_{p} \cos \phi_{p} - \Omega_{xb}^{2}(x_{p} + r_{c}) \sin \phi_{p} \cos \phi_{p} \\ - \Omega_{xb}^{2} y_{p} \cos^{2} \phi_{p} - 2\Omega_{xb} \dot{z}_{p} \cos \phi_{p}) \mathbf{j}_{p}$$

$$+ (\ddot{z}_{p} \dot{\Omega}_{xb} \sin \phi_{p}(x_{p} + r_{c}) - \dot{\Omega}_{xb} \cos \phi_{p} y_{p} \\ - \Omega_{xb}^{2}(z_{p} + z_{b}) + 2\Omega_{xb} (\dot{x}_{p} \sin \phi_{p} + \dot{y}_{p} \cos \phi_{p})) \mathbf{k}_{p} \end{cases}$$

$$(6-20)$$

$$\begin{cases} \mathbf{v}_{GI\text{-}as} = (\dot{x}_s - \omega_c y_s + \dot{z}_b \sin \theta_{sb} \sin \theta_c - \Omega_{sb} (z_b + z_s + z_{s0}) \sin \theta_c) \cdot \mathbf{i}_c \\ + (\dot{y}_s + \omega_c x_s + \dot{z}_b \sin \theta_{sb} \cos \theta_c - \Omega_{sb} (z_b + z_s + z_{s0}) \cos \theta_c) \cdot \mathbf{j}_c \\ + (\dot{z}_s + \Omega_{sb} (x_s \sin \theta_c + y_s \cos \theta_c) + \dot{z}_b \cos \theta_{sb}) \cdot \mathbf{k}_c \\ \mathbf{a}_{GI\text{-}as} = (\ddot{x}_s - 2\omega_c \dot{y}_s - \dot{\omega}_c y_s - \omega_c^2 x_s - \dot{\Omega}_{sb} (z_s + z_{s0}) \sin \theta_c \\ - \Omega_{sb}^2 \sin \theta_c (x_s \sin \theta_c + y_s \cos \theta_c) \\ - 2\Omega_{sb}^2 \dot{z}_s \sin \theta_c + \Omega_{sb} \omega_c (z_s + z_{s0}) \cos \theta_c) \cdot \mathbf{i}_c \\ + (\ddot{y}_s + 2\omega_c \dot{x}_s + \dot{\omega}_c x_s - \omega_c^2 y_s - \dot{\Omega}_{sb} (z_s + z_{s0}) \cos \theta_c \\ - \Omega_{sb}^2 \cos \theta_c (x_s \sin \theta_c + y_s \cos \theta_c) \\ - 2\Omega_{sb} \dot{z}_s \cos \theta_c - \Omega_{sb} \omega_c (z_s + z_{s0}) \sin \theta_c) \cdot \mathbf{j}_c \\ + (\ddot{z}_s + \dot{\Omega}_{sb} (x_s \sin \theta_c + y_s \cos \theta_c) - \Omega_{sb}^2 (z_s + z_{s0} + z_b) \\ + 2\Omega_{sb} (\dot{x}_s \sin \theta_c + \dot{y}_s \cos \theta_c) - \Omega_{sb} \dot{\omega}_c (x_s \cos \theta_c - y_s \sin \theta_c)) \cdot \mathbf{k}_c \end{cases}$$

$$\begin{cases} \mathbf{v}_{GI\text{-}ap} = (\dot{x}_p - \omega_c y_p + \dot{z}_b \sin \theta_{sb} \sin (\theta_c + \phi_p) - \Omega_{sb} \sin (\theta_c + \phi_p) (z_b + z_p)) \cdot \mathbf{i}_p \\ + (\dot{y}_p + \omega_c (x_p + r_c) + \dot{z}_b \sin \theta_{sb} \cos (\theta_c + \phi_p) \\ - \Omega_{sb} \cos (\theta_c + \phi_p) (z_b + z_p)) \cdot \mathbf{j}_p \\ + (\dot{z}_p + \dot{z}_b \cos \theta_{sb} + \Omega_{sb} \sin (\theta_c + \phi_p) (x_p + r_c) \\ + \Omega_{sb} \cos (\theta_c + \phi_p) y_p \cdot \dot{k}_p \end{cases}$$

$$\mathbf{a}_{GI\text{-}ap} = (\ddot{\xi}_p - 2\omega_c \dot{\eta}_p - \omega_c^2 \ddot{\xi}_p - \omega_c^2 r_c \\ - \Omega_{sb}^2 (x_p + r_c) \sin^2 (\theta_c + \phi_p) - \dot{\Omega}_{sb} z_p \sin (\theta_c + \phi_p) \cdot \mathbf{i}_p \\ + (\ddot{\eta}_p + 2\omega_c \dot{\xi}_p - \omega_c^2 \eta_p - \dot{\omega}_c r_c \\ - \Omega_{sb}^2 (x_p + r_c) \sin (\theta_c + \phi_p) \cos (\theta_c + \phi_p) - \dot{\Omega}_{sb} z_p \cos (\theta_c + \phi_p) \\ - \Omega_{sb} \dot{z}_p \cos (\theta_c + \phi_p) - \Omega_{sb} \omega_c z_p \sin (\theta_c + \phi_p) \cdot \dot{y}_p \\ + (\ddot{z}_p - \Omega_{sb}^2 (z_p + z_b) + \dot{\Omega}_{sb} \sin (\theta_c + \phi_p) (x_p + r_c) \\ - \dot{\Omega}_{sb} \cos (\theta_c + \phi_p) + \dot{y}_p \sin (\theta_c + \phi_p) \sin (\theta_c + \phi_p) \cdot \dot{y}_p \\ + (\ddot{z}_p - \Omega_{sb}^2 (z_p + z_b) + \dot{\Omega}_{sb} \sin (\theta_c + \phi_p) (x_p + r_c) \\ - \dot{\Omega}_{sb} \cos (\theta_c + \phi_p) + \dot{y}_p \sin (\theta_c + \phi_p) + \dot{y}_p \sin (\theta_c + \phi_p) \cdot \dot{y}_p \sin (\theta_c + \phi_p) \\ + (\ddot{z}_p - \Omega_{sb}^2 (z_p + z_b) + \dot{\Omega}_{sb} \sin (\theta_c + \phi_p) (x_p + r_c) \\ - \dot{\Omega}_{sb} \cos (\theta_c + \phi_p) + \dot{y}_p \sin (\theta_c + \phi_p) + \dot{y}_p \sin (\theta_c + \phi_p) \cdot \dot{y}_p \sin (\theta_c + \phi_p) \\ + (\dot{\Omega}_{sb}$$

Additionally, given the presence of multiple coordinate systems in the dynamic equations and the continuously varying rotation angle of the planet frame,

the expressions for the gravitational components of each component along the axes of its own coordinate system are represented as follows

$$\begin{cases}
G_{GIj} = m_{Gj}g \cdot \cos \theta_{xb} \cdot (-\sin(\theta_c) \cdot \boldsymbol{i}_c - \cos(\theta_c) \cdot \boldsymbol{j}_c + 0 \cdot \boldsymbol{k}_c) \\
G_{GIp} = m_{Gp}g \cdot \cos \theta_{xb} \cdot (-\sin(\theta_c + \phi_p) \cdot \boldsymbol{i}_c - \cos(\theta_c + \phi_p) \cdot \boldsymbol{j}_c + 0 \cdot \boldsymbol{k}_c)
\end{cases}$$

$$\begin{cases}
G_{G2j} = m_{Gj}g \cdot \cos \theta_{xb} \cdot (0 \cdot \boldsymbol{i}_c - 1 \cdot \boldsymbol{j}_c + 0 \cdot \boldsymbol{k}_c) \\
G_{G2p} = m_{Gp}g \cdot \cos \theta_{xb} \cdot (-\sin(\phi_p) \cdot \boldsymbol{i}_c - \cos(\phi_p) \cdot \boldsymbol{j}_c + 0 \cdot \boldsymbol{k}_c)
\end{cases}$$
(6-23)

6.5.2 Vibration response analysis of components considering ship pitching motion

The rocking motion of ship is characterized by the alignment of the rocking plane parallel to the ship own XOY coordinate plane, with an angle of 0° . In contrast, during pitching motion, the pitching plane is perpendicular to the ship XOY coordinate plane, resulting in a 90° angle. Consequently, the pitching plane is also at a 90° angle to the XOY plane of the compound planetary gear system. Although the coordinate systems of the compound gear system and the ship are parallel, there is a specific distance along the Z-axis between them, as indicated by z_b in the equations. Furthermore, a comparison of the absolute acceleration formulas for both motions reveals that the pitching motion has more influencing terms on the coordinate system of the planetary gear system. This section first analyzes the dynamic response of the model during pitching to validate the accuracy of the dynamic model. Fig.6-12 illustrates the lateral vibration response of sun gear and planet gear #1 in their own moving coordinate system (MC) for the first stage. Fig.6-12 (a) illustrates that the trajectory of the sun gear under pitching motion differs from that in Chapter 3, which did not consider pitching. The presence of pitching results in a triangular shape formed by three branches in the trajectory of the sun gear. Analysis indicates that in the moving coordinate system of the compound gear system, regardless of changes in the external noninertial frame, the first stage can always be viewed as a fixed-axis gear system. Since the first stage system comprises three planet gears with sequential phasing, the trajectory in the moving coordinate system displays a triangular shape. This further supports the accuracy of the dynamic model established under two noninertial frames, demonstrating that all terms related to pitching motion in

equations (6-19) to (6-22) were fully considered without omitting any terms from the absolute acceleration. Fig.6-12 (b) shows a similar triangular trajectory for the planet gears that mesh with the sun gear.

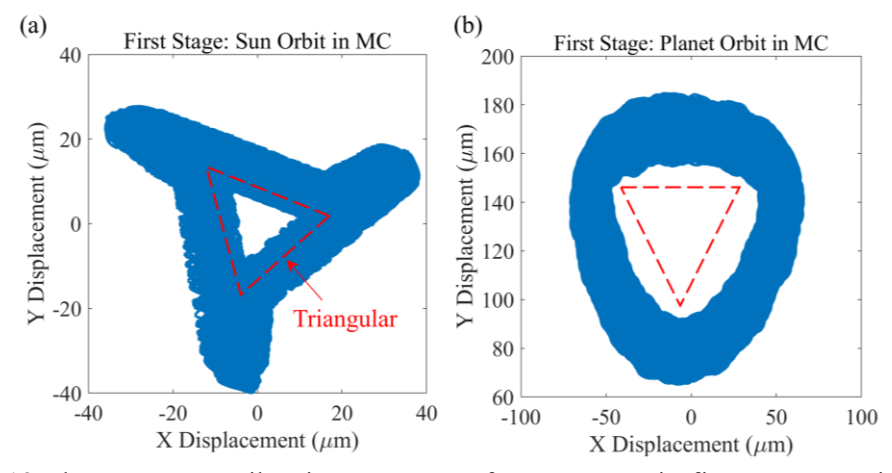


Fig.6-12 The transverse vibration response of components in first stage considering pitching motion: (a) sun, (b) planet #1

Additionally, the lateral vibration response of other components of the first-stage gear system, such as the carrier and the ring, is depicted in Fig.6-13. The axial trajectory shapes presented in Fig.6-13 also corroborate the triangular conclusion. Together with the results from Fig.6-12 for the sun and planets, this indicates that although the plane of the pitching motion is not the same as that of the axial trajectory, unlike rocking motion, the pitching motion of the ship hull still significantly influences the axial trajectories of the components in the first stage.

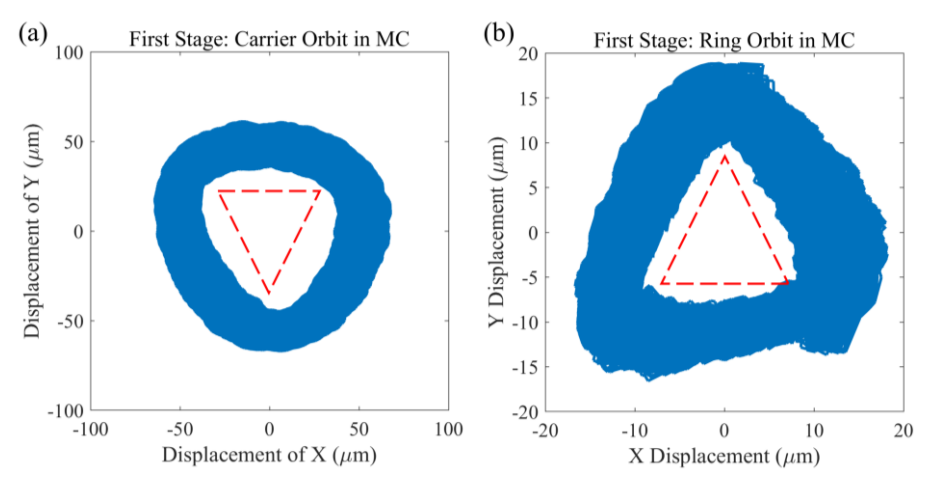


Fig.6-13 The transverse vibration response of components in first stage considering pitching motion: (a) carrier, (b) ring

6.5.3 Influence of picthing motion on the meshing characteristics

According to Section 6.5.2, although the pitching plane is at a 90° angle to the cross-section (XOY) of the compound gear system, the system position behind the ship, which closes to the propeller, indicating that under pitching motion, the XOY plane of the compound gear system is not always vertical, it may also rock with hull. This can potentially affect the meshing between gears. Therefore, analyzing the meshing characteristics of the gear system under pitching motion is essential. This section primarily focuses on the variation of the meshing forces. As the load sharing ratio carried by each planet gear reflects the changes in meshing force, the load-sharing ratios (LSR) of each planet gear within the system is analyzed.

Considering the pitching motion of ship and the reasonable eccentricity errors in the components of the compound gear system, Fig.6-14 presents the load sharing ratios (LSR) of the first stage.

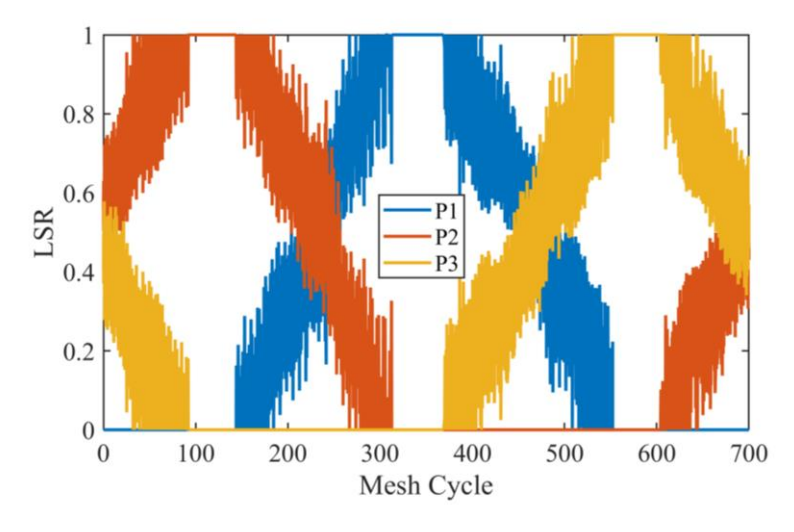


Fig.6-14 Sequential phase transmission of the first stage: LSR of planets

It is seen that, for planet gear #1, there are periods where it fully carries the transmitted load, as indicated by LSR=1, while during other intervals, it transfers no load (LSR=0). Throughout the remaining periods, the LSR for planet gear #1 varies between 0 and 1. This phenomenon is similarly observed in the other two planet gears, indicating that the load-bearing occurs in a rotating time among the three gears. Consequently, when one planet gear fully supports the load, the other two are disengaged, suggesting that the pitching motion negatively impacts the

meshing between the gears. The significant variation in load carried by the gears is detrimental to their lifespan, ultimately affecting the operational reliability of the entire compound gear system.

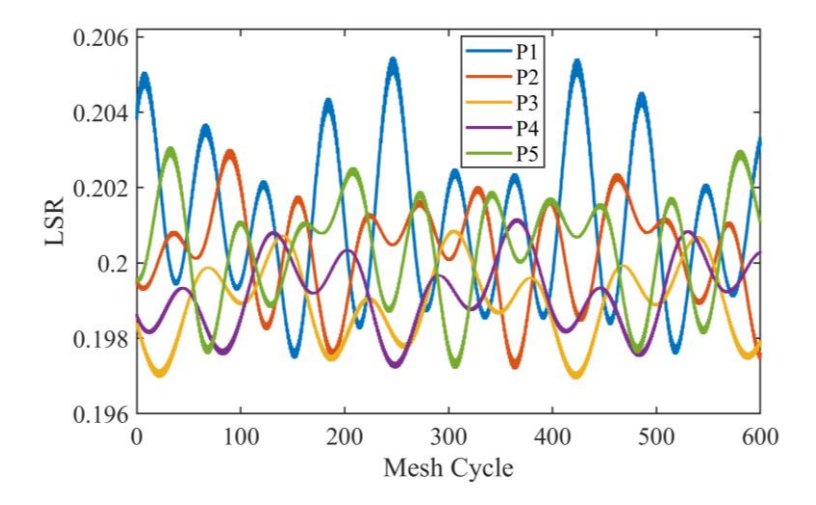


Fig.6-15 In phase transmission of the second stage: LSR of planets

Fig.6-15 illustrates the load sharing ratios (LSR) of the second stage. Although the LSR in the second stage exhibits less variation compared to the first stage, the meshing phase aligns with that of the first stage. The load sharing ratio of each planet gear deviates from the ideal value of 0.2, indicating changes in the loading conditions for each gear

Based on the analysis of the load sharing ratios for each stage of the gear system, it can be concluded that the pitching motion significantly affects the meshing characteristics of the first stage gear system more than the second stage. Severe pitching motions can lead to disengagement of gears within the differential gear system. To enhance the lifespan of the entire compound gear system, it is recommended that ships sould avoid significant vertical pitching motions during missions.

6.6 Brief summary

In this chapter, the formulas for the absolute accelerations of various components in a two-stage parallel compound gear system are derived, taking into account the external non-inertial reference frame. A dynamic model for the marine two-stage parallel compound gear system during navigation is established, and its dynamic characteristics under marine rocking and pitching motions are analyzed.

The main conclusions are as follows:

- (1) The absolute acceleration formulas indicate that the components of the compound gear system are influenced not only by the speed (ω_c) of carrier but also by the motion speed (Ω) of ship, including coupling terms between Ω and ωc .
- (2) The analysis of the lateral vibration response in the ship coordinate system shows that the motion trend of the central gear aligns with the rocking motion of ship. Because the angular velocities of the rocking motion and the carrier rotation being in the same plane, which verifies the validity of the established dynamic model of the entire compound gear system under rocking conditions.
- (3) During rocking motion, although the angular velocity of rocking (1.5708 rad/s) is significantly lower than that of the carrier (18.8496 rad/s) under normal conditions, the midpoint of the planet gear in first stage increases by 19.58% radially, indicating a significant impact of rocking on the dynamic response of the compound gear train.
- (4) Following the consideration of pitching motion, despite the introduction of additional variables in the absolute acceleration expression, the axial trajectory results of the components in first stage still align with the characteristics of fixed-axis gear systems, confirming the accuracy of the dynamic model under pitching motions. Furthermore, the analysis of load sharing ratios in both stages reveals that pitching motion can lead to disengagement of gears in the first stage at certain moments, negatively affecting the operational lifespan of the entire compound gear system.

Conclusions

In this paper, a two-stage parallel compound gear transmission system for ships is taken as the research object, and the modelling methods of the two-stage parallel compound gear system in fixed and moving coordinate systems are proposed, respectively. The equations for absolute acceleration in the fixed coordinate system are derived. The dynamic and static models of the two-stage parallel compound marine gear transmission system considering the flexible deformation of double-helical gears are developed. Furthermore, an improved Newmark-beta numerical calculation method is proposed. The accuracy of the established modeling method is verified by comparative analysis of the dynamic and static models, and the vibration response behaviour of the two-stage parallel compound gear system is investigated using this method. The pure torsional and translational-torsional nonlinear dynamic model of the two-stage parallel compound marine gear transmission system are developed and its dynamic characteristics are revealed. Finally, the dynamic model of the compound marine gear system under the external non-inertial coordinate system of the ship hull is established, and the impact rule of the dynamic characteristics of the compound gear system is analysed under the rocking and pitching motions of the ship. The conclusions obtained in this paper are as follows:

- (1) A dynamic and static modelling method for a two-stage parallel compound gear system for ships is proposed. Based on the combined use of fixed and moving coordinate systems, a projection vector about the vibration displacement of the carrier to the S-Pi and R-Pi meshing equations for the first-stage is introduced in this method. Thus, the problem of inaccurate dynamical equations caused by the absence of key acceleration terms such as implicated acceleration and Koch acceleration due to the rotation of the carrier is avoided. The forms of absolute velocity and absolute acceleration of different components in the first-stage under the moving coordinate system are derived. The lumped mass model under the moving coordinate system of the carrier in first stage is established. At the same time, considering the flexibility of the shaft, the overall dynamic model of the whole two-stage parallel compound gear system is obtained.
- (2) The influence laws of different error types on the load sharing ratio and global transmission error of the two-stage parallel compound gear system are revealed. The results show that the load sharing ratio of the gear train is affected by the meshing phase configuration, especially the fluctuation range of the load

change of the sequential phase configuration is larger than that of the in-phase configuration. The excitation frequency of the output shaft of the two-stage parallel compound gear system shows the coupling effect of the meshing frequencies of each stage. The tangential error under different meshing phase conditions affects the global transmission error differently, i.e., the sequential phase introduces additional excitation frequencies generated by the eccentricity error, whereas the in-phase does not activate any new frequency components. The floating configuration of sun improves the load distribution of the system in both mesh phasing configurations compared to the fixed configuration, which is more significant in the sequential phase configuration.

- (3) For the meshing time-varying stiffness matrix equation of the gear system, an improved Newmark-beta method suitable for this type of equation is proposed. The method adds a judgement on the relative error of the iteration results of adjacent time steps to avoid the influence of error accumulation on the process of solving the system dynamics equations. The vibration response of the system under the dynamics model was calculated using this method, and the dynamic and static results were compared to verify the accuracy of the modelling method proposed in this paper. The effects of gravity and centrifugal force on the transverse vibration response are further investigated. The results show that gravity and centrifugal force have important effects on the axial trajectory, in which the trajectory of the planets in first-stage changes significantly at high speed. The acceleration spectrograms of the planets in the two-stage show a strong coupling relationship. The rotational frequencies associated with time-varying errors (indexing error and eccentricity error) all appear on both sides of the meshing frequency, i.e., a frequency modulation phenomenon occurs.
- (4) Pure torsional and translational-torsional nonlinear dynamics models of the studied two-stage parallel compound gear system, which takes into account the segmental nonlinearity of the meshing displacements, are established. Based on the pure torsion model, the influence laws of each key parameter (meshing damping ratio, rotational speed, and magnitude of meshing error) on the nonlinear motion state of the compound gear system are investigated. The results show that under the condition of constant rotational speed, with the gradual increase of the meshing damping ratio in the range of 0.03-0.17, the compound gear system is first in the state of chaotic motion, and then enters into a longer period of quasi-periodic motion, and finally the system falls into a stable motion of 7 times periodic motion, and the Poincaré map, phase trajectory map, and time history diagrams that are consistent with the motion state are all observed under different

meshing damping ratio. When the damping ratio coefficient, input speed and torque are used as bifurcation parameters, the bifurcation of the system from unsteady state to stable state is Hopf bifurcation. When the meshing error is used as the bifurcation parameter, the multiply-periodic bifurcation appears in addition to the Hopf bifurcation. Unlike the law of the influence of the magnitude of the meshing error on the nonlinear dynamic response of the system, the system gradually transforms into a stable multiply-periodic motion as the damping ratio coefficients, input speed and torque increase.

- (5) The nonlinear vibration characteristics of the translational-torsional model are further investigated, and the results show that the motion states of both transverse vibration and relative torsional displacement are quasi-periodic motions and do not change significantly with the changes of damping ratio coefficients and rotational speed. Compared with the 7T periodic steady motion of the pure torsion model, the basic motion state of the translation-torsion model system is 700T periodic motion, which is the least common multiple of the meshing stiffness period of the two-stage and the period of the gravity term. It also shows that for the nonlinear study of complex structures, the strategy of starting from a pure torsion model and gradually exploring to a translational-torsion model is more detailed and perfect in explaining the arising complexity phenomena.
- (6) Considering the external non-inertial system, a dynamics model of the two-stage parallel compound marine gear transmission system is established. On the basis of the internal moving coordinate system of carrier, the model couples the overall motion of the ship, the dynamic behaviour of the two-stage compound marine gear transmission system during operation condition of ship is analyzed. when the ship is in the rocking and pitching motion, the dynamic characteristics of the whole compound gear system are obtained. The results of the study show that the form of absolute acceleration of the two-stage parallel compound gear system for ships under the non-inertial system shows obvious changes, and the acceleration terms under the influence of the extrinsic non-inertial system are significantly more than those under the internal non-inertial system. It indicates that the single external excitation applied to the compound gear system is not sufficient to establish an accurate dynamic model when the motion of the external non-inertial system is considered. The presence of the rocking motion of ship expands the radial vibration response range of the planets, leading to a change in the state of motion of this marine compound gear system from 700T periodic motion to chaotic motion. The study results of the pitching motion suggest that

ships should try to avoid severe waves in the forward direction to avoid disengagement of gears in high-speed stage.

References

- [1] F. Viadero, A. Fernández, M. Iglesias, A. De-Juan, E. Liaño, M.A. Serna, Non-stationary dynamic analysis of a wind turbine power drivetrain: Offshore considerations, Applied Acoustics 77 (2014) 204–211. https://doi.org/10.1016/j.apacoust.2013.10.006.
- [2] R. Chen, D. Qin, Y. Yi, C. Liu, J. Shi, Dynamic characteristics of electromechanical coupling of wind turbine drive system under multi-source excitation, Wind Energy 25 (2022) 391–418. https://doi.org/https://doi.org/10.1002/we.2678.
- [3] Y. Nie, F. Li, L. Wang, J. Li, M. Sun, M. Wang, J. Li, A mathematical model of vibration signal for multistage wind turbine gearboxes with transmission path effect analysis, Mechanism and Machine Theory 167 (2022) 104428. https://doi.org/10.1016/J.MECHMACHTHEORY.2021.104428.
- [4] Y.H. Xie, L.X. Xu, Y.Q. Deng, A dynamic approach for evaluating the moment rigidity and rotation precision of a bearing-planetary frame rotor system used in RV reducer, Mechanism and Machine Theory 173 (2022) 104851. https://doi.org/https://doi.org/10.1016/j.mechmachtheory.2022.104851.
- [5] M. Cammalleri, A. Castellano, Analysis of hybrid vehicle transmissions with any number of modes and planetary gearing: kinematics, power flows, mechanical power losses, Mechanism and Machine Theory 162 (2021). https://doi.org/10.1016/j.mechmachtheory.2021.104350.
- [6] A. Kahraman, Free torsional vibration characteristics of compound planetary gear sets, Mechanism and Machine Theory 36 (2001) 953–971. https://doi.org/10.1016/S0094-114X(01)00033-7.
- [7] S. Wang, R. Zhu, Nonlinear dynamic analysis of GTF gearbox under friction excitation with vibration characteristics recognition and control in frequency domain, Mechanical Systems and Signal Processing 151 (2021) 107373. https://doi.org/https://doi.org/10.1016/j.ymssp.2020.107373.
- [8] J.H. Kuang, Y.T. Yang, An Estimate of Mesh Stiffness and Load Sharing Ratio of a Spur Gear Pair, (1992) 1–9. https://doi.org/10.1115/DETC1992-0001.
- [9] Y. Cai, T. Hayashi, The Linear Approximated Equation of Vibration of a Pair of Spur Gears (Theory and Experiment), Journal of Mechanical Design 116 (1994) 558–564.

- https://doi.org/10.1115/1.2919414.
- [10] X. Liang, H. Zhang, L. Liu, M.J. Zuo, The influence of tooth pitting on the mesh stiffness of a pair of external spur gears, Mechanism and Machine Theory 106 (2016) 1–15. https://doi.org/https://doi.org/10.1016/j.mechmachtheory.2016.08.005.
- [11] H. Ma, J. Zeng, R. Feng, X. Pang, B. Wen, An improved analytical method for mesh stiffness calculation of spur gears with tip relief, Mechanism and Machine Theory 98 (2016) 64–80. https://doi.org/https://doi.org/10.1016/j.mechmachtheory.2015.11.017.
- [12] M.B. Sánchez, M. Pleguezuelos, J.I. Pedrero, Approximate equations for the meshing stiffness and the load sharing ratio of spur gears including hertzian effects, Mechanism and Machine Theory 109 (2017) 231–249. https://doi.org/https://doi.org/10.1016/j.mechmachtheory.2016.11.014.
- [13] Z. Li, C. Zhu, H. Liu, Z. Gu, Mesh stiffness and nonlinear dynamic response of a spur gear pair considering tribo-dynamic effect, Mechanism and Machine Theory 153 (2020)
 https://doi.org/https://doi.org/10.1016/j.mechmachtheory.2020.103989.
- [14] Z. Zhao, H. Han, P. Wang, H. Ma, S. Zhang, Y. Yang, An improved model for meshing characteristics analysis of spur gears considering fractal surface contact and friction, Mechanism and Machine Theory 158 (2021) 104219. https://doi.org/https://doi.org/10.1016/j.mechmachtheory.2020.104219.
- [15] W. Chen, Y. Lei, Y. Fu, L. Hou, A study of effects of tooth surface wear on time-varying mesh stiffness of external spur gear considering wear evolution process, Mechanism and Machine Theory 155 (2021) 104055. https://doi.org/https://doi.org/10.1016/j.mechmachtheory.2020.104055.
- [16] M. Pleguezuelos, M.B. Sánchez, J.I. Pedrero, Analytical model for meshing stiffness, load sharing, and transmission error for spur gears with profile modification under non-nominal load conditions, Applied Mathematical Modelling 97 (2021) 344–365. https://doi.org/https://doi.org/10.1016/j.apm.2021.03.051.
- [17] Z. Sun, S. Chen, Z. Hu, X. Tao, Improved mesh stiffness calculation model of comprehensive modification gears considering actual manufacturing, Mechanism and Machine Theory 167 (2022) 104470. https://doi.org/https://doi.org/10.1016/j.mechmachtheory.2021.104470.
- [18] C.G. Cooley, C. Liu, X. Dai, R.G. Parker, Gear tooth mesh stiffness: A comparison of calculation approaches, Mechanism and Machine Theory 105 (2016) 540-553.

- https://doi.org/10.1016/j.mechmachtheory.2016.07.021.
- [19] T. Kiekbusch, D. Sappok, B. Sauer, I. Howard, Calculation of the combined torsional mesh stiffness of spur gears with two- and three-dimensional parametrical FE models, Strojniski Vestnik/Journal of Mechanical Engineering 57 (2011) 810–818. https://doi.org/10.5545/sv-jme.2010.248.
- [20] H. Jerrar, A. El Marjani, E. Boudi, Calculation Model of Gear Meshing Stiffness Using FEM, International Review on Modelling and Simulations (IREMOS) 8 (2015) 477. https://doi.org/10.15866/iremos.v8i4.6492.
- [21] J. Zhan, M. Fard, R. Jazar, A CAD-FEM-QSA integration technique for determining the time-varying meshing stiffness of gear pairs, Measurement: Journal of the International Measurement Confederation 100 (2017) 139–149. https://doi.org/10.1016/j.measurement.2016.12.056.
- [22] L. Vedmar, B. Henriksson, A General Approach for Determining Dynamic Forces in Spur Gears, Journal of Mechanical Design 120 (1998) 593–598. https://doi.org/10.1115/1.2829320.
- [23] A. Fernandez del Rincon, F. Viadero, M. Iglesias, P. García, A. de-Juan, R. Sancibrian, A model for the study of meshing stiffness in spur gear transmissions, Mechanism and Machine Theory 61 (2013) 30–58. https://doi.org/https://doi.org/10.1016/j.mechmachtheory.2012.10.008.
- [24] M. Iglesias, A. Fernandez del Rincon, A. de-Juan, A. Diez-Ibarbia, P. Garcia, F. Viadero, Advanced model for the calculation of meshing forces in spur gear planetary transmissions, Meccanica 50 (2015) 1869–1894. https://doi.org/10.1007/s11012-015-0130-3.
- [25] X. Zheng, W. Luo, Y. Hu, Z. He, S. Wang, Study on the mesh stiffness and nonlinear dynamics accounting for centrifugal effect of high-speed spur gears, Mechanism and Machine Theory 170 (2022) 104686. https://doi.org/https://doi.org/10.1016/j.mechmachtheory.2021.104686.
- [26] Z. Wan, H. Cao, Y. Zi, W. He, Y. Chen, Mesh stiffness calculation using an accumulated integral potential energy method and dynamic analysis of helical gears, Mechanism and Machine Theory 92 (2015) 447–463. https://doi.org/https://doi.org/10.1016/j.mechmachtheory.2015.06.011.
- [27] M. Rezaei, M. Poursina, S.H. Jazi, F.H. Aboutalebi, Calculation of time dependent mesh stiffness of helical planetary gear system using analytical approach, Journal of

- Mechanical Science and Technology 32 (2018) 3537–3545. https://doi.org/10.1007/s12206-018-0704-9.
- [28] M. Feng, H. Ma, Z. Li, Q. Wang, B. Wen, An improved analytical method for calculating time-varying mesh stiffness of helical gears, Meccanica 53 (2018) 1131– 1145. https://doi.org/10.1007/s11012-017-0746-6.
- [29] Q. Wang, B. Zhao, Y. Fu, X. Kong, H. Ma, An improved time-varying mesh stiffness model for helical gear pairs considering axial mesh force component, Mechanical Systems and Signal Processing 106 (2018) 413–429. https://doi.org/https://doi.org/10.1016/j.ymssp.2018.01.012.
- [30] C. Zhang, H. Dong, D. Wang, B. Dong, A new effective mesh stiffness calculation method with accurate contact deformation model for spur and helical gear pairs, Mechanism and Machine Theory 171 (2022) 104762. https://doi.org/https://doi.org/10.1016/j.mechmachtheory.2022.104762.
- [31] W.-J. Chung, J.-H. Park, H.-G. Yoo, Y.-J. Park, S. Kim, J. Sohn, G. Lee, Improved analytical model for calculating mesh stiffness and transmission error of helical gears considering trochoidal root profile, Mechanism and Machine Theory 163 (2021) 104386. https://doi.org/https://doi.org/10.1016/j.mechmachtheory.2021.104386.
- [32] H. Yang, W. Shi, Z. Chen, N. Guo, An improved analytical method for mesh stiffness calculation of helical gear pair considering time-varying backlash, Mechanical Systems and Signal Processing 170 (2022) 108882. https://doi.org/https://doi.org/10.1016/j.ymssp.2022.108882.
- [33] S. Wang, R. Zhu, An improved mesh stiffness calculation model for cracked helical gear pair with spatial crack propagation path, Mechanical Systems and Signal Processing 172 (2022) 108989. https://doi.org/https://doi.org/10.1016/j.ymssp.2022.108989.
- [34] A.A. Ross, High speed gears, American Gear Manufacturers Association Paper (1927).
- [35] E. Bckingham, Dynamic loads on gear teeth, American Society of Mechanical Engineers Special Research Publication, 1931.
- [36] W.A. Tuplin, Dynamic Loads on Gear Teeth, Machine Design 25 (1953).
- [37] R.W. Gregory, S.L. Harris, G. R. G. Munro, Dynamic Behaviour of Spur Gears, Proceedings of the Institution of Mechanical Engineers 178 (1963) 207–218. https://doi.org/10.1177/002034836317800130.
- [38] H.N. Özgüven, A non-linear mathematical model for dynamic analysis of spur gears

- including shaft and bearing dynamics, Journal of Sound and Vibration 145 (1991) 239–260. https://doi.org/10.1016/0022-460X(91)90590-G.
- [39] A. Kahraman, H. Nevzatozguven, D.R. Houser, J.J. Zakrajsek, Dynamic analysis of geared rotors by finite elements, Journal of Mechanical Design, Transactions of the ASME 114 (1992) 507–514. https://doi.org/10.1115/1.2926579.
- [40] C.-S. Chen, S. Natsiavas, H.D. Nelson, Coupled Lateral-Torsional Vibration of a Gear-Pair System Supported by a Squeeze Film Damper, Journal of Vibration and Acoustics 120 (1998) 860–867. https://doi.org/10.1115/1.2893912.
- [41] W.D. MARK, ANALYSIS OF VIBRATORY EXCITATION OF GEAR SYSTEMS BASIC THEORY, JOURNAL OF THE ACOUSTICAL SOCIETY OF AMERICA 63 (1978) 1408–1430.
- [42] M.S. TAVAKOLI, D.R. HOUSER, OPTIMUM PROFILE MODIFICATIONS FOR THE MINIMIZATION OF STATIC TRANSMISSION ERRORS OF SPUR GEARS, JOURNAL OF MECHANISMS TRANSMISSIONS AND AUTOMATION IN DESIGN-TRANSACTIONS OF THE ASME 108 (1986) 86–95. https://doi.org/10.1115/1.3260791.
- [43] H.N. OZGUVEN, D.R. HOUSER, DYNAMIC ANALYSIS OF HIGH-SPEED GEARS BY USING LOADED STATIC TRANSMISSION ERROR, JOURNAL OF SOUND AND VIBRATION 125 (1988) 71–83. https://doi.org/10.1016/0022-460X(88)90416-6.
- [44] D.R. Houser, V.M. Bolze, J.M. Graber, A comparison of predicted end measured dynamic and static transmission error for spur and helical gear sets, in: PROCEEDINGS OF THE 14TH INTERNATIONAL MODAL ANALYSIS CONFERENCE, VOLS I \& II, 1996: pp. 1057–1062.
- [45] Y. Zhang, Z. Fang, Analysis of transmission errors under load of helical gears with modified tooth surfaces, JOURNAL OF MECHANICAL DESIGN 119 (1997) 120–126. https://doi.org/10.1115/1.2828773.
- [46] S. He, R. Singh, Dynamic transmission error prediction of helical gear pair under sliding friction using Floquet theory, JOURNAL OF MECHANICAL DESIGN 130 (2008). https://doi.org/10.1115/1.2890115.
- [47] F. Bruzzone, T. Maggi, C. Marcellini, C. Rosso, 2D nonlinear and non-Hertzian gear teeth deflection model for static transmission error calculation, Mechanism and Machine

 Theory 166 (2021) 104471.

- https://doi.org/https://doi.org/10.1016/j.mechmachtheory.2021.104471.
- [48] J.-H. Lee, H.-S. Choi, J.-H. Sohn, G.-H. Lee, D.-I. Park, J.-G. Kim, Statistical analysis for transmission error of gear system with mechanical and thermal deformation uncertainties, Applied Sciences 11 (2021) 6582.
- [49] H.H. LIN, D.P. TOWNSEND, F.B. OSWALD, PREDICTION OF GEAR DYNAMICS USING FAST FOURIER-TRANSFORM OF STATIC TRANSMISSION ERROR, MECHANICS OF STRUCTURES AND MACHINES 21 (1993) 237–260. https://doi.org/10.1080/08905459308905188.
- [50] P. Velex, M. Ajmi, On the modelling of excitations in geared systems by transmission errors, JOURNAL OF SOUND AND VIBRATION 290 (2006) 882–909. https://doi.org/10.1016/j.jsv.2005.04.033.
- [51] P. Velex, M. Ajmi, Dynamic tooth loads and quasi-static transmission errors in helical gears Approximate dynamic factor formulae, MECHANISM AND MACHINE THEORY 42 (2007) 1512–1526. https://doi.org/10.1016/j.mechmachtheory.2006.12.009.
- [52] P. Velex, J. Bruyere, D.R. Houser, Some Analytical Results on Transmission Errors in Narrow-Faced Spur and Helical Gears: Influence of Profile Modifications, JOURNAL OF MECHANICAL DESIGN 133 (2011). https://doi.org/10.1115/1.4003578.
- [53] T. Lin, Z. He, Analytical method for coupled transmission error of helical gear system with machining errors, assembly errors and tooth modifications, MECHANICAL SYSTEMS AND SIGNAL PROCESSING 91 (2017) 167–182. https://doi.org/10.1016/j.ymssp.2017.01.005.
- [54] J. Bruyere, P. Velex, B. Guilbert, D.R. Houser, An analytical study on the combination of profile relief and lead crown minimizing transmission error in narrow-faced helical gears, MECHANISM AND MACHINE THEORY 136 (2019) 224–243. https://doi.org/10.1016/j.mechmachtheory.2019.03.005.
- [55] M.R. Kang, A. Kahraman, An experimental and theoretical study of the dynamic behavior of double-helical gear sets, JOURNAL OF SOUND AND VIBRATION 350 (2015) 11–29. https://doi.org/10.1016/j.jsv.2015.04.008.
- [56] M.R. Kang, A. Kahraman, An Experimental and Theoretical Study of Quasi-Static Behavior of Double-Helical Gear Sets, JOURNAL OF MECHANICAL DESIGN 143 (2021). https://doi.org/10.1115/1.4047906.

- [57] M. Amabili, A. Rivola, Dynamic analysis of spur gear pairs: Steady-state response and stability of the SDOF model with time-varying meshing damping, MECHANICAL SYSTEMS AND SIGNAL PROCESSING 11 (1997) 375–390. https://doi.org/10.1006/mssp.1996.0072.
- [58] S. Li, A. Kahraman, A transient mixed elastohydrodynamic lubrication model for spur gear pairs, Journal of Tribology 132 (2010) 1–9. https://doi.org/10.1115/1.4000270.
- [59] S. Li, A. Kahraman, A spur gear mesh interface damping model based on elastohydrodynamic contact behaviour, International Journal of Powertrains 1 (2011) 4. https://doi.org/10.1504/ijpt.2011.041907.
- [60] M. VAISHYA, R. SINGH, ANALYSIS OF PERIODICALLY VARYING GEAR MESH SYSTEMS WITH COULOMB FRICTION USING FLOQUET THEORY, Journal of Sound and Vibration 243 (2001) 525–545. https://doi.org/https://doi.org/10.1006/jsvi.2000.3419.
- [61] S.H. Choi, J. Glienicke, D.C. Han, K. Urlichs, Dynamic gear loads due to coupled lateral, torsional and axial vibrations in a helical geared system, JOURNAL OF VIBRATION AND ACOUSTICS-TRANSACTIONS OF THE ASME 121 (1999) 141–148. https://doi.org/10.1115/1.2893956.
- [62] M. Li, L. Yu, Analysis of the coupled lateral torsional vibration of a rotor-bearing system with a misaligned gear coupling, JOURNAL OF SOUND AND VIBRATION 243 (2001) 283–300. https://doi.org/10.1006/jsvi.2000.3412.
- [63] C. Li, S. Zhou, J. Liu, Numerical Simulation of a Bending-Torsion Coupling Gear Transmission System, in: M. Sun, Y. Zhang (Eds.), RENEWABLE ENERGY AND ENVIRONMENTAL TECHNOLOGY, PTS 1-6, 2014: pp. 3403–3407. https://doi.org/10.4028/www.scientific.net/AMM.448-453.3403.
- [64] Z. Ren, J. Li, K. Wang, S. Zhou, Nonlinear dynamic analysis of a coupled lateral-torsional spur gear with eccentricity, JOURNAL OF VIBROENGINEERING 18 (2016) 4776–4791. https://doi.org/10.21595/jve.2016.17067.
- [65] S. Zhou, Z. Ren, G. Song, B. Wen, Dynamic Characteristics Analysis of the Coupled Lateral-Torsional Vibration with Spur Gear System, INTERNATIONAL JOURNAL OF ROTATING MACHINERY 2015 (2015). https://doi.org/10.1155/2015/371408.
- [66] Z. Hu, J. Tang, S. Chen, Analysis of coupled lateral-torsional vibration response of a geared shaft rotor system with and without gyroscopic effect, PROCEEDINGS OF THE INSTITUTION OF MECHANICAL ENGINEERS PART C-JOURNAL OF

- MECHANICAL ENGINEERING SCIENCE 232 (2018) 4550–4563. https://doi.org/10.1177/0954406217753457.
- [67] J. Wang, R. Li, X. Peng, Survey of nonlinear vibration of gear transmission systems, Applied Mechanics Reviews 56 (2003) 309–329. https://doi.org/10.1115/1.1555660.
- [68] C. Gill-Jeong, Analysis of the nonlinear behavior of gear pairs considering hydrodynamic lubrication and sliding friction, JOURNAL OF MECHANICAL SCIENCE AND TECHNOLOGY 23 (2009) 2125–2137. https://doi.org/10.1007/s12206-009-0623-x.
- [69] S. Zhou, J. Liu, C. Li, B. Wen, Nonlinear behavior of a spur gear pair transmission system with backlash, JOURNAL OF VIBROENGINEERING 16 (2014) 3850–3861.
- [70] G.J. Cheon, Effects of a one-way clutch on the nonlinear dynamic behavior of spur gear pairs under periodic excitation, Journal of Mechanical Science and Technology 20 (2006) 941–949. https://doi.org/10.1007/BF02915993.
- [71] J.-Y. Yoon, I. Lee, Nonlinear Analysis of Vibro-Impacts for Unloaded Gear Pairs With Various Excitations and System Parameters, JOURNAL OF VIBRATION AND ACOUSTICS-TRANSACTIONS OF THE ASME 136 (2014). https://doi.org/10.1115/1.4026927.
- [72] C.-W. Chang-Jian, S.-M. Chang, Bifurcation and chaos analysis of spur gear pair with and without nonlinear suspension, NONLINEAR ANALYSIS-REAL WORLD APPLICATIONS 12 (2011) 979–989. https://doi.org/10.1016/j.nonrwa.2010.08.021.
- [73] Y. Xia, Y. Wan, Z. Liu, Bifurcation and chaos analysis for a spur gear pair system with friction, JOURNAL OF THE BRAZILIAN SOCIETY OF MECHANICAL SCIENCES AND ENGINEERING 40 (2018). https://doi.org/10.1007/s40430-018-1443-7.
- [74] S. Yang, Y. Shen, Nonlinear dynamics of a spur gear pair with slight wear fault, in: H.Y. Hu, E. Kreuzer (Eds.), IUTAM SYMPOSIUM ON DYNAMICS AND CONTROL OF NONLINEAR SYSTEMS WITH UNCERTAINTY, 2007: p. 177+. https://doi.org/10.1007/978-1-4020-6332-9_18.
- [75] T. Eritenel, R.G. Parker, COMPUTATIONAL NONLINEAR VIBRATION ANALYSIS OF GEAR PAIRS USING A THREE-DIMENSIONAL MODEL, in: DETC2009: PROCEEDINGS OF THE ASME INTERNATIONAL DESIGN ENGINEERING TECHNICAL CONFERENCES/COMPUTERS AND INFORMATION IN ENGINEERING CONFERENCE, 2010: pp. 149–165.

- [76] J. Wei, A. Zhang, G. Wang, D. Qin, T.C. Lim, Y. Wang, T. Lin, A study of nonlinear excitation modeling of helical gears with Modification: Theoretical analysis and experiments, MECHANISM AND MACHINE THEORY 128 (2018) 314–335. https://doi.org/10.1016/j.mechmachtheory.2018.06.005.
- [77] Q. Chen, Y. Wang, W. Tian, Y. Wu, Y. Chen, An improved nonlinear dynamic model of gear pair with tooth surface microscopic features, NONLINEAR DYNAMICS 96 (2019) 1615–1634. https://doi.org/10.1007/s11071-019-04874-1.
- [78] M. Molaie, F.S. Samani, H. Motahar, Nonlinear vibration of crowned gear pairs considering the effect of Hertzian contact stiffness, SN APPLIED SCIENCES 1 (2019). https://doi.org/10.1007/s42452-019-0439-y.
- [79] Z. Geng, K. Xiao, J. Wang, J. Li, Nonlinear Dynamic Analysis of a Rigid-Flexible Gear Transmission Considering Geometric Eccentricities, JOURNAL OF COMPUTATIONAL AND NONLINEAR DYNAMICS 15 (2020). https://doi.org/10.1115/1.4047336.
- [80] P. Liu, L. Zhu, X. Gou, J. Shi, G. Jin, Modeling and analyzing of nonlinear dynamics for spur gear pair with pitch deviation under multi-state meshing, MECHANISM AND MACHINE THEORY 163 (2021). https://doi.org/10.1016/j.mechmachtheory.2021.104378.
- [81] R. Xu, J. Zhang, J. Wang, R. Li, Research on nonlinear dynamic model and characteristics of a spur gear pair considering the meshing state of multiple pairs of teeth, JOURNAL OF ADVANCED MECHANICAL DESIGN SYSTEMS AND MANUFACTURING 15 (2021). https://doi.org/10.1299/jamdsm.2021jamdsm0068.
- [82] N. Gao, S. Wang, M.A.U.R. Bajwa, Nonlinear dynamics of a spur gear pair with tooth root crack based on an amplitude modulation function, ENGINEERING COMPUTATIONS 39 (2022) 1575–1596. https://doi.org/10.1108/EC-06-2020-0334.
- [83] A. Donmez, A. Kahraman, Characterization of Nonlinear Rattling Behavior of a Gear Pair Through a Validated Torsional Model, JOURNAL OF COMPUTATIONAL AND NONLINEAR DYNAMICS 17 (2022). https://doi.org/10.1115/1.4053367.
- [84] C.G. Cooley, R.G. Parker, A Review of Planetary and Epicyclic Gear Dynamics and Vibrations Research, Applied Mechanics Reviews 66 (2014). https://doi.org/10.1115/1.4027812.
- [85] A. Kahraman, Planetary gear train dynamics, Journal of Mechanical Design, Transactions of the ASME 116 (1994) 713–720. https://doi.org/10.1115/1.2919441.

- [86] M. Yin, G. Chen, H. Su, Theoretical and experimental studies on dynamics of double-helical gear system supported by journal bearings, Advances in Mechanical Engineering 8 (2016) 1–13. https://doi.org/10.1177/1687814016646977.
- [87] C.G. Cooley, R.G. Parker, S.M. Vijayakar, A frequency domain finite element approach for three-dimensional gear dynamics, Journal of Vibration and Acoustics, Transactions of the ASME 133 (2011). https://doi.org/10.1115/1.4003399.
- [88] R.G. Parker, V. Agashe, S.M. Vijayakar, Dynamic response of a planetary gear system using a finite element/contact mechanics model, Journal of Mechanical Design, Transactions of the ASME 122 (2000) 304–310. https://doi.org/10.1115/1.1286189.
- [89] V. Abousleiman, P. Velex, A hybrid 3D finite element/lumped parameter model for quasi-static and dynamic analyses of planetary/epicyclic gear sets, Mechanism and Machine Theory 41 (2006) 725–748. https://doi.org/https://doi.org/10.1016/j.mechmachtheory.2005.09.005.
- [90] V. Abousleiman, P. Velex, S. Becquerelle, Modeling of spur and helical gear planetary drives with flexible ring gears and planet carriers, Journal of Mechanical Design, Transactions of the ASME 129 (2007) 95–106. https://doi.org/10.1115/1.2359468.
- [91] S. Portron, P. Velex, V. Abousleiman, A hybrid model to study the effect of tooth lead modifications on the dynamic behavior of double helical planetary gears, Proceedings of the Institution of Mechanical Engineers, Part C: Journal of Mechanical Engineering Science 233 (2019) 7224–7235. https://doi.org/10.1177/0954406219846156.
- [92] C. Liu, Z. Fang, F. Wang, An improved model for dynamic analysis of a double-helical gear reduction unit by hybrid user-defined elements: Experimental and numerical validation, Mechanism and Machine Theory 127 (2018) 96–111. https://doi.org/https://doi.org/10.1016/j.mechmachtheory.2018.04.022.
- [93] A. Kahraman, A.A. Kharazi, M. Umrani, A deformable body dynamic analysis of planetary gears with thin rims, Journal of Sound and Vibration 262 (2003) 752–768. https://doi.org/10.1016/S0022-460X(03)00122-6.
- [94] C. Wang, J. Wei, Z. Wu, L. Lu, H. Gao, Load Sharing Performance of Herringbone Planetary Gear System with Flexible Pin, International Journal of Precision Engineering and Manufacturing 20 (2019) 2155–2169. https://doi.org/10.1007/s12541-019-00236-4.

- [95] T.M. Ericson, R.G. Parker, Experimental measurement and finite element simulation of elastic-body vibration in planetary gears, Mechanism and Machine Theory 160 (2021)
 https://doi.org/https://doi.org/10.1016/j.mechmachtheory.2021.104264.
- [96] X. Guan, J. Tang, Z. Hu, Q. Wang, X. Kong, A new dynamic model of light-weight spur gear transmission system considering the elasticity of the shaft and gear body, Mechanism and Machine Theory 170 (2022) 104689. https://doi.org/https://doi.org/10.1016/j.mechmachtheory.2021.104689.
- [97] H. Ge, Y. Shen, Y. Zhu, Y. Xiong, B. Yuan, Z. Fang, Simulation and experimental test of load-sharing behavior of planetary gear train with flexible ring gear, Journal of Mechanical Science and Technology 35 (2021) 4875–4888. https://doi.org/10.1007/s12206-021-1006-1.
- [98] A. Kahraman, Natural Modes of Planetary Gear Trains, Journal of Sound and Vibration 173 (1994) 125–130. https://doi.org/10.1006/jsvi.1994.1222.
- [99] A. Saada, P. Velex, An Extended Model for the Analysis of the Dynamic Behavior of Planetary Trains, Journal of Mechanical Design 117 (1995) 241–247. https://doi.org/10.1115/1.2826129.
- [100] J. Lin, R.G. Parker, Analytical characterization of the unique properties of planetary gear free vibration, Journal of Vibration and Acoustics, Transactions of the ASME 121 (1999) 316–321. https://doi.org/10.1115/1.2893982.
- [101] D.R. Kiracofe, R.G. Parker, Structured vibration modes of general compound planetary gear systems, Journal of Vibration and Acoustics, Transactions of the ASME 129 (2007) 1–16. https://doi.org/10.1115/1.2345680.
- [102] W. Sun, X. Ding, J. Wei, X. Hu, Q. Wang, An analyzing method of coupled modes in multi-stage planetary gear system, International Journal of Precision Engineering and Manufacturing 15 (2014) 2357–2366. https://doi.org/10.1007/s12541-014-0601-9.
- [103] W. Sun, X. Ding, J. Wei, A. Zhang, A method for analyzing sensitivity of multi-stage planetary gear coupled modes to modal parameters, Journal of Vibroengineering 17 (2015) 3133–3146.
- [104] A. Kahraman, Load sharing characteristics of planetary transmissions, Mechanism and Machine Theory 29 (1994) 1151–1165. https://doi.org/10.1016/0094-114X(94)90006-X.
- [105] A. Kahraman, Static load sharing characteristics of transmission planetary gear sets:

- Model and experiment, SAE Technical Papers (1999). https://doi.org/10.4271/1999-01-1050.
- [106] A. Bodas, A. Kahraman, Influence of carrier and gear manufacturing errors on the static load sharing behavior of planetary gear sets, JSME International Journal, Series C: Mechanical Systems, Machine Elements and Manufacturing 47 (2004) 908–915. https://doi.org/10.1299/jsmec.47.908.
- [107] H. Ligata, A. Kahraman, A. Singh, A closed-form planet load sharing formulation for planetary gear sets using a translational analogy, Journal of Mechanical Design, Transactions of the ASME 131 (2009) 0210071-0210077. https://doi.org/10.1115/1.3042160.
- [108] B. Boguski, A. Kahraman, T. Nishino, A new method to measure planet load sharing and sun gear radial orbit of planetary gear sets, Proceedings of the ASME Design Engineering Technical Conference 8 (2011) 169–180. https://doi.org/10.1115/DETC2011-47196.
- [109] N.D. Leque, A. Kahraman, A three-dimensional load sharing model of planetary gear sets having manufacturing errors, Proceedings of the ASME Design Engineering Technical Conference (2015). https://doi.org/10.1115/DETC201547470.
- [110] M. Benatar, D. Talbot, A. Kahraman, An experimental investigation of the load distribution of splined joints under gear loading conditions, Journal of Advanced Mechanical Design, Systems and Manufacturing 11 (2017). https://doi.org/10.1299/jamdsm.2017jamdsm0084.
- [111] Y. Hu, D. Talbot, A. Kahraman, A Load Distribution Model for Planetary Gear Sets, Journal of Mechanical Design 5 (2017). https://doi.org/10.1115/detc2017-68354.
- [112] Y. Hu, D. Talbot, A. Kahraman, A Gear Load Distribution Model for a Planetary Gear Set with a Flexible Ring Gear Having External Splines, Journal of Mechanical Design, Transactions of the ASME 141 (2019). https://doi.org/10.1115/1.4041583.
- [113] A. Singh, Load sharing behavior in epicyclic gears: Physical explanation and generalized formulation, Mechanism and Machine Theory 45 (2010) 511–530. https://doi.org/10.1016/j.mechmachtheory.2009.10.009.
- [114] M. Iglesias, A. Fernandez del Rincon, A. de-Juan, P. Garcia, A. Diez-Ibarbia, F. Viadero, Planetary transmission load sharing: Manufacturing errors and system configuration study, Mechanism and Machine Theory 111 (2017) 21–38. https://doi.org/10.1016/j.mechmachtheory.2016.12.010.

- [115] J. Sanchez-Espiga, A. Fernandez-del-Rincon, M. Iglesias, F. Viadero, Influence of errors in planetary transmissions load sharing under different mesh phasing, Mechanism and Machine Theory 153 (2020). https://doi.org/10.1016/j.mechmachtheory.2020.104012.
- [116] J. Sanchez-Espiga, A. Fernandez-del-Rincon, M. Iglesias, F. Viadero, Planetary gear transmissions load sharing measurement from tooth root strains: Numerical evaluation of mesh phasing influence, Mechanism and Machine Theory 163 (2021). https://doi.org/10.1016/j.mechmachtheory.2021.104370.
- [117] J. Sanchez-Espiga, A. Fernandez-del-Rincon, M. Iglesias, F. Viadero, Numerical evaluation of the accuracy in the load sharing calculation using strain gauges: Sun and ring gear tooth root, Mechanism and Machine Theory 175 (2022). https://doi.org/10.1016/j.mechmachtheory.2022.104923.
- [118] A. Kahraman, G.W. Blankenship, Planet Mesh Phasing in Epicyclic Gear Sets, International Gearing Conference (1994) 99–104.
- [119] R.G. Parker, J. Lin, Mesh Phasing Relationships in Planetary and Epicyclic Gears, Proceedings of the ASME Design Engineering Technical Conference 4 A (2003) 525–534. https://doi.org/10.1115/detc2003/ptg-48067.
- [120] Y. Guo, R.G. Parker, Analytical determination of mesh phase relations in general compound planetary gears, Mechanism and Machine Theory 46 (2011) 1869–1887. https://doi.org/10.1016/j.mechmachtheory.2011.07.010.
- [121] S.V. Canchi, R.G. Parker, Effect of ring-planet mesh phasing and contact ratio on the parametric instabilities of a planetary gear ring, Journal of Mechanical Design, Transactions of the ASME 130 (2008). https://doi.org/10.1115/1.2803716.
- [122] C. Wang, R.G. Parker, Dynamic modeling and mesh phasing-based spectral analysis of quasi-static deformations of spinning planetary gears with a deformable ring, Mechanical Systems and Signal Processing 136 (2020). https://doi.org/10.1016/j.ymssp.2019.106497.
- [123] C. Wang, B. Dong, R.G. Parker, Impact of planet mesh phasing on the vibration of three-dimensional planetary/epicyclic gears, Mechanism and Machine Theory 164 (2021). https://doi.org/10.1016/j.mechmachtheory.2021.104422.
- [124] X. Gu, P. Velex, On the dynamic simulation of eccentricity errors in planetary gears,

 Mechanism and Machine Theory 61 (2013) 14–29.

 https://doi.org/10.1016/j.mechmachtheory.2012.10.003.

- [125] F. Ren, A. Li, G. Shi, X. Wu, N. Wang, The effects of the planet-gear manufacturing eccentric errors on the dynamic properties for herringbone planetary gears, Applied Sciences (Switzerland) 10 (2020). https://doi.org/10.3390/app10031060.
- [126] Z. Cao, Y. Shao, M. Rao, W. Yu, Effects of the gear eccentricities on the dynamic performance of a planetary gear set, Nonlinear Dynamics 91 (2018) 1–15. https://doi.org/10.1007/s11071-017-3738-0.
- [127] H. Dong, C. Zhang, S. Bai, D. Wang, Modeling, Analysis and Testing of Load Distribution for Planetary Gear Trains with 3D Carrier Pinhole Position Errors, International Journal of Precision Engineering and Manufacturing 20 (2019) 1381– 1394. https://doi.org/10.1007/s12541-019-00166-1.
- [128] W. Liu, J. Li, Y. Kang, Y. Liu, X. Xu, P. Dong, Load Sharing Behavior of Double-Pinion Planetary Gear Sets Considering Manufacturing Errors, IOP Conference Series: Materials Science and Engineering 677 (2019). https://doi.org/10.1088/1757-899X/677/5/052068.
- [129] Z. Xu, W. Yu, Y. Shao, X. Yang, C. Nie, D. Peng, Dynamic modeling of the planetary gear set considering the effects of positioning errors on the mesh position and the corner contact, Nonlinear Dynamics (2022). https://doi.org/10.1007/s11071-022-07570-9.
- [130] P. Sondkar, A. Kahraman, A dynamic model of a double-helical planetary gear set,

 Mechanism and Machine Theory 70 (2013) 157–174.

 https://doi.org/https://doi.org/10.1016/j.mechmachtheory.2013.07.005.
- [131] Sondkar Prashant, Dynamic Modeling of Double-Helical Planetary Gear Sets, The Ohio State University, 2012.
- [132] W. Tan, J. Wu, D. Ni, H. Yan, E. Xiang, S. Liu, Dynamic Modeling and Simulation of Double-Planetary Gearbox Based on Bond Graph, Mathematical Problems in Engineering 2021 (2021). https://doi.org/10.1155/2021/3964808.
- [133] Z. Sheng, J. Tang, S. Chen, Z. Hu, Modal Analysis of Double-Helical Planetary Gears with Numerical and Analytical Approach, Journal of Dynamic Systems, Measurement and Control, Transactions of the ASME 137 (2015). https://doi.org/10.1115/1.4028788.
- [134] S. Mo, Y. Zhang, Q. Wu, H. Houjoh, S. Matsumura, Research on natural characteristics of double-helical star gearing system for GTF aero-engine, Mechanism and Machine Theory 106 (2016) 166–189.

- https://doi.org/10.1016/j.mechmachtheory.2016.09.001.
- [135] M. K Khoozani, M. Poursina, A. P Anaraki, Study of gyroscopic effects on the dynamics and vibrations of double-helical planetary gear set, Proceedings of the Institution of Mechanical Engineers, Part K: Journal of Multi-Body Dynamics 232 (2017) 199–223. https://doi.org/10.1177/1464419317725947.
- [136] M. Chapron, X. Gu, P. Velex, S. Becquerelle, A simplified 3D dynamic model of helical and double-helical planetary gears to study the influence of some usual position and geometrical errors, in: International Gear Conference 2014: 26th–28th August 2014, Lyon, Elsevier, 2014: pp. 879–888. https://doi.org/10.1533/9781782421955.879.
- [137] S. Wang, C. Zhang, F. Wang, The analysis of dynamic load coefficients of double-helical planetary gear sets, in: P. Velex (Ed.), International Gear Conference 2014: 26th–28th August 2014, Lyon, 2014: pp. 889–895. https://doi.org/10.1533/9781782421955.889.
- [138] B. Schlecht, T. Schulze, K. Riedel, Tooth contact analysis under load on double helical-geared planetary gearboxes, in: VDI Berichte, 2017: pp. 1596–1609. https://doi.org/10.51202/9783181022948-83.
- [139] M. Chapron, P. Velex, J. Bruyère, S. Becquerelle, Optimization of profile modifications with regard to dynamic tooth loads in single and double-helical planetary gears with flexible ring-gears, Journal of Mechanical Design, Transactions of the ASME 138 (2016). https://doi.org/10.1115/1.4031939.
- [140] N.D. Leque, Development of Load Sharing Models for Double-Helical Epicyclic Gear Sets Dissertation, The Ohio State University, 2015.
- [141] J. Goetz, F. Siglmueller, M. Fuerst, M. Otto, K. Stahl, Experimental investigation of the dynamic load sharing of planetary gearboxes, FORSCHUNG IM INGENIEURWESEN-ENGINEERING RESEARCH (2021). https://doi.org/10.1007/s10010-021-00507-5.
- [142] X. Liu, Z. Fang, H. Jia, N. Zhao, Y. Shen, H. Guo, X. Zhang, Investigation of Load Sharing and Dynamic Load Characteristics of a Split Torque Transmission System with Double-Helical Gear Modification, Shock and Vibration 2021 (2021). https://doi.org/10.1155/2021/9912148.
- [143] F. Lu, R. Zhu, H. Wang, H. Bao, M. Li, Dynamic characteristics of double helical planetary gear train with tooth friction, in: Proceedings of the ASME Design

- Engineering Technical Conference, 2015. https://doi.org/10.1115/DETC201548022.
- [144] C. Wang, The effect of planetary gear/star gear on the transmission efficiency of closed differential double helical gear train, Proceedings of the Institution of Mechanical Engineers, Part C: Journal of Mechanical Engineering Science 234 (2020) 4215–4223. https://doi.org/10.1177/0954406220921205.
- [145] C. Hu, G. Geng, P.D. Spanos, Stochastic dynamic load-sharing analysis of the closed differential planetary transmission gear system by the Monte Carlo method, Mechanism and Machine Theory 165 (2021) 104420. https://doi.org/10.1016/j.mechmachtheory.2021.104420.
- [146] J. Xu, C. Jiao, D. Zou, N. Ta, Z. Rao, Dynamic Stability Research on the Double-Cylinder Turbines Marine Propulsion System With Unsymmetrical Load, Journal of Computational and Nonlinear Dynamics 16 (2021). https://doi.org/10.1115/1.4051995.
- [147] M. Inalpolat, A. Kahraman, A theoretical and experimental investigation of modulation sidebands of planetary gear sets, Journal of Sound and Vibration 323 (2009) 677–696. https://doi.org/10.1016/j.jsv.2009.01.004.
- [148] D. Peng, W.A. Smith, R.B. Randall, Z. Peng, Use of mesh phasing to locate faulty planet gears, Mechanical Systems and Signal Processing 116 (2019) 12–24. https://doi.org/10.1016/j.ymssp.2018.06.035.
- [149] J. Wei, A. Zhang, D. Qin, T.C. Lim, R. Shu, X. Lin, F. Meng, A coupling dynamics analysis method for a multistage planetary gear system, Mechanism and Machine Theory 110 (2017) 27–49. https://doi.org/https://doi.org/10.1016/j.mechmachtheory.2016.12.007.
- [150] M. AJMI, P. VELEX, GDN-24 A MODEL FOR SIMULATING THE QUASI-STATIC AND DYNAMIC BEHAVIOUR OF DOUBLE HELICAL GEARS(GEAR DYNAMICS AND NOISE), The Proceedings of the JSME International Conference on Motion and Power Transmissions I.01.202 (2001) 132–137. https://doi.org/10.1299/jsmeimpt.I.01.202.132.
- [151] Y. Hu, L. Ryali, D. Talbot, A. Kahraman, A theoretical study of the overall transmission error in planetary gear sets, in: Proceedings of the Institution of Mechanical Engineers, Part C: Journal of Mechanical Engineering Science, 2019: pp. 7200–7211. https://doi.org/10.1177/0954406219830436.
- [152] M. Maatar, P. Velex, An analytical expression for the time-varying contact length in

- perfect cylindrical gears: Some possible applications in gear dynamics, Journal of Mechanical Design, Transactions of the ASME 118 (1996) 586–589. https://doi.org/10.1115/1.2826933.
- [153] R.G. Parker, J. Lin, Mesh Phasing Relationships in Planetary and Epicyclic Gears, Journal of Mechanical Design 126 (2004) 365–370. https://doi.org/10.1115/1.1667892.
- [154] G. Huo, M. Iglesias-Santamaria, X. Zhang, J. Sanchez-Espiga, E. Caso-Fernandez, Y. Jiao, F. Viadero-Rueda, Influence of eccentricity error on the orbit of a two-stage double-helical compound planetary gear train with different mesh phasing configurations, Mechanism and Machine Theory 196 (2024) 105634. https://doi.org/https://doi.org/10.1016/j.mechmachtheory.2024.105634.
- [155] G. Huo, J. Sanchez-Espiga, M.I. Santamaria, A. Fernandez-Del-Rincon, Y. Jiao, F. Viadero-Rueda, Influence of Manufacturing Errors on the Behaviour of a Two-Stage Planetary Gear Train, Dyna (Spain) 98 (2023) 384–390. https://doi.org/10.6036/10879.
- [156] S. Li, Q. Wu, Z. Zhang, Bifurcation and chaos analysis of multistage planetary gear train, Nonlinear Dynamics 75 (2014) 217–233. https://doi.org/10.1007/s11071-013-1060-z.
- [157] Q. Zhang, X. Wang, S. Wu, S. Cheng, F. Xie, Nonlinear characteristics of a multi-degree-of-freedom wind turbine's gear transmission system involving friction, Nonlinear Dynamics 107 (2022) 3313–3338. https://doi.org/10.1007/s11071-021-07092-w.

Appendix

A.1 Timoshenko Beam Element Matrices

Considering Timoshenko beam with 12-DOF as a connecting structure due to shear deformation, as shown in Fig.A1, nodes j and j+1 make up an element, l is length of the element. Therefore, the displacement vector of the element is shown as follows.

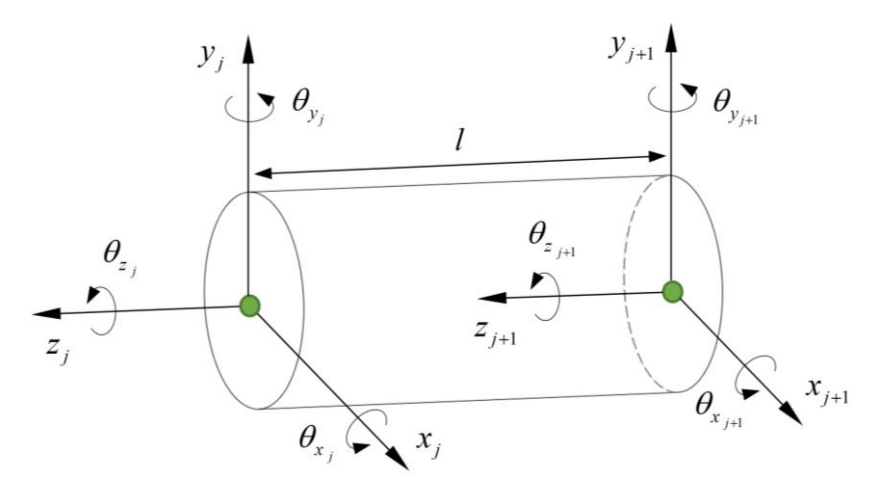


Fig.A1 A Timoshenko beam element

$$q^{(e)} = \begin{bmatrix} x_j & y_j & z_j & \theta_{x_j} & \theta_{y_j} & \theta_{z_j} & x_{j+1} & y_{j+1} & z_{j+1} & \theta_{x_{j+1}} & \theta_{y_{j+1}} & \theta_{z_{j+1}} \end{bmatrix}$$

where, x_j , y_j , z_j , x_{j+1} , y_{j+1} , z_{j+1} are translation displacement of two nodes j and j+1 along the x, y, and z axes, separately. θ_{x_j} , θ_{y_j} , θ_{z_j} , $\theta_{x_{j+1}}$, $\theta_{y_{j+1}}$, $\theta_{z_{j+1}}$ are angular displacement of two nodes j and j+1 rotated about the x, y, and z axes, respectively.

The free vibration equation of Timoshenko beam element is obtained.

$$\mathbf{M}^{(e)}\left\{\ddot{q}^{(e)}\right\} + (\Omega \mathbf{G}^{(e)})\left\{\dot{q}^{(e)}\right\} + \mathbf{K}^{(e)}\left\{q^{(e)}\right\} = \mathbf{0}$$

in which, Ω is the rotational speed, $\mathbf{M}^{(e)}, \mathbf{G}^{(e)}, \mathbf{K}^{(e)}$ are mass, stiffness and gyroscopic matrix, respectively.

A.1.1 Element Mass Matrix

Timoshenko beam element mass matrix is given as follows:

where, the letters in the matrix are defined as follows.

$$a = \frac{\rho A l}{(1+\Phi)^2} \left[\frac{13}{35} + \frac{7}{10} \Phi + \frac{1}{3} \Phi^2 + \frac{6}{5} \left(\frac{r_g}{l} \right)^2 \right],$$

$$b = \frac{\rho A l}{(1+\Phi)^2} \left[\frac{9}{70} + \frac{3}{10} \Phi + \frac{1}{6} \Phi^2 - \frac{6}{5} \left(\frac{r_g}{l} \right)^2 \right],$$

$$c = \frac{\rho A l^2}{(1+\Phi)^2} \left[\frac{11}{210} + \frac{11}{120} \Phi + \frac{1}{24} \Phi^2 + \left(\frac{1}{10} - \frac{1}{2} \Phi \right) \left(\frac{r_g}{l} \right)^2 \right],$$

$$d = \frac{\rho A l^2}{(1+\Phi)^2} \left[\frac{13}{420} + \frac{3}{40} \Phi + \frac{1}{24} \Phi^2 - \left(\frac{1}{10} - \frac{1}{2} \Phi \right) \left(\frac{r_g}{l} \right)^2 \right],$$

$$f = -\frac{\rho A l^3}{(1+\Phi)^2} \left[\frac{1}{140} + \frac{1}{60} \Phi + \frac{1}{120} \Phi^2 + \left(\frac{1}{30} + \frac{1}{6} \Phi - \frac{1}{6} \Phi^2 \right) \left(\frac{r_g}{l} \right)^2 \right],$$

$$g = \frac{\rho A l^3}{(1+\Phi)^2} \left[\frac{1}{105} + \frac{1}{60} \Phi + \frac{1}{120} \Phi^2 + \left(\frac{2}{15} + \frac{1}{6} \Phi + \frac{1}{3} \Phi^2 \right) \left(\frac{r_g}{l} \right)^2 \right],$$

$$r_g = \sqrt{\frac{I}{A}}, \quad \Phi = \frac{12EI}{K'GAl^2}.$$

where, A is shaft cross sectional area, E is young's modulus, G is shear modulus, I is the area moment of inertia, J is polar moment of inertia moment of inertia, lis length of element, r_g is the radius of gyration, Φ is transverse shear parameter. K' is shape factor, relating to shape of cross section, which is given as.

$$K' = \begin{cases} 6(1+\mu)/(7+6\mu), & \text{circular section} \\ 6(1+\mu)(1+m^2)^2/\left\{(7+6\mu)(1+m^2)^2+(20+12\mu)m^2\right\}, & \text{hollow circular section} \\ 10(1+\mu)/(12+11\mu), & \text{rectangular section} \\ 2(1+\mu)/(4+3\mu), & \text{thin-walled tube section} \end{cases}$$

where, μ is Poisson's Ratio, m=r/R, r and R are radius of section.

A.1.2 Element Stiffness Matrix

Timoshenko beam element stiffness matrix is obtained as sum of three matrices, which is given as follows:

$$\mathbf{K}^{(e)} = \begin{bmatrix} a & & & & & & & & & & & \\ 0 & a & & & & & & & & \\ 0 & 0 & \frac{AE}{l} & & & & sym \\ 0 & -b & 0 & c & & & & \\ b & 0 & 0 & 0 & c & & & \\ 0 & 0 & 0 & 0 & 0 & \frac{JG}{l} & & & & \\ -a & 0 & 0 & 0 & -b & 0 & a & & \\ 0 & -a & 0 & b & 0 & 0 & 0 & a & & \\ 0 & -a & 0 & b & 0 & 0 & 0 & 0 & \frac{AE}{l} & & & \\ 0 & -b & 0 & d & 0 & 0 & 0 & b & 0 & c & & \\ b & 0 & 0 & 0 & d & 0 & -b & 0 & 0 & 0 & c & \\ b & 0 & 0 & 0 & d & 0 & -b & 0 & 0 & 0 & \frac{JG}{l} \end{bmatrix}$$

in which, the letters are defined as

$$a = \frac{12EI}{l^3(1+\Phi)}, b = \frac{6EI}{l^2(1+\Phi)}, c = \frac{(4+\Phi)EI}{l(1+\Phi)}, d = \frac{(2-\Phi)EI}{l(1+\Phi)}$$

A.1.3 Element Gyroscopic Matrix

Timoshenko beam element gyroscopic matrix is given as follows:

in which,

$$a = \frac{\rho A l}{(1+\Phi)^2} \frac{6}{5} \left(\frac{r_g}{l}\right)^2,$$

$$b = -\frac{\rho A l}{(1+\Phi)^2} \left(\frac{1}{10} - \frac{1}{2}\Phi\right) \left(\frac{r_g}{l}\right)^2,$$

$$c = \frac{\rho A l}{(1+\Phi)^2} \left(\frac{2}{15} + \frac{1}{6}\Phi - \frac{1}{3}\Phi^2\right) r_g^2,$$

$$d = -\frac{\rho A l}{(1+\Phi)^2} \left(\frac{1}{30} + \frac{1}{6}\Phi - \frac{1}{6}\Phi^2\right) r_g^2.$$

Papers Published in the Period of Ph.D. Education

- [1] Guanghe Huo, Miguel Iglesias-Santamaria, Xiang Zhang, Javier Sanchez-Espiga, Enrique Caso-Fernandez, Yinghou Jiao, Fernando Viadero-Rueda. Influence of eccentricity error on the orbit of a two-stage double-helical compound planetary gear train with different mesh phasing configurations. Mechanism and Machine Theory, 2024, 196: 105634.
 - DOI: https://doi.org/10.1016/j.mechmachtheory.2024.105634
- [2] Guanghe Huo, Javier Sanchez-Espiga, Miguel Iglesias-Santamaria, Alfonso Fernandez-Del-Rincon, Yinghou Jiao, Fernando Viadero-Rueda. INFLUENCE OF MANUFACTURING ERRORS ON THE BEHAVIOUR OF A TWO-STAGE PLANETARY GEAR TRAIN. DYNA. 2023, 98(4), 384-390. DOI: https://doi.org/10.6036/10879
- [3] **Huo, G**. et al. (2024). Torsional Vibration Modelling of a Two-Stage Closed Differential Planetary Gear Train. In: Chu, F., Qin, Z. (eds) Proceedings of the 11th IFToMM International Conference on Rotordynamics. IFToMM 2023. Mechanisms and Machine Science, vol 140. Springer, Cham.

DOI: https://doi.org/10.1007/978-3-031-40459-7 13

Ackowledgement

I would like to express my sincere appreciation to my supervisors, Prof. Dr. Fernando Viadero Rueda and Prof. Dr. Miguel Iglesias Santamaria, from the University of Cantabria for accepting me as their student. Their professional guidance, valuable suggestions, and enduring patience during my entire PhD studies have been invaluable to me. I also want to thank my advisor, Prof. Dr. Yinghou Jiao from the Harbin Institute of Technology, for enduring supporting my visiting study and life at the University of Cantabria. It is a great honor to work with my supervisors. I would also like to thank all members of the jury for their careful and professional review suggestions improving my doctoral thesis.

I would like to take this opportunity to express my heartfelt gratitude to Dr. Alfonso Fernandez-Del-Rincon, Dr. Enrique Caso Fernandez, Dr. Javier Sanchez Espiga, Dr. Alberto Diez Ibarbia, Dr. Pablo Garcia Fernandez, Dr. Ana Magdalena De Juan De Luna, Dr. Ala Eddin Chakroun, Mr. Adrián Solórzano Terán and Ms. Kasia Słupik for helping me in all aspects, whenever I ask for help. I will never forget the experience of working and living with them at Santander.

I would also like to express my special thanks to my friends: Ms. Jingyun Gui, Ms. Mohan Liu, Ms. Fan Zhang, and Mr. Shuowen Yang for their kind help and companionship during my visiting and learning trip to Italy, Vatican, France, Portugal, and Spain.

Furthermore, I would like to gratefully acknowledge the financing of my stay at the University of Cantabria by means of the CSC (China Scholarship Council) grant number 202106120133, which is financed by the government of the People's Republic of China.

Finally, I would like to express my appreciation to my parents (Mr. Shirui Huo and Ms. Lianxiang Zhang), my grandparents (Mr. Yuzhi Huo and Ms. Baolian

Du), my grandaunt and granduncle (Mr. Youshan Gao and Ms. Yuzhi Zhang) for their love and care. I am very grateful to my parents, two ordinary and diligent Chinese farmers, for raising me and supporting me on my way to study, no word can describe their love and devotion to me.